Universidad de Málaga
Escuela Técnica Superior de Ingeniería de Telecomunicación
(Programa de doctorado en Ingeniería de Telecomunicación)

TESIS DOCTORAL

High-Performance Integrated Photonic Systems for Near- and Mid-Infrared Sensing Applications

Autora:

Antonia Torres Cubillo

Directores:

Robert Halir
Íñigo Molina Fernández

2025

DECLARACIÓN DE AUTORÍA Y ORIGINALIDAD DE LA TESIS PRESENTADA PARA OBTENER EL TÍTULO DE DOCTOR

D./Dña ANTONIA TORRES CUBILLO
Estudiante del programa de doctorado EN INGENIERÍA DE TELECOMUNICACIÓN de la Universidad de Málaga, autor/a de la tesis, presentada para la obtención del título de doctor por la Universidad de Málaga, titulada: HIGH-PERFORMANCE INTEGRATED PHOTONIC SYSTEMS FOR NEAR- AND MIR-INFRARED SENSING APPLICATIONS

Realizada bajo la tutorización de ROBERT HALIR y dirección de ROBERT HALIR E ÍÑIGO MOLINA FERNÁNDEZ. (si tuviera varios directores deberá hacer constar el nombre de todos)

DECLARO QUE:

La tesis presentada es una obra original que no infringe los derechos de propiedad intelectual ni los derechos de propiedad industrial u otros, conforme al ordenamiento jurídico vigente (Real Decreto Legislativo 1/1996, de 12 de abril, por el que se aprueba el texto refundido de la Ley de Propiedad Intelectual, regularizando, aclarando y armonizando las disposiciones legales vigentes sobre la materia), modificado por la Ley 2/2019, de 1 de marzo.

Igualmente asumo, ante a la Universidad de Málaga y ante cualquier otra instancia, la responsabilidad que pudiera derivarse en caso de plagio de contenidos en la tesis presentada, conforme al ordenamiento jurídico vigente.

En Málaga, a 17 de OCTUBRE de 2024

Fdo.: ANTONIA TORRES CUBILLO Doctorando/a	Fdo.: ROBERT HALIR Tutor/a
Fdo.: ROBERT HALIR Director/es de tesis	ÍÑIGO MOLINA FERNÁNDEZ

Yo, Robert Halir, tutor y director de la tesis titulada “High-performance photonic systems for near- and mid-infrared sensing applications”, realizada por la estudiante del programa de doctorado en Ingeniería de Telecomunicación Antonia Torres Cubillo, autorizo la lectura de dicha tesis doctoral.

De igual forma, confirmo que las publicaciones que avalan esta tesis no han sido utilizadas en tesis anteriores.

En Málaga, a 28 de octubre de 2024.

Fdo. Robert Halir
Director y tutor de tesis

Edificio Pabellón de Gobierno. Campus El Ejido. 29071
Tel.: 952 13 10 28 / 952 13 14 61 / 952 13 71 10
E-mail: doctorado@uma.es

Yo, Íñigo Molina Fernández, director de la tesis titulada “High-performance photonic systems for near- and mid-infrared sensing applications”, realizada por la estudiante del programa de doctorado en Ingeniería de Telecomunicación Antonia Torres Cubillo, autorizo la lectura de dicha tesis doctoral.

De igual forma, confirmo que las publicaciones que avalan esta tesis no han sido utilizadas en tesis anteriores.

En Málaga, a 28 de octubre de 2024.

Fdo. Íñigo Molina Fernández
Director de tesis

Edificio Pabellón de Gobierno. Campus El Ejido. 29071
Tel.: 952 13 10 28 / 952 13 14 61 / 952 13 71 10
E-mail: doctorado@uma.es

High-Performance Integrated Photonic Systems for Near- and Mid-Infrared Sensing Applications

Antonia Torres Cubillo

In memoriam Linda.

Agradecimientos

Esta tesis es el fruto del trabajo de cuatro años, complicados, en los que he recibido el apoyo, en distintos ámbitos y medidas, de muchas personas. Todas ellas han contribuido a que mis esfuerzos se hayan materializado en la consecución del título de doctora, al que yo le otorgo suma importancia. Por ello, quiero expresarles mi gratitud.

Desde que en 2017 me concedieron la Beca de Colaboración, he trabajado en el Photonics and RF Research Lab de la Universidad de Málaga bajo la dirección de Robert Halir. Fui primero becaria de grado, luego, de máster y, por último, investigadora predoctoral FPU, periodo que concluye con esta tesis. Con el paso de los años, Robert y yo, tan diferentes, hemos aprendido a trabajar cada vez mejor juntos. He de agradecerle, entre tantas cosas, su optimismo ante la adversidad, la claridad de sus ideas, su paciencia con mis particularidades, cómo ha sabido respetar y fomentar mi independencia. Agradezco también al resto de miembros del grupo el que hayan aportado sus distintos enfoques para abordar problemas enquistados. Especialmente, agradezco los consejos de Íñigo Molina, mi codirector de tesis, y de Gonzalo Wangüemert, capaz de cuestionar todo aquello que se da por sentado.

A lo largo del doctorado he tenido el privilegio de realizar dos estancias internacionales, que me dieron la oportunidad de trabajar junto a personas extraordinarias a quienes tengo mucho que agradecer. A la profesora Jana Jágerská le agradezco que me acogiese como a una más de su equipo en Tromsø, en 2022, cuando el mundo aún se agitaba por la pandemia. Jana, con su inteligencia y su bondad, no tardó en convertirse en un referente para mí, a quien admiro y en quien confío académica y personalmente. Le agradezco encarecidamente el tiempo que ha invertido en ayudarme, fuera y dentro del laboratorio, permitiéndome aprender tanto de ella. Sigo aprendiendo a día de hoy. El resto de compañeros de la UiT contribuyeron a que no me sintiese tan lejos de casa como realmente estaba. Agradezco a Jehona las conversaciones sinceras y las catas de té, a Henock su ayuda para preparar los chips en la *cleanroom* y a Marek su amabilidad y resolutividad, llegando a imprimirme en 3D la pieza que hizo que todo el sistema de medidas encajase.

Fue en Tromsø donde conocí al profesor Boris Mizaikoff, con quien volvería a coincidir en el ASCOS 2022, la escuela de verano, celebrada en otoño, a la que tuve la suerte de asistir. Allí, Boris me cautivó con su entusiasmo, contagioso, capaz de reavivar mi ilusión por la investigación. Con ese mismo entusiasmo, me recibió en Ulm en la primavera del 2023 para realizar mi segunda estancia. Le agradezco de corazón sus ánimos efusivos, la pasión con la que comparte sus conocimientos, que son tan amplios, y todas las oportunidades que me ha brindado. Su confianza en mí me ha ayudado a madurar científicamente y a creerme capaz de afrontar desafíos antes inimaginables. También agradezco a Andrea y Gabi los estimulantes intercambios de ideas que hicieron tan ameno y productivo mi tiempo en Ulm.

Fuera del ámbito académico, mi familia es mi mayor sostén. Mi padre, mi doctor de referencia, lleva ya una década aprendiendo, primero, telecomunicaciones, y, después,

fotónica, hasta especializarse en sensores y en espectroscopía infrarroja. Este aprendizaje lo ha realizado movido, en parte, por su curiosidad insaciable, pero, más que nada, por amor. Ha podido así seguir mi trayectoria al milímetro, celebrando cada avance y lamentando cada tropiezo. Viviéndolo todo a la par que yo. Con su implicación absoluta, no ha permitido jamás que afrontase nada sola. Le doy las gracias por acompañarme paso a paso, día a día. El equipo que formamos lo completan mi madre y mi hermana, ambas imprescindibles. Mi madre, incondicional, vive a la búsqueda constante de maneras de ayudarme, ya sea comprándome un detallito (paños, velas, calcetines) de manera espontánea, ofreciéndome la mejor comida cada domingo o, simplemente, animándome a descansar cuando nota que lo necesito. Aprecio y agradezco todas las energías que vuelca en mí. A Anita, mi hermana maravillosa, de la que me enorgullezco, le agradezco la complicidad constante, su cordura estética y las risas, las risas ante todo. Acumulamos grandes momentos en lo sencillo y cotidiano, que valen tanto. Juntos los cuatro, y con Linda —siempre— y Argos, convertimos nuestras casas, ya sea en Alhaurín o en la Mancha, en refugios de paz y de cariño. Es inmensa la suerte de que sean los míos.

Pero somos muchos más. A mi tata Fran, mi tía casi hermana, le agradezco las horas charlando durante nuestros animados viajes en coche, reivindicando el derecho a perdernos o a cambiar de ruta, porque al final acabamos llegando a nuestro destino. Agradezco también el apoyo de mi abuela Paqui, un ejemplo de carácter y fortaleza, y del resto de mis tíos y primos, en quienes siempre encuentro ánimos e interés por lo que hago. Por último, me es imposible obviar que quienes ya no viven, y por ello habitan dentro de mí, me han impulsado a lo largo de este camino. Así, no puedo acabar este apartado familiar sin acordarme de mi abuelo Alfonso, resolutivo, con su espíritu de verdadero ingeniero, y de mi abuelito Miguel, trabajador incansable, narrador de las mejores historias. Pero, sobre todo, me acuerdo de mi abuelita Sebastiana, que estaría tan orgullosa, y que habría movido cielo y tierra para conseguir que la trajesen al acto de defensa, ¡lo que lo hubiera disfrutado ella!

Reservo estas últimas líneas para Alejandro, quien, cuando nuestra historia no había hecho más que empezar, ya me dijo que la escritura de la tesis, para cuyo inicio faltaban aún dos años, sería un proceso duro, pero también bonito, en el que él querría acompañarme. Ha sido como predijo: duro, bonito y con él acompañándome. Ha estado a mi lado, ayudándome, desde el primer esbozo de este manuscrito, que inicié en Münster, hasta los últimos retoques de la versión definitiva, en la Navidad de 2024. Me regaló, en sucesivos cumpleaños, la tinta Kaweco y la pluma Lamy, ambas moradas, con las que he tomado tantas notas, disfrutando cada vez. Compartió conmigo su licencia de Affinity Designer para que pudiese elaborar mejores figuras. Ha sido mi mayor consejero. Todo cuanto ha hecho, se lo agradezco, pero, más allá de eso, le doy las gracias por la conversación interminable en la que vivimos, por cuidarme siempre, animarme siempre, creer en mí más que yo misma. A Alejandro, mi par y mi amor, le agradezco que me acompañe no ya en la tesis, sino en la vida.

Antonia
Málaga, enero de 2025

The research work leading to this doctoral thesis has been funded by a Formación del Profesorado Universitario grant (FPU19/03330) from the Spanish Ministerio de Ciencia, Innovación y Universidades and by the Junta de Andalucía (Agencia Andaluza del Cononicimiento PY18-793).

Acronyms

AWGN Additive white Gaussian noise

BI Bimodal interferometer

BOX Buried oxide

BR Back-reflections

BSA Bovine serum albumin

CE Coupling efficiency

CMOS Complementary metal-oxide semiconductor

DAQ Data acquisition (board)

DI Deionized (water)

DSP Digital signal processing

EDFA Erbium-doped fiber amplifier

FA Fiber array

FEM Finite element method

FIB Focused ion beam

FIR Finite impulse response

FOM Figure of merit

FP Fabry-Pérot

FSR Free spectral range

FTIR Fourier transform infrared (spectroscopy)

FWHM Full width at half maximum

GC Grating coupler

GOS Germanium-on-silicon

GUI Graphical user interface

ICL Inter-band cascade laser

IL Insertion loss

IPA Isopropyl alcohol

IQ In-phase and quadrature

KK Kramers-Kronig (relations)

LOC Lab-on-chip

MFS Minimum feature size

MIR Mid-infrared

MM Multimode

MMI Multimode interference (coupler)

MPW Multi-project wafer

MSE Minimum squared error

MZI Mach-Zehnder interferometer

NIR Near-infrared

PC Photonic crystal

PCD Polycrystalline diamond

PD Photodetector

PDMS Polydimethylsiloxane

PIC Photonic integrated circuit

PML Perfectly matched layer

POC Point of care

PSD Power spectral density

QCL Quantum cascade laser

RIN Relative intensity noise

RR Ring resonator

SEM Scanning electron microscope

SiNOI SiN-on-insulator

SM Single-mode

SNR Signal-to-noise ratio

SOI Silicon-on-insulator

SWG Subwavelength grating

TDLAS Tunable diode laser absorption spectroscopy

TE Transverse electric

TFWG Thin-film waveguide

TIA Transimpedance amplifier

TM Transverse magnetic

UMZI Unbalanced Mach-Zehnder interferometer

VIS Visible

VOC Volatile organic compound

XT Cross-talk

Contents

Chapter 1

Introduction

Integrated photonic sensors are key to addressing many current global challenges, such as those derived from climate change and aging populations. These devices can precisely detect small quantities of the chemical substances involved in threatening processes, including greenhouse-effect gases or illness biomarkers. This thesis is concerned with advancing photonic sensing architectures for improved performance in different environmental and medical applications. In this introductory chapter, the motivation behind this work is explained (Section 1.1) and the field of optical sensing is presented (Section 1.2), showing how waveguide-based photonic sensors are powerful tools for the detection of critical analytes. Afterwards, the main contributions of this thesis are outlined (Section 1.3) and the organization of the document is described (Section 1.4).

1.1 Addressing XXI century challenges with photonic sensors

The Global Trends for 2040 report [1], published in April 2024 by the European Strategy and Policy Analysis System (ESPAS), defined the forthcoming era as one of polycrises. Of the different challenges identified in the document, current and future environmental emergencies and global health management stand out as two major concerns. Three out of the nine vital processes that maintain the stability of the planet, defined by the scientific community in the past decade [2, 3], have already been pushed beyond safety levels: climate change, loss of biodiversity and changes in the nitrogen cycle. Climate change is arguably the most visible of the former, especially in Europe, being the fastest-warming continent on Earth [4]. The massive emission of greenhouse gases, as carbon dioxide (CO_2), methane (CH_4) or nitrous oxide (N_2O), that results from human activity is the main cause of the accelerated global warming. In fact, the Intergovernmental Panel on Climate Change (IPCC) estimated that, compared to 2019 levels, a 43% reduction in global emissions by 2030, and a 69% by 2040, should be accomplished in order to limit the rising of temperatures to 1.5°C [5]. These goals seem unattainable with current policies, so a tougher global-scale pollution control is expected in the near future.

The environmental degradation imposes threats to human health [6], such as the spread of zoonotic diseases passed from animals to humans, increased health risks due to heat stress and even the possible emergence of ancient viruses from permafrost [7]. As the recent COVID-19 pandemic showed, the proliferation of contagious illnesses is vastly facilitated by globalization. Furthermore, the longer life expectancy achieved during the past decades, despite being a positive ongoing trend, induces a higher prevalence of age-related illnesses, e.g., cancer, diabetes and Alzheimer [8]. Longer-living humans, combined with a generalized decline in birth rates in developed countries, result in an increasingly aging global population with a higher demand for healthcare. However, the

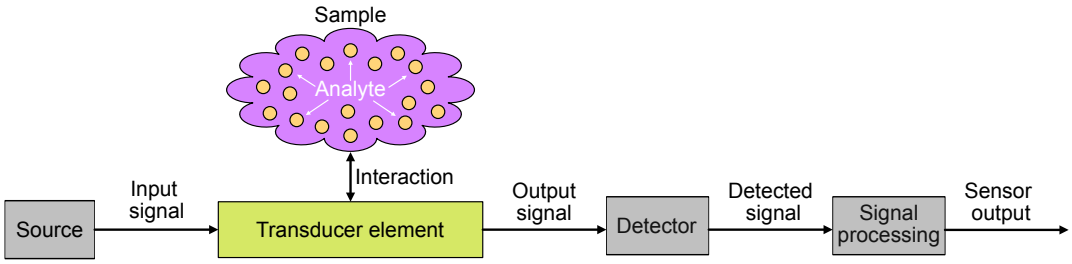

Figure 1.1: Schematic representation of a generic sensor, composed of a signal source, a transducer element, which is in contact with the sample containing the analyte, a signal detector and a signal processor.

impact of health inequalities is still significant. Even in advanced economies, like those of EU countries, a lower life expectancy is strongly correlated to a lower socio-economic position [9]. Finally, despite its huge economic footprint, amounting to 10.9% of EU's gross domestic product in 2020 [9], and being a major employer [10], the health sector is finding difficulties in recruiting highly skilled professionals since the pandemic. Knowing that the cost of early diagnosis is trivial compared to the economic consequences of large-scale disease [11], widely available rapid diagnosis tools have become essential.

A crucial step toward facing the highlighted challenges is detecting and monitoring the problem-causing substances, which may be pollutant gases, volatile organic compounds (VOCs), disease biomarkers or viruses. At this point, sensors play a decisive role [12, 13]. A generic sensor, as the one schematized in Fig. 1.1, can be defined as a device which detects or measures physical properties or their changes and provides a certain output or measurement in response [14]. In the case of gas and biological sensors, the device is usually composed of an input signal source, a transducer element, an output signal detector and a signal processing stage to produce the sensor output. The transducer element needs to be in contact with a sample where the target analyte is present, e.g., CO_2 in air or bovine serum albumin (BSA) protein in blood. Such sensors can be broadly classified according to the operating principle of the transducer element [15]. According to this criterion, sensors can be either optical [16, 17], electrochemical [18, 19], electrical [20, 21], mass-sensitive [22, 23], magnetic [24, 25] or thermal [26, 27], among others. For each of these categories, several implementation approaches have been proposed. Waveguide-based photonic sensors, which belong to the group of optical sensors, constitute the core of this thesis. Hence, a dedicated introduction to the field of optical sensing is provided in Section 1.2.

The desired characteristics of a sensor are generally shared by the different implementations, regardless of the type of transducer employed. In the first place, analytes should be detected in small amounts, as required for most sensing applications, i.e., the limit of detection (LOD) should be as small as possible. A low LOD benefits from a high sensitivity, defined as the relationship between the output signal and the concentration of analyte, and a low uncertainty in the read-out. Sensors yielding a quantitative output favor precise detection and monitoring. Furthermore, many use-cases require specificity, guaranteeing that the sensor only reacts to the targeted substance, thus avoiding the risk of false positives. Other interesting properties are label-free operation, compact size, cost-effectiveness, high detection speed and ease of use.

1.2 Optical sensors

The history of optical sensing dates back to the 16th century, when methods based on absorption, emission and fluorescence were first proposed, but did not achieve maturity un-

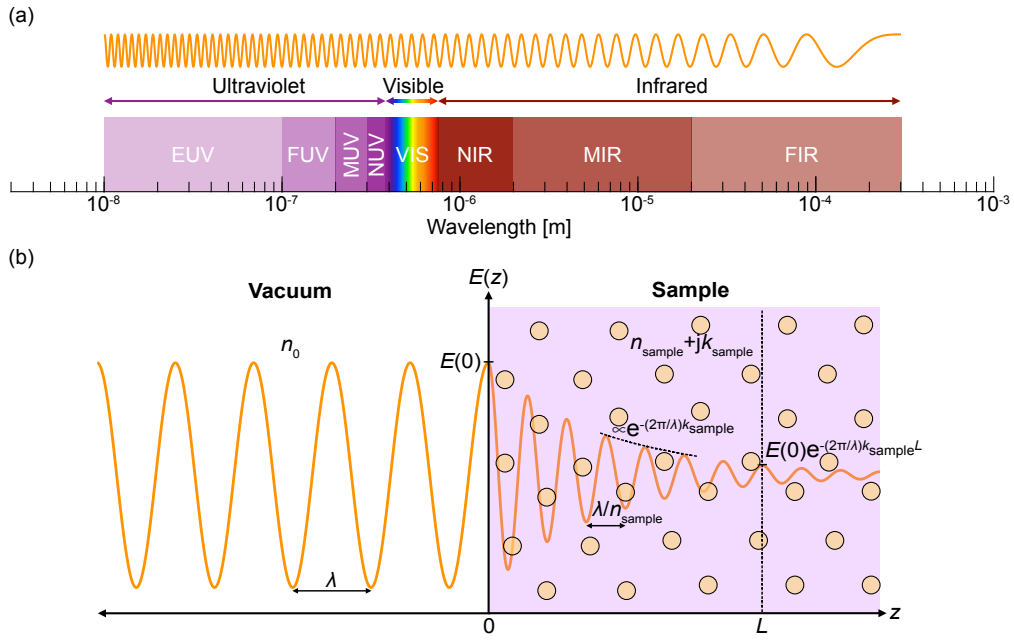

Figure 1.2: (a) A portion of the electromagnetic spectrum. Abbreviations: extreme-ultraviolet (EUV), far-ultraviolet (FUV), mid-ultraviolet (MUV), near-ultraviolet (NUV), visible (VIS), near-infrared (NIR), mid-infrared (MIR), far-infrared (FIR). (b) Free-space propagation of a lightwave. In a homogeneous medium, the real part of the complex refractive index influences the accumulated phase shift, whereas the imaginary part is associated to light absorption. Light can propagate in a sample and interact with a target analyte.

til the first laser was demonstrated in 1960 [28]. An optical transducer transforms changes in optical properties, which take place as a result of the interaction between light and the sample, into a measurable output signal. According to the monitored property, optical sensors can be divided into refractive index [29, 30], absorption [31, 32], reflectance [33, 34], luminiscence [35, 36], fluorescence [37, 38], optothermal [39, 40] or scattering sensors [41, 42]. This section is focused on refractive index and absorption sensors, as those are the kinds that are treated in this work. A possible sub-categorization arises from the operation wavelength. Of the whole electromagnetic spectrum [43], a portion of which is shown in Fig. 1.2(a), the near-infrared (0.76–2 μm) and the mid-infrared (2–20 μm) are the two regions which will receive the most attention throughout this thesis. As it will be further explained in Sections 1.2.1 and 1.2.3, working in the NIR takes advantage of well-developed telecom technologies, while operating at MIR wavelengths provides inherent sensor specificity.

1.2.1 Refraction and absorption sensors

For a high-level understanding of the principles of refractive index and absorption sensing, it be can useful to consider the free-space propagation of a monochromatic lightwave in a homogeneous medium, schematized in Fig. 1.2(b). Each medium can be characterized by its complex refractive index $(n + \mathrm{j}k)$, whose value is a function of the wavelength (λ). The wavelength in the medium is inversely proportional to the real part of the complex refractive index (n), and, therefore, the phase shift accumulated by the wave is proportional to the latter, i.e.,

$$\varphi = \varphi_{\text{in}} + \frac{2\pi}{\lambda} nL, \tag{1.1}$$

where φ_{in} is the initial phase shift of the wave and L is the interaction length. In turn, light absorption is influenced by the imaginary part of the index (k) and follows an exponential

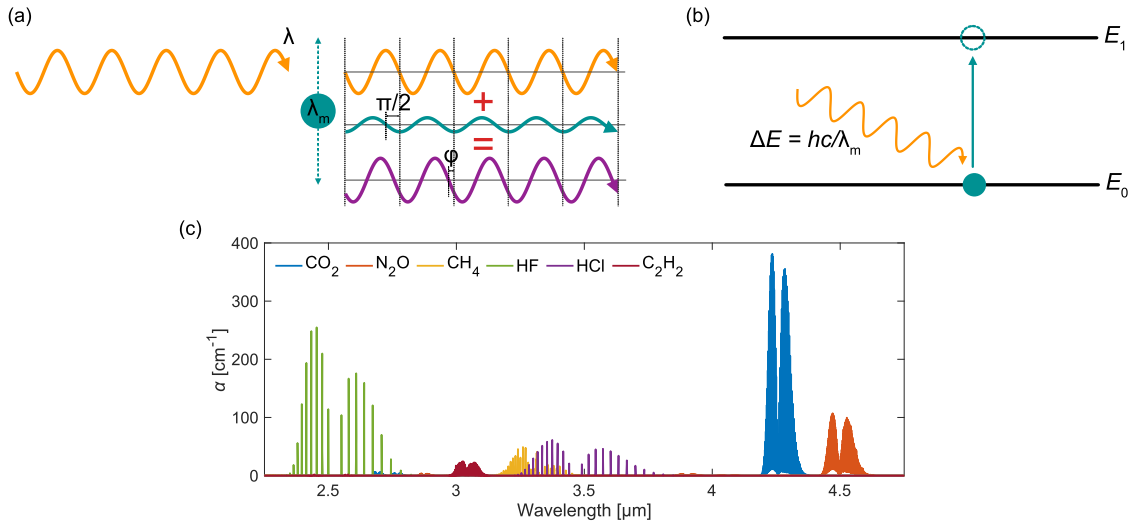

Figure 1.3: (a) Schematic representation of the fundamental origin of refraction. (b) Schematic representation of the absorption of a photon with energy ΔE. (c) Light absorption spectra of different gases, represented in terms of the absorption coefficient (α). All data are extracted from [46].

pattern, described by the Beer-Lambert law under standard conditions [44, 45]:

$$I = I_{\text{in}} e^{-\alpha L}, \tag{1.2}$$

where I is the transmitted intensity, I_{in} is the intensity before interaction with the medium and $\alpha = (4\pi/\lambda)k$ is the power absorption coefficient (in m^{-1}). The complex refractive index of a sample is dependent on both the wavelength and the presence of an analyte. In fact, the absorption coefficient from Eq. (1.2) can be expressed as

$$\alpha = \kappa C, \tag{1.3}$$

where κ is the molar napierian absorption coefficient (in $\text{m}^2\text{mol}^{-1}$) and C is the concentration (in $\text{mol}\,\text{m}^{-3}$). The relationship between the real refractive index of a sample and the concentration of a specific analyte can be found in literature and databases or measured. This way, quantitative detection of changes either in light refraction or absorption leads to the determination of the presence and quantity of the analyte.

On the physical origins of refraction and absorption

The apparent reduction of the propagation speed in a medium described by the real refractive index (n) can be explained more thoroughly by considering the medium as a continuum of discrete layers. When light shines onto one of said layers, it acts as an external force on the electrons in that layer, which begin moving up and down with a behavior that can be modeled as an oscillator. This motion generates a secondary electrical field (E_{a}), which shares the same frequency as the field from the source, but with a relative phase change $\pi/2$, as schematically represented in Fig. 1.3(a). The amplitude of such field is small compared to the amplitude of the source, and depends on the relationship between the frequency of incident light ($\omega = (2\pi/\lambda)c$, where $c = 3 \cdot 10^8$ m/s is the vacuum speed of light) and the natural frequency of the oscillator (ω_{m}), so that [47]

$$|E_{\text{a}}| \propto \frac{q}{m(\omega_{\text{m}}^2 - \omega^2)}, \tag{1.4}$$

where $q = 1.6 \cdot 10^{-19}$ C and $m = 9.1 \cdot 10^{-31}$ kg are the electron charge and mass, respectively. Adding the incident and the induced fields yields a total field which is identical

to the incident one, but phase-shifted by an amount that depends on $|E_a|$. The successive phase shifts provoked by the continuum of layers result in an effective reduction of the wavelength, by the factor referred to as n, which is intrinsically related to the atomic properties of the material. Due to the described frequency dependence of E_a, different wavelengths are subject to different phase shifts when entering the same medium. That is the reason behind dispersion, i.e., the relationship between the refractive index of a material and the wavelength of propagating light.

Light absorption (and emission) is due to either electronic, vibrational or rotational transitions between the different energy levels of a molecule [48]. These transitions can occur separately or in combinations. Simultaneous changes in rotational and vibrational states are denoted as ro-vibrational transitions. Vibrational motions can be decomposed into a sum of normal modes, each of them associated to a natural wavelength λ_m and a quantized energy level. The fundamental wavelengths of most chemical bonds correspond to the MIR regime, while their overtones are located in the NIR. At room temperature, a normal mode can transit from its ground state (E_0) to the first excited state (E_1, $E_1 > E_0$) if the energy $\Delta E = E_1 - E_0$ is supplied to the molecule [49]. This means that if a photon with energy

$$\Delta E = \frac{hc}{\lambda_m}, \tag{1.5}$$

where $h = 6.63 \cdot 10^{-34}$ m^{2}kg/s is the Plank's constant, interacts with the molecule, it can be absorbed, as shown schematically in Fig. 1.3(b). Each of these transitions generates an absorption line at the natural absorption frequencies and their overtones. A specific line can be characterized by its profile, generally Lorentzian or Voigt, and strength. Here it is worth highlighting that the overtone's absorption lines in the NIR are around two orders of magnitude weaker than the fundamental ones, located in the MIR. The set of characteristic absorption lines of each molecule creates a unique absorption spectrum, which can be considered as a molecular fingerprint and used to quantitatively identify a substance, as will be further emphasized in Chapter 2 (Section 2.4). In Fig. 1.3(c), a fraction of the MIR absorption spectra of different gases can be observed as an illustrative example, evidencing the differences in position, shape and strength. As it has been previously explained, molecules also show unique dispersion spectra. A detailed explanation of the relationship between absorption and dispersion features in a resonant medium, using a Lorentzian oscillator as a model, can be found in [50].

1.2.2 Benchtop optical sensors

Analyte concentration measurements via refractive index sensing, especially in fluids, can be performed by benchtop refractometers, mostly based on prisms, as the one schematized in Fig. 1.4(a), or on interferometers, represented in Fig. 1.4(b). In the former, light rays with varying angles impinge on the interface between a prism and the sample. By detecting the reflected light as a function of the emission angle, the critical angle can be monitored [55]. This magnitude is proportional to the refractive index of the sample and can be used to determine analyte concentration. In the latter, differences between the refractive indices of the sample and a reference substance are extracted from an interference pattern, generated when the two branches of the interferometer are combined [56]. Interferometric refractometers are often called differential refractometers and can operate at a fixed wavelength.

The two dominant techniques for absorption-based sensing are Fourier transform infrared (FTIR) and tunable diode laser absorption spectroscopy (TDLAS), which can both be considered as packaged free-space systems and are schematically shown in Figs. 1.4(c) and 1.4(d), respectively. FTIR is traditionally used when a broad absorption spectrum of

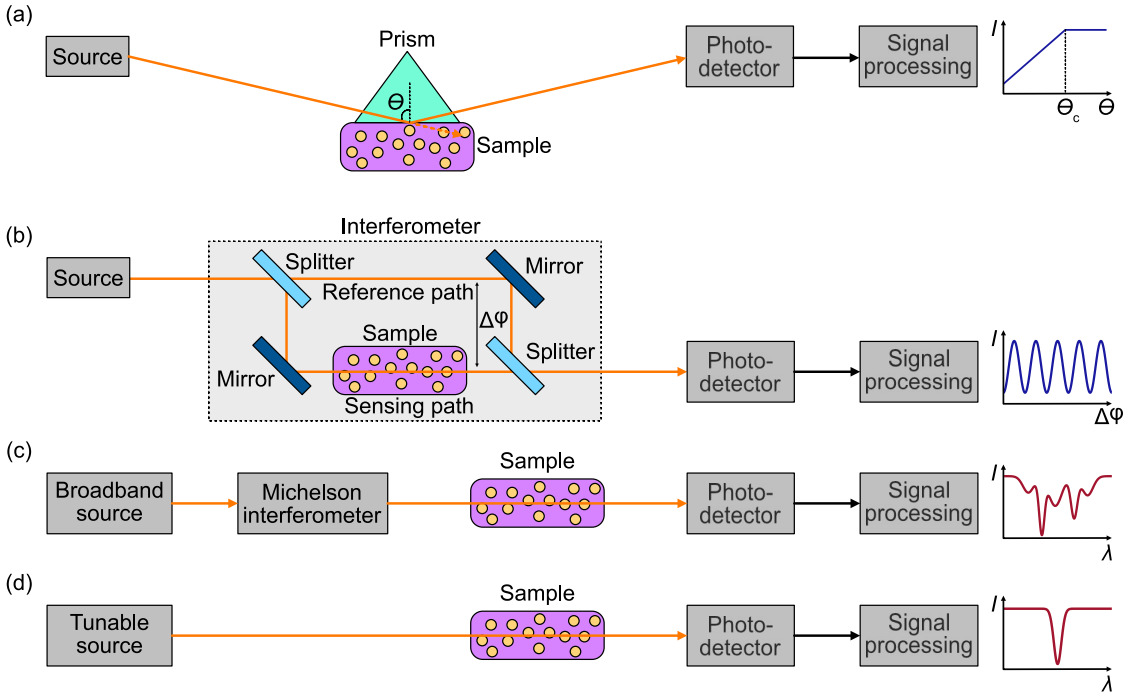

Figure 1.4: Schematic representation of benchtop optical sensors. (a) Prism-based refractometer. (b) Interferometric refractometer. (c) FTIR absorption spectrometer. (d) TDLAS absorption spectrometer.

a sample is needed [57]. Light radiated from a broadband source enters a Michelson interferometer with moving mirrors to select the transmitted wavelengths. After light interacts with the sample, an interferogram as a function of mirror displacement is converted into an absorption spectrum via computational Fourier-transform. TDLAS are more straightforward systems, motivated by the advent of quantum cascade lasers (QCLs) and interband cascade laser (ICLs), which are narrow-linewidth tunable sources working around a single wavelength [58]. In a basic TDLAS configuration, the wavelength of the source is scanned around a specific absorption feature of the target analyte, allowing for substance identification while using just a fraction of its spectrum [59].

While high-end benchtop implementations can achieve proficient results, these systems are bulky, expensive and fragile, especially considering that they contain free-space optics. In addition, they require relatively high sample volumes and careful maintenance, making them unsuitable for in situ analysis in point-of-care (POC) or point-of-

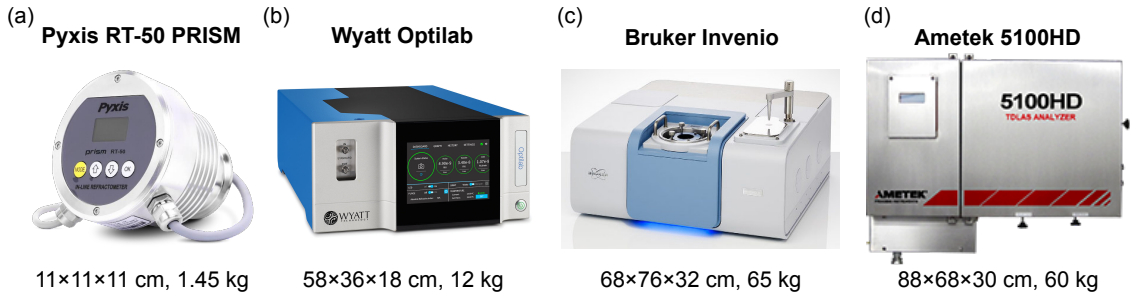

Figure 1.5: Commercial optical refractive index and absorption benchtop sensors. (a) Pyxis RT-50 PRISM prism-based refractomer [51]. (b) Wyatt Optilab interferometric refractometer [52]. (c) Bruker Invenio FTIR absorption spectrometer [53]. (d) Ametek 5100HD TDLAS absorption spectrometer [54].

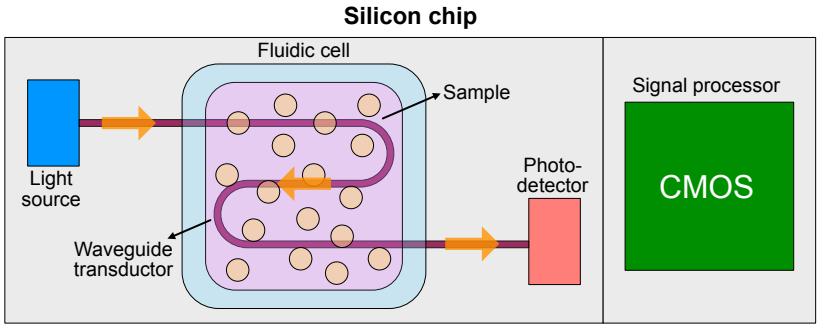

Figure 1.6: Schematic representation of a lab-on-chip based on a photonic waveguide sensor. A light source, a photonic waveguide acting as a transducer element, a photodetector and a CMOS signal processing stage are integrated on a silicon chip. A microfluidic cell incorporating the sample is placed over the sensing region.

need (PON) settings or distributed sensor networks. In Fig. 1.5, commercially available models are shown as representative examples [51, 52, 53, 54]. Only the Pyxis RT-50 prism-based refractive index sensor can be considered moderately compact, but its accuracy and measurement range are low compared to the remaining alternatives. The expansion of optical sensing techniques beyond laboratory environments would deeply benefit from more compact, robust and easily transportable approaches. In this context, the field of integrated photonics emerges as a powerful tool for sensor miniaturization.

1.2.3 Integrated photonic sensors

Integrated photonics has become a key technology in tele- and data-communications over the past decades [60]. As a dynamic field, it is increasingly finding new applications in areas such as data centers [61], computing [62], autonomous vehicles [63], astronomy [64] and sensing [65]. Within the different photonic platforms, Group IV photonics, also known as silicon photonics, are of particular interest, because they leverage the same materials and fabrication processes as complementary metal-oxide semiconductor (CMOS) microelectronics. This enables robust, high-yield device processing [66], contributing to cost-effectiveness. Telecommunications wavelengths, i.e., 1.31 μm and 1.55 μm, have been the preferred operation regime, mostly due to the existence of high-quality light sources and detectors, along with optical fibers with virtually no loss or dispersion. However, as it was outlined at the beginning of this section, the MIR regime is highly interesting for sensing applications due to its intrinsic molecular selectivity and has been driving increasing attention. Even though MIR technologies are not as mature as their NIR counterparts, promising advances are being made toward MIR sensing systems, which benefit from operating in the spectral fingerprint regions and achieve unprecedented results in terms of sensitivity, selectivity and limit of detection [67, 68].

By guiding light confined in optical waveguides instead of relying on free-space propagation, photonic integrated sensors offer sub-millimeter-sized solutions which can operate with microliter sample volumes and are suitable for dense integration in multiplexed sensing platforms [69, 70, 71]. These sensors can achieve an outstanding performance and deliver quantitative, real-time measurements with minimal to none sample pre-treatment. Moreover, mass production in microelectronics foundries is enabled, which cuts costs so that devices can be totally or partially disposed of after use, an interesting feature when working with biological samples. CMOS compatibility also brings the possibility of implementing lab-on-chip (LOC) systems as the one schematized in Fig. 1.6: miniaturized chips incorporating sources, photonic transductors, detectors, microfluidics and signal

processing elements [72, 73]. Such devices could directly deliver the relevant results in an user-oriented format, or report them to a secure repository, and could therefore be operated by untrained personnel. This concept could entirely transform the chemical sensing field. For example, LOC designed for clinical diagnosis could be brought to developing countries and used in regions with limited access to medical centers. Environmental sensors could be deployed in remote locations, implementing distributed networks for localized data collection and the creation of real-time pollution maps. Space exploration robots could be equipped with a set of ultra-light, multi-purpose spectroscopic LOCs, avoiding the cost and delay of transporting samples back to Earth. Other potential beneficiaries are the security (e.g., detection of hazardous leakages), transport (e.g., emission monitoring) and food (e.g., freshness and quality control) industries.

This work focuses on dielectric waveguide-based photonic integrated sensors, as a versatile way to implement high-performance devices within a reduced footprint. However, there are many other alternatives to free-space optical sensors [74, 75], such as those based on optical fibers [76, 77], attenuated total reflection (ATR) elements [78, 79], photonic crystals (PC) [80, 81] and surface plasmon resonance (SPR) [82, 83]. A comprehensive review of these implementations is beyond the scope of this thesis, so the reader is referred to the provided references for further information.

1.3 Overview of this thesis

This thesis is devoted to the investigation of different integrated photonic sensing architectures, providing novelty and improvements with respect to the state of the art. The ultimate goal of any sensor could be minimizing the LOD, but additional factors such as the amount of retrieved information per measurement, the sensor footprint or the complexity of the system should also be taken into account. Three main contributions arise from these considerations and support the aim of this work: two novel near-infrared sensing architectures (Sections 1.3.1 and 1.3.2) and a theoretical study of thin-film mid-infrared waveguides (Section 1.3.3). The new NIR sensing configurations incorporate the coherent phase read-out technique which was earlier proposed for sensing applications by the Photonics & RF Research Lab of the University of Málaga [84, 85]. A graphical overview of these three main contributions can be found in Fig. 1.7.

1.3.1 Complex refractive index sensor

Most photonic integrated sensors detect changes in either the (real) refractive index or the absorption of the sample, related to the imaginary index, as seen in Section 1.2. While analyzing these magnitudes independently may suffice to detect many analytes, such techniques do not provide a complete description of the sample. Complex refractive index sensors delivering simultaneous information about refraction and absorption have great potential in areas such as material science or multi-analyte detection [86]. Besides providing a deeper insight into the nature of a substance, such sensors could leverage the high sensitivity of refractive index measurements with the specificity of absorption and perform redundant measurements in critical scenarios. Moreover, their versatility, enabling the operation of a single design in a wide range of use-cases, makes these sensors excellent candidates for mass production. However, despite their scientific interest and growing popularity in free-space systems [87, 88], few implementations can be found in the field of integrated photonics.

Such a sensor, based on a modified Mach-Zehnder interferometer that simultaneously provides phase and intensity measurements, has been suggested as a proof-of-concept. Two generations of sensors were designed for a silicon nitride platform for near-infrared

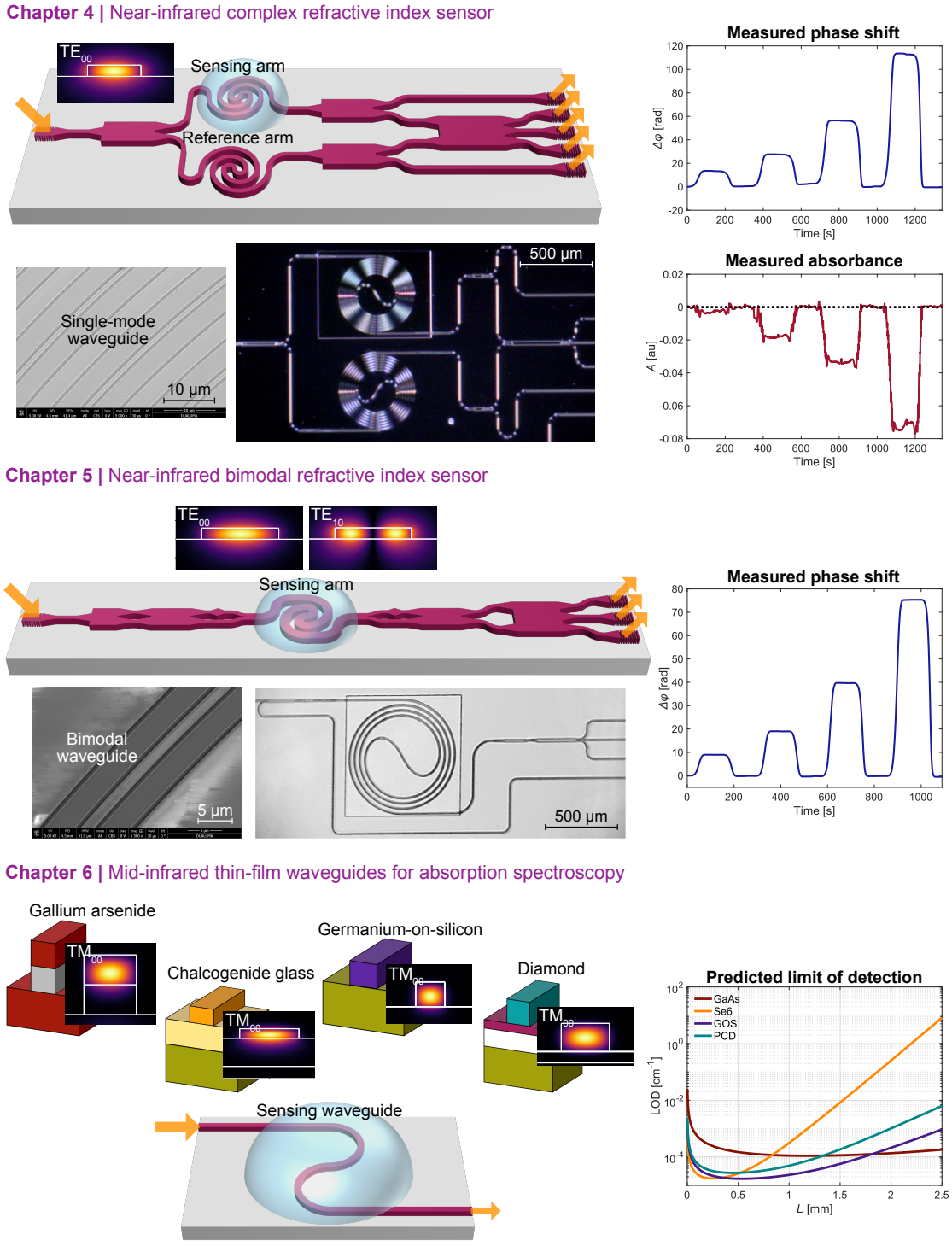

Figure 1.7: Overview of the main contributions of this thesis, including 3D illustrations (not to scale), simulated mode profiles, SEM and optical microscope images and results. The results shown for Chapters 4 and 5 include experimental demonstrations, while those from Chapter 6 are theoretical.

wavelengths. First-generation sensors exhibited several problems, such as excessive propagation losses and uncontrolled reflections, and were discarded after preliminary evaluations. Design improvements were incorporated to the successful second-generation sensors. These sensors were validated with bulk sensing experiments with liquid samples at a fixed ($\lambda_0 = 1.55\,\mu m$) wavelength, and an analytical cross-talk model was developed to improve the quality of absorption measurements. The best sensor achieved a LOD in the order of 10^{-6} RIU both for the real and imaginary parts of the index. To best of the author's knowledge, this is the first time that both quantities are simultaneously measured with such low LODs. Tentative spectroscopic measurements showed promising results, while highlighting further improvements required for high-precision scanned-wavelength operation. The main results related to this contribution can be found in [89].

1.3.2 Bimodal refractive index sensor

Conventional interferometric refractive index sensors, as the example shown in Fig. 1.4(b), split the input signal into two physically different paths, thus increasing the footprint of the device. With the aim of providing a more compact alternative, photonic integrated sensors based on bimodal waveguides avoid including a reference branch. Instead, two different modes supported by a multimode waveguide, which experience different optical paths and serve as sensing and reference channels, are excited [90]. This is an attractive approach for dense sensor integration in multiplexed-detection platforms. However, these sensors usually face challenges associated with an inadequate mode excitation and the read-out of their sinusoidal output signal, which may deteriorate performance to levels below those required in highly-demanding applications such as early medical diagnosis.

To overcome these limitations, a novel near-infrared bimodal sensing architecture combining a bimodal waveguide with a controlled modal excitation and coherent phase detection is proposed. First-generation sensors were designed for a silicon-on-insulator platform at $\lambda_0 = 1.31\mu m$, incorporating a mode converter based on mode evolution in counter-tapered waveguides. However, experimental measurements revealed that the designed configuration did not work properly. Additionally, the fabricated waveguides were fragile and chemically reactive, resulting in irreparable physical and chemical damage after measurements. A second generation was implemented in a silicon nitride platform at $\lambda_0 = 1.55\,\mu m$, allowing for bigger dimensions that increased mechanical robustness. As a mode converter, a well-trusted architecture based on a MMI, a phase shifter and a Y-junction was employed [91, 92]. This generation showed excellent performance in bulk sensing experiments, reaching a LOD in the order of 10^{-7} RIU, which is the best reported, to the best of the author's knowledge, for a bimodal sensor operating at NIR wavelengths. This contribution is published in [93].

1.3.3 Waveguides for absorption spectroscopy

Mid-infrared absorption spectroscopy of aqueous solutions, such as most biological fluids, is a well-trusted analytical tool for biomedical and environmental applications, owing to the combination of a great sensitivity and inherent selectivity. Although essential in many fields, working with water-based samples is challenging because of its high absorption and spectral overlap with several organic compounds. This fact highlights the need for devices with a proficient performance. As a result of the growing interest in integrated photonic approaches, a wide variety of platforms to implement MIR waveguide-based absorption sensors populate the state of the art [94]. However, as such sensors have usually been designed for different wavelengths and tested with different analytes, fair comparisons between existing alternatives are often difficult to establish. This in turn hinders the

development of fully optimized spectroscopic systems, and, ultimately, the realization of lab-on-chips devices suitable for real-world operation.

In this thesis, an analytical expression of the LOD of waveguide-based absorption spectroscopic systems is derived, and the existence of an optimum interaction length is shown. With the aim of optimizing the LOD, four representative thin-film waveguide platforms (gallium arsenide, chalcogenides, germanium-on-silicon and diamond), typically employed in the analysis of aqueous samples [94], are modeled and rigorously designed at $\lambda_0 = 6\,\mu m$ (amide vibrational band). A single figure of merit is used to evaluate the trade-off between sensitivity and losses, and it is demonstrated that this metric determines the optimum achievable performance of the sensor. This approach, besides defining a general waveguide design framework for optimum results, enables, for the first time, a fair comparison between four popular platform alternatives. Most of this work was carried out during a research stay at the University of Ulm (Ulm, Germany) under the supervision of Prof. Boris Mizaikoff, and is published in [95].

1.4 Organization of this thesis

This thesis is organized as follows:

Chapter 1 is this current introduction.

Chapter 2 explains the fundamentals of photonic integrated sensors based on dielectric waveguides and key performance metrics, including sensitivity and LOD, are defined. To complete the chapter, a review of the state of the art of such sensors is provided.

Chapter 3 contains the methods and protocols, concerning electromagnetic simulations, layout design and experimental characterization, followed throughout this thesis.

Chapter 4 introduces the concept of complex refractive index sensors and demonstrates a near-infrared sensor based on a Mach-Zehnder interferometer for simultaneous phase and absorption measurements.

Chapter 5 proposes and experimentally validates a near-infrared refractive index sensor based on a bimodal waveguide, which combines a controlled modal excitation with a coherent phase read-out.

Chapter 6 presents a theoretical study of four representative thin-film waveguide platforms for mid-infrared absorption spectroscopy of aqueous solutions, enabling a comparison of their limit of detection.

Chapter 7 draws the conclusions and suggests further research lines.

In addition, seven appendices are included:

Appendix A shows the relationship between the radiation angle of a grating coupler and the polishing angle of a fiber.

Appendix B provides expressions to calculate the noise-floor of a sensing setup and a set of noise reduction strategies.

Appendix C describes the fabrication of the microfluidics flow-cells employed in the near-infrared sensing experiments.

Appendix D includes brief information about the measurement setup used to perform gas sensing experiments at the University of Tromsø (Tromsø, Norway), under the supervision of Prof. Jana Jágerská, and the obtained results.

Appendix E introduces the designed suspended silicon waveguides for methane detection at mid-infrared wavelengths, and discusses their expected performance.

Appendix F includes a short curriculum vitae of the author.

Appendix G summarizes the thesis in Spanish.

Chapter 2

Waveguide-based photonic integrated sensors

The aim of this chapter is providing the fundamentals of waveguide-based photonic integrated sensors, which are the focus of this thesis. For that purpose, the field of integrated photonics (Section 2.1) will be briefly introduced before specifically studying photonic sensing waveguides and how light interacts with the sample (Section 2.2). Afterwards, refractive index sensing architectures will be covered, with an emphasis on interferometric approaches (Section 2.3). Typical strategies to achieve analyte selectivity will also be explained (Section 2.4), and the figures of merit that allow comparisons between different sensor implementations will be defined (Section 2.5). This chapter concludes with a review of the state of the art of integrated photonic sensors (Section 2.6).

2.1 Integrated photonics

The growing field of integrated photonics was already introduced in Chapter 1 (Section 1.2.3). The key components of integrated photonic circuits are photonic waveguides, which can be engineered for a wide variety of applications, and used to implement more sophisticated devices [96]. This section focuses on said waveguides and on two photonic devices which are especially relevant for this work: multimode interference couplers (MMIs) and surface grating couplers (GCs).

2.1.1 Photonic waveguides

Photonic dielectric waveguides are made of materials such as silicon and germanium and confine light into a guiding layer, which has a higher refractive index (n_1) than the upper- and lower-cladding layers (n_2). Although the full electromagnetic description of the waveguide must be obtained by solving Maxwell's equations [97], the concept of total internal reflection from ray theory, schematized in Fig. 2.1(a), provides an intuitive explanation of the physics underneath [43]. When light impinges on the interface between the core and the cladding of an internal reflection element with an incident angle $\theta_i > \arcsin(n_2/n_1)$, it is not refracted into the cladding medium, but, instead, it is reflected back to the core. This way, light is confined and guided along the waveguide. An exponentially-decaying evanescent field appears at the locations where the ray is in contact with the waveguide interface. As the thickness of the guiding layer decreases, the number of total internal reflections increases. When the core dimensions are comparable to the wavelength, modal behavior is reached and a continuous evanescent wave appears all over the interface. This is the case of the waveguides studied in this thesis.

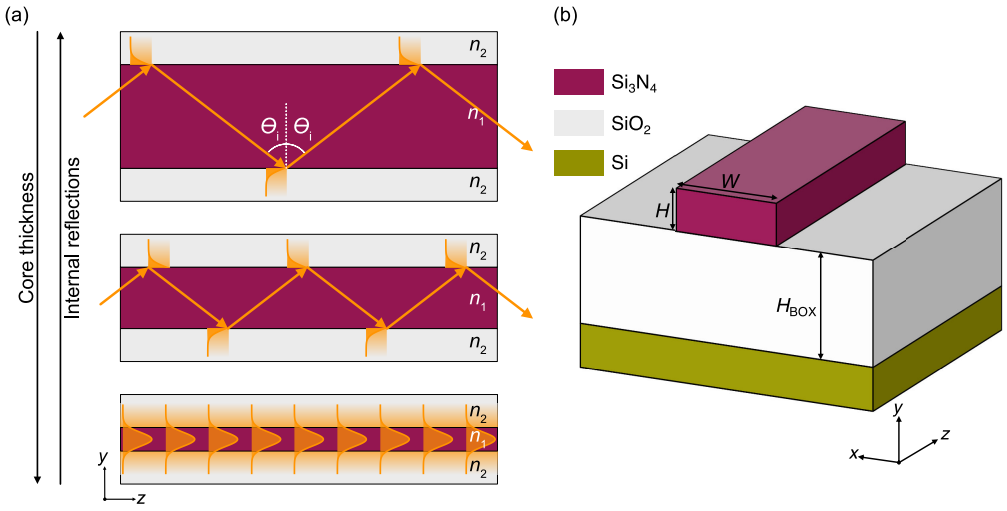

Figure 2.1: (a) Evolution from a macroscopic internal reflection element to a single-mode waveguide. As the higher-index core thickness decreases, the number of internal reflections increases. Modal behavior is achieved when the waveguide dimensions approach the working wavelength. (b) Silicon nitride strip waveguide. The silica upper cladding is not shown to ease visualization.

Waveguide modes

Waveguides generally support two different types of field distributions, called modes, according to the polarization, i.e., the direction at which the main component of the electric field points. In practical waveguides where there are both vertical and horizontal light confinements, such as the strip waveguide shown in Fig. 2.1(b), these modes are called quasi-TE and quasi-TM. When the polarization is quasi-TE, the main electric field component (E_x) is parallel to the chip surface, whereas in the case of quasi-TM polarization, the main electric field component (E_y) is perpendicular to the chip surface. To simplify nomenclature, it is common to refer to TE and TM modes. Figure 2.2 shows the field profile of the fundamental and the first high-order TE and TM modes of a silicon nitride strip waveguide with a silica cladding, a height of $H = 0.3\,\mu m$ and a width of $W = 3\,\mu m$, for a 1.55-µm wavelength. Each mode has a different complex effective index ($n_{eff} + jk_{eff}$), and is guided when the real part of its effective index is larger than the maximum index of the upper or lower cladding of the waveguide. Here it is worth highlighting that, even though the majority of the field intensity is confined to the waveguide core, there is a fraction of the field which extends to the cladding in the form of an evanescent wave. In fact, the imaginary part of the effective index of the represented modes accounts for absorption losses in the silica cladding, as will be seen in Section 2.2.2. The number of modes supported by a waveguide depends on its index contrast, dimensions, and the operating wavelength. A waveguide is considered single-mode for the TE or TM polarization when only the fundamental mode of that polarization is guided.

Propagation losses

In Chapter 1 (Section 1.2), the concept of light absorption in a dielectric medium was introduced. In a waveguide, the absorption coefficient of each mode is related to the imaginary part of its complex effective index, as will be detailed in Section 2.2.2. The most common sources of loss in a waveguide are:

Absorption by the materials. Each of the materials conforming the waveguide absorbs light to some extent, by the physical principles explained in Section 1.2.1. When the effect of this phenomenon is negligible ($k \approx 0$), the material is considered

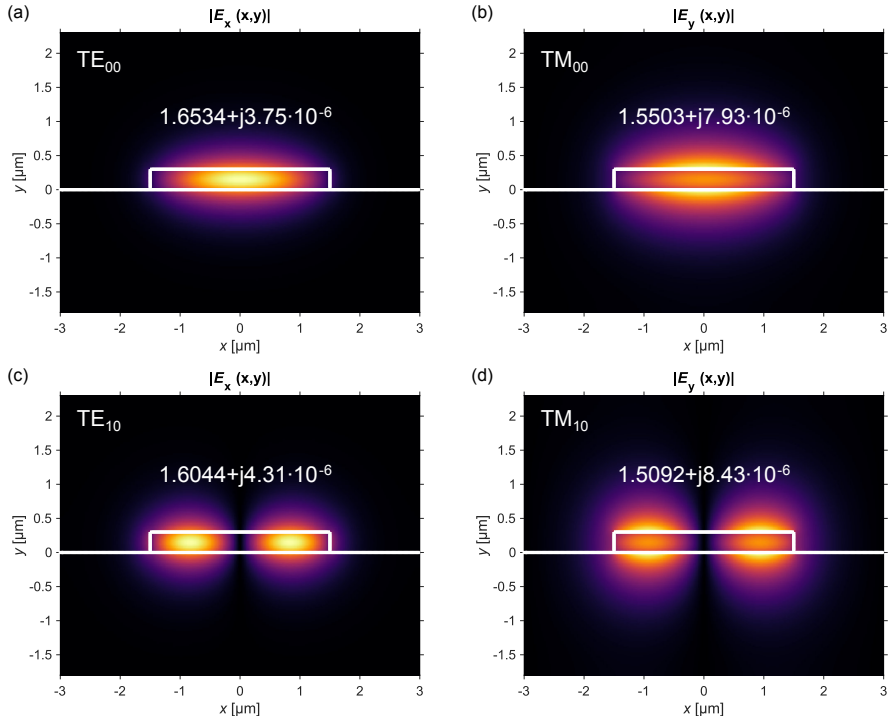

Figure 2.2: Mode field profiles of a silicon nitride strip waveguide with height $H = 0.3\,\mu\text{m}$ and width $W = 3\,\mu\text{m}$ at the wavelength $\lambda = 1.55\,\mu\text{m}$. (a) Fundamental TE mode. (b) Fundamental TM mode. (c) First high-order TE mode. (d) First high-order TM mode.

transparent at the operation wavelength. Otherwise, the material is an absorbent. For instance, water, which acts as an upper-cladding material for sensors working with aqueous samples, has an imaginary refractive index of $k_{\text{H}_2\text{O}} = 1.49 \cdot 10^{-4}$ at $\lambda_0 = 1.55\,\mu\text{m}$. In a sensing waveguide with a moderate evanescent-field overlap with the sample, such as those employed in the configurations presented in Chapters 4 and 5, water induces losses in the order of 10 $\text{dB}\,\text{cm}^{-1}$.

Light scattering. Fabrication imperfections such as surface roughness and defects in the waveguide materials lead to propagation losses due to light scattering at the defect points [98]. The larger the roughness is in relation to the wavelength, the stronger the scattering losses are [99]. A modeling approach to enable the computation of scattering losses due to sidewall roughness can be found in [100].

Leakage to a higher-index substrate. In most photonic integrated platforms, materials are stacked over a substrate, such as silicon in Fig. 2.1(b). When the refractive index of the substrate is higher than that of the lower cladding, the electric field of the mode may leak to the former if the thickness of the latter (H_{BOX}) is insufficient [101]. Typical buried oxide (BOX) thicknesses in silicon and silicon nitride platforms, such as those which will be described in Chapter 3 (Section 3.2.1), are 2 μm and 3 μm, respectively. Such values are usually large enough to prevent significant leakage.

Curvature losses. In bent waveguides, radiation losses and mode mismatch losses in the transition between straight and bent waveguides must be accounted for [102]. In the silicon nitride NIR sensing architectures presented in this work, 90-degree single-mode bent waveguides have a minimum 50 μm radius to minimize such losses, as it will be discussed in Chapter 4. If the remaining sources of loss, i.e., absorption, scattering and leakage, are expected to be significant, the bending radius should

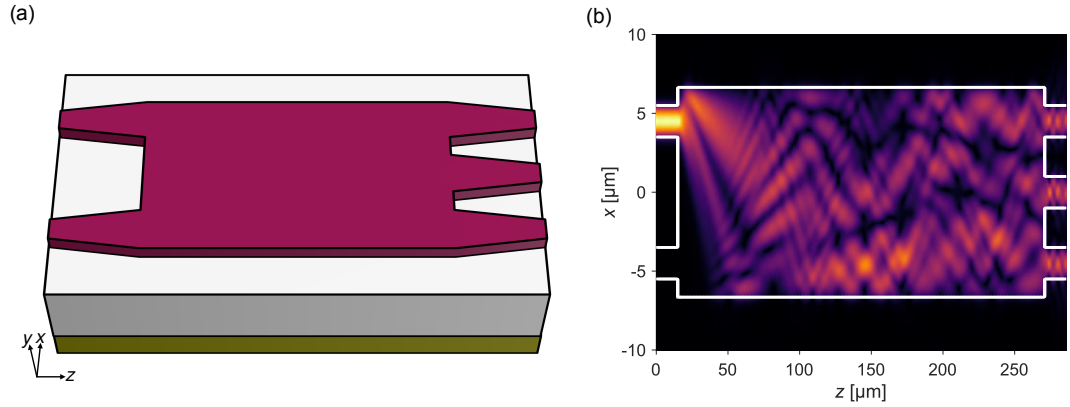

Figure 2.3: (a) 2×3-MMI implemented in silicon nitride. (b) Electric field propagation along the MMI. The input signal is split into the three outputs, which have a 120° relative phase difference.

be adjusted to achieve a trade-off between avoiding curvature losses and increasing propagation losses.

For a more comprehensive study of loss mechanisms in dielectric waveguides, the reader is referred to [103].

2.1.2 Other photonic structures

Apart from being routed, light can also be further processed by more complex waveguide-based devices, thus increasing the capabilities of integrated photonic circuits. In this section, multimode interference and surface grating couplers will be briefly discussed due to their importance in the sensing architectures presented in Chapters 4 and 5. Some other useful photonic devices are tapers [104], resonators [105], phase shifters [106], polarization rotators [107], and filters [108].

Multimode interference couplers

Multimode interference couplers are waveguide-based devices used to split and combine guided light into different output paths. They rely on the self-imaging principle, which describes how replicas of an input electric field appear at several positions of a multimode waveguide section [109, 110]. In this work, 1×2-, 2×2- and 2×3-MMIs are used for light routing and recombination in the NIR sensors. The 2×3-MMI, represented in Fig. 2.3(a), is of particular interest, as it enables the coherent phase detection scheme which will be introduced in Section 2.3.2. In this structure, input light is split into three output ports. Each of the output signals has a relative phase shift of 120° with respect to the rest. This behavior can be expressed by the transfer function

$$\mathbf{H}_{2\times3} = \frac{1}{\sqrt{3}} e^{\mathrm{j}\varphi_{2\times3}} \begin{bmatrix} 1 & e^{-\mathrm{j}\frac{2\pi}{3}} \\ e^{\mathrm{j}\frac{2\pi}{3}} & e^{\mathrm{j}\frac{2\pi}{3}} \\ e^{-\mathrm{j}\frac{2\pi}{3}} & 1 \end{bmatrix}, \tag{2.1}$$

where $\varphi_{2\times3}$ is a constant phase value [111]. A top view of the electric field propagation along such a silicon nitride MMI can be observed in Fig. 2.3(b). MMI performance is usually measured in terms of insertion losses, phase error and port imbalance, which should all be minimized below reference values as 1 dB, 3° and 0.5 dB, respectively.

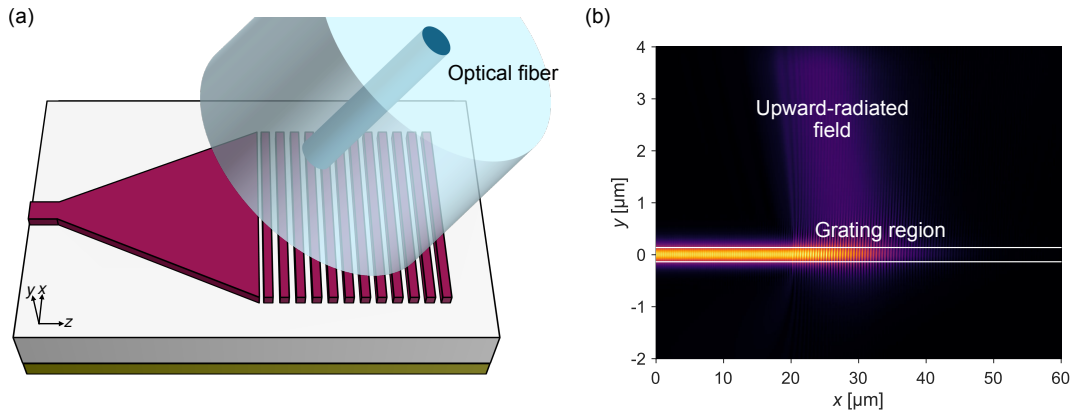

Figure 2.4: (a) Surface grating coupler. Guided light is coupled to/from the chip from/to an optical fiber. (b) Field propagation in a grating coupler, showing how light is radiated out of the chip.

Surface grating couplers

A grating coupler like the one depicted in Fig. 2.4(a) is a planar diffractive structure, periodic or quasi-periodic, which couples the waveguide mode to an off-chip free-space plane wave [112]. Such devices are necessary due to the large size mismatch between the mode field diameter of a standard optical fiber ($\sim 10\,\mu$m in the NIR) and the micrometric dimensions of photonic waveguides. A side view of the electromagnetic field radiation in a silicon grating coupler is shown in Fig. 2.4(b). The diffracted beam can be detected by a CMOS camera or intercepted by an optical fiber positioned at a specific angle over the grating (see Appendix A), and guided toward a photodetector. In virtue of the reciprocity principle, the behavior of the device is equal for light coupling to and from the chip. An ideal grating coupler should have a high efficiency, a wide bandwidth and negligible back-reflections (BR). Typical values for the coupling efficiency of a standard grating coupler are around $-3\,$dB, while the 1-dB bandwidth is in the order of 30 nm. Reflections can be neglected when BR $< -20\,$dB.

2.2 Sensing waveguides

In waveguide-based photonic integrated sensors, at least one photonic waveguide is employed as a transducer element. To enable light-matter interaction, the waveguide core is exposed to the sample, which can now be considered as the upper-cladding material, as shown in Fig. 2.5(a). The analyzed sample usually corresponds to a target analyte, diluted at a certain concentration (C), into a gaseous or liquid solvent. As discussed in Section 1.2 (Chapter 1), the sample can be characterized by its complex refractive index, $n_{\text{sample}}(\lambda, C) + \text{j}k_{\text{sample}}(\lambda, C)$, which is dependent on the wavelength and on analyte concentration. Due to the overlap between the evanescent field of the mode and the sample, the complex effective index of the mode, $n_{\text{eff}}(\lambda, C) + \text{j}k_{\text{eff}}(\lambda, C)$, reflects the variations of the refractive index of the sample with wavelength and concentration. These changes in the complex effective index alter light propagation properties, i.e., accumulated phase shift and absorption, which can be correlated with the quantity of analyte. This is known as bulk evanescent-field sensing, and is schematically illustrated in Fig. 2.5(b). For compactness, wavelength and concentration dependencies will be omitted for the remainder of this chapter.

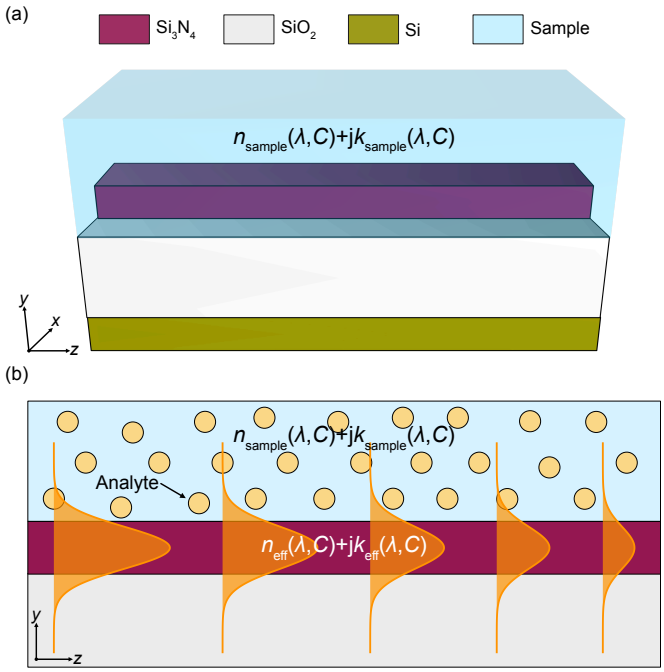

Figure 2.5: (a) Sensing waveguide. The waveguide core is exposed to the sample, which acts as an upper cladding. (b) Evanescent field light-sample interaction. The variations in the refractive index of the sample with wavelength and analyte concentration change the effective index of the mode via its evanescent field.

2.2.1 The confinement factor

The confinement factor (Γ_i) of a guided mode in the *i*-th layer of the waveguide is a measurement of the light-matter interaction within that area. It has traditionally been defined as the proportionality constant between the losses experienced by the mode (α_{eff}) and the absorption coefficient of each material (α_i), when no other sources of loss are considered, so that

$$\alpha_{\text{eff}} = \sum_i \Gamma_i \alpha_i. \tag{2.2}$$

This definition can be extended to the relationship between the complex effective index of the mode and complex refractive index of the material ($n_i + \text{j}k_i$):

$$n_{\text{eff}} + \text{j}k_{\text{eff}} = \sum_i \Gamma_i (n_i + \text{j}k_i). \tag{2.3}$$

In evanescent-field photonic sensors, the main focus is upon the external confinement factor, i.e., the confinement factor in the analyzed sample (Γ_{sample}). As Γ_{sample} defines the sensitivity of the waveguide mode, as it will be further emphasized in Section 2.5, and is therefore a key design parameter, it is convenient to express it in meaningful terms. Although an expression can be derived from Poynting theorem [113], Robinson et al.[114] proposed an alternative formula for Γ_{sample} by following a perturbational approach for dielectric waveguides,

$$\Gamma_{\text{sample}} = \frac{n_{\text{g}}}{n_{\text{sample}}} \frac{\iint_{\text{sample}} \varepsilon |E|^2 dxdy}{\iint_{-\infty}^{\infty} \varepsilon |E|^2 dxdy}, \tag{2.4}$$

where n_{g} denotes the group index, ε the electric permittivity and E the electric field. In periodic waveguides, this calculation should be done in a volume-unit accounting for a

complete period [115]. From this expression, it is clear that the confinement factor is ruled both by the energy density fraction and by waveguide dispersion, made explicit by the fraction $n_{\mathrm{g}}/n_{\mathrm{sample}}$. Consequently, two strategies to enhance the confinement factor arise: delocalizing the mode (higher overlap with the sample) and engineering waveguide dispersion (higher n_{g}). In fact, by properly combining both approaches, Γ_{sample} can be greater than unity [116]. As the main interest for the design of photonic sensors is set upon in the confinement factor in the sample, Γ_{sample} will be simply referred as Γ throughout this thesis.

2.2.2 Light-sample interaction

In this section, the fundamental mode of the waveguide shown in Fig. 2.5 will be considered. As was established in Section 2.1.1, said mode propagates with a complex effective index $n_{\mathrm{eff}} + \mathrm{j}k_{\mathrm{eff}}$, which is influenced by the complex refractive index of the sample (Eq. (2.3)). After propagating through the waveguide over an interaction length L, the amplitude of the electric field can be expressed as

$$E(L) = E(0)e^{\mathrm{j}\frac{2\pi}{\lambda}(n_{\mathrm{eff}}+\mathrm{j}k_{\mathrm{eff}})L}. \tag{2.5}$$

From this expression, a phase constant

$$\beta_{\mathrm{eff}} = \frac{2\pi}{\lambda}n_{\mathrm{eff}}, \tag{2.6}$$

which is proportional to n_{eff}, can be defined. The accumulated phase shift of the mode can thus be expressed as

$$\varphi(L) - \varphi(0) = \beta_{\mathrm{eff}}L = \frac{2\pi}{\lambda}n_{\mathrm{eff}}L, \tag{2.7}$$

where $\varphi(0)$ is the initial value of the phase shift, considered zero throughout this thesis unless said otherwise. Detecting this phase shift would lead to a measure of n_{eff}, which can be correlated to the presence of analyte. Analogously, the modal absorption coefficient, in terms of power and with m^{-1} units, can be expressed as

$$\alpha_{\mathrm{eff}} = \frac{4\pi}{\lambda}k_{\mathrm{eff}}, \tag{2.8}$$

where the direct proportionality occurs with k_{eff}. The absorption of the analyzed sample contributes to the effective absorption coefficient, so that

$$\alpha_{\mathrm{eff}} = \alpha_{\mathrm{int}} + \Gamma\alpha_{\mathrm{sample}}, \tag{2.9}$$

where α_{int} is the intrinsic loss coefficient of the waveguide, which accounts for the remaining sources of loss, and $\alpha_{\mathrm{sample}} = (4\pi/\lambda)k_{\mathrm{sample}}$. It is worth noting that α_{sample} includes both the absorption of the analyte (α_{a}) and the solvent ($\alpha_{\mathrm{solvent}}$), i.e., $\alpha_{\mathrm{sample}} = \alpha_{\mathrm{solvent}} + \alpha_{\mathrm{a}}$.

Photodetection of the lightwave yields a measure of the field intensity, which is proportional to the squared field amplitude, i.e., $I(L) \propto |E(L)|^2$. The output intensity signal can be expressed as

$$I(L) = I(0)e^{-\alpha_{\mathrm{eff}}L}, \tag{2.10}$$

from which the absorbance of the analyte can be calculated by taking

$$A = -\log_{10}\left(\frac{I(L)}{I_0(L)}\right) = \Gamma\epsilon CL, \tag{2.11}$$

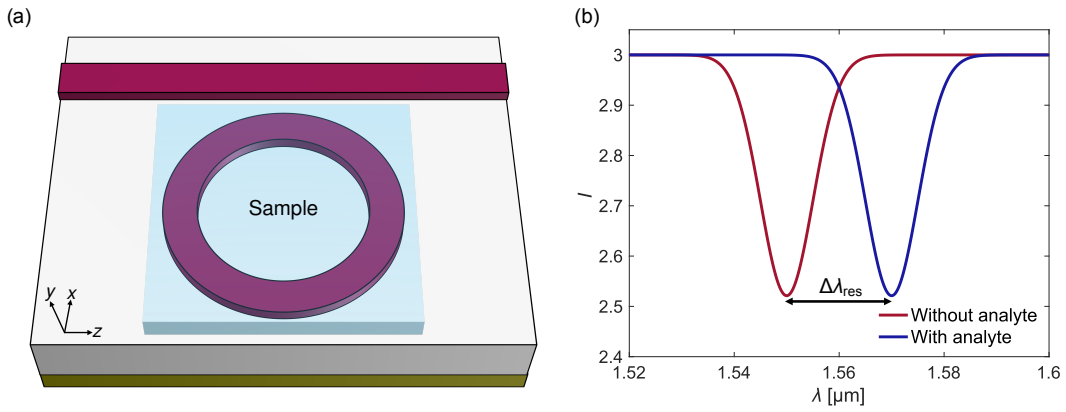

Figure 2.6: (a) Ring resonator. Light with a resonant wavelength circulates along the ring and is not transmitted. (b) Output signal of a ring resonator. The presence of analyte induces a change in the resonant peak of the transmission spectrum.

where $I_0(L) = I(0)e^{-(\alpha_{\text{int}}+\Gamma\alpha_{\text{solvent}})L}$ is the background output intensity, C is the concentration of analyte (in $\text{mol}\,\text{m}^{-3}$) and $\epsilon = \log_{10}(e)\alpha_{\text{a}}/C$ is the decadic molar absorption coefficient of the analyte (in $\text{m}^2\,\text{mol}^{-1}$), which is related to the napierian decadic coefficient (κ) introduced in Section 1.2.1 of Chapter 1 (Eq. (1.3)) as $\epsilon = \kappa\log_{10}(e)$. Therefore, by monitoring changes in light absorption at the output of a waveguide, an analyte with a known molar absorption coefficient can be quantitatively detected. This is often referred to as evanescent-field absorption sensing. However, with this technique, the phase shift of the lightwave has been lost in the detection process, so no information about changes in the real part of the effective index can be retrieved. More sophisticated sensing architectures must be employed to recover this magnitude.

2.3 Refractive index sensing architectures

The goal of the different refractive index sensing architectures is transforming changes in the real effective index (n_{eff}) of a mode into variations in output intensity signals, which are readily measurable with photodiodes. As a consequence, the imaginary part of the complex effective index will be omitted in this section. Most of the sensors with the ability to deliver refractive-index information are based on either resonators or interferometers.

2.3.1 Resonant sensors

Resonant sensors have become very popular due to their high sensitivity and reduced footprint, which enables dense integration and multiplexed detection of different analytes [117]. Several resonating architectures, such as rings [118], racetracks [119], disks [120], spirals [121] or Bragg gratings [122] have been proposed. In a simple ring resonator (RR) as the one schematized in Fig. 2.6(a), light is coupled from a straight waveguide via its evanescent field into a ring-shaped waveguide, which is exposed to the analyzed sample. When the resonant condition for a ring with radius R,

$$Ln_{\text{eff}} = m\lambda_{\text{res}}, \quad m \in \mathbb{N}, \tag{2.12}$$

where $L = 2\pi R$ is the ring perimeter, is fulfilled, light with a wavelength λ_{res} is trapped inside the resonator. As a consequence, the transmission spectrum of the device shows a resonance dip around λ_{res}, as in the example in Fig. 2.6(b). The quality factor measures the sharpness of the resonance, and can be expressed as

$$Q = \frac{\lambda_{\text{res}}}{\text{FWHM}}, \tag{2.13}$$

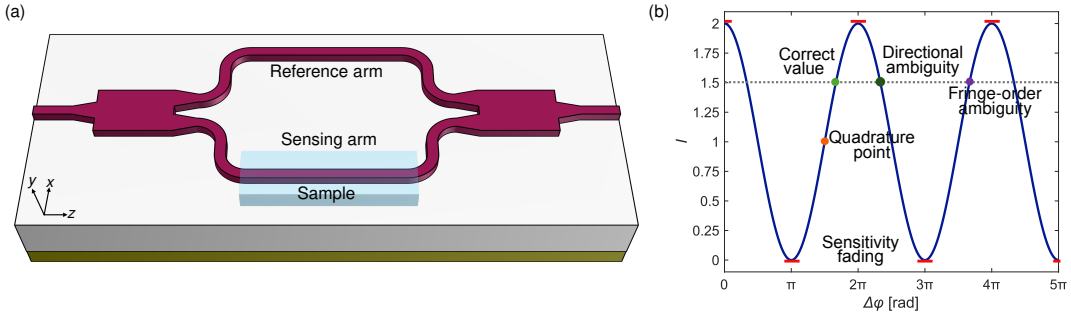

Figure 2.7: (a) Conventional MZI sensor. Signal splitting and recombination is performed by a 1×2-MMI. (b) Output signal of a conventional interferometer. The most important read-out limitations are sensitivity fading, directional ambiguity and fringe order ambiguity.

where FWHM denotes the full width at half maximum. The spectrum is periodic, with a distance between adjacent resonance peaks called free spectral range (FSR). A change in the concentration of the analyte induces a shift in the position of the resonant wavelength [117]:

$$\Delta\lambda_{\text{res}}(\Delta n_{\text{eff}}) = \frac{\lambda_{\text{res}}}{n_{\text{g}}}\Delta n_{\text{eff}}. \tag{2.14}$$

Therefore, by measuring $\Delta\lambda_{\text{res}}$, Δn_{eff} can be determined and correlated to changes in the concentration of the analyte. This technique requires a tunable laser source or a spectrometer, thus elevating system complexity and cost. Other limiting factors for this architecture are propagation losses, which degrade performance, and the length of the FSR, which may compromise the measurement range of the sensor.

2.3.2 Interferometric sensors

Optical interferometers generate constructive and destructive interferences between two lightwaves with different optical paths. Interferometric sensing configurations can achieve a remarkably high sensitivity and are therefore used in highly demanding applications such as the detection of gravitational waves [123] or precision astrometry [124]. When they are employed for chemical sensing applications, changes in the generated interference pattern are quantitatively linked to the presence of the target analyte. Among the different integrated interferometric sensing configurations, Young interferometers (YI) [125], Hartman interferometers (HI) [126], dual-polarization interferometers (DPI) [127], Mach-Zehnder interferometers (MZI) [128] and bimodal interferometers (BI) [129] are the most commonly employed. Extensive reviews of the aforementioned architectures can be found in [130] and [131]. With the exception of the BI, which will be specifically studied in Chapter 5, all these configurations include two physically separated paths. The sensing path is exposed to the sample, whereas the reference one is isolated from it.

In a conventional MZI as the one schematized in Fig. 2.7(a), the mode propagating through the reference waveguide has an effective index $n_{\text{eff}}^{\text{R}}$, which differs from that of the mode of the sensing waveguide, $n_{\text{eff}}^{\text{S}}$. As a consequence, after traveling through the sensor arms, which will be assumed to be equal in length (L) for simplicity, the modes have accumulated a relative phase shift

$$\Delta\varphi(\Delta n_{\text{eff}}) = \frac{2\pi}{\lambda}\Delta n_{\text{eff}}L, \tag{2.15}$$

where $\Delta n_{\text{eff}} = n_{\text{eff}}^{\text{S}} - n_{\text{eff}}^{\text{R}}$. By detecting changes in $\Delta\varphi$, changes in Δn_{eff} can be calculated, and so can changes in the refractive index of the sample be monitored. A key advantage of these interferometers is that they can work at a fixed wavelength when the changes in

the concentration of the analyte are dynamic. However, these devices are sometimes operated by scanning the wavelength while keeping the analyte concentration stable. In this case, a concentration-dependent wavelength shift is recorded, similarly to the resonant architectures described in Section 2.3.1 [132].

In conventional MZIs, there is a direct recombination of the reference and sensing paths. As a result, an output intensity signal

$$I(\Delta\varphi) = I_{\mathrm{R}} + I_{\mathrm{S}} + 2\sqrt{I_{\mathrm{R}} I_{\mathrm{S}}}\cos(\Delta\varphi), \tag{2.16}$$

where I_{R} and I_{S} are the intensities of the reference and sensing paths, respectively, is detected. This output is a periodic function of $\Delta\varphi$, i.e., $I \propto \cos(\Delta\varphi)$, whose sinusoidal nature imposes the following analytical challenges, highlighted in Fig. 2.7(b):

Sensitivity fading. Maximum sensitivity ($|\partial I/\partial\Delta\varphi|$) is only achieved at the quadrature point, while it completely fades at the maxima and minima of the intensity function.

Directional ambiguity. It is impossible to determine whether the concentration of analyte has increased or decreased, as the cosine is an even function, i.e., $\cos(\Delta\varphi) = \cos(-\Delta\varphi)$.

Fringe-order ambiguity. Phase shifts greater than 2π cannot be resolved, so continuous phase-tracking is required. This is not a substantial limitation, as in most practical systems the sampling rate is much faster than the changing speed of the output.

Different phase compensation and modulation techniques, like those based on electro-optic [133], thermal [134] and liquid crystal [135] modulators, have been applied to overcome these drawbacks. Spectral interrogation techniques have also been proposed [136]. However, the practical implementation of said solutions is usually complex and expensive, as it requires adding costly equipment as tunable laser sources and spectrometers or a substantial modification of standard fabrication processes. Another approach arises from adapting coherent receiver techniques from telecommunications [111] to sensing applications [84]. Due to their importance for the work compiled in this thesis, these coherent read-out techniques are explained in further detail.

Coherent phase detection

Coherent read-out techniques provide a solution for the sensitivity fading and directional ambiguity which hinder the performance of conventional interferometric sensors, at the expense of increasing the number of output signals to be detected. Although most configurations can benefit from this detection scheme, this explanation is particularized for a MZI, like the one depicted in Fig. 2.8(a). The 2×1 combiner from the conventional MZI is substituted by a 2×3-MMI as the one described in Section 2.1.2. As a result of the combination in the MMI (see Eq. (2.1)), each detected output

$$I_m(\Delta\varphi) = \frac{1}{3}\left[I_{\mathrm{R}} + I_{\mathrm{S}} + 2\sqrt{I_{\mathrm{R}} I_{\mathrm{S}}}\cos\left(\Delta\varphi + \frac{2\pi}{3}(m-2)\right)\right], \quad m = \{1,2,3\} \tag{2.17}$$

constitutes an interferometric signal, equivalent to those obtained from conventional configurations (see Eq. (2.16)), but with a 120° phase shift between them. An example of such signals can be observed in Fig. 2.8(b). Once digitized, the three output signals can be combined by a read-out matrix, with ideal-case coefficients

$$\mathbf{C} = \begin{bmatrix} \frac{-1}{2} + \mathrm{j}\frac{\sqrt{3}}{2} \\ 1 \\ \frac{-1}{2} - \mathrm{j}\frac{\sqrt{3}}{2} \end{bmatrix}, \tag{2.18}$$

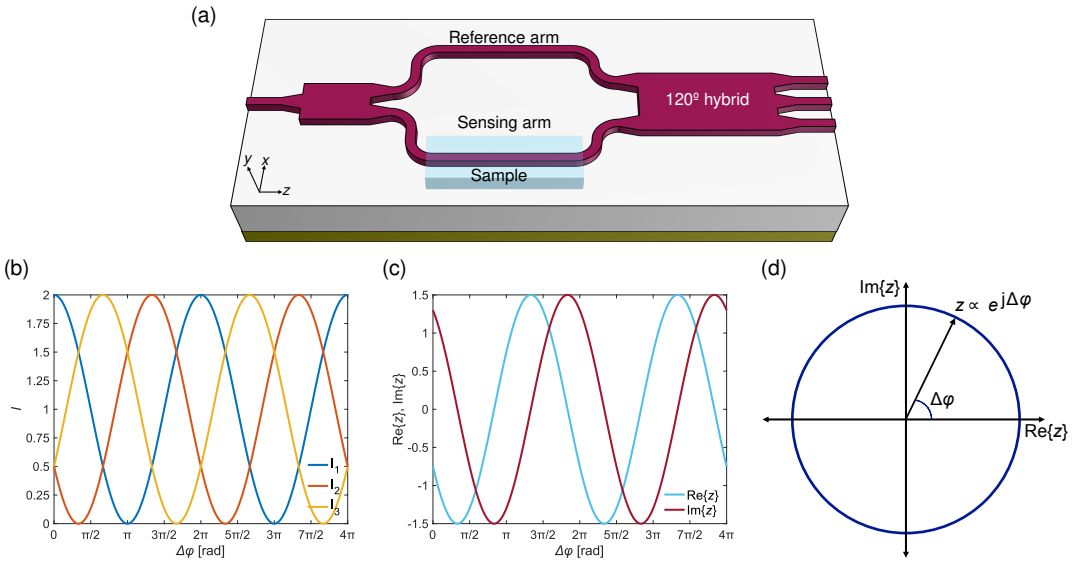

Figure 2.8: (a) MZI sensor with coherent readout. The sensing and reference arms are combined in a 2×3-MMI. (b) Output signals of the MZI. Each of the outputs is an interferometric signal with a 120° phase shift with respect to the other two. (c) In-phase (real) and quadrature (imaginary) parts of the generated complex signal. (d) Complex plane representation of the generated signal, projecting a circle in the IQ plane.

to generate a complex signal in the in-phase and quadrature (IQ) plane

$$z = \mathbf{C}^{\mathrm{T}} \cdot \mathbf{I}, \tag{2.19}$$

where $\mathbf{I} = [I_1\, I_2\, I_3]^{\mathrm{T}}$. Expressing z by its real and imaginary parts, shown in Fig. 2.8(c), yields

$$z = \sqrt{I_{\mathrm{R}} I_{\mathrm{S}}}\,(\cos(\Delta\varphi) + \mathrm{j}\sin(\Delta\varphi)) = \sqrt{I_{\mathrm{R}} I_{\mathrm{S}}}e^{\mathrm{j}\Delta\varphi}, \tag{2.20}$$

which, with continuous changes of $\Delta\varphi$, projects a circle with a radius $R = \sqrt{I_{\mathrm{R}} I_{\mathrm{S}}}$ in the IQ plane, as shown in Fig. 2.8(d). Now, the pursued phase shift can be directly retrieved as $\Delta\varphi = \arg(z)$, thus achieving an unambiguous measurement with a constant sensitivity ($|\partial z/\partial\Delta\varphi|$). In practical implementations, hardware non-idealities transform the described IQ-plane circle into an ellipse, provoking read-out errors. These deterministic errors can be corrected with calibration methods, as will be described in Section 3.4 of Chapter 3.

2.4 Specificity to the analyte

The aforementioned waveguide-based sensor alternatives translate changes in the imaginary or real refractive index of the sample, induced by changes in analyte concentration, into intensity changes in the output signal, which can be measured with photodetectors and used to calculate absorbance or phase shifts, respectively. However, this alone does not guarantee that the sensor is specific to the target analyte, as any change in the composition of the sample, e.g., the addition of a further component, would induce a complex refractive index change, which would be misinterpreted. Specificity strategies are thus mandatory to ensure that the sensor discriminates between the different elements that can be found in the analyzed substances. The method of choice depends on whether the sensor measures absorbance or phase-shift changes, and, most importantly, on whether these measurements are performed at a fixed wavelength or over a spectral range. Two of the most prominent approaches are molecular fingerprints and surface functionalization. These are not mutually exclusive and can be combined for improved results [137, 138].

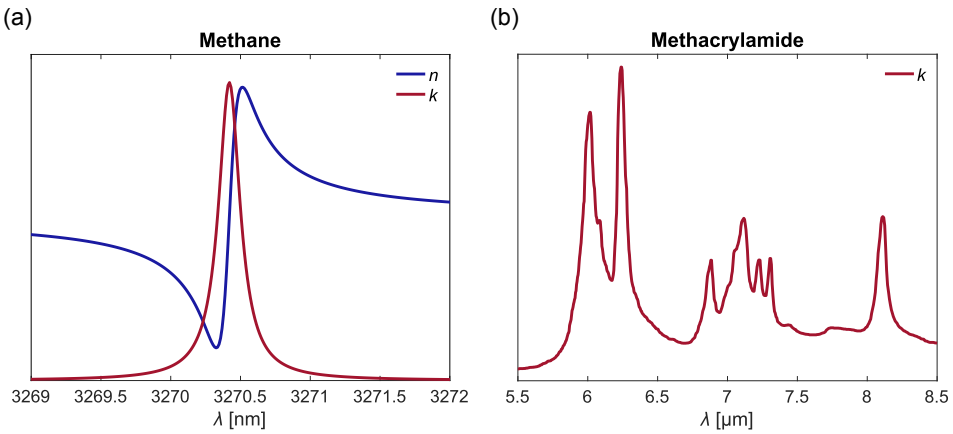

Figure 2.9: (a) Methane absorption and dispersion spectra around $\lambda = 3.27\,\mu m$ calculated from the HITRAN database [46]. (b) Methacrylamide spectrum in the amide rotational band (5.5-$8.5\,\mu m$), extracted from the NIST database [139]. Dispersion spectra cannot be calculated from the available data.

2.4.1 Molecular fingerprints

In Section 1.2.1 of Chapter 1, the physical principles behind light refraction and absorption were introduced. It was thus seen that each molecule exhibits a characteristic absorption spectrum, induced by vibrational, rotational and ro-vibrational transitions, which is called molecular fingerprint and acts as a unique identifier. In the spectroscopic analysis of simple molecules, like gases, recording a narrow spectral bandwidth around a characteristic absorption peak, as the example shown in Fig. 2.9(a), is sufficient to determine the presence and concentration of the target. In more complex molecules, like peptide chains, the same functional groups can be found in different substances, generating shared absorption bands. It is thus preferred to examine a wider range of the molecular fingerprint, as shown in Fig. 2.9(b), rather than a single peak. With an increasing number of bands and the overlap between them, more sophisticated approaches, as chemometrics and multivariate data analysis, are needed to unequivocally identify the analyte [140]. These techniques are especially useful in spectral regions with weaker absorption features, like the NIR. Although molecular fingerprints are usually related to absorption spectroscopy, dispersion spectra can also be recorded and employed for analyte identification. This technique has the potential to overcome some of the limitations of absorption spectroscopy, such as non-linearity and a limited dynamic range [141]. Unfortunately, the reference dispersion values of relevant molecules are not always available in chemistry databases, so a pre-calibration of the sensor may be needed.

2.4.2 Surface functionalization

Surface functionalization consists in the chemical modification of the waveguide surface with chemical groups that capture specific molecules. Although this technique is also useful for absorption sensors [142], refractive index sensors take the most advantage of it. In the detection of gases or VOCs, enrichment layers such as mesoporous coatings [143] or metal-organic frameworks (MOF) [144], which preferentially adsorb the target molecules, are widely used. In biosensing applications, it is common to add a biorecognition layer, formed by bioreceptors as enzymes, antibodies, or nucleic acids [145]. These recognition elements only bind to a specific analyte. Functionalization steps include surface activation, bioreceptor immobilization and blocking the free areas [146]. A schematic representation of a functionalized waveguide can be seen in Fig. 2.10. In this scenario,

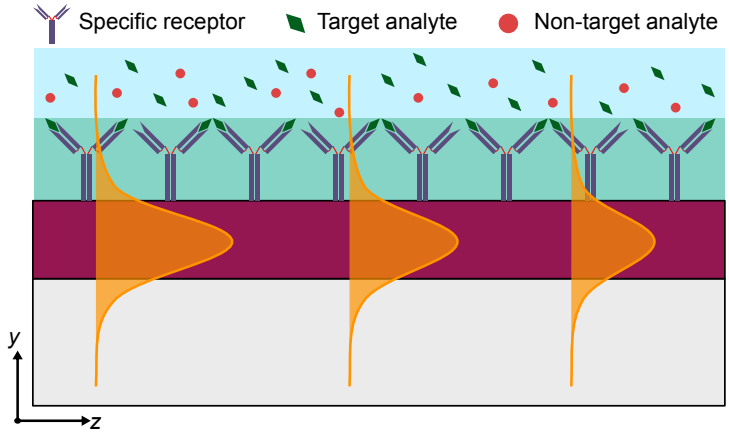

Figure 2.10: Functionalized waveguide. A layer of biorecognition elements guarantees that changes in the complex effective index of the mode are only due to the adsorption of the target analyte.

known as surface sensing, changes in the complex effective index of the guided mode can only be attributed to the adherence of the target analyte.

2.5 Figures of merit

As it will be evidenced in the state of the art reviewed in Section 2.6, a vast variety of sensing waveguides and configurations have been proposed over the last years. As a consequence, meaningful and quantitative metrics are needed in order to compare between different alternatives with as much independence of their specific implementations as possible. For a better understanding of the scope of such metrics, it can be useful to distinguish between different performance levels: that of the waveguide, the architecture, the device and the whole system [147]. The general expressions given in this section will be particularized to each specific sensing architecture in Chapters 4, 5 and 6.

2.5.1 Waveguide-level

The sensitivity of the waveguide mode reflects the rate at which a physical change in the sample is mapped into a change in the real or imaginary part of the effective index. This can be expressed as

$$\begin{aligned} S_{\mathrm{m},n_{\mathrm{eff}}} &= \frac{\partial n_{\mathrm{eff}}}{\partial \xi}, \\ S_{\mathrm{m},k_{\mathrm{eff}}} &= \frac{\partial k_{\mathrm{eff}}}{\partial \xi}, \end{aligned} \tag{2.21}$$

where ξ is any physical parameter. In pure absorption sensors, it can sometimes be more straightforward to define the mode sensitivity as

$$S_{\mathrm{m},\alpha_{\mathrm{eff}}} = \frac{\partial \alpha_{\mathrm{eff}}}{\partial \xi}, \tag{2.22}$$

which, considering Eq. (2.8), reduces to $S_{\mathrm{m},\alpha_{\mathrm{eff}}} = (4\pi/\lambda) S_{\mathrm{m},k_{\mathrm{eff}}}$. The physical magnitude represented by ξ can be electromagnetic or chemical, and depends on whether bulk or surface sensing is performed. Table 2.1 summarizes some typical examples, along with commonly employed units. Here it is worth noting that, considering Eq. (2.3), the confinement factor coincides with the modal sensitivity to changes in the (complex) refractive

Table 2.1: Typical definitions of waveguide mode sensitivity for different considered physical magnitudes.

Parameter	Type	Expression	Units
Complex refractive index	Bulk	$\partial n_{\text{eff}}/\partial n_{\text{sample}}$ $\partial k_{\text{eff}}/\partial k_{\text{sample}}$	RIU/RIU
Analyte concentration	Bulk	$\partial n_{\text{eff}}/\partial C$ $\partial k_{\text{eff}}/\partial C$	RIU/M
Thickness of adsorbed layer	Surface	$\partial n_{\text{eff}}/\partial t$ $\partial k_{\text{eff}}/\partial t$	RIU/nm
Mass-density of adsorbed layer	Surface	$\partial n_{\text{eff}}/\partial \rho$ $\partial k_{\text{eff}}/\partial \rho$	RIU/pg $\cdot$ mm^{-2}

Table 2.2: Architectural sensitivities of three typical sensor alternatives: waveguide, ring resonator and Mach-Zehnder interferometer.

Architecture	Expression	Units
Waveguide	$\partial A/\partial k_{\text{eff}}$	au/RIU
Ring resonator	$\partial \lambda_{\text{res}}/\partial n_{\text{eff}}$	nm/RIU
Mach-Zehnder Interferometer	$\partial \varphi/\partial n_{\text{eff}}$	rad/RIU

index of the sample, i.e.,

$$\frac{\partial n_{\text{eff}}}{\partial n_{\text{sample}}} = \frac{\partial k_{\text{eff}}}{\partial k_{\text{sample}}} = \Gamma. \tag{2.23}$$

2.5.2 Architecture-level

The sensitivity of the architecture is the relationship between the change in the real or imaginary parts of the effective index of the mode and the measured magnitude (X).

$$\begin{aligned} S_{\text{a},n_{\text{eff}}} &= \frac{\partial X}{\partial n_{\text{eff}}} \\ S_{\text{a},k_{\text{eff}}} &= \frac{\partial X}{\partial k_{\text{eff}}} \end{aligned} \tag{2.24}$$

The particular expressions for the waveguide, RR and MZI sensors explained in this chapter are given in Table 2.2. Note that S_{a} is the same for MZIs with direct and coherent readout.

2.5.3 Device-level

The total sensitivity of the photonic device can be calculated as the product of the waveguide modal and architectural sensitivities, so that

$$S = S_{\text{a}} S_{\text{m}} = \frac{\partial X}{\partial \xi}, \tag{2.25}$$

which can be calculated considering the different partial sensitivity alternatives in accordance to the sensor type and application.

2.5.4 System-level

While the previous performance levels depended only on the integrated photonic circuit, the detection capabilities of the sensor depend also on the resolution of the system, ΔX_{min},

which is conditioned by the noise-floor. It is common practice to express ΔX_{min} as three times the standard deviation of the measured signal, σ_X [148]. Consequently, the limit of detection (LOD), defined as the smallest change in the sample which can be resolved by the system, can be calculated as

$$\text{LOD} = \Delta\xi_{\text{min}} = \frac{3\sigma_X}{|S|}, \tag{2.26}$$

and shares the units of ξ.

2.6 State of the art

Once the fundamentals of integrated photonic sensors have been introduced, and the main figures of merit defined, the state of the art is reviewed in this section. The different sensors are divided according to whether they detect the real (refraction) or imaginary (absorption) parts of the complex refractive index. The confinement factor (Γ), the sensitivity of the device (S) and the LOD will be regarded as the key comparative performance metrics.

2.6.1 Refraction sensors

In Section 2.3, refractive index sensors were divided into resonant and interferometric architectures. However, as it will be seen below, both approaches can be indeed combined for improved performance. Table 2.3 gives an overview of a selection of recently published refractive index sensors, along with their most important characteristics. The sensitivity is given in $\partial\lambda/\partial\xi$ for sensors measuring wavelength displacement and in $\partial\varphi/\partial\xi$ in those measuring phase shift, with ξ referring either to n_{sample} or C. LODs are expressed in RIU whenever possible to facilitate comparisons.

Resonant sensors

The popularity of resonant architectures is mainly due to their potential for dense integration, as in the RR with an integrated bank spectrometer proposed in [149] to detect C-reactive protein (CRP) concentrations as low as 32 pg/mL at NIR wavelengths. Cascaded RR with a resolution improved through the Vernier effect have been proposed to detect glucose at $\lambda = 1.55$ µm [150]. At the same wavelength, a MZI-assisted RR achieved an eight-fold enhancement on the measurement range, and up to three rings were multiplexed to perform NaCl bulk sensing experiments [151]. Nitric oxide (NO) has been in-vitro monitorized in a mouse-wound model with a biofunctionalized SOI RR supporting a TM mode at $\lambda = 1.55$ µm, achieving a LOD $= 500$ nM [152]. For gas sensing at $\lambda = 1.57$ µm, a SOI ring resonator was functionalized with a ZIF-8 polymer for selectivity and a polydimethylsiloxane (PDMS) layer to increase gas diffusion, detecting CO_2 concentrations down to 0.16% [153]. Resonant refractive index sensors are also being increasingly used in the MIR. Two cascaded SOI RR working at $\lambda = 3.8$ µm were employed in the detection of acetone and isopropyl alcohol (IPA) in the liquid phase [154]. By using suspended membrane Si waveguides with $\Gamma = 0.8$, a RR designed at $\lambda = 2.1$ µm has been used to detect CO_2 with an LOD $= 38000$ ppm, which could potentially be improved by reducing measurement noise [155].

Interferometric sensors

In the last years, several improved versions of MZI sensors have appeared, working either at a fixed or scanned wavelength. Even though liquid samples are the most commonly used, gas detection has also been demonstrated. A spectrally interrogated unbalanced

MZI (UMZI) functionalized with a mesoporous silica top-layer was used to detect gas vapors such as acetone, isopropyl alcohol and ethanol with LODs as low as 195, 741 and 4.8 ppb, respectively [156]. Another scanned-wavelength UMZI achieved a confinement factor as high as $\Gamma = 0.8$ by using double-slot SOI waveguides at 1.55 μm, and has been validated with KCl [157]. To compensate for spurious thermal and wavelength drifts, two cascaded UMZI in a SiO_2 platform have been designed and simulated, yielding promising results [158]. Another approach to compensate temperature fluctuations consisted in coupling a temperature-reference RR to a UMZI, enabling gas sensing in the NIR [159]. There have also been different approximations to achieve a linear phase read-out. In [160], a MZI with phase-generated carrier (PGC) modulation working with TM polarization at $\lambda = 1.31$ μm, where water is less absorbing than at 1.55 μm, has achieved a remarkable $\Gamma = 0.5$ for a SiN strip waveguide, and a LOD $= 2.24 \cdot 10^{-7}$ RIU. A coherent MZI as the one described in Section 2.3.2 was functionalized and used to detect CRP with a LOD $= 184$ pg/mL, furthermore showing that this configuration can still offer a high performance while operating with a cheap handheld laser source [85]. Bimodal interferometers, which will be specifically reviewed in Chapter 5 (Section 5.1.1), are attracting an increased interest due to their potential to reduce the sensor footprint. In [161], the sensitivity of a SOI BI in the NIR was enhanced by regional mode engineering, i.e., leaving localized sections of upper cladding over the core layer instead of opening a sensing window over the full waveguide, achieving a LOD $= 2.44 \cdot 10^{-5}$ RIU. Finally, it is worth mentioning that all mentioned sensors operate in the NIR, even though MZI integrated sensors in a GaAs/AlGaAs platform were developed as early as 2013 and validated at $\lambda = 6$ μm with deionized (DI) water droplets [162].

2.6.2 Absorption sensors

Evanescent-field absorption sensing is possible just by analyzing the absorbance spectrum of a photonic waveguide, as explained in Section 2.2. As a consequence, most photonic absorption sensors avoid further architectural complexity and instead rely on highly sensitive, low-loss, straight or spiraled waveguides. Due to the specific challenges associated with each regime, NIR and MIR absorption sensors are usually considered different categories. An overview of recent absorption sensors is presented in Table 2.4. Sensitivity is expressed as $\partial A/\partial C$ and the LOD is given as analyte concentration in ppm whenever possible. LODs calculated by a 1-σ criterion, typical in gas sensing, were scaled to 3σ for consistency.

Near-infrared absorption sensors

There have been scarce advances in integrated absorption sensors in the NIR during the last years, due to the weakness of spectral features in said regime and the frequent overlap between spectra of different compounds, paired to the advances on MIR technologies, a more interesting operation regime. Some contributions can still be found, as the methane sensor based on a SOI strip with a SiN thin top-layer demonstrated in [164], which exhibited a LOD under 100 ppm. More recently, a nanoporous silica strip waveguide was employed to perform spectral analysis of different VOCs both in the liquid and gas phases [165]. A surface-enhanced infrared absorption (SEIRA) effect chalcogenide (ChG) rib waveguide has also been proposed for improved water absorption detection, but requires further investigation [166].

Mid-infrared absorption sensors

The MIR is the preferred operating regime for absorption sensors, as numerous molecules present fingerprint spectra (Section 2.4.1) at those wavelengths. This inherent molecular

Table 2.3: Selection of the state of the art of refractive-index sensors. Dashed lines separate sensors operating in the NIR to those in the MIR, while solid lines separate resonant from interferometric architectures. Abbreviations: tunable source (TS), surface functionalization (SF), not determined (n.d.), suspended (susp.). Whenever possible, the LOD has been expressed in RIU for analyte-independent comparison.

Ref.	Year	Regime	λ_0[μm]	TS	Platform	Architecture	Analyte	SF	Γ	S	LOD
[150]	2022	NIR	1.55	Yes	SOI	Cascaded RR	Glucose	No	n.d.	7071 nm/RIU	$1.74 \cdot 10^{-5}$ RIU*
[151]	2022	NIR	1.55	Yes	SOI	MZI coupled RR	NaCl	No	n.d.	49.4 nm/RIU	n.d.
[152]	2022	NIR	1.58	Yes	SOI	RR	NO	Yes	n.d.	545 pm/μM	500 nM
[149]	2022	NIR	1.55	Yes	SiNOI	Multiplexed RR	CRP	Yes	n.d.	179.6 nm/RIU	$2.43 \cdot 10^{-5}$ RIU
[153]	2024	NIR	1.57	Yes	SOI	RR	CO_2	Yes	n.d.	146.9 nm/RIU	$1.6 \cdot 10^{-3}$ RIU
[154]	2020	MIR	3.8	Yes	SOI	Cascaded RR	IPA	No	0.16	3000 nm/RIU	$9.9 \cdot 10^{-3}$ RIU
[155]	2024	MIR	2.1	Yes	Susp. Si	RR	CO_2	No	0.8	700 nm/RIU	$3.8 \cdot 10^{-2}$ RIU
[156]	2020	NIR	0.85	Yes	SiNOI	UMZI	Acetone	Yes	n.d.	$1.63 \cdot 10^{5}$ nm/RIU	$2.7 \cdot 10^{-7}$ RIU
[85]	2020	NIR	1.55	No	SiNOI	Coherent MZI	CRP	Yes	0.2	3.1 mrad/ngL^{-1}	184 pg/mL
[159]	2022	NIR	1.55	Yes	SOI	RR assisted UMZI	He	No	n.d.	1458 nm/RIU	$8.5 \cdot 10^{-5}$ RIU
[157]	2023	NIR	1.55	Yes	SOI	UMZI	KCl	No	0.8	700 nm/RIU	$2.85 \cdot 10^{-5}$ RIU
[160]	2024	NIR	1.31	No	SOI	Modulated MZI	Glycerol	No	0.5	$5.77 \cdot 10^{3}$ rad/RIU	$2.25 \cdot 10^{-7}$ RIU
[163]	2024	NIR	1.55	No	nLOF/TiO_2	Strip-loaded MZI	Ethanol	No	0.13	$2.69 \cdot 10^{3}$ rad/RIU	10^{-6} RIU
[161]	2024	NIR	1.55	Yes	SOI	BI	NaCl	No	0.1	726.7 rad/RIU	$2.44 \cdot 10^{-5}$ RIU

* Intrinsic LOD.

selectivity practically eliminates the need of surface functionalization. A variety of strip and rib waveguides in different platforms have been proposed. In [167] a germanium-on-silicon (GOS) multimode waveguide is used to evaluate the structure of bovine serum albumine (BSA) proteins and their composites by scanning the three amide vibrational bands (5.5–$13\,\mu$m). Porous germanium waveguides have been used for the detection of CO_2 ($\lambda = 4.3\,\mu$m) and CH_4 ($\lambda = 7.7\,\mu$m) gases with LODs of 3.36 and 5.67 ppm, respectively [168]. Chalcogenide glass waveguides are also widely spread, such as the waveguide employed in [138] to sense liquid benzene at $7.7\,\mu$m with a LOD of 250 ppb. Detection of methane was improved in another ChG waveguide by using wavelength modulation spectroscopy (WMS) [169]. This same gas was detected with a limit of detection of 234 ppm with a SOI waveguide at $\lambda = 3.29\,\mu$m [27]. A five-fold improvement in VOCs (acetone, ethanol, isoprene) sensing was achieved with a SiN waveguide, compared to SOI [170]. Another enhancement to the SOI platform was performed by synthesizing a SWG metamaterial waveguide, which, paired with artificial intelligence (AI), could detect low concentrations of IPA and glycerine mixtures and determine their mixing ratio [171]. A robust and chemically inert diamond waveguide with a AlN lower cladding was proposed to detect IPA at $6.25\,\mu$m, exhibiting a LOD $= 0.083$v% [172]. In gas sensing applications, where mechanical stability constrains are less restrictive than for liquids, slot and suspended waveguides provide significantly improved sensitivities. A SOI slot waveguide with double-tip fork couplers for ethalon suppression achieved sub-ppm CH_4 detection working at $3.27\,\mu$m [173]. A confinement factor beyond free-space ($\Gamma = 1.07$) was demonstrated in [116] for the first time with a suspended Ta_2O_5 waveguide by careful waveguide geometry optimization, and was used to detect acetylene (C_2H_2, $\lambda = 2.6\,\mu$m). Recently, the same group achieved isotope-specific CO_2 detection with high accuracy using a suspended-membrane SiN waveguide, reaching a LOD down to tens of ppb, thank to balancing the external and internal mode confinement factors [115]. As a final remark, there is room for different photonic architectures to enhance the performance of this plethora of waveguides. For example, a ChG ring resonator achieved a four-fold enhancement in the detection of aromatic aldehydes in a C_2Cl_4 solvent when compared to a waveguide [174]. To the best of the author's knowledge, no interferometric-based absorption sensors have been proposed for the MIR up to date.

Table 2.4: Selection of the state of the art of absorption sensors. Solid lines separate sensors operating in the NIR to those in the MIR, while dashed lines separate waveguides from resonators. Abbreviations: tunable source (TS), surface functionalization (SF), not determined (n.d.), suspended (susp.). Whenever possible, the LOD has been expressed in ppm.

Ref.	Year	Regime	λ_0[µm]	TS	Platform	Architecture	Analyte	SF	Γ	S	LOD
[164]	2017	NIR	1.65	Yes	SOI	Strip	CH_4	No	0.25	n.d.	< 100 ppm
[165]	2023	NIR	1.7	Yes	Porous SiO_2	Strip	VOCs	No	n.d.	n.d.	n.d.
[166]	2023	NIR	1.37	Yes	ChG	Rib	Water	Yes	n.d.	n.d.	n.d.
[167]	2020	MIR	6	Yes	GOS	Strip	BSA	No	n.d.	$5.3 \cdot 10^{-3}$ au/mgmL^{-1}	0.1 mg/mL
[168]	2021	MIR	4.3	Yes	Porous Ge	Rib	CO_2	No	0.45	23 nW/ppm	3.36 ppm†
[116]	2021	MIR	2.6	Yes	Susp. Ta_2O_5	Rib	C_2H_2	No	1.07	$2.97 \cdot 10^{-6}$ au/ppm	21 ppm
[172]	2021	MIR	6.25	Yes	PCD/AlN	Slab	IPA	No	0.13	$3.3 \cdot 10^{-6}$ au/ppm	830 ppm
[138]	2022	MIR	7.7	Yes	ChG	Rib	Benzene	No	0.09	0.11 au/ppm‡	0.25 ppm
[170]	2022	MIR	3.3	Yes	SiNOI	Strip	Acetone	No	1	10^{-6} au/ppm	12000 ppm
[169]	2022	MIR	3.29	Yes	ChG	Trapezoid	CJ_4	No	0.078	$1.25 \cdot 10^{-8}$ V/ppm	5100 ppm
[27]	2022	MIR	3.29	Yes	SOI	Rib	CH_4	No	0.23	$1.5 \cdot 10^{-6}$ au/ppm	234 ppm
[173]	2023	MIR	3.27	Yes	SOI	Slot	CH_4	No	0.7	$2.58 \cdot 10^{-5}$ au/ppm	0.9 ppm
[171]	2023	MIR	3.77	Yes	SOI	SWG Strip	IPA/Glycerin	No	0.33	n.d.	972 ppm
[115]	2024	MIR	4.35	Yes	Susp. SiN	Strip	CO_2	No	1.02	n.d.	0.1 ppm
[174]	2023	MIR	3.66	Yes	ChG	RR	Adelhyde	No	0.43	5 dB cm^{-1}/µmol mL^{-1}	0.25 µmoL mL^{-1}

† Value obtained from simulations.
‡ Calculated from the peak area.

Chapter 3

Methodology

This chapter contains the methods and protocols employed to develop and validate the different sensing architectures presented throughout this thesis. First, basic waveguide design is covered (Section 3.1), including calculations of sensitivity, losses and coupling. Then, the selected commercial chip fabrication platforms are introduced and mask layout preparation is discussed (Section 3.2). The near-infrared characterization setup is described (Section 3.3), along with its different subsystems: optoelectronic, microfluidic and software. Afterwards, the calibration technique used to compensate hardware errors in phase measurements is explained (Section 3.4). Finally, cleaning protocols to remove protective resin from fabrication and leftover impurities after experiments are specified (Section 3.5).

3.1 Waveguide design

In this work, the focus is set upon creating sophisticated sensing architectures which improve the current state of the art and can achieve a high performance while using standard waveguide components (Chapters 4 and 5), and on optimizing the geometry of conventional mid-infrared waveguides to enhance their detection capabilities (Chapter 6). For these matters, the photonic design of the different elements of the sensor is key. This section covers the analysis of the sensing waveguides, whose characteristics pose a great influence on the overall results. For classical guidelines to design MMIs and grating couplers, the reader is referred to [110, 175] and [112, 176], respectively.

A silicon nitride ($n_1 = 1.9963$, $k_1 = 0$) strip waveguide over a silica ($n_2 = 1.444$, $k_2 = 0$) substrate, with dimensions $H = 0.3\,\mu\text{m}$, $W = 1\,\mu\text{m}$ and $H_{\text{BOX}} = 3\,\mu\text{m}$, working at $\lambda_0 = 1.55\,\mu\text{m}$, is considered in the examples contained in this section. Pure water ($n_{\text{H}_2\text{O}} = 1.3154$, $k_{\text{H}_2\text{O}} = 1.5 \cdot 10^{-4}$) is used as a top cladding. This is the same geometry utilized in the near-infrared complex refractive index sensors presented in Chapter 4. Unless said otherwise, the TE polarization is analyzed.

3.1.1 Modal analysis

Waveguide modeling was done with Synopsys® FemSIM™, which is a general-purpose mode solver based on the finite element method (FEM) [177]. Using this software, waveguide geometry and materials are defined, and the computational domain is divided into a non-uniform mesh. Perfectly matched layers (PML) can be added as boundary conditions to calculate leaky modes, e.g., for the calculation of substrate leakage. Once defined, the solver is able to find the indicated number of modes supported by the structure and sort them by either the real or the imaginary part of their effective index. As an example,

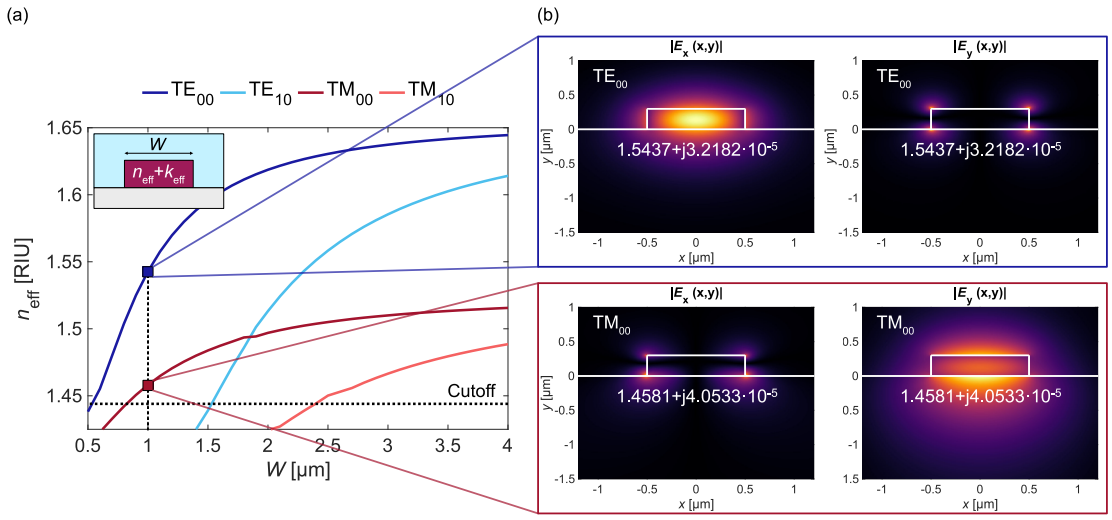

Figure 3.1: (a) Evolution of the effective index as a function of width for a waveguide with $H = 0.3\,\mu\text{m}$ at $\lambda = 1.55\,\mu\text{m}$. The waveguide materials are a silicon nitride ($n_1 = 1.9963$, $k_1 = 0$) core, a silicon dioxide ($n_2 = 1.444$, $k_2 = 0$) substrate and a water ($n_{\text{H}_2\text{O}} = 1.3154$, $k_{\text{H}_2\text{O}} = 1.5 \cdot 10^{-4}$) cladding. (b) Electrical field distributions of the TE and TM modes supported by the waveguide for $W = 1\,\mu\text{m}$.

in Fig. 3.1(a), the evolution of n_{eff} as a function of waveguide width for a strip waveguide with $H = 0.3\,\mu\text{m}$ at $\lambda_0 = 1.55\,\mu\text{m}$ is shown. The field profiles of the fundamental TE and TM modes for the width $W = 1\,\mu\text{m}$ can be seen in Fig. 3.1(b). The calculated n_{eff} gives information about whether the mode is guided, i.e., $n_{\text{eff}} > n_2$, and the degree of confinement into the core, as a larger effective index indicates a higher overlap with the high-index core material. The total propagation loss coefficient (α_{eff}) can be calculated from k_{eff} (Chapter 2, Eq. (2.8)). For photonic designers, it may be useful to express propagation losses (L_{prop}) in $\text{dB}\,\text{cm}^{-1}$:

$$L_{\text{prop}} = 10\log_{10}(e)\alpha_{\text{eff}}10^{-2} = 10\log_{10}(e)\frac{4\pi}{\lambda}k_{\text{eff}}10^{-2}. \tag{3.1}$$

The propagation losses of the TE mode shown in Fig. 3.1(b) are dominated by absorption in the water cladding and amount to $11.33\,\text{dB}\,\text{cm}^{-1}$.

3.1.2 Sensitivity

The most common parameter to describe the bulk sensing capabilities of the waveguide is the mode confinement factor in the sample, which is equivalent to the mode bulk sensitivity. Even though it is possible to implement Eq. (2.4) from Chapter 2 after calculating the electrical field distribution of the mode and its group index, a simpler approach arises from Eq. (2.23) (Chapter 2). Following said definition, either the real or the imaginary part of the index of the upper-cladding material can be swept around their reference value. The rate at which the effective index changes can then be calculated, yielding a good approximation for Γ:

$$\Gamma \approx \frac{\Delta n_{\text{eff}}}{\Delta n_{\text{sample}}} \approx \frac{\Delta k_{\text{eff}}}{\Delta k_{\text{sample}}}. \tag{3.2}$$

Figure 3.2(a) shows a typical curve for the determination of $\Gamma = 0.22$, where only the real part of the refractive index is considered. On the other hand, surface sensitivity can be calculated by adding a biorecognition layer with appropriate refractive index and absorption values to the model [178], as represented in the inset of Fig. 3.2(b). Representing the

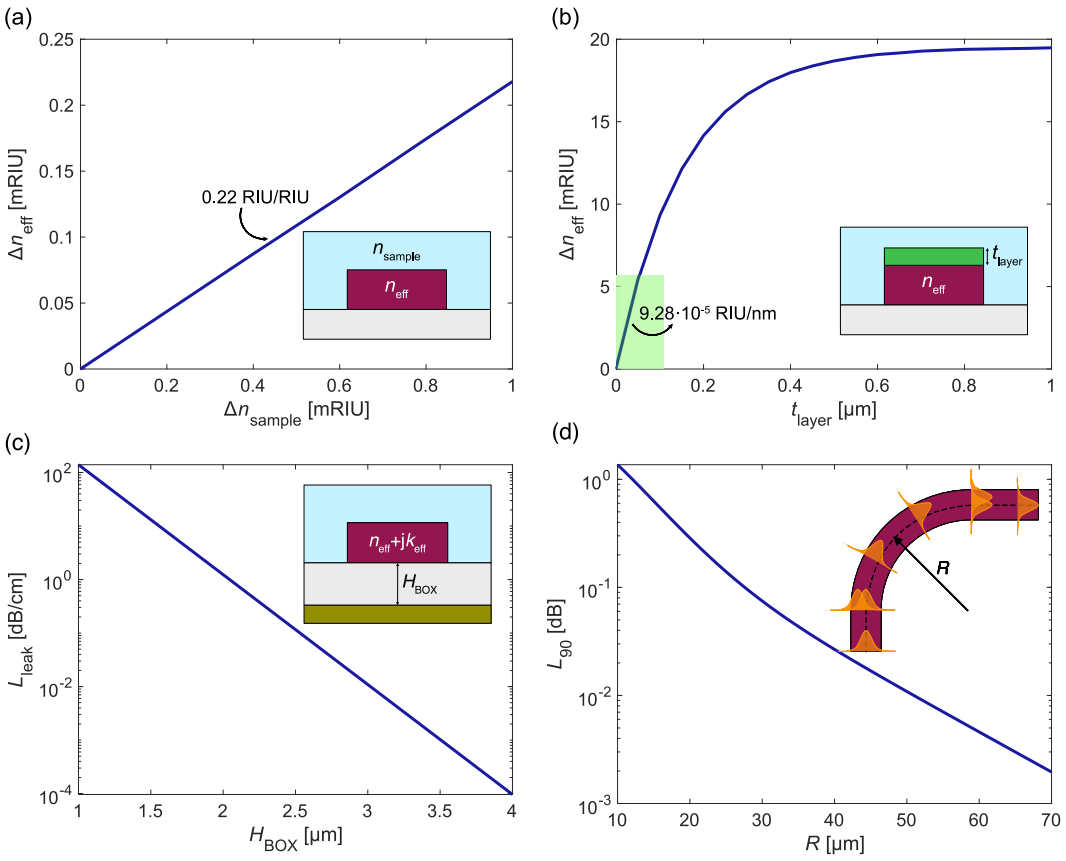

Figure 3.2: (a) Typical variation of the effective index of the mode as a consequence of variations in the sample index. (b) Typical variation of the effective index of the mode with an increasing thickness of an adsorbed protein layer. (c) Evolution of leakage loss with lower-cladding thickness. (d) Losses per 90-degree bend as a function of the bending radius.

calculated n_{eff} against the layer thickness (t_{layer}) yields a curve as the one shown in Fig. 3.2(b), for a lossless layer with refractive index $n_{\text{layer}} = 1.45$. The saturation of the curve is consistent with the exponential decay of the evanescent field. Surface sensitivity can be approximated from the linear section as

$$S_{\text{m,surf}} \approx \frac{\Delta n_{\text{eff}}}{\Delta t_{\text{layer}}} \approx \frac{\Delta k_{\text{eff}}}{\Delta t_{\text{layer}}}. \tag{3.3}$$

In the represented example, such sensitivity reaches $9.28{\cdot}10^{-5}$ RIU/nm.

Effect of thermal fluctuations

The value of the complex refractive index of a material depends on temperature (T). Therefore, changes in temperature induce changes in the effective index of the mode, which for chemical sensing applications is considered a drawback. To help with temperature management, it is useful to calculate the modal thermal sensitivity as

$$S_{\text{m,temp}} = \frac{\partial n_{\text{eff}}}{dT} + \text{j}\frac{\partial k_{\text{eff}}}{dT} = \sum_i \Gamma_i \left(\frac{\partial n_i}{\partial T} + \text{j}\frac{\partial k_i}{\partial T} \right), \tag{3.4}$$

where Γ_i and $n_i + \text{j}k_i$ are the confinement factor in and the complex refractive index of the i-th material of the waveguide, respectively. Equation (3.4) will be useful in the analysis of the sensing architectures presented in Chapters 4 and 5.

3.1.3 Leakage loss

Certain aspects must be considered when calculating a leaky mode. In the first place, a sufficiently large fraction of the substrate must be included in the computational domain. The minimum substrate thickness should be determined after carrying out a convergence study. Then, lossless materials should be assumed, so that the entire modal loss coefficient can be attributed to leakage. In the waveguide used as an example in this section, this means that water losses are disregarded. Last, PML boundaries should be set in the vertical direction. Another convergence study should be performed to select a PML thickness. Once modes are calculated under these conditions, their leakage loss will be given by Eq. (3.1). However, it is recommended to scan the thickness of the lower cladding and evaluate leakage in the swept range to avoid numerical errors. The results should exhibit an exponential trend as in the example from Fig. 3.2(c). Although the exact value depends on the target application, leakage losses below $0.1\,\mathrm{dB\,cm^{-1}}$ are typically acceptable.

3.1.4 Bending loss

As will be further discussed in Section 3.2.2, curved waveguides are employed for on-chip routing and for achieving large interaction lengths while keeping a reduced footprint. However, waveguide bends have associated losses, which are due to radiation and mode mismatch between the bent and straight waveguides, as schematized in the inset of Fig. 3.2(d). FemSIM™ supports the calculation of bent modes by two different simulation methods: conformal index-mapping, which translates bent into straight waveguides [179], and direct, which solves Maxwell's equations in cylindrical coordinates without approximations [180]. Once the method is selected and the bending radius (R) is set, pure radiation losses can be calculated in a similar way to leakage (Section 3.1.3), but adding PMLs in the horizontal direction and scanning the radius. Mode mismatch losses are calculated by the overlap integral

$$\mathrm{OL} = \frac{\left|\iint_{-\infty}^{\infty} E_1(x,y)E_2^*(x,y)dxdy\right|^2}{\iint_{-\infty}^{\infty}|E_1(x,y)|^2dxdy\iint_{-\infty}^{\infty}|E_2(x,y)|^2dxdy}, \tag{3.5}$$

where E_1 and E_2 are the electric field distributions of the straight and curved waveguide modes, respectively, and the symbol * indicates the complex conjugate [181]. This expression is also valid to calculate mode mismatch losses between bent waveguides with different radii. Curvature losses are usually expressed as the loss induced by a 90-degree bend,

$$L_{90} = L_{\mathrm{rad}} + 2L_{\mathrm{trans}}, \tag{3.6}$$

where $L_{\mathrm{rad}} = -10\log_{10}(e)\alpha_{\mathrm{eff}}(\pi/2)R$ and $L_{\mathrm{trans}} = -10\log_{10}(\mathrm{OL})$. Figure 3.2(d) shows an example of the evolution of L_{90} with an increase in R. The selected bending radius should yield negligible losses, e.g., $L_{90} < 0.1\,\mathrm{dB}$.

3.1.5 Waveguide coupling

Besides the bending losses, whose calculation has just been described, power coupling between adjacent waveguides is a limiting factor in the design of spirals. This can be studied by analyzing two identical parallel waveguides, which form a directional coupler. In such devices, there is a continuous power transference between the waveguides as light propagates [182]. This structure supports pairs of even and odd supermodes. The final field distribution results from the combination of the supermodes, which are equally excited by the input mode, as schematically shown in Fig. 3.3(a). As they have slightly different propagation constants ($\beta_{\mathrm{e}}, \beta_{\mathrm{o}}$), after propagating a certain distance (z'), part of the light

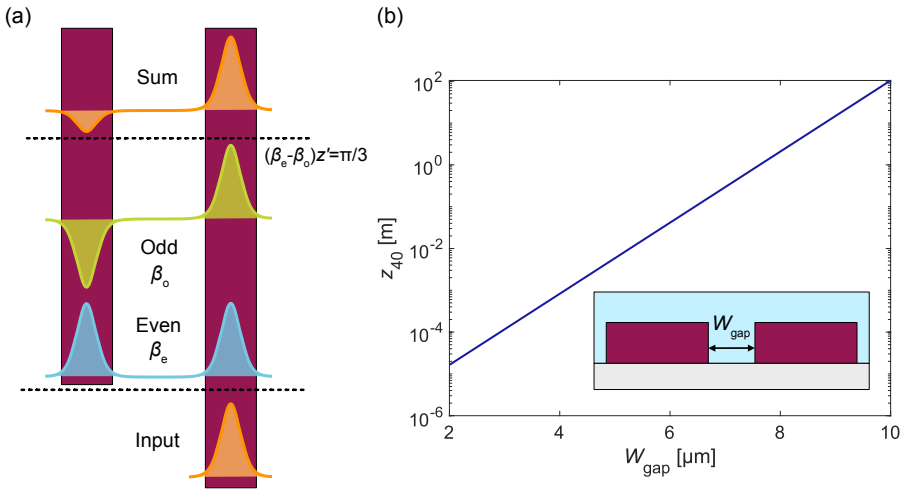

Figure 3.3: (a) Even and odd supermodes supported by two parallel waveguides. After a distance z', a fraction of the power launched in one waveguide is transferred to the other. (b) Evolution of the 40-db coupling distance with the separation between waveguides.

launched in one waveguide has been coupled to the other. Power is completely transferred at a distance

$$L_\pi = \frac{\pi}{\beta_\mathrm{e} - \beta_\mathrm{o}}. \tag{3.7}$$

Waveguides must be separated by a distance W_gap that guarantees negligible coupling over the lengths expected in the sensor. A typical criterion for setting the lower bound of W_gap is the 40-dB coupling length, i.e., the propagation length that yields 40-dB coupling between adjacent waveguides. This separation distance can be calculated from the sum of the two supermodes as [182]

$$z_{40} = \frac{L_\pi}{\pi} \cos^{-1}(1 - 2 \cdot 10^{-4}). \tag{3.8}$$

Here it is worth highlighting that the 40-dB limit is an arbitrary criterion that can be made either more strict or relaxed depending of the design specifications. In Fig. 3.3(b), the increase of z_{40} with an augmented gap is shown. Once the gap is selected, it is good practice to perform light propagation simulations to verify the waveguides are indeed decoupled [183, 184].

3.2 Chip fabrication

The fabrication of the different generations of sensing chips that were developed throughout this thesis was carried out in commercial foundries, namely Cornerstone [185] and Applied Nanotools (ANT) [186]. These companies offer multi-project wafer (MPW) runs, allowing customers to share manufacturing costs by combining their designs in a single mask set. The foundry thus receives a mask layout, processes it and delivers the fabricated chips. Therefore, a suitable sensing chip layout for each platform ought to be prepared.

3.2.1 Foundries and platforms

Cornerstone's silicon nitride platform

Cornerstone is an open source and license-free silicon photonic prototyping foundry which works in collaboration with the University of Southampton (United Kingdom) and the

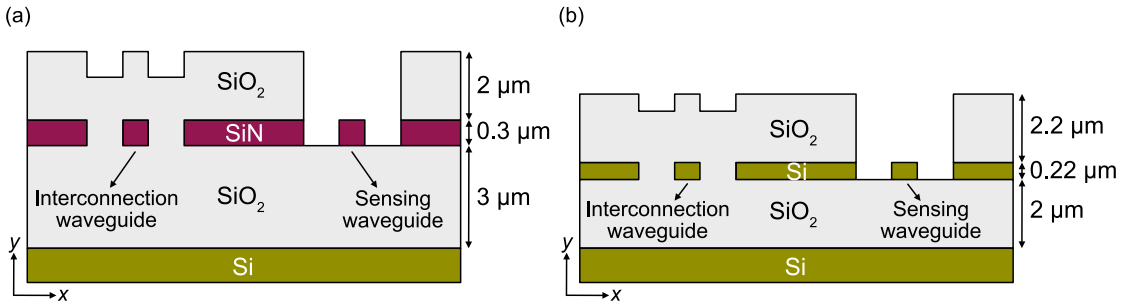

Figure 3.4: (a) SiNOI and (b) SOI platforms provided by Cornerstone and ANT, respectively. Both foundries offer opening windows on the silica cladding to expose the waveguide to the sample.

University of Glasgow (United Kingdom). Their prototyping platforms use industry-compatible deep-UV projection lithography. Among the different options they provide, the silicon nitride platform was the one selected in this thesis to fabricate two generations of chips. In this platform, schematized in Fig. 3.4(a), patterns are processed in a single-side polished SiN-on-insulator (SiNOI) wafer with the following characteristics:

- Crystalline silicon substrate.
- Thermal silica buried oxide (BOX) with a thickness of 3 µm.
- Low pressure chemical vapor deposited (LPCVD) silicon nitride (Si_3N_4) device layer with 300 ± 15 nm thickness.

Silicon nitride structures are fully etched with a minimum feature size (MFS) of 250 nm. A 2-µm silica upper cladding is deposited over the device layer. However, to achieve light-matter interaction, said cladding is selectively removed from the sensing regions. This is a standardized custom step in the fabrication of integrated photonic sensors. The available design area is $11.47 \times 15.45\,\text{mm}^2$.

Applied Nanotools' silicon-on-insulator platform

Applied Nanotools is a silicon photonics foundry based in Edmonton (Canada). Their NanoSOI Fabrication Service counts with a 100-keV electron-beam lithography (EBL) system with negligible stitching errors. The selected ANT platform, schematically represented in Fig. 3.4(b), was a silicon-on-insulator (SOI) one, including:

- High-resistivity silicon substrate.
- BOX layer with a thickness of 2 µm.
- Monocrystalline silicon device layer with a thickness of 220 nm.

Silicon structures are fully etched, with a MFS of 60 nm, although the resolution may decrease due to proximity effects. In an analogous way as with the previous platform, a 2.2 µm silica cladding was deposited. Sensing windows were also requested as a custom step. The design area for this platform is $9 \times 9\,\text{mm}^2$

3.2.2 Layout design

Masks were created with Nazca Design [187], an open source photonic integrated circuit (PIC) design framework based on Python-3, which is designed to efficiently prepare layouts via scripting. This tool includes modules such as Interconnects and Geometries

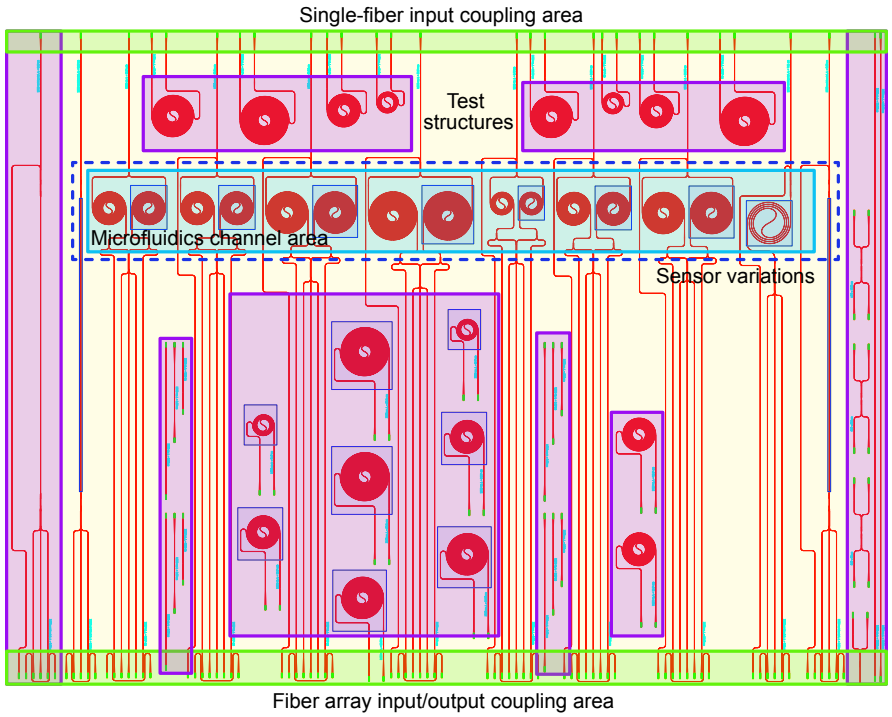

Figure 3.5: Mask layout submitted to Cornerstone's SiN MPW#3. The structures included are either sensor variations (blue discontinuous) or test structures (purple areas). The upper and lower edges (green areas) are used for surface coupling with a single fiber or an array. Sensing spirals are aligned in the (light blue) area intended for the microfluidic channel.

[188], which were combined to implement custom component libraries. The mask layout submitted to Cornerstone's SiN MPW#3 is presented in Fig. 3.5 as an example of a sensing chip mask. Several spiral waveguides are integrated to increment propagation distances while keeping a reduced footprint. Both sensing and test structures are spatially organized to optimize the available design area while meeting the constrains imposed by the measurement setup (Section 3.3), especially those regarding the position of light-coupling and microfluidics areas. These crucial design aspects will be further discussed in Section 3.3.2.

3.3 Measurement setup

Once the fabricated chips are received, they need to be characterized, both optically and as sensors. The sensing results obtained in this thesis correspond to sensing experiments performed with liquid samples and operating in the near-infrared. For this purpose, the measurement setup schematized in in Fig. 3.6(a) was built. A picture of said setup can be observed in Fig. 3.6(b). Different subsystems, which will be independently detailed in Sections 3.3.1, 3.3.2 and 3.3.3, can be distinguished: the optoelectronics, the microfluidics and the software interface. The behavior of the complete system is as follows. NIR light is emitted by the laser and boosted by an erbium-doped fiber amplifier (EDFA). Input polarization is manually optimized with a polarization controller. An angled-polished fiber array (FA) mounted into a 3-axis nanopositioning stage is employed to couple light into the chip, which is in turn placed in a 4-axis stage to facilitate alignment. The sample circulates over the sensing areas in a microfluidic channel defined by a PDMS flow-cell, in alternation with a buffer solution, and interacts with the evanescent field of the guided mode, thus provoking changes in the output of the sensor. The output signals are coupled

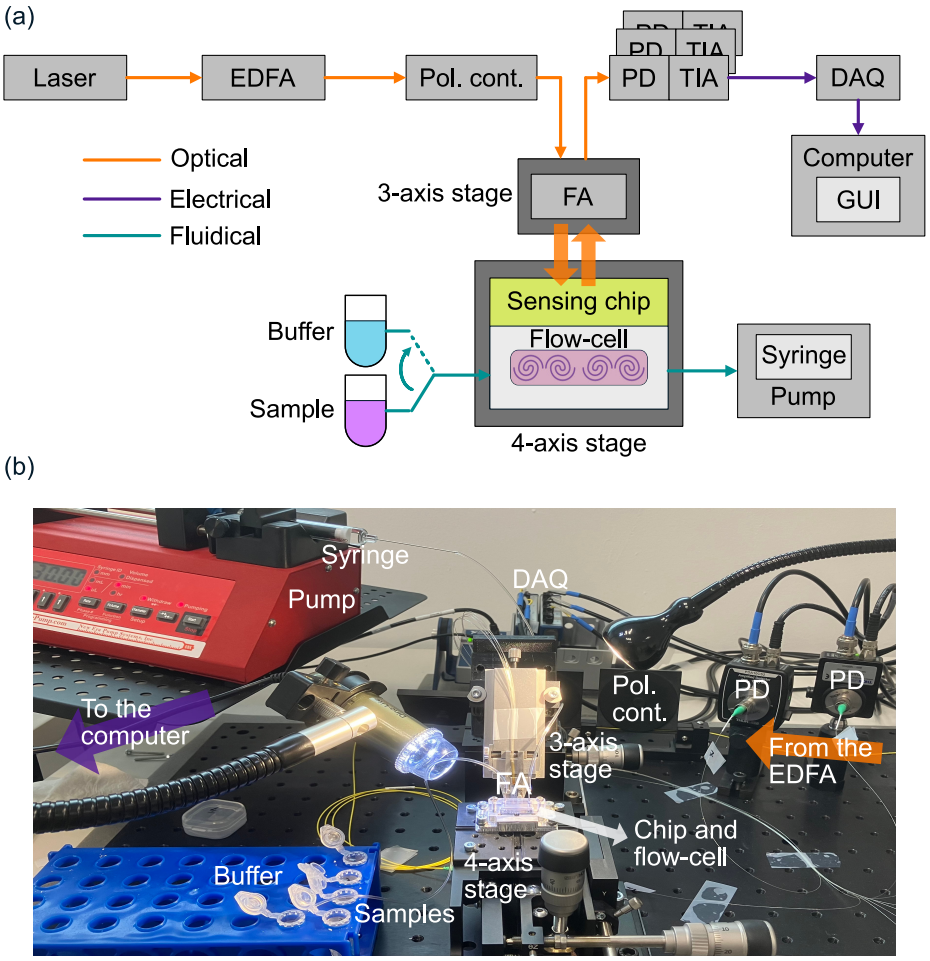

Figure 3.6: (a) Schematic and (b) picture of the sensor characterization setup, which combines optics, electronics, microfluidics and software. Abbreviations: erbium-doped fiber amplifier (EDFA), polarization controller (Pol. cont.), fiber array (FA), photodetector (PD), transimpedance amplifier (TIA), data acquisition board (DAQ), graphical user interface (GUI).

back to the FA, and directed towards amplified (TIA) photodetectors (PD). The resulting voltage signals are digitized by a data acquisition board (DAQ) and recorded by an in-house pre-processing software controlled by a Matlab graphical user interface (GUI).

3.3.1 Optics and electronics components

The optics and electronics components are involved in generating the input signal, coupling it to the chip, recollecting the sensor outputs, detecting them and converting them to digital signals. The specific elements of the setup are described here.

Laser source. The laser source was a Santec TSL-700, a low-noise external cavity laser (ECL), which is tunable in the 1.48–1.64 µm wavelength range and delivers an optical power up to 13 dBm (20 mW). For most experiments, it was used at a fixed wavelength $\lambda_0 = 1.55$ µm with an output power of 10 dBm (10 mW).

Erbium-doped fiber amplifier. The EDFA was an EAD-500-C from IPG Photonics, working on the C-band (1537–1565 nm). The output power ranges from 18 to 27 dBm for an input within −3 and 10 dBm (0.5–10 mW). It was typically set at the 27 dBm maximum power.

Polarization controller. Polarization was manually optimized with the Thorlabs FPC562 by sequentially adjusting its three paddles.

Fiber array. Light input/output coupling was performed via an angle-polished 8-fiber array from O/E Land. Fibers were separated by a 127-µm pitch. The polishing angle was customized according to the radiation angle of the grating coupler. The exact relationship between the radiation and polishing angles can be found in Appendix A. The array was placed on a Thorlabs HFA001 fiber array holder, mounted on a Thorlabs MAX300 3-axis stage.

Photodetectors. Outputs were detected by a set of Thorlabs PDA10CS2 InGaAs detectors with built-in transimpedance amplifiers. The responsivity at $\lambda_0 = 1.55$ µm was around 1.05 A/W and the transimpedance gain was switchable between 8 different levels. Depending on the measured architecture, between three and five different photodetectors were needed.

Data acquisition board. The data acquisition stage consisted in two independent NI 9239 modules mounted in a NI sbRIO-9239 chassis, both from National Instruments. Each module had 4 channels, which were digitized at a sampling rate $f_s = 50$ kHz with 24-bit precision. This allowed for the simultaneous recording of a up to 8 channels. The maximum input voltage range was fixed at ± 10 V.

Setup noise-floor

In Section 2.5 of Chapter 2, it was explained how the noise-floor of the system determines the LOD of a sensor, which is the highest-level performance metric and the best suited to establish comparisons between different configurations. Each of the components of the setup introduces uncertainty to the measurement. Generally, the laser source introduces relative intensity (RIN) and phase noises, the EDFA adds on excess noise, mechanical vibrations affecting the fiber array induce a stochastic modulation of the coupling efficiency (often known as mechanical noise), the photodiode suffers from shot noise, the electrical components of the TIA have an associated thermal noise and the imperfect digitization process in the DAQ can be modeled as quantization noise. All of these elevate the total noise level of the measurements, so it is important to understand and minimize the influence of each source on a system-specific basis [189, 190]. Detailed parametric expressions of the most relevant noise contributions and a noise-floor optimization strategy can be found in Appendix B.

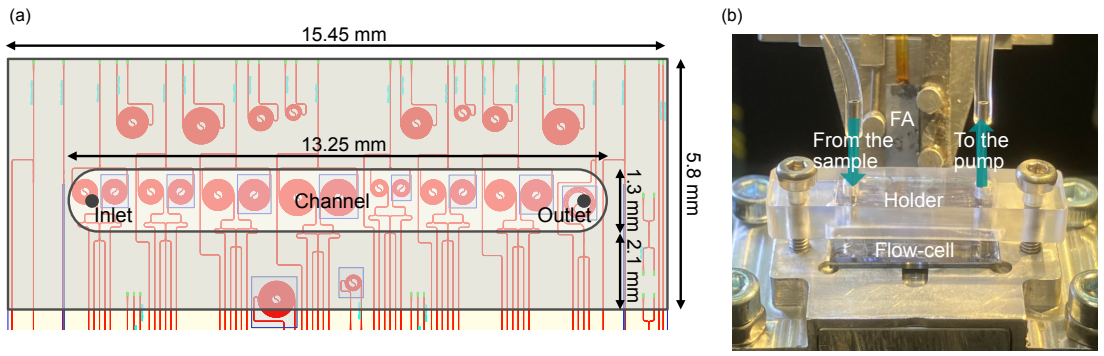

Figure 3.7: (a) PDMS flow-cell design for Cornerstone's SiN MPW#3 chip. The channel covers all sensing regions. (b) Close-up picture of the assembly formed by the cell and its holder.

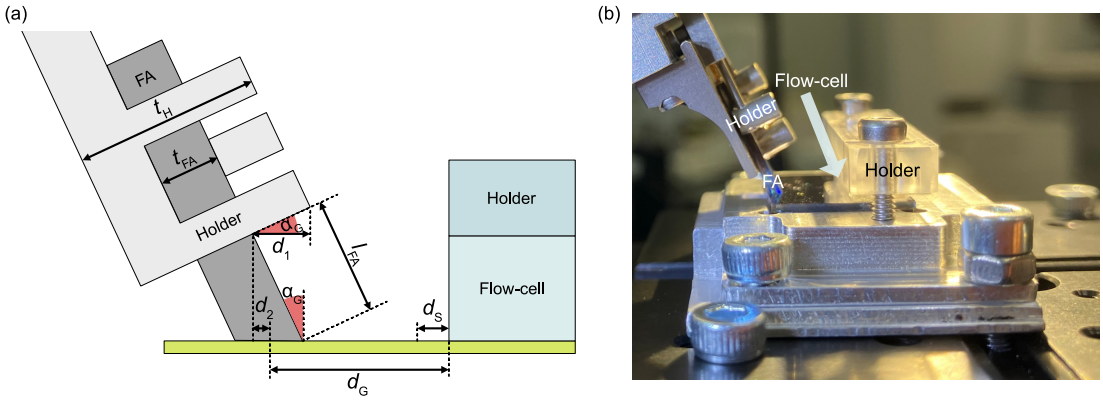

Figure 3.8: (a) Lateral view of the aligned fiber array and the PDMS flow-cell. Their separation distance must ensure that their respective holders do not collide. (b) Picture of the FA aligned to the grating couplers of Cornerstone's SiN MPW#3 chip. The mask was successfully designed to avoid collisions.

3.3.2 Microfluidics

The microfluidics system is composed by a NE-1000 Multi-Phaser syringe pump from New Era operating in withdrawal mode, a gastight 5 mL Hamilton 1005 LTN syringe and a custom-made PDMS flow-cell with a methacrylate holder. Liquid flow-tubes with 0.51 mm internal diameter connect the solutions, which are stored in 5 mL Eppendorf containers, to the channel inlet, and the channel outlet to the syringe. The goal of the whole system is providing a controlled flow of liquids over the sensing areas, avoiding the formation of spurious air bubbles. Normally, in a sensing experiment, different samples are alternated with a buffer solution, which in this work was MilliQ deionized (DI) water. To alternate between sample and buffer, the start of the inlet tube is simply changed from one Eppendorf to another, with the precaution of stopping the pump 10 seconds prior to said change. This ensures that no air is sucked in the transition. The flow is re-started once the tube is inside the new solution.

The design and fabrication of the PDMS flow-cell requires special attention due to its capital importance in optimum sensor operation. A perfect microfluidic channel must achieve both full coverage of the sensing areas and hermetical sealing. In Fig. 3.7(a), the design made for Cornerstone's SiN MPW#3 chips is shown as an example. To fabricate the cells, custom PMMA molds were filled with an in-house PDMS preparation using the Dow SYLGARD™ 182 Silicone Elastomer Clear 0.5 kg Kit from Ellsworth Adhesives, which includes the PDMS and a curing agent. The exact procedure can be consulted in Appendix C. Once cut out of the mold, liquid inlet and outlet perforations were made to the channels with 0.5 mm punchers from Darwin Microfluidics. To guarantee optimum performance, PDMS flow-cells were single-use. A methacrylate holder was designed and fabricated to maintain the flow-cell in proper position during experiments. Figure 3.7(b) shows a picture of the whole assembly.

Microfluidics and light coupling

As shown in the layout of Fig. 3.5, the surface of the chip is shared by test, sensing and coupling structures. When a new chip is being designed, the relative position of the latter two must be considered. Test structures are not problematic because they are not typically measured together with microfluidics. Figure 3.8(a) shows a schematic side view of the fiber array, aligned to a grating coupler, and the microfluidic flow-cell and its holder, placed on top of the sensing area. It can be seen that, if the separation between the end of

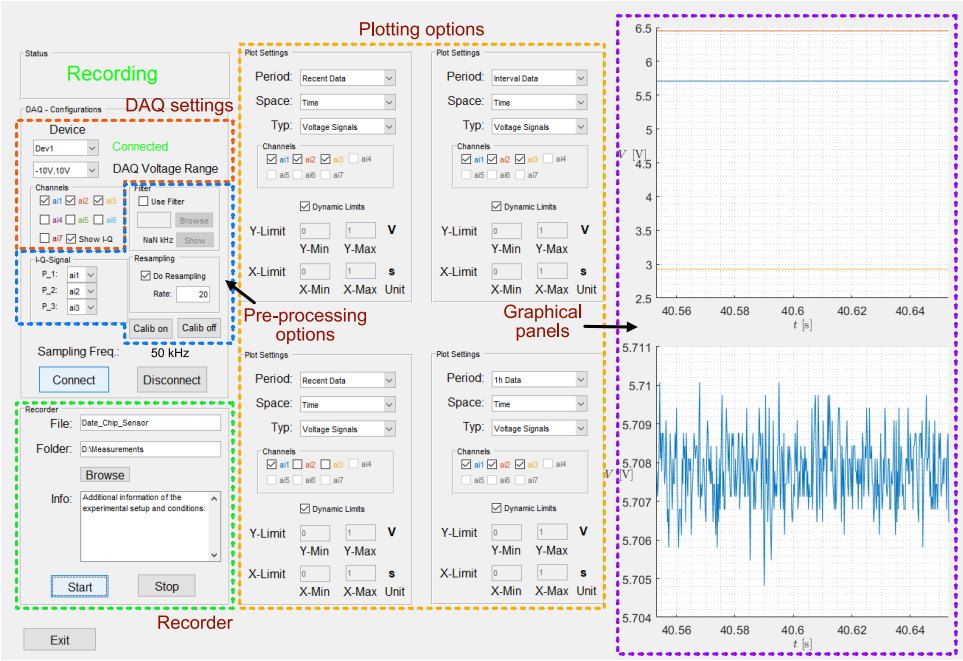

Figure 3.9: Screenshot of the acquisition and pre-processing GUI. Two additional graphics panels are not shown for compactness.

the cell and the grating coupler (d_G) is not large enough, the FA holder will collide with the methacrylate holder, impeding correct alignment. Considering a safety distance d_S, a lower limit for d_G can be established as

$$d_G \geq d_S + d_1 - d_2 \tag{3.9}$$

where d_1 and d_2 are the distances marked in Fig. 3.8(a). Using trigonometry,

$$\begin{aligned} d_1 &= (t_H - t_{FA})\cos(\alpha_G) \\ d_2 &= l_{FA}\sin(\alpha_G) - \frac{t_{FA}}{2\cos(\alpha_G)} \end{aligned} \tag{3.10}$$

where t_{FA} and t_H are the thicknesses of the FA and its holder, respectively, l_{FA} is the length of the FA outside the holder and α_G is the radiation angle of the grating coupler. For the presented setup, $t_H = 5\,\text{mm}$, $t_{FA} = 1.5\,\text{mm}$ and $l_{FA} \approx 2\,\text{mm}$. Both α_G and d_G are degrees of freedom in the design. The grating couplers designed for Cornerstone's SiN MPW#3 mask radiated with an angle of $\alpha_G = 26°$ to a polished fiber ($\lambda_0 = 1.55\,\mu\text{m}$), yielding $d_G \geq 4.8\,\text{mm}$ for $d_S = 0$. Figure 3.8(b) shows a picture of the coupled array, evidencing that the selected separation between the sensing and coupling areas is much larger than the calculated minimum.

3.3.3 Acquisition and pre-processing software

Signal acquisition is controlled by a GUI implemented in Matlab [191], of which a screenshot is presented in Fig. 3.9. This software enables selecting one of the two available DAQ modules, connecting to it and adjusting settings. Additionally, pre-processing options such as digital resampling, filtering or FFT calculations are available. In this thesis, the only followed pre-processing step was low-pass filtering followed by resampling with a factor of 20 when long experiments were performed, thus reducing the effective sampling frequency to $f_s^{'} = 50/20\,\text{kHz} = 2.5\,\text{kHz}$. The digitized signals can be displayed, showing either instant (lower panel in Fig. 3.9) or averaged values (upper panel in Fig. 3.9), in

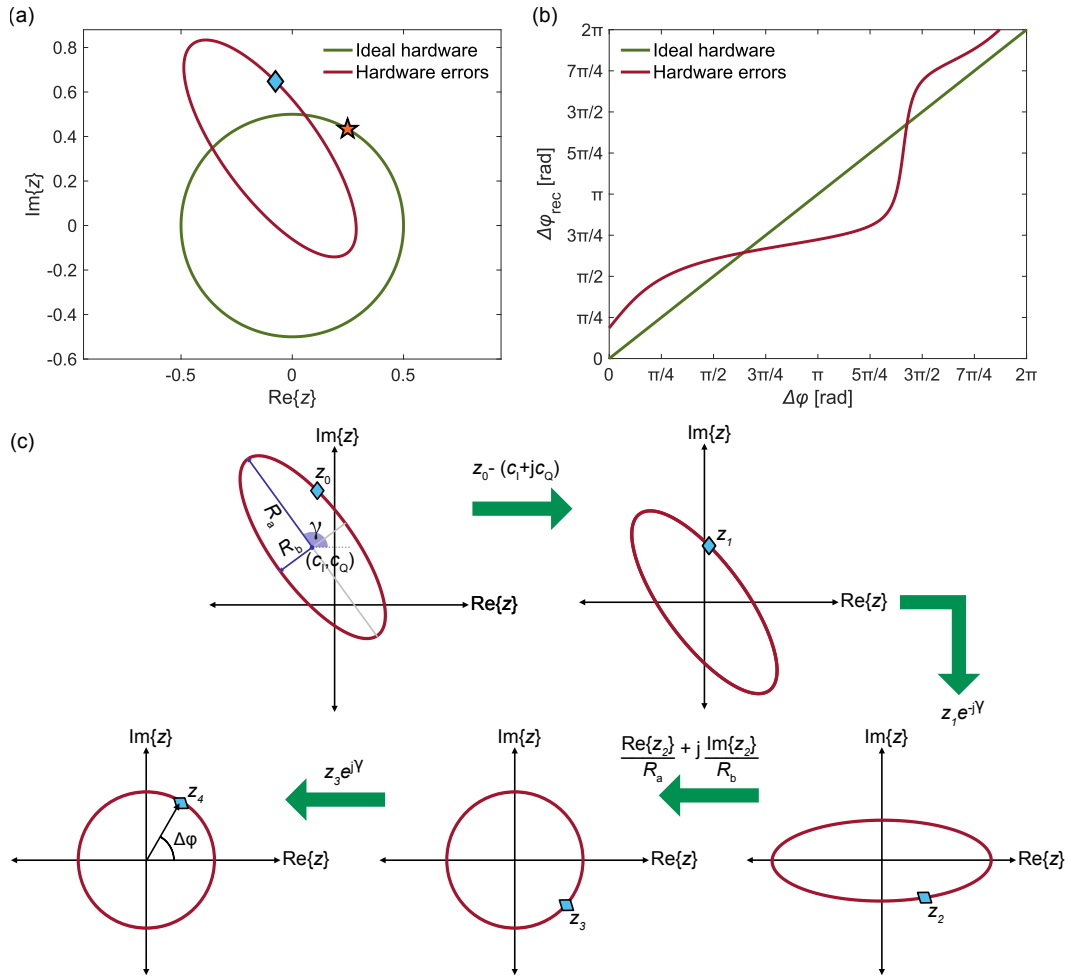

Figure 3.10: (a) Recovered complex signal in the IQ plane. Hardware errors transform the ideal circle into an ellipse. (b) Phase read-out. When hardware errors are not handled, the recovered phase is incorrect. (c) Illustration of the blind calibration algorithm used to recover the original phase shift, based on fitting the measured data to an ellipse and transforming it into a circle.

graphical panels. The recording option saves the acquired data and additional experimental information to a Matlab file. Here it is worth noting that the GUI was originally implemented for a different setup with a single DAQ board. As a consequence, it does not support the connection to two different modules at once. To work around this issue, the data acquired by each module was displayed and recorded simultaneously by two independent GUI instances. When needed, the signals from both modules were synchronized using timestamps. Further signal processing tasks such as digital low-pass filtering, baseline correction, read-out or calibration (Section 3.4) were performed off-line with in-house Matlab scripts.

3.4 Phase signal calibration

In Section 2.3.2 (Chapter 2), the coherent read-out technique employed in the refractive index sensors from this work was explained. However, the coefficients of the read-out matrix of Eq. (2.18) are only valid under the assumption of ideal hardware. In practical systems, there are two major measurement impairments. In a first place, fabrication deviations from the nominal design of the 2×3-MMI can result in phase errors at the outputs, causing their relative phase shifts to differ from $120°$. Second, the output intensities I_1, I_2

and I_3 may not be coupled to the FA with the same efficiencies. Power imbalances due to coupling have the greatest effect, as tolerances in the standard fabrication processes are small compared to fiber alignment errors. When seen in the complex plane, the combination of phase and amplitude imbalances provokes a linear transformation of the expected circle into an ellipse, as illustrated in Fig. 3.10(a). This in turn leads to read-out errors like those in Fig. 3.10(b). Fortunately, these errors are deterministic and can be canceled with calibration techniques. In this thesis, a blind calibration technique was implemented.

3.4.1 Blind calibration algorithm

The term *blind* means that only the measured data is required for calibration. This technique is based on geometrical properties and works by transforming the obtained ellipse into a circle centered at the origin of the complex plane. For that matter, the following steps, schematized in Fig. 3.10(c) are followed.

1. Apply the ideal-case read-out matrix to the output signals to obtain the uncalibrated signal z_0.
2. Select a fragment of the signal and fit its datapoints to the coefficients of an ellipse using Taubin's method [192].
3. Convert the algebraic coefficients into the radius of the major (R_a) and minor (R_b) axes, the angle of the mayor axis (γ) with the real axis and the center of the ellipse $(c_\mathrm{I} + \mathrm{j}c_\mathrm{Q})$.
4. Center at the origin: $z_1 = z_0 - (c_\mathrm{I} + \mathrm{j}c_\mathrm{Q})$.
5. Rotate to align the major axis with the real axis: $z_2 = z_1 e^{-\mathrm{j}\gamma}$.
6. Scale into a circle: $z_3 = \frac{\mathrm{Re}\{z_2\}}{R_\mathrm{a}} + \mathrm{j}\frac{\mathrm{Im}\{z_2\}}{R_\mathrm{b}}$.
7. Restore original angle: $z_4 = z_3 e^{\mathrm{j}\gamma}$.

The main disadvantage from this approach is that the accumulated phase shift must be large enough to correctly fit the calibration fragment to an ellipse ($\Delta\varphi \geq \pi$). This is not a problem in most characterization experiments, because the induced phase shifts are usually around tens of radians. In real applications with very low concentrations of analyte, a calibration solution, prepared to provoke a sufficiently large phase shift, can be flowed over the sensor prior to the experiment itself. However, there may be scenarios where pre-calibrating is not an option, or where the expected $\Delta\varphi$ is so low that small deviations due to a sub-optimal fit cannot be tolerated. In such cases, mean squared error (MSE) calibration techniques can be employed to calculate a corrected read-out matrix (Chapter 2, Eq. (2.18)) which compensates imbalances [111]. Such techniques need the generation of a set of estimators $\hat{z}$, which are based on previous knowledge about the expected shape of the signal. Commonly used estimation functions are polynomials and sigmoids.

The performance of any calibration technique depends on the variance of the measurement, as a noisier dataset increases the error of the fit. However, it must be noted that calibrating does not change the original signal-to-noise ratio. The reason behind this is that linear transformations affect all data alike. Finally, if imbalances change during an experiment, e.g., due to a progressive misalignment of the FA or a change in the spectral response of the gratings and MMIs when the wavelength is swept, calibration parameters must be updated. This would mean selecting different calibration fragments with which to calibrate different signal fragments.

3.5 Cleaning protocols

Chip cleanliness, especially in the interaction area, is fundamental for the outcome of sensing experiments. Unwanted residues could, in one respect, reduce sensor sensitivity by creating an obstacle between the sample and the waveguide. Additionally, localized residues could significantly increase scattering losses. This is critical for sensors with longer sensing paths, which already accumulate a high power loss due to sample-induced absorption and intrinsic waveguide losses (see Section 3.1). In this section, the protocols to remove the protecting resist of new chips and to clean chips after bulk sensing experiments are described. Here it is worth mentioning that there is a risk that the sonication steps included in the following protocols damage the uncladded waveguides, especially considering that the wafers from the platforms described in Section 3.2.1 are not thermally grown and thus exhibit lower adhesion between layers. However, similar cleaning protocols had been intensively used on SiNOI platforms, without damaging any structure, by other members of the Photonics & RF Research Lab prior to this thesis [191], so they were considered safe.

3.5.1 Resist removal protocol

This protocol is designed for dissolving and removing the protective resist which is deposited after chips are fabricated in order to protect them during the dicing and shipping processes. This must be performed before any sensor characterization measurement to ensure that the sensing waveguide is completely exposed to the sample.

1. Sonicate in isopropanol for 15 minutes.
2. Sonicate in acetone for 15 minutes.
3. Sonicate in isopropanol for 7 minutes.
4. Sonicate in acetone for 7 minutes.
5. Pressure-wash with DI water.
6. Dry with N_2 stream.

3.5.2 Residues removal protocol

This protocol is designed for removing residual traces left over the sensing surface after bulk characterization experiments performed with NaCl solutions, which could significantly elevate propagation losses if they are not effectively removed. After the correct implementation of the steps below, the chip can be reused.

1. Sonicate in DI water for 5 minutes.
2. Pressure-wash with DI water.
3. Dry with N_2 stream.
4. Sonicate in isopropanol for 5 minutes.
5. Sonicate in acetone for 5 minutes.
6. Pressure-wash with DI water.
7. Dry with N_2 stream.

Chapter 4

Near-infrared complex refractive index sensor

This chapter presents a complex refractive index sensor, which is the first near-infrared novel sensing architecture developed in this thesis. After an introduction to simultaneous complex refractive index detection (Section 4.1), the proposed sensing architecture is detailed (Section 4.2). Then, the design of the two implemented generations of sensors is addressed (Section 4.3), including the challenges encountered during the characterization of first-generation sensors and the improvements made in the second generation. Afterwards, the fixed-wavelength (Section 4.4) and spectroscopic (Section 4.5) experiments carried out for sensor validation are described and discussed. The chapter ends with a set of conclusions (Section 4.6).

The sensing approach and most of the experimental results presented in this chapter are published in A. Torres-Cubillo, A. Sánchez-Postigo, J. Jágerská, J. G. Wangüemert-Pérez, and R. Halir, "Simultaneous measurement of refraction and absorption with an integrated near-infrared Mach–Zehnder interferometer," Optics & Laser Technology **177**, 111154 (2024).

4.1 Introduction

In Chapter 2, it was explained how changes in the real refractive index (n) of a sample can be extracted either from wavelength shifts ($\Delta\lambda_{\text{res}}$) in resonant and spectrally resolved interferometric sensors (Eq. (2.14)), or from phase shifts ($\Delta\varphi$) in fixed-wavelength interferometers (Eq. (2.15)). Alternatively, changes in the imaginary refractive index (k) can be measured from the output intensity, generally by calculating the absorbance (A) of the sample (Eq. (2.11)). In Section 2.4, it was also explained how spectral fingerprinting provides inherent selectivity to a target analyte, whereas non-spectroscopic sensors require some kind of chemical surface functionalization to achieve specificity. Finally, in the state of the art (Section 2.6), the division between refraction and absorption sensors was drawn to simplify comparisons. Sensors falling under one of these categories provide partial information, because the variations in one part of the refractive index are ignored.

While it is possible to detect analytes by monitoring either refraction or absorption, both n and k are needed to optically characterize a substance, and are indeed intrinsically related by Kramers-Kroning (KK) relations, which are bidirectional mathematical relations which connect the real and imaginary parts of complex functions [193, 194]. When

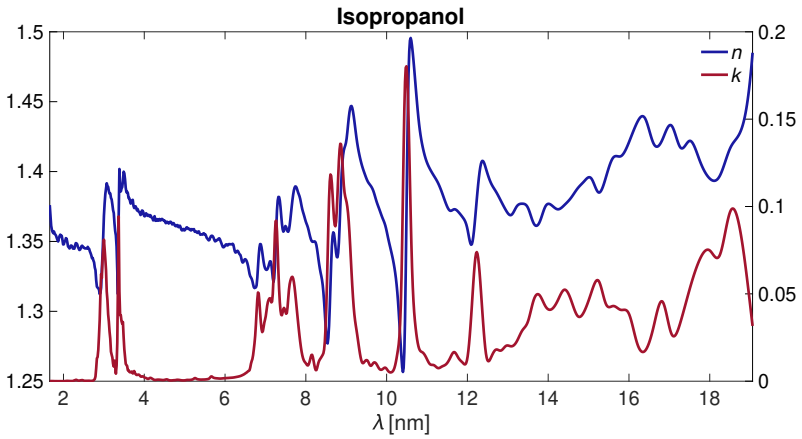

Figure 4.1: Complex refractive index of isopropanol in the 1.67–19.1 µm wavelength range. Data extracted from [197].

they are particularized to the complex refractive index, KK equations can be written as

$$\begin{aligned} n(\omega) &= 1 + \frac{2}{\pi} P \int_0^\infty \frac{\omega' k(\omega')}{\omega'^2 - \omega^2} d\omega' \\ k(\omega) &= -\frac{2\omega}{\pi} P \int_0^\infty \frac{n(\omega') - 1}{\omega'^2 - \omega^2} d\omega', \end{aligned} \tag{4.1}$$

where $\omega = c/\lambda$ and P is the Cauchy's principal value [195]. Here it is worth noting that the whole spectra of one part of the index must be known in order to calculate the value of its counterpart at a single wavelength. In practice, these relations are implemented by numerical approximations, whose accuracy depends on wide spectral-range measurements [196], thus limiting their application for on-site, rapid detection.

There is therefore a need for sensors which directly deliver information about both the real and imaginary parts of the complex refractive index in a single measurement, thus leading to a greater insight into the nature of the sample. Some promising field applications are materials science [86, 198], astrophysics [199, 200] and the detection of volatile organic compounds. The latter present comparably pronounced absorption and dispersion features [201], as shown in Fig. 4.1, taking isopropanol (IPA) as a representative example. Furthermore, complex refractive index sensors could potentially leverage the high sensitivity achieved with refraction sensing with the molecular specificity of absorption. This could in turn pave the way toward improved detection schemes.

4.1.1 State of the art

Complex refractive index sensing appears more frequently in free-space implementations using frequency combs [87] and cavities [88]. However, a few examples of integrated complex refractive index sensors can be found, disseminated in different wavelength regimes. In the visible range, a Young interferometer in a polymer platform was proposed and evaluated with ethanol and tartrazine [202]. A PC microdisk resonator performed multi-biomarker detection by considering both phase and intensity measurements [203]. In the near-infrared, a SWG ring resonator in SOI incorporated absorption sensing by measuring changes in the gradient of the Fano resonance [204]. The same read-out scheme has been proposed for a PC Fano cavity, and numerically shown to distinguish between different ternary mixtures [205]. In another simulation work, a SOI RR employs multiple wavelengths to selectively detect methanol, ethanol, propanol and water by their complex refractive indices [206]. An unbalanced MZI with spectral readout

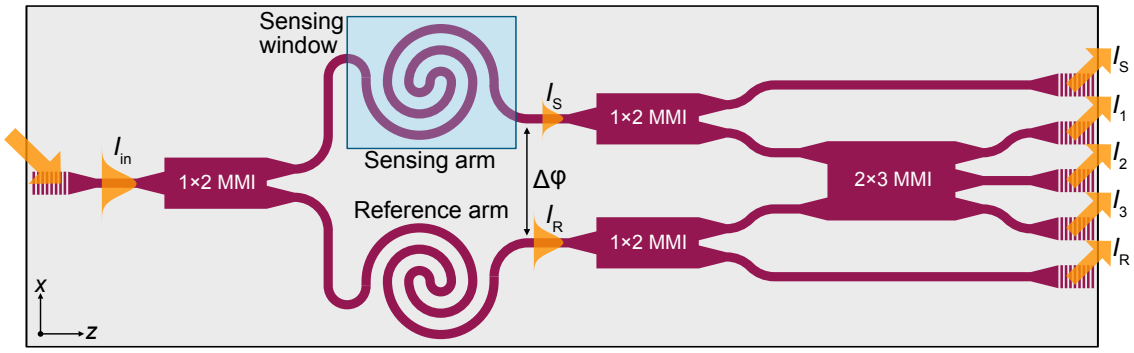

Figure 4.2: Schematic diagram of the MZI-based complex refractive index sensor. The five provided outputs enable the simultaneous detection of phase and absorption changes.

in a SOI platform was used to effectively characterize the complex refractive index of different molybdenum thin-films, but the structure was not evaluated in terms of sensitivity or limit of detection [207]. In the mid-infrared, a suspended RR was demonstrated for absorption and dispersion spectroscopy of CO_2 in concentrations as low as 1% [208]. Finally, in the work presented in [154], two SOI RR were cascaded to detect changes in the refractive index of IPA diluted in acetone by taking advantage of the Vernier effect.

In this chapter, a NIR complex refractive index sensor in a silicon nitride platform is presented. The proposed architecture, which will be explained in Section 4.2, is based on a coherent MZI, modified to simultaneously perform direct evanescent-field absorption measurements. This is the first implementation of an integrated interferometric complex refractive index sensor with a linear phase retrieval, which can operate both at a fixed and scanned wavelength.

4.2 Sensor architecture

A schematic representation of the proposed sensing architecture is shown in Fig. 4.2. The sensor is based on a coherent MZI, as those explained in Section 2.3.2 of Chapter 2, but provides five output signals instead of three. The two additional outputs enable direct measurements of the attenuation due to the sample. Surface grating couplers are employed for light input and output, and MMIs for splitting and recombination. Spiraled single-mode waveguides are used to increase interaction lengths without compromising footprint. The bulk sensing operation of the sensor and its performance metrics are explained in the following.

4.2.1 Working principle

Light from the source is coupled into the chip and divided into the sensing and reference arms, which are equal in length (L), as shown in Fig. 4.2. In the reference arm, the mode propagates undisturbed, with a wavelength-dependent effective index $n_{\text{eff}}^{\text{R}}(\lambda) + \text{j}k_{\text{eff}}^{\text{R}}(\lambda)$. The sensing arm, in turn, is exposed to the sample, which can be considered as the mixture of a solvent and an analyte diluted at a concentration C. The sensing mode, with a confinement factor $\Gamma(\lambda)$, is able to interact with the analyte through its evanescent field. A change in concentration modifies the refractive index of the sample:

$$\begin{aligned} n_{\text{sample}}(\lambda, C) &= n_{\text{sample}}(\lambda, 0) + \Delta n_{\text{sample}}(\lambda, C), \\ k_{\text{sample}}(\lambda, C) &= k_{\text{sample}}(\lambda, 0) + \Delta k_{\text{sample}}(\lambda, C), \end{aligned} \tag{4.2}$$

where $n_{\text{sample}}(\lambda, 0) + \text{j}k_{\text{sample}}(\lambda, 0)$ is the complex refractive index of the solvent without any analyte. Due to light-matter interaction, the effective index of the sensing mode de-

pends on the analyte concentration as well as on the wavelength, and can be expressed as

$$\begin{aligned} n_{\text{eff}}^{\text{S}}(\lambda, C) &= n_{\text{eff}}^{\text{S}}(\lambda, 0) + \Gamma(\lambda)\Delta n_{\text{sample}}(\lambda, C), \\ k_{\text{eff}}^{\text{S}}(\lambda, C) &= k_{\text{eff}}^{\text{S}}(\lambda, 0) + \Gamma(\lambda)\Delta k_{\text{sample}}(\lambda, C), \end{aligned} \tag{4.3}$$

where $n_{\text{eff}}^{\text{S}}(\lambda, 0) + \text{j}k_{\text{eff}}^{\text{S}}(\lambda, 0)$ is the effective index when the upper cladding is purely composed of the solvent. At the end of the arms of the interferometer, each mode has accumulated a phase shift

$$\begin{aligned} \varphi_{\text{R}}(\lambda) &= \frac{2\pi}{\lambda} n_{\text{eff}}^{\text{R}}(\lambda) L, \\ \varphi_{\text{S}}(\lambda, C) &= \frac{2\pi}{\lambda} n_{\text{eff}}^{\text{S}}(\lambda, C) L \end{aligned} \tag{4.4}$$

with respect to the start of the waveguide, and has an intensity

$$\begin{aligned} I_{\text{R}}(\lambda) &= \frac{I_{\text{in}}}{2} e^{-\frac{4\pi}{\lambda} k_{\text{eff}}^{\text{R}}(\lambda) L}, \\ I_{\text{S}}(\lambda, C) &= \frac{I_{\text{in}}}{2} e^{-\frac{4\pi}{\lambda} k_{\text{eff}}^{\text{S}}(\lambda, C) L}, \end{aligned} \tag{4.5}$$

where I_{in} is the intensity of the input-coupled signal from the source.

As it was already explained in Chapter 2 (Section 2.3.2), the relative accumulated phase shift between the sensing and the reference modes can be written as

$$\Delta\varphi(\lambda, C) = \varphi_{\text{S}}(\lambda, C) - \varphi_{\text{R}}(\lambda) = \frac{2\pi}{\lambda} \Delta n_{\text{eff}}(\lambda, C) L, \tag{4.6}$$

where $\Delta n_{\text{eff}}(\lambda, C) = n_{\text{eff}}^{\text{S}}(\lambda, C) - n_{\text{eff}}^{\text{R}}(\lambda)$. The difference between the relative phase shift with and without analyte gives a measurement proportional to Δn_{sample}, from which the concentration can be calculated:

$$\Delta\varphi(\lambda, C) - \Delta\varphi(\lambda, 0) = \frac{2\pi}{\lambda} \Gamma(\lambda) \Delta n_{\text{sample}}(\lambda, C) L. \tag{4.7}$$

Unless said otherwise, the values of $\Delta\varphi$ given in this thesis are normalized following Eq. (4.7). To detect phase shifts by means of the coherent read-out scheme described in Chapter 2, Section 2.3.2, the reference and intensity signals are routed by 1×2-MMIs to the 120° hybrid, implemented by a 2×3-MMI. The complex signal

$$z(\lambda, C) = \frac{1}{2} \sqrt{I_{\text{R}}(\lambda) I_{\text{S}}(\lambda, C)} e^{\text{j}\Delta\varphi(\lambda, C)}, \tag{4.8}$$

is generated by combining the three outputs of the 2×3-MMI.

With the introduction of the 1×2-MMI at the output of each spiral, proportional intensities to I_{R} and I_{S} can be directly detected. The absorbance of the analyte can thus be determined by taking

$$A(\lambda, C) = -\log_{10}\left(\frac{I_{\text{S}}(\lambda, C)}{I_{\text{S}}(\lambda, 0)}\right) = \log_{10}(e) \frac{4\pi}{\lambda} \Gamma(\lambda) \Delta k_{\text{sample}}(\lambda, C) L, \tag{4.9}$$

where $I_{\text{S}}(\lambda, 0)$ is the intensity detected in the absence of analyte. Absorbance is therefore directly proportional to Δk_{sample}. Moreover, the relationship between Δk_{sample} and C can be made explicit by using the molar absorption coefficient (ϵ) defined in Section 2.2.2 of Chapter 2:

$$\Delta k_{\text{sample}}(\lambda, C) = \frac{\epsilon(\lambda)}{\log_{10}(e) \frac{4\pi}{\lambda}} C. \tag{4.10}$$

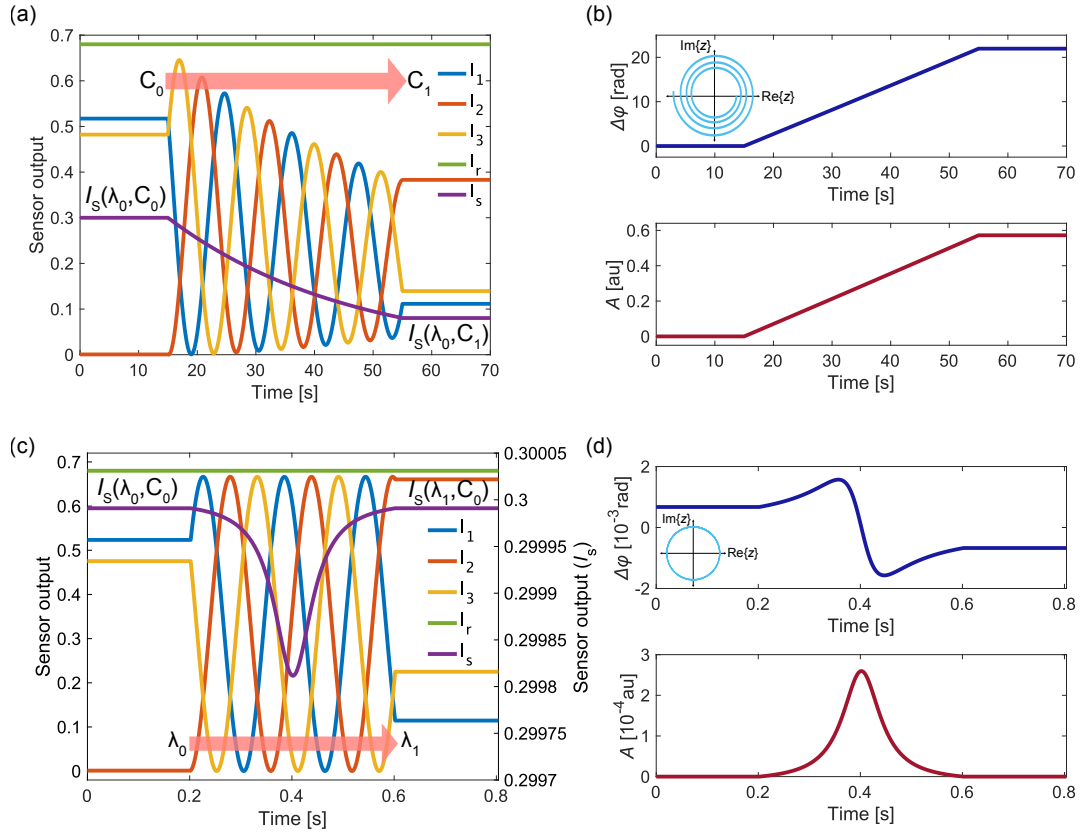

Figure 4.3: Modeled output of the complex refractive index sensor. (a) Detected signals in fixed wavelength operation. (b) Calculated phase shift and absorbance when concentration is increased with time. The complex signal is shown as an inset in the upper panel. (c) Detected signals in scanned wavelength operation. The sensing intensity (I_S) is represented in a different axis for visibility. (d) Phase shift (dispersion) and absorbance responses when the wavelength is swept with time. The complex signal is shown as an inset in the upper panel.

This is turn means that the concentration of analyte can be retrieved from absorbance as

$$C = \frac{A(\lambda, C)}{\Gamma(\lambda)\epsilon(\lambda)L}. \tag{4.11}$$

In practical situations where any of the parameters Γ, ϵ or L are unknown, absorbance and concentration can be experimentally correlated by measuring sets of pre-calibrated samples. Even though the reference intensity I_R is not strictly needed for analyte detection, having access to it can be useful to monitor baseline drifts or estimate the impact of thermal fluctuations.

Figure 4.3(a) presents the expected detected outputs of such a sensor, featuring $\Gamma = 0.22$ and $L = 5\,\text{mm}$, while operating at a fixed wavelength $\lambda_0 = 1.55\,\mu\text{m}$. A linear change in analyte concentration from C_0 to C_1, occurring in a 40-s time span determined by the pumping speed of the fluidics system, results in a linear increase of both parts of the complex refractive index of the upper cladding ($\Delta n_{\text{sample}} + \text{j}\Delta k_{\text{sample}} = 5 \cdot 10^{-3} + \text{j}3 \cdot 10^{-2}\,\text{RIU}$). This in turn provokes a series of oscillations of the interferometric outputs (I_1, I_2, I_3) and an exponential decay of the sensing intensity I_S. In this ideal model, the reference intensity I_R does not suffer any alteration. From these signals, $\Delta\varphi$ and A can be calculated as previously explained, and are shown in the upper and lower plots of Fig. 4.3(b), respectively. Both magnitudes linearly follow the shape of the index change.

In Fig. 4.3(c), the modeled swept-wavelength behavior is shown. In this example, $\Gamma = 0.5$ and $L = 10\,\text{mm}$ for enhanced sensitivity, and the wavelength is scanned at a speed

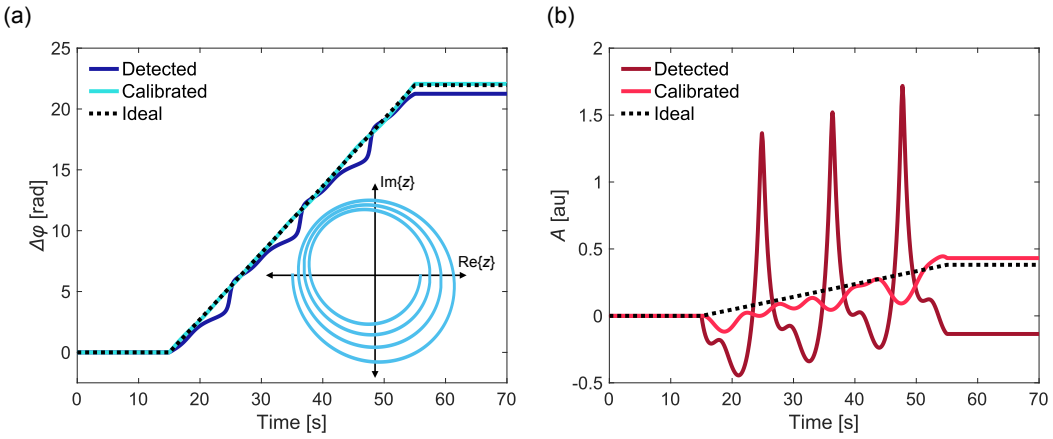

Figure 4.4: Modeled output of the complex refractive index sensor operating at a fixed wavelength, with non-ideal hardware. (b) Calculated phase shift and (c) absorbance, with and without calibration, along with the ideal sensor response.

of 0.5 nm/s around one of the resonance peaks of pure CO_2 in the NIR ($\lambda_0 \sim 1.58\,\mu m$). The combination of the wavelength responses of the MZI and of the sample causes the oscillations in the phase signals, while the sensing intensity signal dips reflecting the transimision spectrum of the sample. Calculated dispersion and absorbance spectra are shown in Fig. 4.3(d). To retrieve the dispersion spectrum, the wavelength response of the MZI in the absence of analyte was obtained and subtracted from the output in the presence of CO_2. In the NIR, the amplitude of analyte-induced spectral changes, especially for gases, is very small compared to the spectral response of the interferometer itself. This is evident when the number of recorded oscillations are compared with the magnitude of the retrieved phase shift. The change in absorbance is also remarkably weak. As a consequence, an extremely high SNR would be required to perform these kind of measurements.

Measuring the imaginary index from the complex signal

After examining Eq. (4.8) and looking at the envelope of the interferometric signals in Fig. 4.3(a), it seems possible to measure the imaginary refractive index directly from the magnitude of the complex signal z, as absorbance could theoretically be obtained by taking

$$A = -\log_{10}\left(\left|\frac{z(\lambda, C)}{z(\lambda, 0)}\right|^2\right). \tag{4.12}$$

Even though this approach is valid in an ideal scenario, practical implementations are not that straightforward. As it was explained in Section 3.4 (Chapter 3), hardware non-idealities distort the complex signal, turning it ellipsoidal. When changes in amplitude are considered in addition to phase shifts, non-linear distortion in $|z|$ is observed. The employed blind calibration method is based on linear transformations, and systematically ignores amplitude information. Therefore, although it is effective for phase detection, it cannot correct absorption signals. An example of this behavior can be observed in Fig. 4.4, which shows the modeled sensor output with realistic hardware errors, while operating at a fixed wavelength under the same concentration change as in the example of Figs. 4.3(a)–(b). Dedicated calibration methods can be implemented for this purpose, but they require a good previous knowledge of the expected shape of the signal in order to generate MSE estimators, and even the inclusion of signal modulation techniques, adding further complexity. Even so, the solutions that can be reached are numerically unstable, only cor-

rect local fragments of the signal and are highly dependent on environmental conditions [209], which are not desirable traits in robust photonic integrated sensors. Taking into account these considerations, the separate measurement of the sensing intensity, i.e., the approach followed throughout this chapter, is preferred.

4.2.2 Figures of merit

The proposed configuration will be evaluated as a bulk complex refractive index sensor. As it was indicated in Chapter 2, Section 2.5 (Eq. (2.23)), the modal sensitivity is the same for the real and the imaginary indices:

$$S_{\mathrm{m}} = \frac{\partial n_{\mathrm{eff}}}{\partial n_{\mathrm{sample}}} = \frac{\partial k_{\mathrm{eff}}}{\partial k_{\mathrm{sample}}} = \Gamma. \tag{4.13}$$

Changes in the real effective index of the mode are measured by phase-shift changes, whereas changes in its imaginary part are measured by the absorbance, yielding the architectural sensitivities

$$\begin{aligned} S_{\mathrm{a},n_{\mathrm{eff}}} &= \frac{\partial \Delta\varphi}{\partial n_{\mathrm{eff}}} = \frac{2\pi}{\lambda} L, \\ S_{\mathrm{a},k_{\mathrm{eff}}} &= \frac{\partial A}{\partial k_{\mathrm{eff}}} = \frac{4\pi}{\lambda} \log_{10}(e) L, \end{aligned} \tag{4.14}$$

which can be related as $S_{\mathrm{a},k_{\mathrm{eff}}} = 2\log_{10}(e) S_{\mathrm{a},n_{\mathrm{eff}}} \approx 0.87 \cdot S_{\mathrm{a},n_{\mathrm{eff}}}$. To calculate the device-level sensitivity, modal and architectural sensitivities are multiplied:

$$\begin{aligned} S_{\mathrm{n}} &= \frac{\partial \Delta\varphi}{\partial n_{\mathrm{sample}}} = \frac{2\pi}{\lambda} \Gamma L, \\ S_{\mathrm{k}} &= \frac{\partial A}{\partial k_{\mathrm{sample}}} = \frac{4\pi}{\lambda} \log_{10}(e) \Gamma L. \end{aligned} \tag{4.15}$$

From Eq. (4.15) it can be concluded that the three means to improve overall sensitivity are decreasing the wavelength, enhancing the confinement factor and increasing the interaction length. The latter strategy is the one emphasized in this work, as it will be discussed in Section 4.3. To determine the LOD, the standard deviation of either the phase-shift or the absorbance signal is evaluated over a steady-state fragment with a near-zero value [148]:

$$\begin{aligned} \mathrm{LOD_n} &= \frac{3\sigma_{\Delta\varphi}}{S_{\mathrm{n}}}, \\ \mathrm{LOD_k} &= \frac{3\sigma_A}{S_{\mathrm{k}}}. \end{aligned} \tag{4.16}$$

4.3 Sensor design and evaluation

A first generation of sensors was designed for Cornerstone's SiNOI platform, described in Section 3.2.1 of Chapter 3. Two wafers of sensing chips were fabricated under a collaboration with the University of Southampton. Unfortunately, after a series of evaluations, these sensors were deemed unsuitable for the detection of analytes, as it will be shown in Section 4.3.3. Therefore, none of the sensing results obtained with them is presented in this thesis. However, the conclusions learnt from this first trial served to refine the design of the second-generation sensors, with which the experimental results included in this chapter were obtained. The second generation of sensors was fabricated on Cornerstone's SiNOI platform as well, specifically in the commercial SiN multi-project wafer run number 3 (MPW#3).

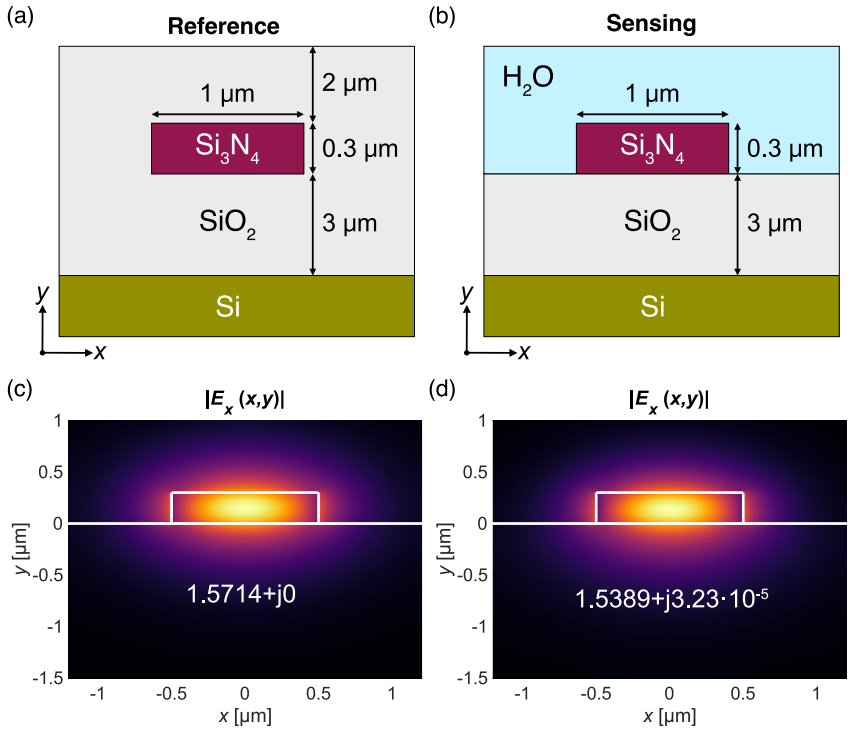

Figure 4.5: Cross section of the (a) reference and (b) sensing waveguides. Thickness is not to scale. Profile of the fundamental TE mode of the (c) reference and (d) sensing waveguides.

Table 4.1: Complex refractive index of the waveguide materials at $\lambda_0 = 1.55\,\mu$m.

Material	n	k	**Ref.**
Si_3N_4	1.9963	0	[210]
SiO_2	1.4440	0	[211]
H_2O	1.3154	$1.5 \cdot 10^{-4}$	[212]

This section covers the design and characteristics of the different components of the sensors, which are analogous in the first and second generations, and the sensor layout and the optical characterization of the first and second generations of sensors, presented separately.

4.3.1 Sensor components

As it was indicated in Section 4.2, the key elements of the sensors are the sensing and reference waveguides, grating couplers and MMIs. First-generation sensors were designed for three different operation wavelengths, $\lambda_0 = 1.31\,\mu$m, $\lambda_0 = 1.58\,\mu$m (CO_2 detection) and $\lambda_0 = 1.65\,\mu$m (CH_4 detection). Second-generation sensors were originally conceived as environmental CO_2 ($\lambda_0 = 1.58\,\mu$m) and CH_4 ($\lambda_0 = 1.65\,\mu$m) sensors. However, due to practical limitations, the experimental results presented in Sections 4.4 and 4.5 were obtained with the CO_2 sensors, albeit using liquid samples and operating at $\lambda_0 = 1.55\,\mu$m. As a consequence, simulations at this latter wavelength will be analyzed in the following.

Waveguides

Figures 4.5(a)–(b) show the cross sections of the reference (and interconnection) and sensing waveguides, respectively, both with equal dimensions $H = 0.3\,\mu$m and $W = 1\,\mu$m. The only difference between them is their upper cladding, which is silica in ref-

Table 4.2: Modal sensitivities to changes in the complex refractive index of the sample (Γ), the thickness of an adsorbed protein layer ($S_{\mathrm{m,surf}}$) and temperature fluctuations ($\partial(n_{\mathrm{eff}}^{\mathrm{S}} - n_{\mathrm{eff}}^{\mathrm{R}})/\partial T$ and $\partial k_{\mathrm{eff}}^{\mathrm{S}}/\partial T$).

Γ	$S_{\mathrm{m,surf}}$ [RIU/nm]	$\partial(n_{\mathrm{eff}}^{\mathrm{S}} - n_{\mathrm{eff}}^{\mathrm{R}})/\partial T$ [RIU/°C]	$\partial k_{\mathrm{eff}}^{\mathrm{S}}/\partial T$ [RIU/°C]
0.22	$9.28 \cdot 10^{-5}$	$-2.34 \cdot 10^{-5}$	$1.11 \cdot 10^{-7}$

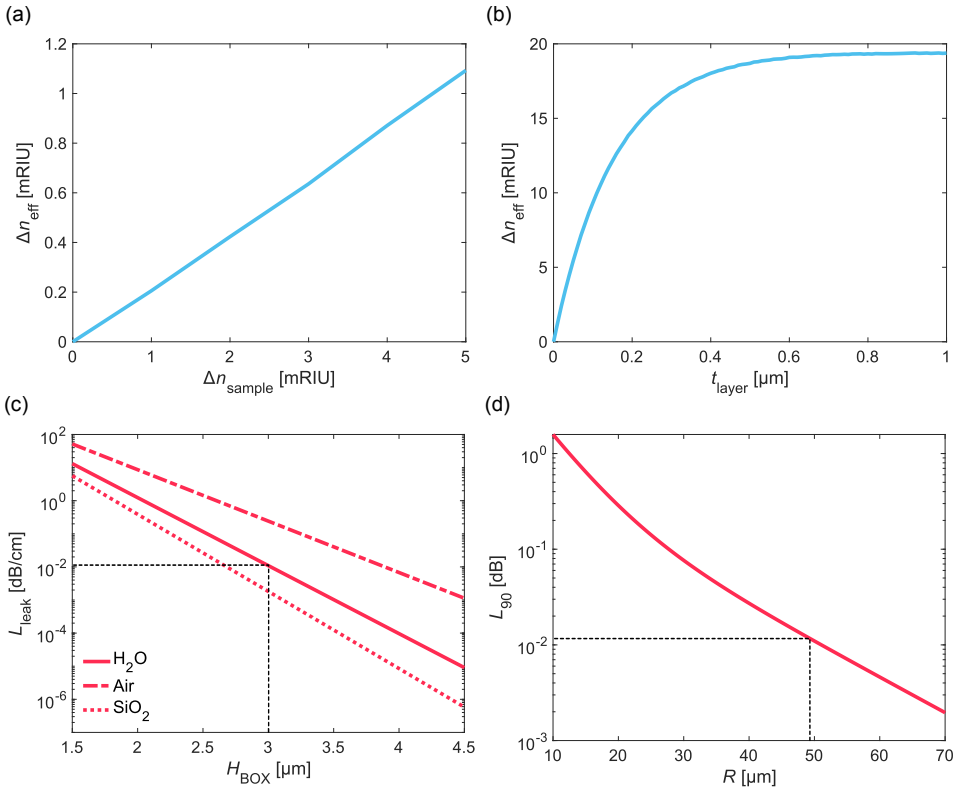

Figure 4.6: Simulation results for the sensing waveguide. (a) Confinement factor. (b) Surface sensitivity. (c) Leakage loss. Results with an air and a silica cladding are shown in addition to those for water for comparison. (d) Loss per 90-degree bend.

erence waveguides and water in sensing waveguides, as aqueous samples are targeted. The complex refractive indices of each material are listed in Table 4.1. Here it is worth noting that water is the only significant absorbent. These waveguides were modeled and simulated as indicated in Chapter 3 (Section 3.1). At the working wavelength, both waveguides only support the fundamental TE and TM modes. In practice, only the TE mode is excited, as the input grating coupler acts as a polarization filter. The field distribution ($|E_{\mathrm{x}}(x, y)|$) of the supported TE modes and their complex effective indices are shown in Figs. 4.5(c)–(d).

To evaluate bulk modal sensitivity, $\Gamma = 0.22$ was calculated from the curve shown in Fig. 4.6(a). This is a moderate value which provides a good balance between sensitivity to the analyte and water absorption. The expected losses will be specified later in this section. A surface sensitivity $S_{\mathrm{m,surf}} = 9.28 \cdot 10^{-5}$ nm/RIU was also obtained by considering an adsorbed protein layer of $n_{\mathrm{layer}} = 1.45$ [178]. The response curve can be seen in Fig. 4.6(b), where only the fragment correspondent to thicknesses below 10 nm can be approximated as linear. Both bulk and surface sensitivities hold the same values for the real and imaginary refractive indices, hence, only the curves for n_{eff} are shown. The thermal sensitivity was evaluated for the sensing and reference modes, which are expected to suffer from the same temperature fluctuations, as the microflui-

Table 4.3: Propagation losses of the sensing mode due to water absorption (L_{H_2O}), leakage (L_{leak}) and curves (L_{90}).

L_{H_2O} [dB cm^{-1}]	L_{leak} [dB cm^{-1}]	L_{90} [dB]
11.38	0.018	0.011

dic channel will be placed over both waveguides. Using the thermo-optical coefficients reported in [213, 214, 215, 216] for the different waveguide materials, the sensitivities $S^{R}_{m,temp} = \partial n^{R}_{eff}/\partial T = 3.42{\cdot}10^{-5}$ RIU/°C and $S^{S}_{m,temp} = \partial n^{S}_{eff}/\partial T + j\partial k^{S}_{eff}/\partial T = 1.08{\cdot}10^{-5} - j1.11\cdot10^{-7}$ RIU/°C were obtained for the reference and sensing modes, respectively. Here it is worth noting that what affects phase read-out is the difference $\partial n^{S}_{eff}/\partial T - \partial n^{R}_{eff}/\partial T = -2.34\cdot10^{-5}$ RIU/°C. All calculated modal sensitivities can be found in Table 4.2.

Losses in the sensing waveguide, which can be critical, were calculated. Propagation losses due to water absorption up to $L_{H_2O} = 11.38\,\text{dB cm}^{-1}$ were obtained from k^{S}_{eff}. As a consequence, even in ideal circumstances, the intensity of the sensing arm is expected to be much weaker than that of the reference one. Leakage losses are represented as a function of BOX thickness in Fig. 4.6(c). The value obtained for the $H_{BOX} = 3\,\mu$m present in the current SiN platform, $L_{leak} = 0.02\,\text{dB cm}^{-1}$, is sustainable even for long sensing paths. Leakage in an air- and silica-cladded waveguide was also calculated for comparative purposes. Air-cladded waveguides show larger losses, around $0.55\,\text{dB cm}^{-1}$, while the reference waveguides experience only $0.003\,\text{dB cm}^{-1}$. Finally, losses per 90-degree bend were calculated and are shown in Fig. 4.6(d) for a range of radii. A bending radius $R = 50\,\mu$m was selected, yielding $L_{90} = 0.011$ dB, which is dominated by a transition loss $L_{trans} = 0.0053$ dB. By comparing all calculated loss values, compiled in Table 4.3, leakage and curvature losses can be considered negligible against water absorption.

MMIs

As it will be explained in Section 4.3.4, in the sensors of the second generation, 2×2-MMIs, as the one schematized in Fig. 4.7(a) are used for dividing the input light into the sensing and reference paths instead of 1×2-MMIs, used in the first sensor design. The 1×2-MMIs at the end of the spirals and the 2×3-MMIs for coherent phase detection were identical in both versions. The dimensions of these devices can be found in Table 4.4. A tapered waveguide of length $L_{taper} = 30\,\mu$m was employed to transit between interconnect and access waveguides.

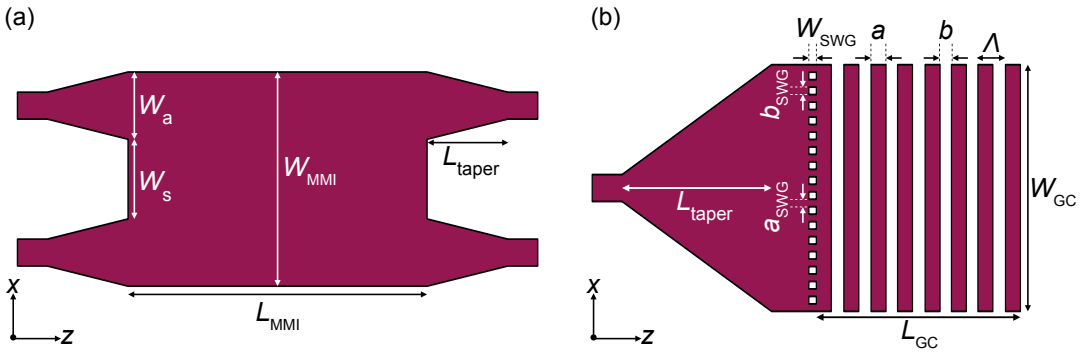

Figure 4.7: (a) 2×2-MMI and (b) grating coupler used in the sensor layout. The most important dimensions are marked. Schematic representations not to scale.

Table 4.4: Dimensions of the MMIs employed in the sensor layout.

Type	W_{MMI} [µm]	L_{MMI} [µm]	W_{a} [µm]	W_{s} [µm]
1×2	8.8	43	2	2.5
2×2	8.8	172	2	2.5
2×3	13.3	256	2	2.5

Table 4.5: Dimensions of the surface grating couplers employed in the sensor layout.

W_{GC} [µm]	L_{GC} [µm]	a [nm]	b [nm]	W_{SWG} [nm]	a_{SWG} [nm]	b_{SWG} [nm]
15	88.75	1350	425	440	342	258

Grating couplers

Single-etch surface grating couplers designed for the TE polarization were employed in both generations of sensors. The silica cladding was removed in the same way as for the sensing areas to expose the gratings to air, as doing so resulted in a better performance compared to maintaining the upper cladding. To reduce back-reflections in the second generation (see Section 4.3.3), a SWG adaptation tooth was added at the interface between the input waveguide and the grating, pushing back-reflections down to BR $= -21$ dB. A schematic representation of such grating coupler is found in Fig. 4.7(b), and its dimensions are given in Table 4.5. The length of the input taper was $L_{\mathrm{taper}} = 300$ µm. The designed gratings radiated with a maximum coupling efficiency of CE $= -4.75$ dB and an angle of 39° to air and of 26° to a polished fiber (see Appendix A).

4.3.2 Layout of the first-generation sensors

Complex refractive index sensors designed for operation at three different wavelengths, $\lambda_0 = 1.31$ µm for sensing liquids, $\lambda_0 = 1.58$ µm for CO_2 and $\lambda_0 = 1.65$ µm for CH_4, in different lengths ranging from 1 to 5 cm, were integrated on the first-generation chip. The mask layout of a $\lambda_0 = 1.65$ µm sensor is presented in Fig. 4.8(a), where fragments of straight interconnection waveguides have been omitted for compactness. As seen in Section 4.3.1, the main components are the spiral sensing and reference waveguides, 1×2-MMIs for light splitting at the input and output of the spirals, the 2×3-MMI to generate the three interferometric signals and surface grating couplers for coupling light to/from the chip. Grating couplers are pitched by 127 µm to match the separation between fibers in the array. In Fig. 4.8(b), it can be seen how the gratings of the input and of the different outputs are arranged. Scanning electron microscope (SEM) images taken after fabrication, such as those shown in Figs. 4.8(c)–(d) for a sensing spiral and a grating coupler, respectively, revealed no significant deviations from nominal dimensions.

Table 4.6: Propagation losses of the first-generation waveguides. Losses in the cladded waveguides ($L^{\mathrm{R}}_{\mathrm{prop}}$) were obtained by the cut-back method, while those of the windowed waveguides ($L^{\mathrm{S}}_{\mathrm{prop}}$) were calculated from the contrast of the interferogram, discounting the expected water absorption.

λ_0 [µm]	$L^{\mathrm{R}}_{\mathrm{prop}}$ [dB cm^{-1}]	$L^{\mathrm{S}}_{\mathrm{prop}}$ [dB cm^{-1}]
1.31	0.58	10.23
1.58	1.56	13.08
1.65	0.68	14.17

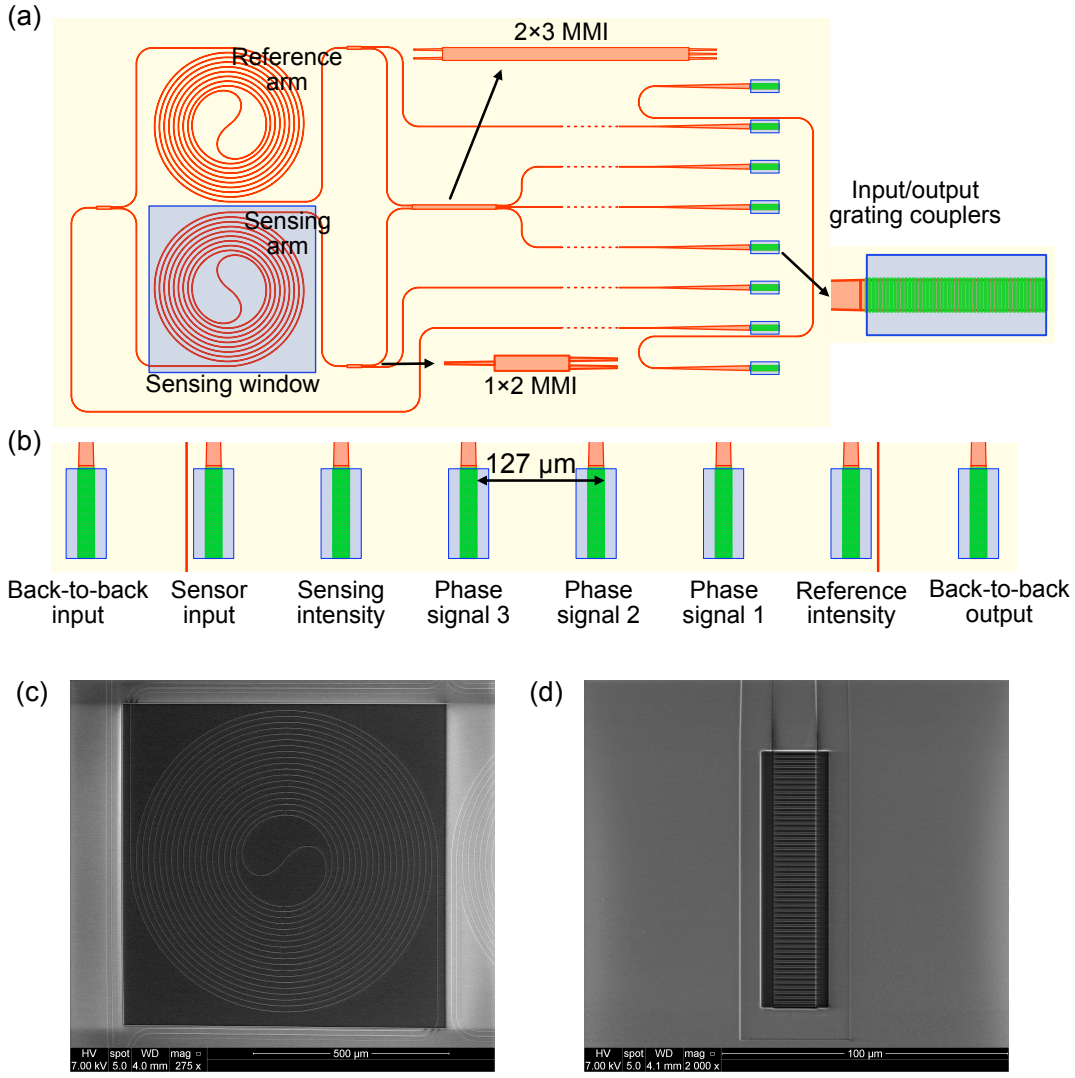

Figure 4.8: (a) First-generation sensor layout, indicating the most relevant building blocks. Long straight sections of interconnecting waveguides have been omitted. (b) Array input/output grating couplers, with their corresponding signals specified. (c) SEM picture of a sensing spiral. (d) SEM picture of a grating coupler.

4.3.3 Optical evaluation of the first-generation sensors

Even though the fabrication of the chip was successful in terms of tolerances, several problems appeared when the evaluation of the different sensors was undertaken. Most of the measurements were performed with the sensors designed for methane detection ($\lambda_0 = 1.65\,\mu\text{m}$), specifically the two shortest, with sensing pathlengths $L_1 = 10\,\text{mm}$ and $L_2 = 30\,\text{mm}$.

Propagation losses of the silica-cladded waveguides ($L^{\text{R}}_{\text{prop}}$) were measured by the cut-back method. Table 4.6 includes the averaged values between 3 different chips for each wavelength. These low values are in good agreement with what is expected for single-mode SiN waveguides. However, when transmission measurements were performed with the sensors exposed to air, poor light throughput in the sensing intensity output was detected. As this could be attributed to a higher leakage than considered in the design process (see Fig. 4.6(c)), measurements were repeated while pure DI water was circulating through the channel, but signal levels did not improve. Fortunately, even though the sensing intensity output was below the noise level, the interferometric out-

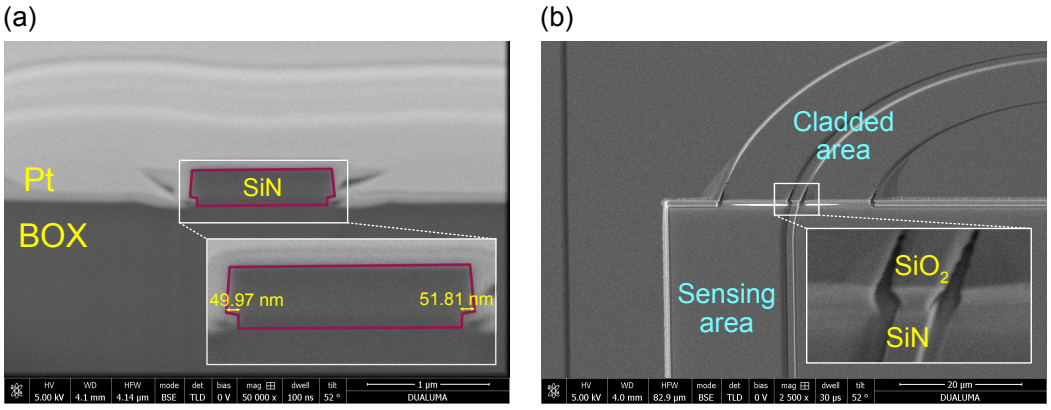

Figure 4.9: (a) Sensing waveguide cross section imaged by FIB-SEM, showing under-etching. Platinum was deposited on top for better contrast. (b) Transition between the cladded and sensing areas. The abrupt change of cladding can induce back-reflections and also create a resonant cavity.

puts were strong enough to obtain oscillations by flowing NaCl solutions. Therefore, the differential losses between the sensing and reference waveguides (ΔL_{prop}) could be calculated from the contrast of the interferograms [217]. The intrinsic propagation loss, i.e., excluding water absorption, of the windowed waveguides for each wavelength was then estimated as

$$L^{\text{S}}_{\text{prop}} \approx L^{\text{R}}_{\text{prop}} + \left(\Delta L_{\text{prop}} - L_{\text{H}_2\text{O}}\right), \tag{4.17}$$

where $L_{\text{H}_2\text{O}}$ took the value expected from simulations. The results are found in Table 4.6. These high losses, to which water absorption must be added, were well above those obtained for cladded waveguides and explained the low output intensity, moreover acknowledging that all spirals were longer than 1 cm. This incremental loss could be attributed to the cladding-etching process, which may have damaged the waveguides. To study this possibility, chips were taken to the focused ion beam (FIB)-SEM. Transversal cuts were made, enabling the view of waveguide cross sections as that shown in Fig. 4.9(a). It was observed that waveguides were indeed under-etched by approximately 50 nm at each side. During that same FIB-SEM session, it was noticed that the abrupt transition from cladded to windowed areas, which can be seen in Fig. 4.9(b), could be a source of reflection, further reducing the input power to the sensing arm and potentially creating a resonant cavity.

As the measurements described above had been performed with single-wavelength lasers, it was decided to conduct wavelength scans to further investigate the issues with sensing spirals, including the formation of on-chip cavities. Back-to-back waveguides and the L_1 and L_2 CH_4 sensors were thus measured with a tunable laser source, and the minimum phase algorithm was applied to calculate the impulse response of the output signals [218]. The reflectogram of the back-to-back waveguide can be seen in Fig. 4.14(a), and its interpretation is straightforward, as there is a dominant peak located at a distance coincident with the separation between the input and output grating couplers. This means that a Fabry-Pérot (FP) cavity is formed due to back-reflections in the grating couplers. In fact, when the reflectograms of the sensing and reference intensity signals, represented in Fig. 4.14(b) were analyzed, the effect of a cavity formed between the output grating and the output of the 1×2-MMI (cavity A) was detected. Most importantly, a family of echoes (cavities B_1 and B_2), which were dominant over the rest, was found exclusively in the sensing branch of each sensor, and their position was consistent among sensors from different chips. However, the origin of such reflections could not be determined by examining the dimensions of potential cavities on the chip layout. The sensing spiral was unlikely to be involved because, even though the length of the cavities did increase

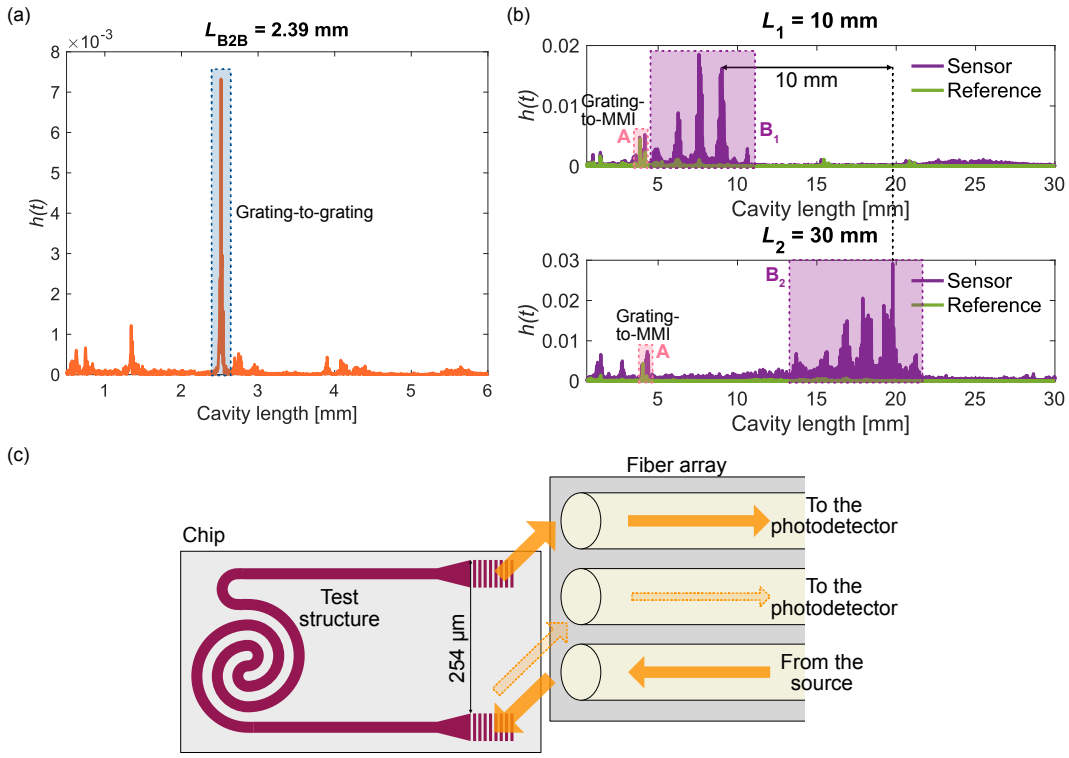

Figure 4.10: (a) Reflectogram of a back-to-back waveguide, with a peak corresponding to the distance between the input and output grating couplers. (b) Reflectogram of the sensing and reference intensity signals for the 10- and 30-mm waveguides. The sensing signal presents strong peaks which are not found in the reference signal. (c) Schematic representation of the measurement of a test structure. Measuring the output of the middle fiber helped determine interference problems.

in longer sensors, it did not scale with the sensing pathlength. Furthermore, the high propagation losses of the windowed waveguides would impede the formation of cavities.

The fiber array was suspected to be introducing the unexplained spurious effects. A test structure whose input and output were separated by 254 µm, this is, which left an unused fiber between the input and output ones, as shown in Fig. 4.14(c), was measured with the tunable source. By recording the intensity of the middle fiber, it was found that a significant signal level, about 6 dB lower than the one recorded in the output fiber, was indeed received. A possible explanation was that said signal was a fraction of the input, after being reflected back to the array from the chip surface. This interference could potentially mask a weak output signal, as was the case, and even beat with it. An additional confirmation that the array was a source of problems came during a research stay at UiT the Arctic University of Norway (Tromsø, Norway). The sensors were taken abroad to perform the spectroscopic detection of methane, given the expertise of the hosting group in waveguide-based gas spectroscopy. The chips had to be adapted to the measurement setup available at the UiT, so they were cleaved at the input of the 1×2-MMI to allow facet input coupling, and the output gratings were read with an infrared camera. More details about the gas measurement setup and the read-out scheme can be found in Appendix D. By changing the read-out system, the spurious effects previously described disappeared [219]. Unfortunately, the sensors were not sensitive enough to detect gases, but the performed experiments were remarkably helpful for diagnosing problems.

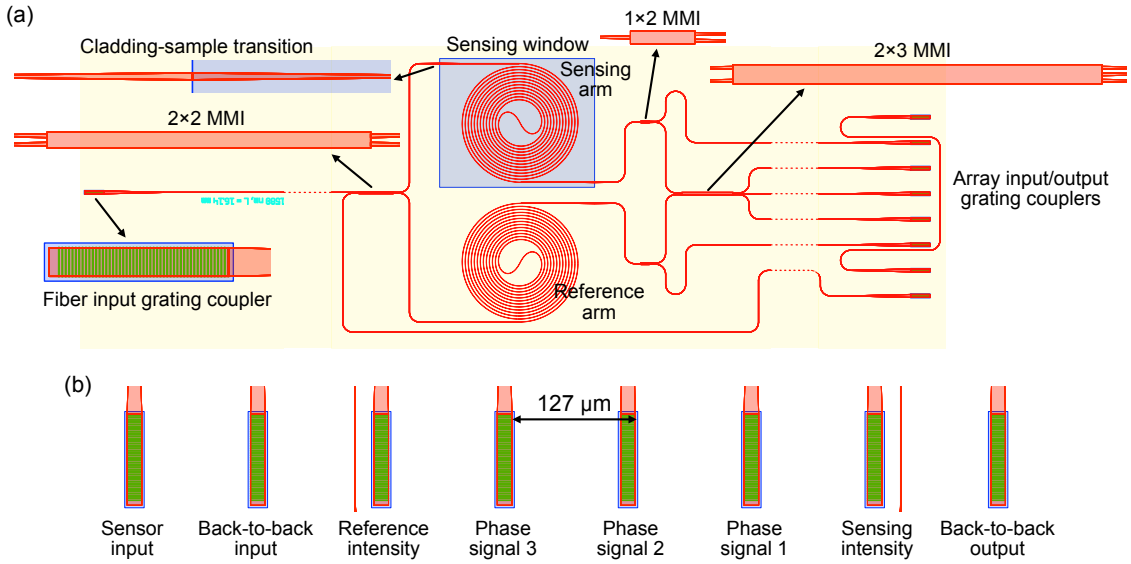

Figure 4.11: (a) Second-generation sensor layout. The most relevant building blocks are zoomed. Long straight sections of interconnecting waveguides have been omitted. (b) Array input/output grating couplers. Interleaving back-to-back gratings minimizes the risk of cross-coupling from the sensor input to their outputs.

Conclusions after optical evaluation

After facing the challenges brought by the first generation of sensors, the following key-points were extracted.

- The window-opening process can increment intrinsic propagation losses of sensing waveguides, by causing damage such as under-etching. Shorter sensors should always be included as a conservative backup in case losses become too high.
- The abrupt transition between a silica and a water or air cladding can potentially induce reflections, reducing the input power to the sensing branch and creating a FP cavity, which can be problematic when intrinsic propagation losses are low.
- Grating couplers are a major source of on-chip reflections, which should be addressed from the design point of view.
- The separation distance of 127 µm between adjacent fibers is not enough to avoid that a strong light input interferes with a weak output signal and masks it.
- Fiber arrays are prone to inducing spurious effects, such as uncontrolled reflections and cross-coupling. If changing the read-out scheme is not possible, these drawbacks should be handled.

Developing an enhanced new generation of chips, incorporating the required design improvements, was thus justified.

4.3.4 Layout of the second-generation sensors

Differences from the first generation

The mask layout of a $\lambda_0 = 1.55\,\mu m$ sensor is presented in Fig. 4.11(a). Some improvements with respect to that of the first-generation sensors (see Fig. 4.8(a)–(b)) were made to address the problems discussed in Section 4.3.3. The main changes are the inclusion

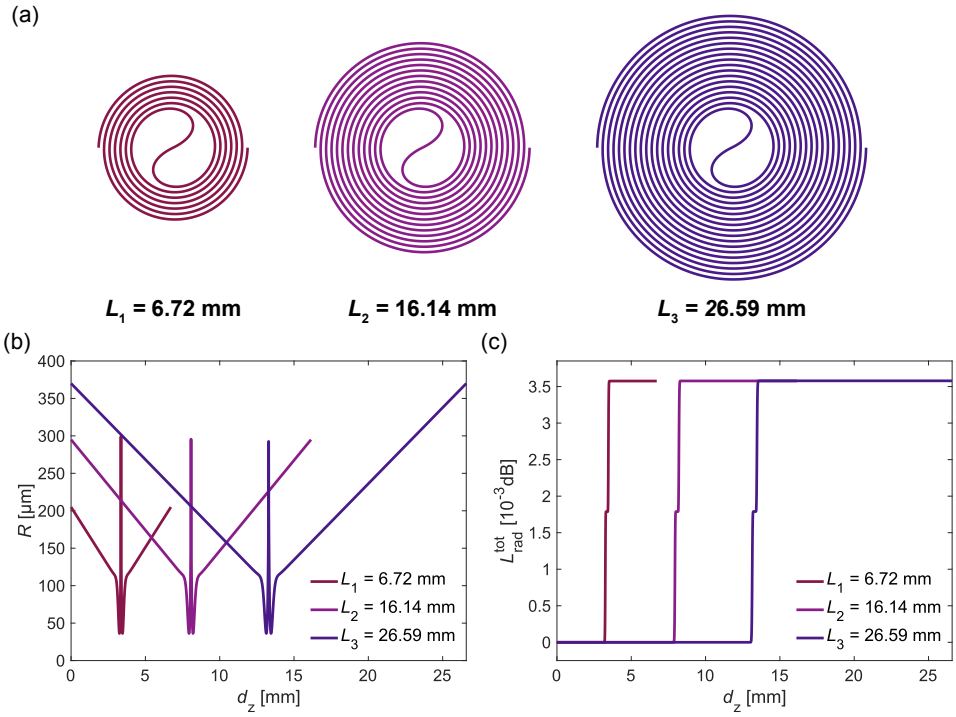

Figure 4.12: (a) Spiral sensing waveguides, drawn to scale. Evolution of (b) the bending radius and (c) accumulated radiation loss with propagation distance in the spiral.

of the additional input grating coupler, swapping the input 1×2-MMI with a 2×2-MMI, adding a transition at the input and output of the sensing window and the re-arrangement of the output grating couplers. Shorter sensing lengths were included in case that the intrinsic propagation losses of the waveguides are limiting. Thank to the incorporation of the 2×2-MMI, input coupling is possible both from the grating coupler and from a single input fiber, aligned to a grating placed on the opposite edge of the chip. This solution provided an alternative configuration to enable measurements if the input signal from the array masks any of the outputs, as explained in Section 4.3.3. The distance from the grating couplers to the expected position of the microfluidic channel is 5.5 mm, which is greater than the lower bound of 4.8 mm calculated in Chapter 3 (Section 3.3.2). In the array-coupling area, grating couplers are still positioned within a 127-µm pitch to match the one from the fibers of the available array. However, the distribution of the output gratings is different. In the close-up of Fig. 4.11(b), it can be seen how the input grating (outer left) is separated by 254 µm from the nearest sensor output, which corresponds to the reference intensity. The sensing intensity output, which, as seen in Section 4.3.1, is expected to be the weakest, is placed as far as 762 µm from the input. These modifications with respect of the first-generation sensors aimed at impeding that weak output signals are masked by interferences from the input, while still using the fiber array for convenience. Furthermore, to avoid potential reflections due to the abrupt transition from a silica to a water cladding at the edges of the sensing window, the corresponding waveguide sections were tapered to a width of 3 µm, for which the impact of the cladding change is expected to be negligible. These two tapered sections were also included in the reference waveguide to ensure identical physical paths.

Spiral sensing waveguides

As it was mentioned in Section 4.2.2, increasing the interaction length yields an enhanced sensitivity. To do so without dramatically increasing sensor footprint, the spiraled wave-

Table 4.7: Characteristics of the spiral waveguides at $\lambda_0 = 1.55\,\mu$m.

L [mm]	Area [mm^2]	S_n [rad/RIU]	S_k [au/RIU]	L^{tot}_{rad} [dB]	$L^{tot}_{H_2O}$ [dB]
6.72	0.39	$5.97 \cdot 10^3$	$5.14 \cdot 10^3$	$3.57 \cdot 10^{-3}$	7.65
16.14	0.57	$14.35 \cdot 10^3$	$12.34 \cdot 10^3$	$3.58 \cdot 10^{-3}$	18.37
26.59	0.72	$23.64 \cdot 10^3$	$20.33 \cdot 10^3$	$3.58 \cdot 10^{-3}$	30.26

guides shown in Fig. 4.12(a), which follow the pattern defined in [220], were used. Sensors with three different spiral lengths $L_1 = 6.72\,$mm, $L_2 = 16.14\,$mm and $L_3 = 26.59\,$mm were included on the mask. The separation distance between adjacent waveguides was $15\,\mu$m, a safe value to avoid coupling ($z_{40} \gg L$, see Section 3.1.5 of Chapter 3). With these parameters, the spirals occupied the areas indicated in Table 4.7 along with the expected bulk sensitivities (Eq. (4.15)). As opposed to Manhattan-type spirals, here the bending radius is variable and kept at large values ($R > 100\,\mu$m), except near the center, where it decreases to $R_{min} = 36.2\,\mu$m during a small distance. The evolution of bending radius with propagation distance in the spiral (d_z) can be seen in Fig. 4.12(b). As the average radius is large, radiation losses are not problematic. Moreover, mode mismatch losses, which, as seen in Section 4.3.1, are the dominant contribution to curvature losses, are alleviated, because there is no discontinuity between waveguide sections. Accumulated radiation losses along the spirals were calculated by integrating the radiation loss coefficient (α_{rad}) over the spiral path (S):

$$L^{tot}_{rad} = -10 \log_{10} \left(e^{-\int_S \alpha_{rad}(R) dS} \right). \tag{4.18}$$

The evolution of this parameter is shown in Fig. 4.12(c) for the three spiral lengths, while the final values are given in Table 4.7. The main contribution to L^{tot}_{rad} occurs at the center of the spirals, as it is determined by R_{min}, and hence accumulated losses do not scale with length. The plateau reached in the curves from Fig. 4.12(c) supports this fact. Because of this quasi-lossless design, using spiraled waveguides does not degrade performance with respect to using straight ones.

Water absorption does however increase with interaction length. The total water-induced loss ($L^{tot}_{H_2O}$) is found in Table 4.7, where it is by far the dominant source of loss. As a consequence, the SNR for the L_3 sensor is expected to be very poor. Indeed, in this scenario, the optimum interaction length can be approximated as [189]

$$L_{opt} \approx \frac{1}{\Gamma \alpha_{H_2O}}, \tag{4.19}$$

yielding $L_{opt} \approx 3.79\,$mm. The L_1 sensor is thus expected to achieve the best results. Here it is worth reminding that the original intention when designing these sensors was detecting CO_2 ($\Gamma\alpha_{CO_2} = 3.26{\cdot}10^{-4}\,$cm^{-1}), for which L_{opt} amounts to $\sim 2.8\,$cm after considering typical intrinsic propagation losses (see Table 4.6). The estimation of optimum interaction lengths will be thoroughly tackled in Chapter 6.

Finally, considering these pathlengths, the thermal sensitivities of the device, $S_{n,temp} = \partial\Delta\varphi/\partial T$ and $S_{k,temp} = \partial A/\partial T$, can be calculated by multiplying the architectural sensitivities defined in Section 4.2.2 and the modal thermal sensitivities given in Table 4.2. The results are shown in Table 4.8. In view of these low values compared to S_n and S_k, thermal drifts are not expected to be problematic.

4.3.5 Optical evaluation of the second-generation sensors

The fabricated chips were cleaned with the resist-removing protocol described in Chapter 3, Section 3.5 and imaged to verify that they were correctly manufactured. Figures

Table 4.8: Device thermal sensitivities at $\lambda_0 = 1.55\,\mu$m for the L_1, L_2 and L_3 sensors.

L [mm]	$S_{n,temp}$ [rad/°C]	$S_{k,temp}$ [au/°C]
6.72	-0.64	-0.0026
16.14	-1.54	-0.0063
26.59	-2.53	-0.0103

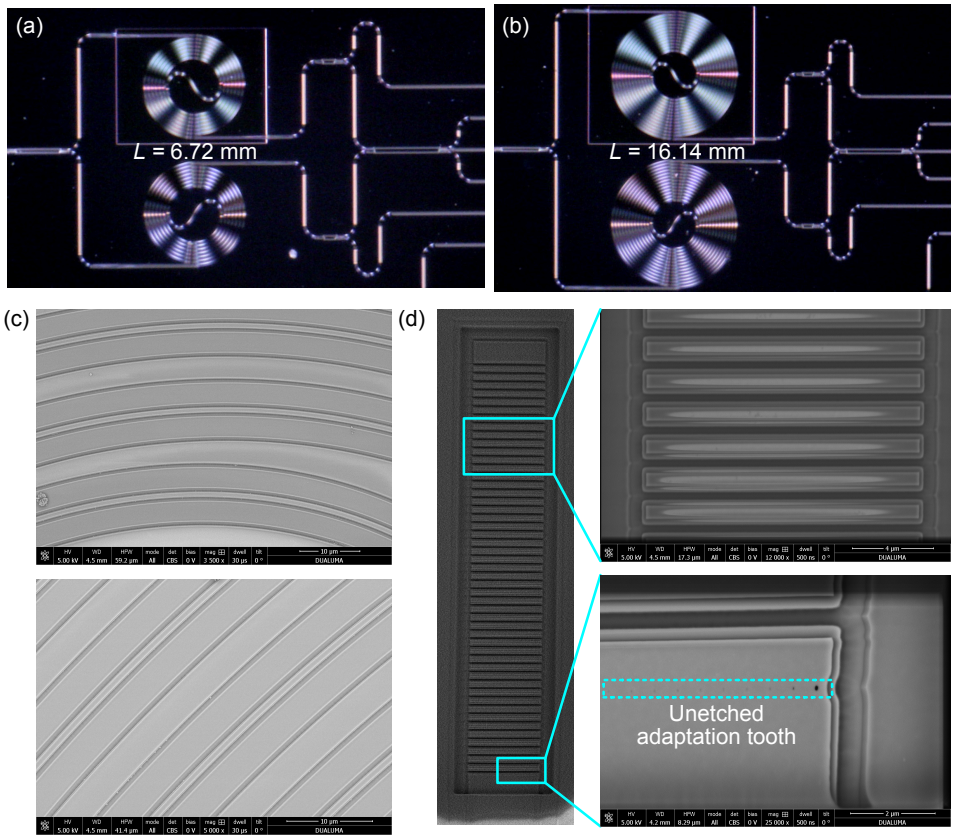

Figure 4.13: Optical microscope picture of the (a) L_1 and (b) L_2 sensors. SEM images of (c) the sensing waveguides and (d) a grating coupler. The SWG adaptation tooth was not etched.

4.13(a)–(b) show optical-microscope pictures of two of the sensors, without significant damage or errors. To more precisely quantify fabrication tolerances, the chips were taken to the SEM. Figure 4.13(c) shows sections of sensing spirals, whereas a grating coupler with augmented details is shown in Fig. 4.13(d). No major deviations from mask specifications were appreciated, except for the fact that the SWG adaptation teeth of the gratings, despite meeting the MFS of the foundry, were not etched. This can be observed in the lower inset of Fig. 4.13(d). As a consequence, increased back-reflections than those obtained in simulation are expected. The propagation losses of the cladded waveguides were assumed to be similar to those of the first-generation chips (Table 4.6).

Sensors exposed to air were aligned in the input/output array configuration and wavelength scans were performed to check the behavior of the 2×3-MMI and the correct transmission of all outputs. The results for the L_1 and L_2 sensors are shown in Figs. 4.14(a)–(b), where the fringes due to on-chip reflections are superimposed on top the minimum-phase filtered signals. The 120°-shifted oscillations in the interferometric outputs confirm that the MMI is working correctly, avoiding the need of testing this component independently. Furthermore, in the absence of water, the sensing and the reference intensity levels are comparable, which indicates that opening the cladding windows did not significantly increase propagation losses this time. To identify the Fabry-Pérot cavities that cause these

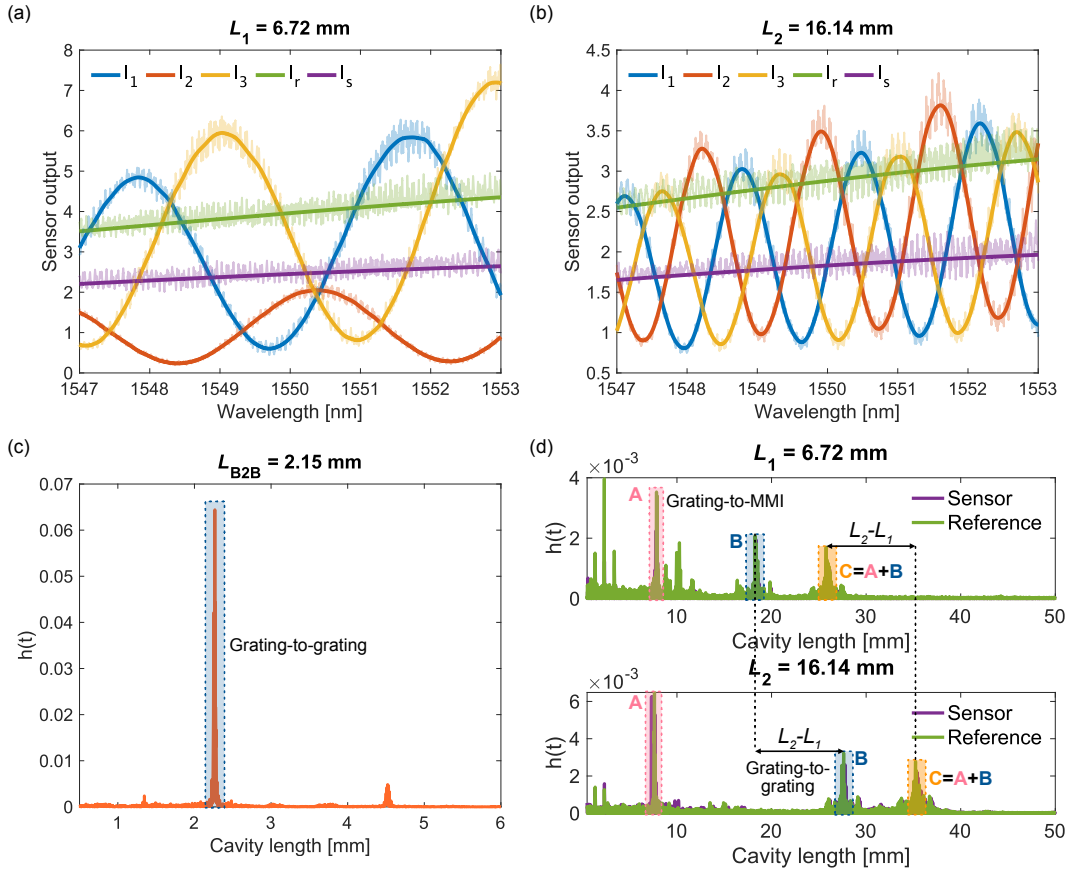

Figure 4.14: (a,b) Sensor output after scanning the input wavelength. The effect of on-chip reflections can be mitigated by minimum-phase filtering. (c) Reflectogram of a back-to-back waveguide, with a peak corresponding to the distance between the input and output grating couplers. (d) Reflectograms of the sensing and reference intensity signals for the L_1 and L_2 sensors. Peak positions help identify the potential cavities.

fringes, reflectograms were calculated for back-to-back alignment waveguides and for every sensor output. The reflectogram of a back-to-back waveguide, shown in Fig. 4.14(c), has the same interpretation as the one shown in Fig. 4.10(a) for the first-generation sensor. Therefore, reflections coming from the grating couplers are not negligible, which was expected given that the designed adaptation teeth were not etched. The reflectograms of the sensor and reference intensity outputs of the L_1 and L_2 sensors are shown in Fig. 4.14(d). Echo patterns are equivalent for the sensing and reference intensity signals of each sensor, whose paths are symmetrical, indicating that there are no specific cavities in the sensing branch. However, the effect of several other cavities is still appreciated. The three that could be identified were marked as A, B, and C. Cavity A corresponds to the distance between the output of the 1×2-MMI and the the measured grating, which is the same in both sensors. Cavity B is formed between the input and the output grating couplers, and, as so, its position is shifted by $L_2 - L_1$ in the L_2 sensor. Finally, cavity C is the combination of cavities A and B. The same analysis can be performed on the phase signals with analogous results. All obtained reflectograms were consistent among sensors from different chips.

The good output transmission and the lack of anomalies in the analysis of reflectograms encouraged validating the second-generation sensors with analyte detection experiments.

Table 4.9: Expected complex refractive index change induced by the prepared NaCl solutions. Pure DI water is considered as the reference.

C [w%]	Δn_{sample} [10^{-3}RIU]	Δk_{sample} [10^{-5}RIU]
1.5	2.44	-0.83
3	4.92	-1.67
6	9.97	-3.33
12	20.37	-6.67

4.4 Fixed-wavelength bulk sensing experiments

Bulk sensing experiments were performed using the setup and the microfluidics system described in Section 3.3 (Chapter 3), and operating at a fixed wavelength $\lambda_0 = 1.55\,\mu$m. As the theoretical thermal sensitivities (Table 4.8) were low, thermal control was not implemented at this stage. The goal was evaluating the capabilities of the proposed sensing architecture in terms of linearity, sensitivity and limit of detection, by inducing dynamic changes in the analyte concentration of liquid samples. For this purpose, using DI water as a solvent, NaCl solutions with weight-percentage (w%) concentrations 1.5w%, 3w%, 6w% and 12w% were prepared. The real refractive index of such solutions was calculated by following the model developed in [221],

$$n_{\text{sample}} = -0.08C^3 + 0.074C^2 + 0.162C + 1.3162, \tag{4.20}$$

where C is expressed as a weight fraction. Unfortunately, due to the strong water absorption at λ_0, accurate imaginary-index information about NaCl solutions is not available in the literature, as the differential change induced by dissolved NaCl is comparatively small and, therefore, difficult to measure. Due to this matter, the imaginary part of the index of the NaCl solutions was estimated from the data provided in [222]. The changes in the complex refractive index of the sample that were considered to be induced by each solution can be found in Table 4.9, where pure DI water is used as a reference (see also Table 4.1). By comparing Δn_{sample} to Δk_{sample}, it can be observed that changes in k_{sample} are around two orders of magnitude smaller than in n_{sample}. The fact that all values for Δk_{sample} are negative is explained by the high absorption of water. Increasing the w% of NaCl implies decreasing, although slightly, the water content of the sample, thus reducing overall optical losses. For this reason, experimental absorbance is expected to be negative. To perform the experiments, the microfluidic channel was placed over the sensing area of the chip as explained in Chapter 3, Section 3.3.2, and NaCl solutions were flowed through it at a constant flow rate of $30\,\mu$L/min, in alternation with a DI water (Milli-Q) buffer solution.

4.4.1 Sensor output

Sensor output during experiments was recorded using the GUI described in Section 3.3.3 (Chapter 3). Afterwards, all five signals were low-pass filtered using a finite impulse response (FIR) filter with a bandwidth of 1 Hz to reduce electrical noise (see Appendix B). Such a narrow bandwidth is suitable given the relatively slow rate of change of the signals, which is imposed by the programmed pumping speed. Measurements with the L_3 sensor were discarded due to insufficient transmission once it was exposed to water, confirming the hypothesis made in view of Table 4.7.

Figure 4.15(a) shows the complete record of a representative experiment with the L_1 sensor, where I_{S} and I_{R} are plotted in a separate graph for visibility. Fragments with constant signal levels correspond to the time intervals in which either the sample or the buffer are circulating through the sensor, whereas the signal-changing fragments reflect

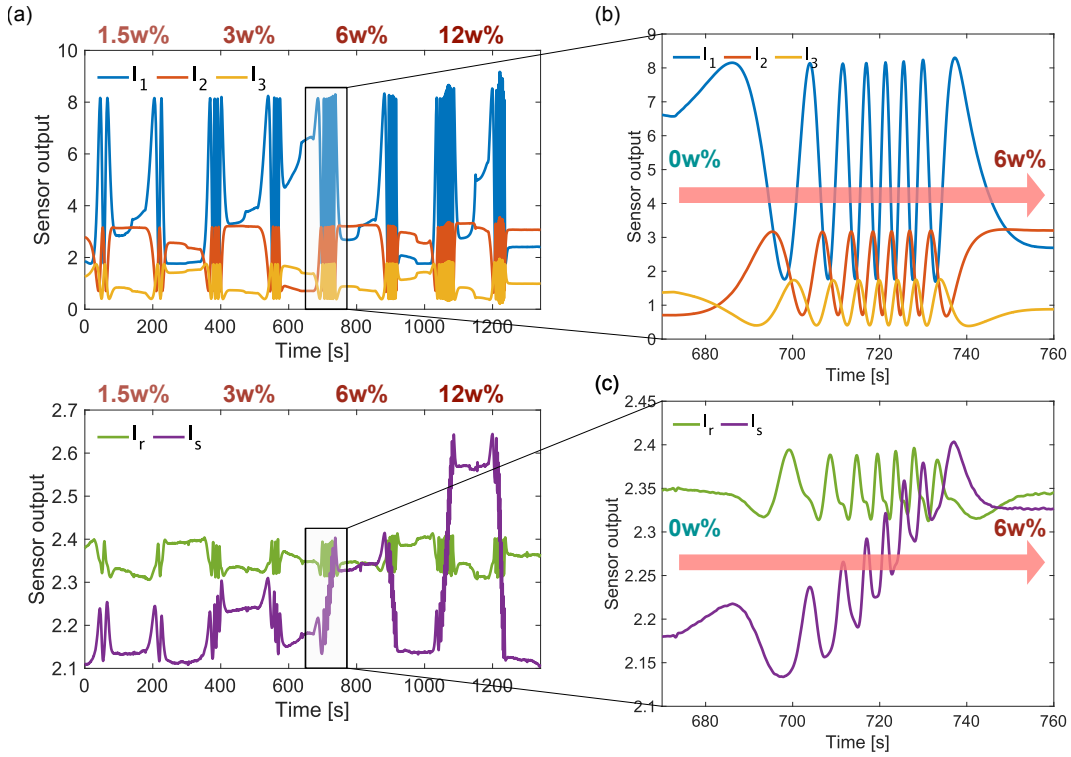

Figure 4.15: (a) L_1 sensor output during a bulk sensing experiment in which NaCl solutions are alternated with a DI water buffer. Fragment of the (b) interferometric and (c) intensity signals, showing several non-idealities.

the transition between different solutions. An averaged differential loss of 11.62 dB cm^{-1} between the sensing and reference arm was calculated from the interferometric signals. This value is in close agreement with the 11.38 dB cm^{-1} that are expected from water absorption (Table 4.3), suggesting that, unlike in the first generation, sensing waveguides do not face increased intrinsic losses. Figures 4.15(b)–(c) show the sensor phase and intensity responses, respectively, during the time interval corresponding to the transition from the buffer to the 6w% NaCl solution. Some non-idealities are observed. First, phase signals show evident signs of amplitude imbalances, which are most likely due to different output-coupling efficiencies. Second, the reference intensity signal does not stay constant as in the models presented in Section 4.2, but instead shows an amount of fringes in the transitions. A similar pattern of oscillations is also present in the sensing intensity. These unexpected phenomena were not considered in the sensor model.

The calculated phase shift and absorbance obtained after correcting the baseline drift by polynomial fitting, calibrating the complex signal as described in Chapter 3 (Section 3.4), normalizing $\Delta\varphi$ via Eq. (4.7) and applying an additional low-pass filter with a 0.2 Hz bandwidth, can be seen in Figs. 4.16(a)–(b) for the L_1 and L_2 sensors, respectively. Both phase shift and absorbance effectively follow analyte concentration changes, but, whereas $\Delta\varphi$ appears clearly defined, the strong oscillations presented in I_S are transferred to the computation of A. The fact that $\Delta\varphi$ does not return to zero after the last solution in the measurement of the L_2 sensor may be attributed to insufficient rinsing of NaCl residues by the buffer solution. Even though sensitivity and LOD evaluation are still possible from the steady-state absorbance signals, fringes introduce uncertainty in the saturation level, especially in the longer sensor. The origin of such oscillations is further analyzed in Section 4.4.2 to find a way to minimize them.

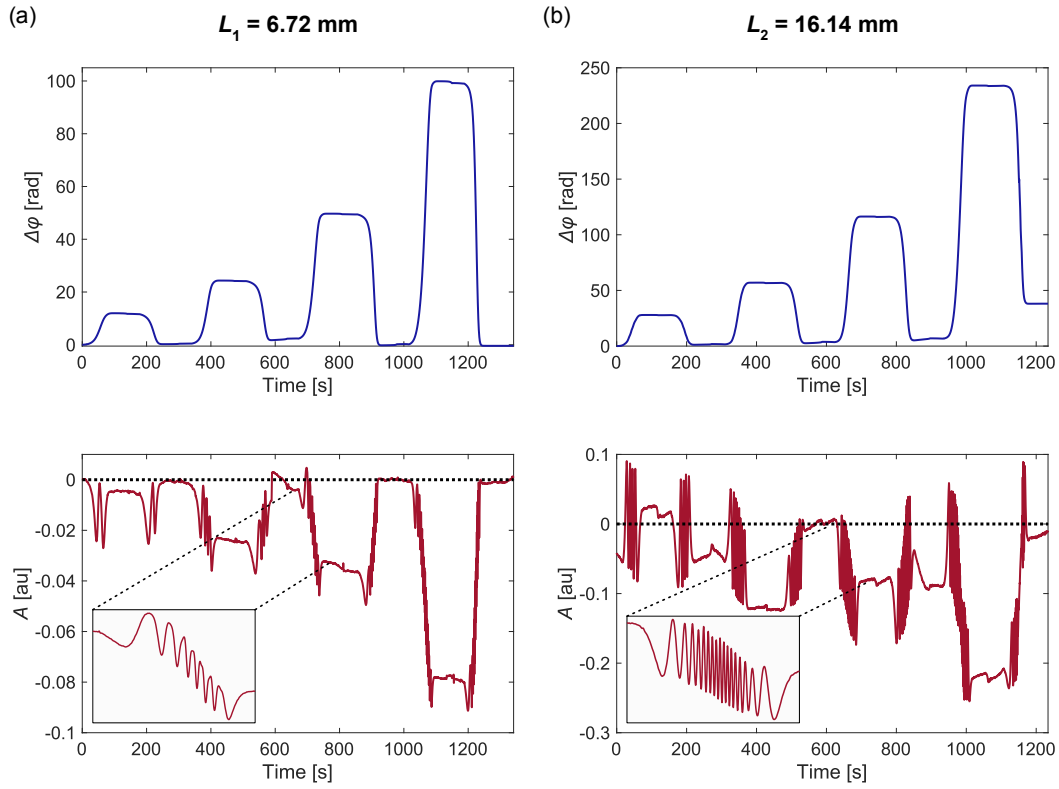

Figure 4.16: Calculated phase shift (upper) and absorbance (lower) of the (a) L_1 and (b) L_2 sensors. The fringes observed in the sensing intensity signal are transferred to the calculated absorbance, hindering a reliable read-out.

4.4.2 Cross-talk between adjacent outputs

When comparing the oscillations in the sensing and reference intensity signals (I_S, I_R) with those in the interferometric signals (I_1, I_2, I_3), a strong correlation is observed. In fact, by superimposing I_S and I_1, as in Fig. 4.17(a) and I_R and I_3, as in Fig. 4.17(b), it can be observed that not only do the signals present the same number of fringes, but they are also nearly in phase. By examining the layout of the sensor, shown in Figs. 4.11(a)–(b), it can be noted that these pairs of correlated signals are out-coupled by adjacent gratings to equally adjacent fibers. It is thus possible for a fraction of the light emitted by one grating to be spuriously coupled into the second-nearest fiber, as schematized in Fig. 4.17(c). This cross-talk phenomenon is likely to occur between interferometric signals as well, but it was not perceived in measurements, probably due to the dominance of the strong oscillations provoked by the real refractive index change in the sample. In any case, the small distortion that the phase signals may suffer is treated as a regular hardware error and corrected by the calibration algorithm. The following model focuses on recovering the sensing intensity signal, as it is critical for measuring absorption, but could be extended to recover the reference one.

Let s be the electromagnetic field signal after traveling through the sensing arm, so that $I_S = |s|^2$, and r its counterpart for the reference path, so that $I_R = |r|^2$. Ignoring the scaling factors introduced by the MMIs, the phase output can be expressed as a combination of s and r, $I_1 = |s + re^{j\Theta_1}|^2$, where Θ_1 accounts for the 120° introduced by the 2×3-MMI, plus any constant phase variations unrelated to the sensing experiment. Considering a cross-talk coefficient γ, the photodetected intensity, which had been directly interpreted

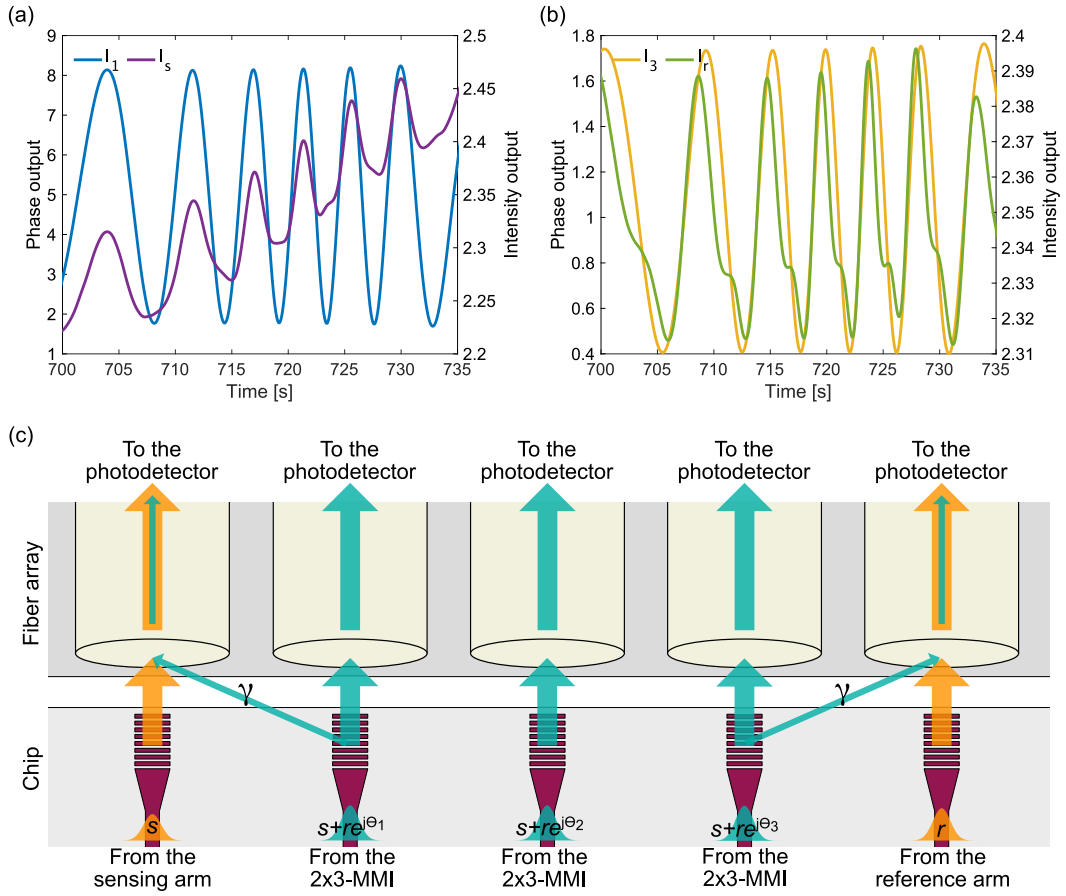

Figure 4.17: Superposition of the (a) sensing intensity (I_S) and first phase (I_1) and (b) reference intensity (I_R) and third phase (I_3) signals during a sensing experiment. The fringe patterns of the intensity signals are correlated to the oscillations in the interferometric signals. (c) Schematic diagram of the cross-talk between neighboring outputs.

as I_S in Section 4.4.1, can be written as

$$I_S^{PD} = \left|s + \gamma(s + re^{j\Theta_1})\right|^2. \tag{4.21}$$

This expression can be expanded to

$$I_S^{PD} = (1 + 2\gamma + \gamma^2)|s|^2 + \gamma^2|r|^2 + 2(\gamma + \gamma^2)\cos(\Delta\varphi - \Theta_1)|r||s|, \tag{4.22}$$

which, under the assumptions of weak cross-coupling ($\gamma \ll 1$) and of a constant reference signal amplitude ($|r| \approx 1$), can be approximated to

$$I_S^{PD} \approx (1 + 2\gamma)|s|^2 + 2\gamma\cos(\Delta\varphi - \Theta_1)|s|. \tag{4.23}$$

The desired I_S can thus be recovered by solving the quadratic equation for $|s|$. In order to do that, $\Delta\varphi$ has to be previously calculated from the interferometric signals, while γ and Θ_1 remain degrees of freedom to be judiciously adjusted.

Equation (4.23) was applied to recover I_S in all performed experiments. As a criterion to select the parameters γ and Θ_1, the correlation coefficient between $\Delta\varphi$ and the recovered I_S was calculated and maximized, as these two signals are expected to have similar shapes in fixed-wavelength experiments with low concentrations of analyte (see Fig. 4.3(b)). To quantify the reduction of fringes, the trend of fragments of both the original and recovered signals was removed, and then their standard deviations (σ_0 and σ_{rec})

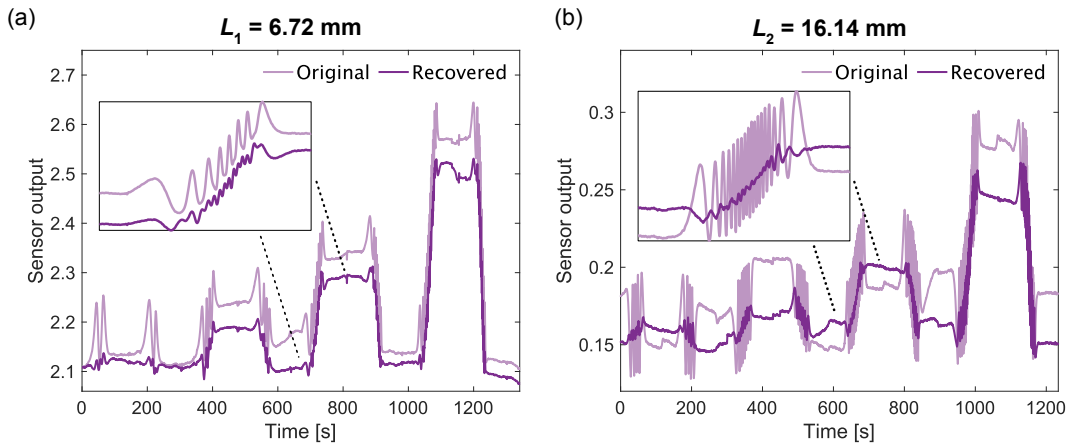

Figure 4.18: Original and recovered sensing intensity for the (a) L_1 and (b) L_2 sensors. A significant reduction of oscillations is achieved.

Table 4.10: Cross-talk cancellation parameters and achieved fringe reduction.

L [mm]	Chip	γ	$-\Theta_1$ [°]	σ_{rec}/σ_0 [%]
6.72	1	0.014	23	31.8
	2	0.030	174	19.6
	3	0.030	180	17.3
16.14	1	0.029	200	18.4
	2	0.037	52	15.8
	3	0.018	38	20.5

were compared. A significant dampening of oscillations was achieved, as can be observed in Figs. 4.18(a)–(b) for the measurements presented in Section 4.4.1. Here it is worth noting that the exact offset of the signals is irrelevant to calculate absorbance, which is a relative measurement. The amplitude of the fringes was reduced to 31.8% and 18.4% for the L_1 and L_2 sensors, respectively. The cross-talk cancellation parameters employed for each of the experiments which will be discussed in Section 4.4.3 are given in Table 4.10. The proposed modeling approach was validated by the high quality-enhancement of the signals, which were conditioned for reliable sensor evaluation.

4.4.3 Results and discussion

Absorbance was re-calculated after minimizing the impact of cross-talk in I_S as described in Section 4.4.2, in addition to correcting baseline drift and filtering in the same way as in Section 4.4.1. Figure 4.19 shows the improved sensor output, which is only different from that already shown in Fig. 4.16 in the absorbance, as phase-shift results did not present anomalies. The saturation levels of the improved absorbance signal were distinguishable and enabled calculations for sensor evaluation in terms of bulk sensitivity and limit of detection.

Bulk sensitivity

Phase-shift and absorbance saturation values, calculated as the mean of the signal fragments highlighted in Fig. 4.19, are presented as a function of NaCl concentration in Figs. 4.20(a) and 4.20(b) for L_1 and L_2 sensors from different chips. All sensors individually show good linearity, with $R^2 > 0.9861$ for phase shift and $R^2 > 0.9631$ for absorbance. The largest variation between chips occurs for the absorbance measurements of the L_1

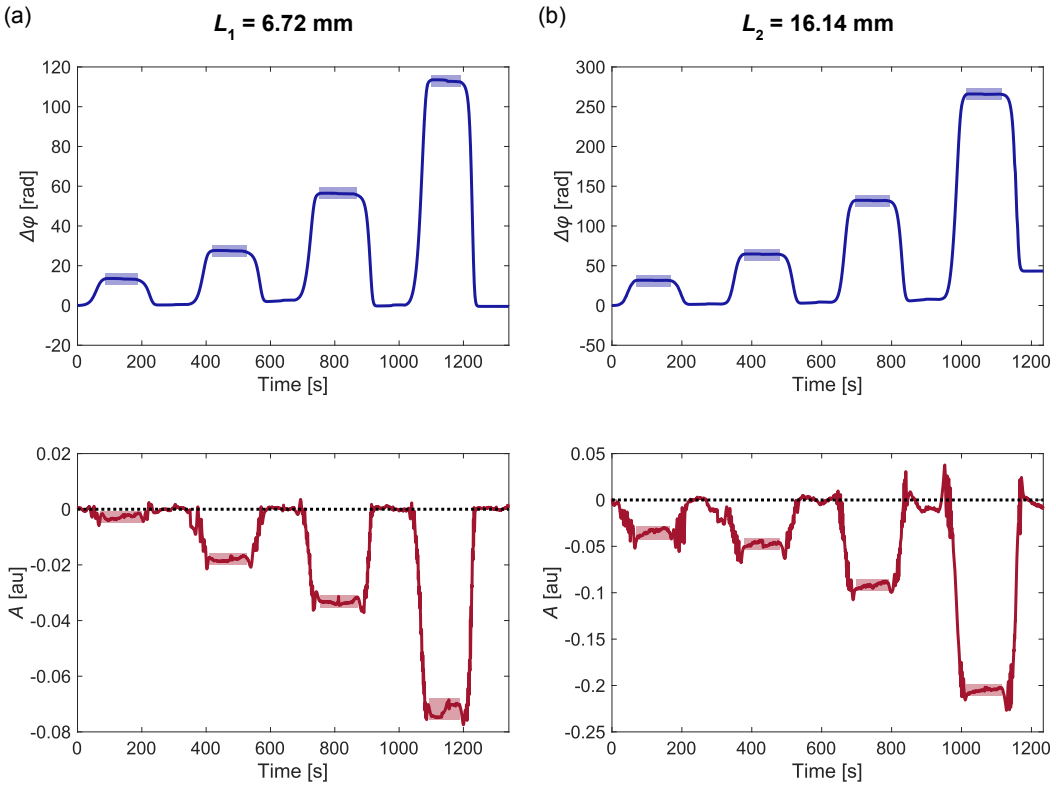

Figure 4.19: Calculated phase shift (upper) and absorbance (lower) of the (a) L_1 and (b) L_2 sensors used for sensor evaluation. The quality of the absorbance was improved by the proposed cross-talk cancellation approach. The areas employed in the calculation of saturation values are highlighted.

Table 4.11: Sensitivity results of the fixed-wavelength bulk sensing experiments. Abbreviations: standard deviation (Std.), theoretical (Theo.).

L [mm]	Chip	S_n [rad/w%]	S_n [rad/RIU]	S_k [au/w%]	S_k [au/RIU]
6.72	1	9.53	$5.57 \cdot 10^3$	-0.0067	$1.21 \cdot 10^3$
	2	8.31	$4.86 \cdot 10^3$	-0.019	$3.32 \cdot 10^3$
	3	8.16	$4.78 \cdot 10^3$	-0.012	$2.16 \cdot 10^3$
	Mean	**8.67**	$\mathbf{5.07 \cdot 10^3}$	**-0.012**	$\mathbf{2.23 \cdot 10^3}$
	Std.	0.75	439.53	0.0059	$1.06 \cdot 10^3$
	Theo.	9.72	$5.97 \cdot 10^3$	-0.029	$5.14 \cdot 10^3$
16.14	1	22.33	$13.06 \cdot 10^3$	-0.017	$2.97 \cdot 10^3$
	2	16.79	$9.82 \cdot 10^3$	-0.020	$3.54 \cdot 10^3$
	3	15.72	$9.19 \cdot 10^3$	-0.023	$4.14 \cdot 10^3$
	Mean	**18.23**	$\mathbf{10.69 \cdot 10^3}$	**-0.020**	$\mathbf{3.55 \cdot 10^3}$
	Std.	3.55	$2.08 \cdot 10^3$	0.0032	584.13
	Theo.	23.35	$14.35 \cdot 10^3$	-0.069	$12.34 \cdot 10^3$

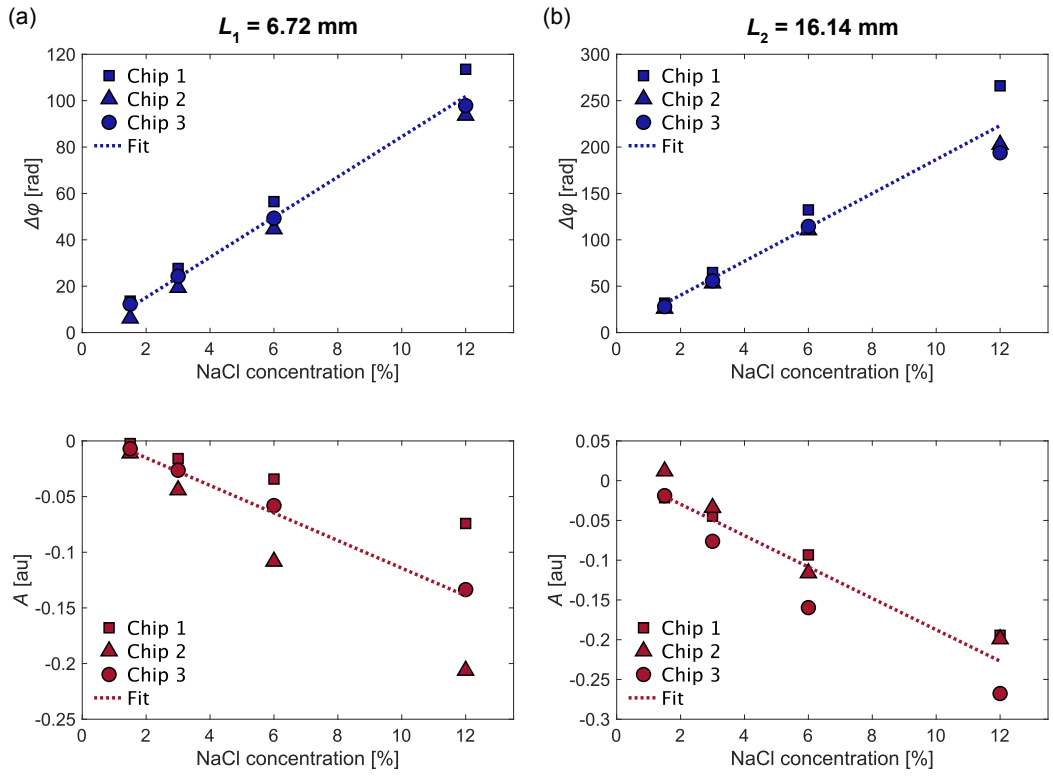

Figure 4.20: Saturation phase-shift (upper) and absorbance (lower) values of the (a) L_1 and (b) L_2 sensors as a function of NaCl concentration. All sensors exhibit high linearity. Absorbance measurements for the shortest (L_1) sensor have the greatest inter-chip variance.

sensor. This may be attributed to the higher impact of cross-talk and other external factors when the expected sensor response is low. Bulk sensitivities were calculated with respect to both NaCl concentration and real or imaginary refractive index change, and are compiled in Table 4.11. Mean device sensitivities to complex refractive index changes $S_\mathrm{n} = 5.07 \cdot 10^3\,\mathrm{rad/RIU}, S_\mathrm{k} = 2.23 \cdot 10^3\,\mathrm{au/RIU}$ and $S_\mathrm{n} = 10.69 \cdot 10^3\,\mathrm{rad/RIU}, S_\mathrm{k} = 3.55 \cdot 10^3\,\mathrm{au/RIU}$ were calculated from the L_1 and L_2 sensors, respectively, by linearly fitting the mean saturation values to the refractive index changes induced by the samples. Whereas S_n fits reasonably well with the theoretical values calculated in Section 4.3.4 (Table 4.7) and reproduced in Table 4.11 for convenience, S_k is significantly lower, especially in the L_2 sensors. One possible explanation is that the values of Δk_sample assumed in Table 4.9 are overestimated.

Limit of detection

To determine the limit of detection as indicated in Section 4.2.2, noise was evaluated over 30-second fragments of the signals, in which pure water was circulating over the sensor, and the output was stable and close to zero. Representative noise fragments for the L_1 and L_2 sensors are shown in Fig. 4.21. The read-out noise shows an additive white Gaussian noise (AWGN) pattern, suggesting that the residual noise is coming mainly from opto-electronic components. This is a reasonable guess providing that quantization noise is minimal using a 24-bit DAQ and that mechanical noise was damped by pressing the fiber array to the chip surface during the light-coupling process (see Appendix B). The standard deviation of the sensors output, as well as the corresponding LODs, expressed in RIU for generality, can be found in Table 4.12. For each sensor, LODs for the real and imaginary parts of the complex refractive index are comparable, therefore indicating that this

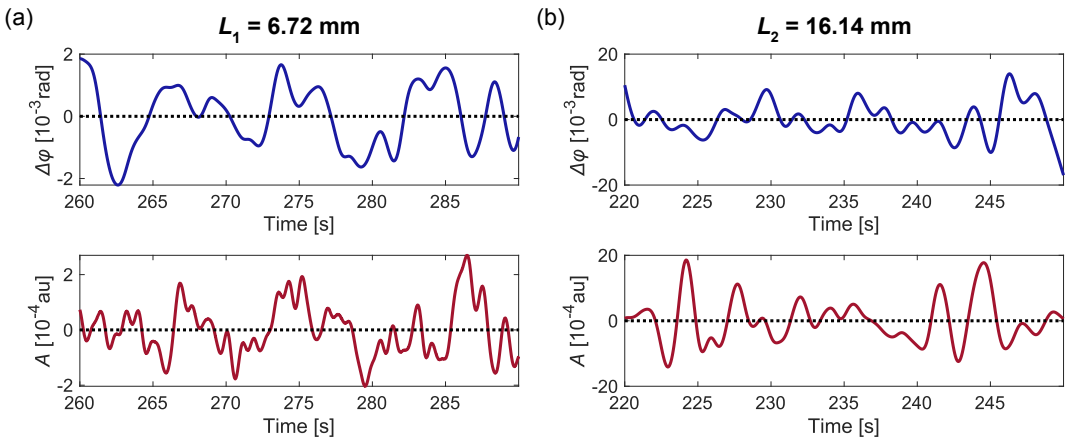

Figure 4.21: Phase-shift (upper) and absorbance (lower) representative noise fragments from the (a) L_1 and (b) L_2 sensors, used for determining the LOD.

Table 4.12: Limit of detection results of the fixed-wavelength bulk sensing experiments. Abbreviations: standard deviation (Std.).

L [mm]	Chip	$\sigma_{\Delta\varphi}$ [rad]	σ_A [au]	$\mathrm{LOD_n}$ [RIU]	$\mathrm{LOD_k}$ [RIU]
	1	0.0010	0.0004	$5.45 \cdot 10^{-7}$	$7.65 \cdot 10^{-7}$
	2	0.0061	0.0012	$3.77 \cdot 10^{-6}$	$1.10 \cdot 10^{-6}$
6.72	3	0.0027	0.0031	$1.69 \cdot 10^{-6}$	$4.36 \cdot 10^{-6}$
	Mean	**0.0033**	**0.0016**	$\mathbf{1.93 \cdot 10^{-6}}$	$\mathbf{2.09 \cdot 10^{-6}}$
	Std.	0.006	0.0014	$1.63 \cdot 10^{-6}$	$1.98 \cdot 10^{-6}$
	1	0.0049	0.0007	$1.13 \cdot 10^{-6}$	$6.69 \cdot 10^{-7}$
	2	0.0105	0.005	$3.2 \cdot 10^{-6}$	$4.26 \cdot 10^{-6}$
16.14	3	0.0112	0.0042	$3.64 \cdot 10^{-6}$	$3.01 \cdot 10^{-6}$
	Mean	**0.0088**	**0.0033**	$\mathbf{2.48 \cdot 10^{-6}}$	$\mathbf{2.77 \cdot 10^{-6}}$
	Std.	0.0034	0.0023	$1.34 \cdot 10^{-6}$	$1.83 \cdot 10^{-6}$

architecture can detect both magnitudes with equivalent precision. Sensors from Chip 1 achieved a LOD one order of magnitude lower than their counterparts from Chips 2 and 3, due to the combination of a similar sensitivity and remarkably lower read-out noise. The calculated mean LODs are $\mathrm{LOD_n} = 1.93 \cdot 10^{-6}$ RIU, $\mathrm{LOD_k} = 2.09 \cdot 10^{-6}$ RIU, and $\mathrm{LOD_n} = 2.48 \cdot 10^{-6}$ RIU, $\mathrm{LOD_k} = 2.77 \cdot 10^{-6}$ RIU for the L_1 and L_2 sensors, respectively. As was expected from the calculation of the optimum interaction length (Eq. (4.19)), the shortest sensor yields the best results, as the higher sensitivity of the L_2 sensor does not compensate for signal degradation due to increased water absorption losses. Considering the results of the L_1 sensor, this work is situated among the best of the state of the art of complex refractive index sensors, as can be observed in the comparison summarized in Table 4.13. Furthermore, the proposed architecture is the only one with equal capabilities to detect n and k, a especially challenging task while operating in the NIR.

4.5 Spectroscopic measurements

Even though the possibility of fixed-wavelength operation is a major advantage of the presented architecture, the sensor could, in principle, also work while scanning the wavelength, as in the modeled example represented in Figs. 4.3(c)-(d). Due to the growing interest in acquiring simultaneous dispersion and absorption wavelength-resolved measurements, pointed out in Section 4.1, the spectroscopic capabilities of the sensors were

Table 4.13: Limits of detection of state-of-the-art integrated complex refractive index sensors operating in different wavelength regimes. Results from this work are in bold letters.

Ref.	Regime	Architecture	$\mathbf{LOD_n}[\mathbf{10^{-6}RIU}]$	$\mathbf{LOD_k}[\mathbf{10^{-6}RIU}]$
[202]	VIS	YI	15	1.6
[203]		PC microdisk	30	200
[204]	NIR	SWG RR	55	1.7
This work		**Coherent MZI**	**1.9**	**2.1**
[208]	MIR	Suspended RR	8	13
[154]		Cascaded RR	9900	210

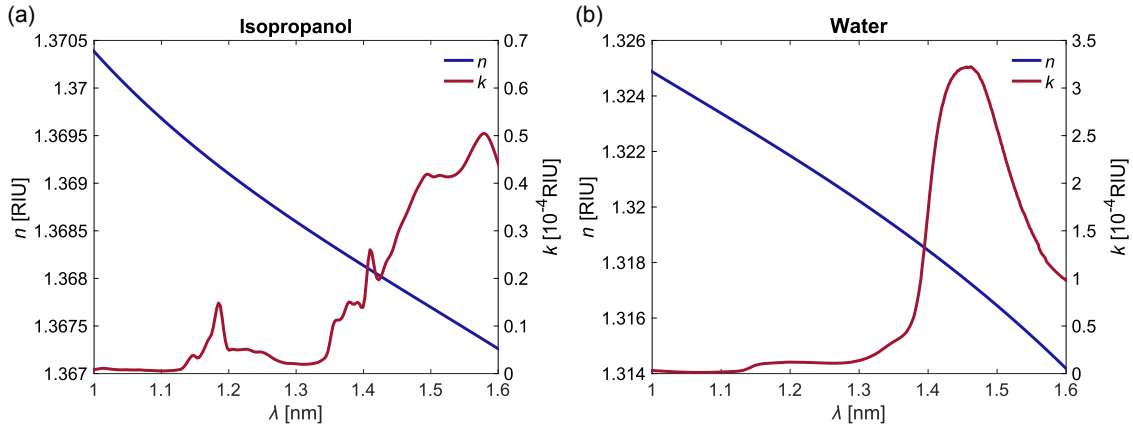

Figure 4.22: Complex NIR refractive index spectra of (a) isopropanol, extracted from [223] and (b) water, extracted from [212].

worth exploring. As a first approximation to spectroscopic measurements, wavelength scans were made when the sensor was exposed to either air, pure isopropanol, or pure water. The NIR complex refractive index spectra of the two latter are represented in Fig. 4.22, while the optical properties of air ($n = 1, k = 0$) are assumed constant. In an additional set of measurements, the wavelength was scanned during bulk sensing experiments as those shown in Section 4.4, in the intervals in which NaCl solutions circulated over the sensor and its output was thus stable.

4.5.1 Sensor output

Figure 4.23 shows the output signals of the L_1 and L_2 sensors, exposed to pure DI water, while the wavelength is being swept from 1545 to 1565 nm. The spurious effect of on-chip cavities was removed by the minimum-phase filter as in Section 4.3.5. The frequency response of the grating coupler can be appreciated in the envelope of the signals, especially in I_S. In contrast to the fixed-wavelength experiments described in Section 4.4, in this case the oscillations of the interferometric signals are not motivated by a change in the composition of the sample, but by the change in wavelength (see Eq. (4.6)). Here it is worth noting that the spectrum of the sample and the wavelength response of the interferometer, i.e., the alteration of the optical path difference between the sensing and the reference arms, are combined. To guarantee adequate performance of the 2×3-MMI, the following measurements are restricted to the 1.55–1.56 µm range.

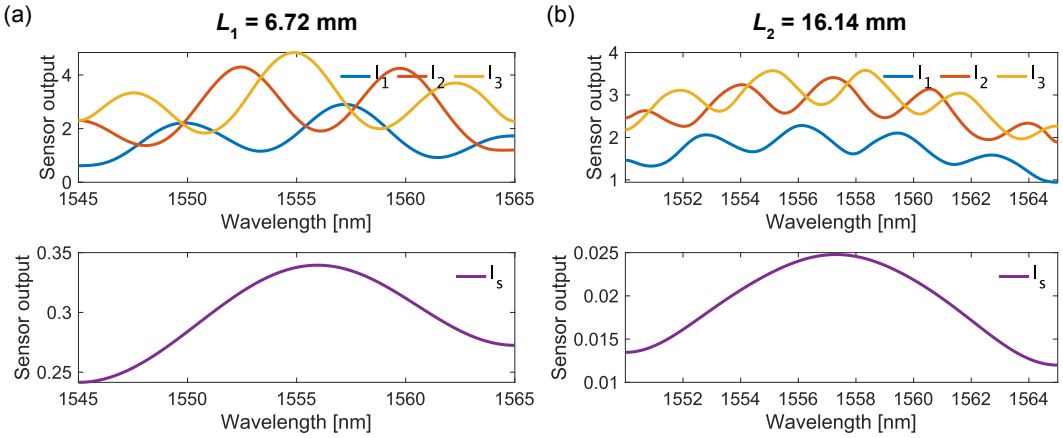

Figure 4.23: (a) L_1 and (b) L_2 sensor output when the sensing spirals are exposed to pure DI water and the wavelength is scanned around the central wavelength.

4.5.2 Results and discussion

Pure air, isopropanol and water

The difference in the effective index of the sensing and reference modes (Δn_{eff}) was extracted from the calculated phase shift as

$$\Delta n_{\text{eff}}(\lambda, C) = \frac{\Delta\varphi(\lambda, C)}{S_{\text{a},n_{\text{eff}}}(\lambda)}. \tag{4.24}$$

This measurement can be correlated to the dispersion spectra of the samples, $n_{\text{sample}}(\lambda, C)$, by referring it to the central wavelength, i.e., $\Delta n_{\text{eff}}(\lambda) - \Delta n_{\text{eff}}(\lambda_0)$. The obtained results for the three different analyzed samples can be seen in Figs. 4.24(a)–(b). A good agreement with the expected outcome, represented in dotted lines, is observed for both interaction lengths. Calculating changes in $n_{\text{sample}}(\lambda)$ directly from these measurements is not straightforward. The real effective index can be expressed as

$$n_{\text{eff}}^{\text{S}}(\lambda, C) = f_{\text{sample}}(\lambda) + \Gamma_{\text{sample}}(\lambda)\Delta n_{\text{sample}}(\lambda, C), \tag{4.25}$$

where $f_{\text{sample}}(\lambda)$ is a function dependent on the field distribution of the waveguide mode. For Eq. (4.7) to apply to different substances (sample 0, sample 1) rather than to different concentrations of analyte in the same solvent, the conditions

$$\begin{aligned} f_{\text{sample},0}(\lambda) &\approx f_{\text{sample},1}(\lambda), \\ \Gamma_{\text{sample},0}(\lambda) &\approx \Gamma_{\text{sample},1}(\lambda) \end{aligned} \tag{4.26}$$

should hold. In other words, the perturbation in the waveguide mode should be small, so that neither the mode profile nor the external confinement factor are affected. Unfortunately, these conditions are not fulfilled when considering the measurements with an air cladding as a reference, due to the big difference between the refractive index of air and that of IPA or water. This yields a different distribution of the waveguide mode, resulting in different f_{sample} and Γ_{sample}, thus making the direct comparison between the outputs invalid. However, it was indeed possible to obtain the spectral response of the difference between water and isopropanol real refractive indices as

$$\Delta n(\lambda) = n_{\text{IPA}}(\lambda) - n_{\text{H}_2\text{O}}(\lambda) = \frac{\Delta\varphi_{\text{IPA}}(\lambda) - \Delta\varphi_{\text{H}_2\text{O}}(\lambda)}{\Gamma S_{\text{a},n_{\text{eff}}}(\lambda)}, \tag{4.27}$$

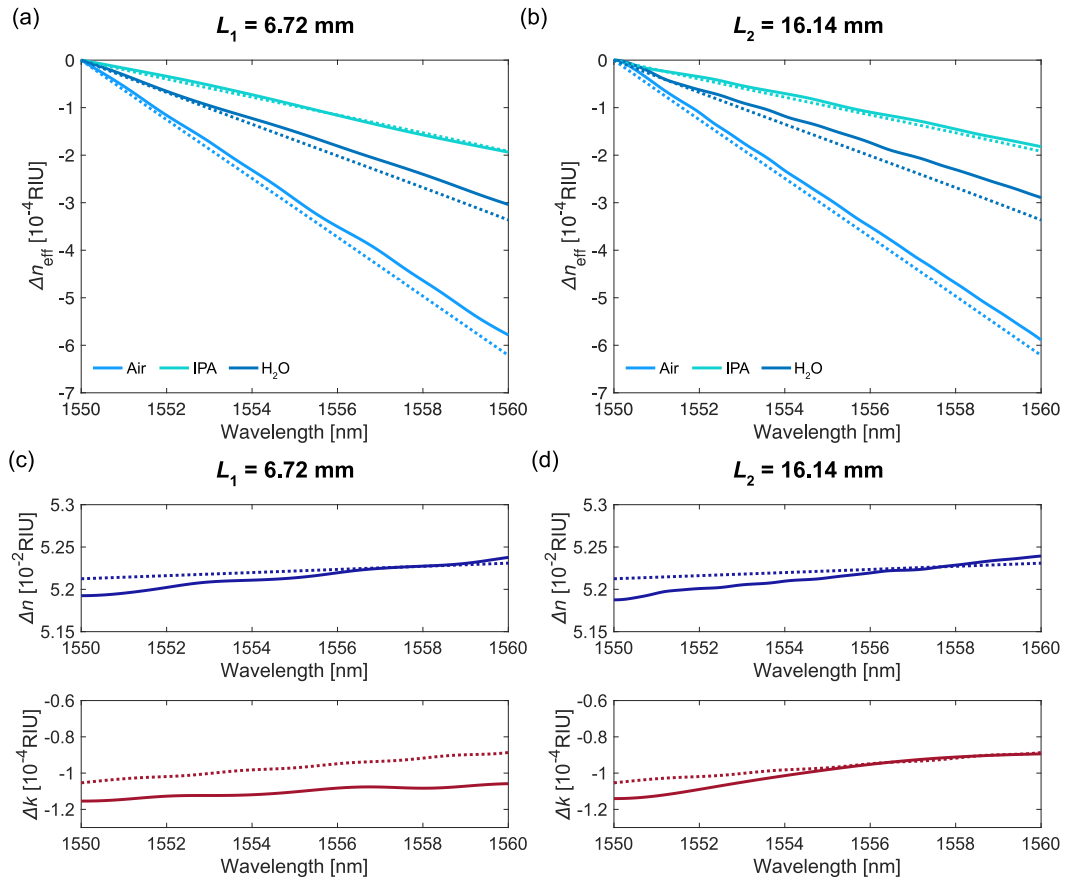

Figure 4.24: Results for the spectroscopic measurements with different samples. Spectra of the effective index difference extracted from the wavelength scans of the (a) L_1 and (b) L_2 sensors, exposed to pure air, isopropanol and water. Difference between isopropanol and water real (upper) and imaginary (lower) indices obtained with the (c) L_1 and (d) L_2 sensors. Theoretical values are represented in dotted lines.

where Γ was assumed constant over the scanned bandwidth. In a similar manner, the differential absorbance between the two substances was calculated as

$$\Delta A(\lambda) = -\log_{10}\left(\frac{I_{\mathrm{S,IPA}}(\lambda)}{I_{\mathrm{S,H_2O}}(\lambda)}\right), \tag{4.28}$$

so that

$$\Delta k(\lambda) = k_{\mathrm{IPA}}(\lambda) - k_{\mathrm{H_2O}}(\lambda) = \frac{\Delta A(\lambda)}{\Gamma S_{\mathrm{a},k_{\mathrm{eff}}}(\lambda)} \tag{4.29}$$

could be obtained. Results are shown in Figs. 4.24(c)–(d) and are in moderate agreement with theory. The errors committed are likely due to deviations from the conditions in Eq. (4.26). The presented results were consistent among sensors from different chips and encouraged the spectroscopic detection of different concentrations of analytes in the same solvent.

NaCl solutions

When the wavelength scans were performed in combination with bulk sensing experiments, the phase-shift and absorbance spectral responses of the sensor were offset by the saturation level for each sample (see Fig. 4.20). In this scenario, the perturbation introduced by the addition of NaCl to DI water is small enough to use the responses with pure water as the reference $\Delta\varphi(\lambda, 0)$ and $I_{\mathrm{S}}(\lambda, 0)$ of Eqs. (4.7) and (4.9), respectively. The

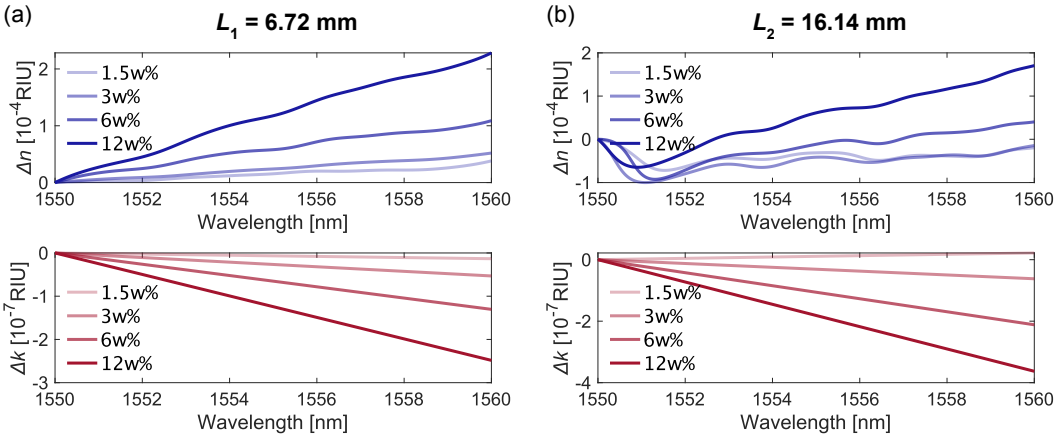

Figure 4.25: Estimated complex refractive index spectra of diluted NaCl by the (a) L_1 and (b) L_2 sensors. The offset of the curves was removed for better comparison.

complex refractive index spectra of NaCl diluted in different concentrations was therefore estimated from the normalized phase shift and absorbance. Results are shown in Figs. 4.25(a)–(b) for both interaction lengths, where the offset of the curves was removed to facilitate comparison. Even though consistent trends can be appreciated, these results cannot be validated, as data containing the spectral responses of diluted NaCl in the NIR are not available. These findings are however promising, and, given the accuracy of dispersion curves in Figs. 4.24(a)–(b), encourage further investigation with a different choice of samples, e.g., IPA-acetone mixtures. Moreover, extending this architecture to the MIR to operate near the fundamental absorption bands of many chemical species, such as methane or taurine, would be interesting. For this purpose, a re-design of the sensor and the measurement system, prioritizing aspects such as broadband operation and fringe mitigation, should be addressed.

4.6 Conclusions

In this chapter, a complex refractive index sensor based on a MZI with a coherent phase read-out was proposed, enabling the simultaneous detection of both parts of the complex refractive index of an analyte. The first implementation, in a SiNOI platform, presented several challenges that impeded validating the architecture. A second generation of sensors was designed for the same SiNOI platform, incorporating improvements derived from the investigation of the preceding chips. This latter generation turned out successfully. Bulk sensing experiments with NaCl solutions were performed to evaluate these sensors, and an output cross-talk model was developed to mitigate the spurious oscillations present in the sensing intensity signal. The best-performing sensor achieved a bulk limit of detection in the order of 10^{-6} RIU for both the real and the imaginary parts of the index, which is among the best of the state of the art. In fact, this is the first time, to the best of the author's knowledge, that both the real and the imaginary parts of the index are simultaneously detected with such a low limit of detection. This opens avenues for the detection of analytes in smaller concentrations and could thus enable the diagnosis of diseases in earlier stages, for instance. Preliminary spectroscopy measurements yielded promising results, encouraging further work toward an improved dispersion and absorption spectroscopic sensor, which could potentially be extended to the MIR. Moving to longer wavelengths would enable operation in the fingerprint region, where unique spectral features of many interesting molecules are located. Particularly, detection and identification of gases at very low concentrations could enable better early-warning systems

in hazardous environments. This novel interferometer-based architecture contributes to the development of integrated complex refractive index sensors operated both at a fixed and a swept wavelength, paving the way toward complete sample characterization in real time.

Chapter 5

Near-infrared bimodal refractive index sensor

A novel near-infrared refractive index sensor based on a bimodal interferometer is presented in this chapter. This is the second contribution of this thesis at near-infrared wavelengths. After an introduction on bimodal interferometric sensors and an overview of their state of the art (Section 5.1), the proposed sensing architecture is described, with an emphasis on coherent detection (Section 5.2). Afterwards, the design of the first and second generations of sensors is addressed (Section 4.3), including a discussion of the issues experienced with the first-generation sensors and a detailed explanation of the successful second generation. Finally, the results of the performed bulk sensing experiments are shown and discussed (Section 5.4), and the chapter is closed with some final remarks (Section 5.5).

The device and most of the experimental results presented in this chapter have been published in A. Torres-Cubillo, J. M. Luque-González, A. Sánchez-Postigo, A. Fernández-Gavela, J. G. Wangüemert-Pérez, Í. Molina-Fernandez, and R. Halir, "High-performance bimodal evanescent-field sensor with coherent phase readout," Journal of Lightwave Technology **42(8)**, 3010–3015 (2024).

5.1 Introduction

When refractive index sensors were presented in Chapter 2, the division between resonant and interferometric sensors was established. Even though interferometric configurations enable fixed-wavelength operation and typically reach higher sensitivities, resonant sensors offer superior compactness and are often preferred for dense sensor integration [70]. This is in part due to the fact that most interferometric configurations, such as the MZI-based complex refractive index sensor proposed in Chapter 4, require two different physical paths for the reference and sensing branches, which increases the sensor footprint. Bimodal interferometers (BIs), theoretically proposed as early as 2009 [224] and experimentally demonstrated two years later [225], emerge as a promising alternative. They are based on multimode (MM) waveguides as the one shown in Fig. 5.1, which support at least two orthogonal modes, traveling with different propagation constants and thus accumulating a relative phase-shift difference ($\Delta\varphi$). Upon recombination in a single-mode (SM) waveguide, an interference pattern is created. This behavior is equivalent to that of a MZI and thus enables refractive index sensing, with the advantage of using just one waveguide instead of two.

The performance of a BI is highly conditioned by two crucial factors. In the first place, the limitations arising from the sinusoidal interferometric output, which were already

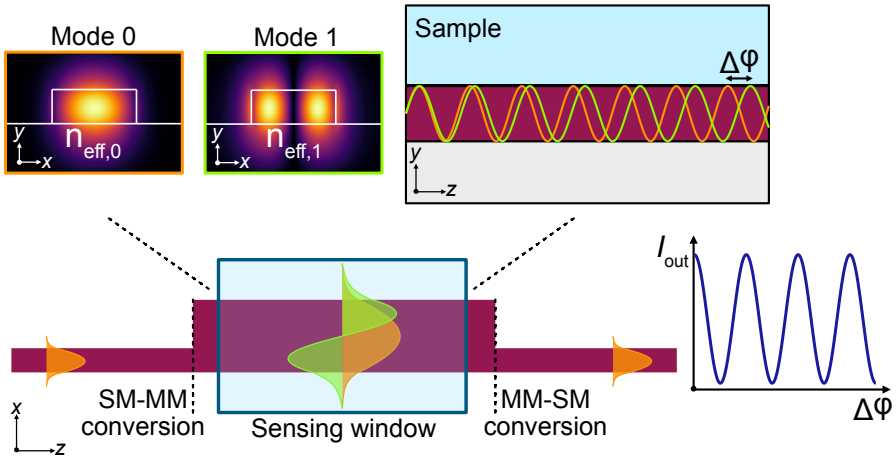

Figure 5.1: Schematic diagram of a conventional bimodal interferometer. The transitions between single-mode (SM) and multimode (MM) waveguides are abrupt discontinuities in waveguide width. Upon recombination in the output waveguide, a sinusoidal interferometric response is formed.

covered in Section 2.3.2 of Chapter 2 for a conventional MZI, hold for this configuration as well. More explicitly, conventional BI sensors suffer from sensitivity fading and directional ambiguity. The second pitfall, which is specific of this concept, is modal excitation and recombination in the transition between single-mode and multimode waveguides. In most configurations, the modes of the bimodal waveguide are excited by an abrupt discontinuity in either the width, as in the example represented in Fig. 5.1, or the height of the waveguide. This is a simple approach, yet is prone to inducing reflections which could potentially lead to FP-ripples, with the risk of masking small sensing signals. Moreover, when such transitions are used, guaranteeing that both modes are excited with equal power becomes challenging. An imbalanced excitation dramatically decreases the contrast of the interferogram, hindering a clear read-out. As a consequence, SM-MM transitions must be carefully designed.

5.1.1 State of the art

Since their first demonstration as biosensors, BIs have experienced a significant growth, both in silicon and polymeric platforms [90]. SiN bimodal sensors operating in the VIS have been employed in the detection of different analytes such as human-growth hormone (hGH) [226] and pesticides in tap water [227]. To enhance sensitivity, periodic silicon-on-insulator waveguides, both operating in the subwavelength regime [228] and as photonic crystals [229], have been implemented. More recently, the concept of regional mode engineering, consisting in patterning a partial cladding in the sensing area to drastically reduce the overlap between the fundamental (reference) mode and the sample, has been proposed and demonstrated [161]. To provide a balanced modal excitation, a grating-assisted BI with nearly lossless conversion was theoretically introduced, but never implemented [230]. A trigonometric algorithm for linear read-out has been applied to detect the spike protein in SARS-CoV-2, but requires a phase modulation of the input signal and using two-sectional photodetectors [231]. Coherent read-out of a SOI BI was enabled by using a 90° hybrid, implemented by cascaded MMIs, but was not validated with sensing experiments [232]. Finally, with few exceptions [233], BI sensors with spiral waveguides are rare, thereby hampering dense integration.

In this chapter, a NIR refractive index sensor based on a spiral bimodal waveguide is presented. This architecture, which will be further explained in Section 5.2, combines a

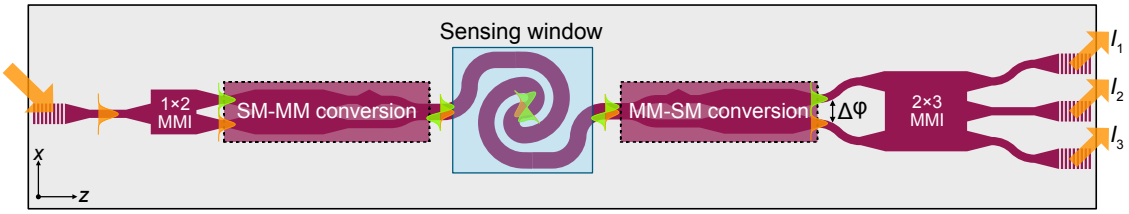

Figure 5.2: Schematic diagram of the proposed coherent bimodal interferometric sensor. A mode converter allows for fully-controlled excitation of the first two TE modes of the bimodal sensing waveguide. The same device acting as a demultiplexer feeds the 120° hybrid which enables coherent phase detection.

fully controlled modal excitation with a coherent read-out scheme. With this novel implementation, the detection capabilities of MZIs are combined with the superior compactness and robustness of BIs.

5.2 Sensor architecture

A schematic diagram of the developed bimodal refractive index sensor can be seen in Fig. 5.2. The sensor is based on a spiraled bimodal waveguide, which supports the fundamental and the first high-order TE modes. A mode converter enables a controlled modal excitation at the input of the sensing waveguide. The same architecture works symmetrically to separate the modes of the bimodal waveguide into two fundamental modes of single-mode waveguides, which enter the 120° hybrid for coherent phase detection. The specific implementations of the two types of mode converters developed in this work will be addressed in Sections 5.3.1 and 5.3.4. Light input/output is performed via surface grating couplers. In the following the sensor working principle and its figures of merit are explained.

5.2.1 Working principle

Input light is split to feed the mode converter, which excites the first two TE modes of the sensing bimodal waveguide. In said waveguide, the fundamental mode propagates with an effective index $n_{\text{eff},0}$, and has a confinement factor Γ_0, whereas the first high-order does so with $n_{\text{eff},1}$ and Γ_1, respectively. The overlap of the first high-order mode with the sample is greater than that of the fundamental one, whose energy is more confined to the core, i.e., $\Gamma_1 > \Gamma_0$. Considering that the wavelength is constant, the mode effective indices can be expressed solely as a function of analyte concentration,

$$\begin{aligned} n_{\text{eff},0}(C) &= n_{\text{eff},0}(0) + \Gamma_0 \Delta n_{\text{sample}}(C), \\ n_{\text{eff},1}(C) &= n_{\text{eff},1}(0) + \Gamma_1 \Delta n_{\text{sample}}(C), \end{aligned} \tag{5.1}$$

where $n_{\text{eff},0}(0)$ and $n_{\text{eff},1}(0)$ are the values of the effective indices in the absence of analyte. After propagation in the waveguide, the modes have accumulated a phase shift

$$\begin{aligned} \varphi_0(C) &= \frac{2\pi}{\lambda_0} n_{\text{eff},0}(C) L, \\ \varphi_1(C) &= \frac{2\pi}{\lambda_0} n_{\text{eff},1}(C) L \end{aligned} \tag{5.2}$$

with respect to their initial phase values. The phase-shift difference between the modes can be defined in an analogous way as for a MZI (see Section 2.3.2 of Chapter 2),

$$\Delta\varphi(C) = \varphi_1(C) - \varphi_0(C) = \frac{2\pi}{\lambda_0} \Delta n_{\text{eff}}(C) L, \tag{5.3}$$

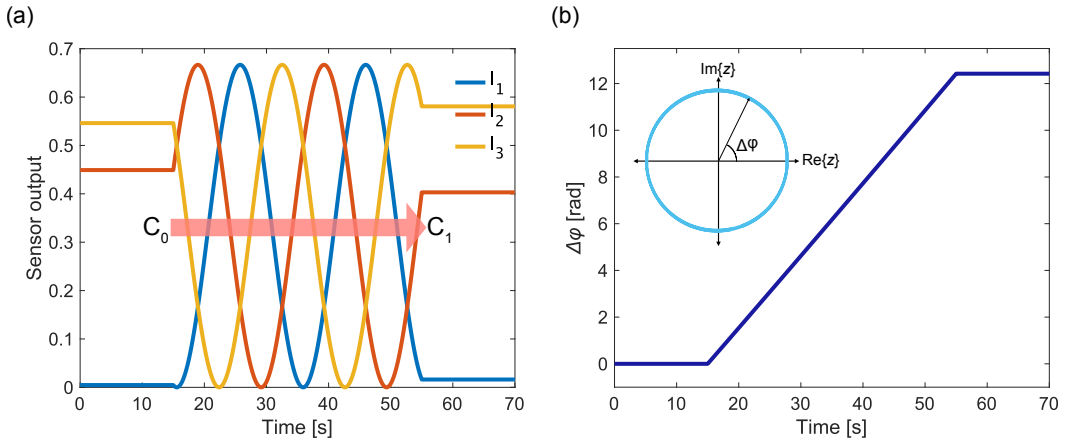

Figure 5.3: Modeled output of the bimodal refractive index sensor. (a) Detected intensity signals for a linear increase of analyte concentration from C_0 to C_1. (b) Calculated phase shift. A linear read-out is achieved from the IQ signal, shown in the inset.

where $\Delta n_{\text{eff}}(C) = n_{\text{eff},1}(C) - n_{\text{eff},0}(C)$. By normalizing the phase-shift difference, so that

$$\Delta\varphi(C) - \Delta\varphi(0) = \frac{2\pi}{\lambda_0}(\Gamma_1 - \Gamma_0)\Delta n_{\text{sample}}(C)L, \tag{5.4}$$

a measurement proportional to Δn_{sample} is obtained. The modes of the bimodal waveguide are demultiplexed into the two fundamentals modes of two single-mode waveguides by the reverse operation of the mode converter. These two fundamental modes, which preserve the phase shift $\Delta\varphi$, are the inputs of the 2×3-MMI. Coherent detection is thus enabled and a complex signal

$$z(C) = \sqrt{I_0 I_1}e^{\mathrm{j}\Delta\varphi(C)}, \tag{5.5}$$

where I_0 and I_1 are the intensities of the TE_{00} and TE_{10} modes, respectively, can be generated. Finally, $\Delta\varphi = \arg(z)$ is unambiguously determined. Figure 5.3(a) shows the modeled interferometric output signals of a 7 mm-long bimodal sensor with $\Gamma_0 = 0.15$ and $\Gamma_1 = 0.24$, as a response to a linear increase of concentration from C_0 to C_1, equivalent to $\Delta n_{\text{sample}} = 5 \cdot 10^{-3}$ RIU. The associated phase shift can be seen in Fig. 5.3(b). Without incorporating a reference arm, an equivalent outcome to that of a coherent MZI (see Fig. 2.8 from Chapter 2) is obtained.

5.2.2 Figures of merit

The performance of the proposed refractive index sensor will be evaluated by bulk sensing experiments. The modal sensitivity of each mode coincides with their confinement factors (Section 2.5, Chapter 2),

$$\begin{aligned} S_{\text{m},0} &= \frac{\partial n_{\text{eff},0}}{\partial n_{\text{sample}}} = \Gamma_0, \\ S_{\text{m},1} &= \frac{\partial n_{\text{eff},1}}{\partial n_{\text{sample}}} = \Gamma_1, \end{aligned} \tag{5.6}$$

but, as seen from Eq. (5.4), what is relevant in bimodal interferometry is the differential modal sensitivity, defined as

$$S_{\text{d}} = \frac{\partial n_{\text{eff},1}}{\partial n_{\text{sample}}} - \frac{\partial n_{\text{eff},0}}{\partial n_{\text{sample}}} = \Gamma_1 - \Gamma_0, \tag{5.7}$$

and which indicates the difference between the confinement factors of the first high-order and fundamental modes. The architectural sensitivity to effective index changes is equivalent for BIs and MZIs (Section 4.2.2, Chapter 2):

$$S_{\mathrm{a}} = \frac{\partial \Delta\varphi}{\partial(n_{\mathrm{eff},1} - n_{\mathrm{eff},0})} = \frac{2\pi}{\lambda_0} L. \tag{5.8}$$

To calculate the sensitivity of the device, the differential and architectural sensitivities are multiplied, yielding

$$S_{\mathrm{n}} = \frac{\partial \Delta\varphi}{\partial n_{\mathrm{sample}}} = \frac{2\pi}{\lambda_0}(\Gamma_1 - \Gamma_0) L. \tag{5.9}$$

In view of this expression, it can be concluded that, apart from the aforementioned strategies consisting on reducing λ_0 and increasing L (Chapter 4, Section 4.2.2), enhancing the differential modal sensitivity (S_{d}), rather than the absolute values of Γ_0 and Γ_1, would enlarge overall device sensitivity. Finally, in the same manner as in a conventional interferometer, the LOD is determined by considering phase read-out noise:

$$\mathrm{LOD} = \frac{3\sigma_{\Delta\varphi}}{S_{\mathrm{n}}}. \tag{5.10}$$

5.3 Sensor design and evaluation

A first generation of sensors was designed for the SOI platform provided by Applied Nanotools, described in Section 3.2.1 (Chapter 3), for an operation wavelength $\lambda_0 = 1.31$ µm, selected in order to reduce water absorption losses. Four chips were fabricated in a commercial SOI MPW run, but, due to several problems related to both the platform and the design, discussed in Section 5.3.3, no valid sensing results were obtained with them. However, the experience with the first-generation sensors encouraged changes and improvements, leading to the development of the high-performance second-generation sensors used in the sensing experiments presented later in this chapter. Such sensors were designed for Cornerstone's SiNOI platform at $\lambda_0 = 1.55$ µm and fabricated in the same chip as the second-generation of complex refractive index sensors (Chapter 4), corresponding to the SiN MPW#3.

This section details the design and characteristics of the different sensor components, the mask layout and the optical characterization of each generation of sensors.

5.3.1 Components of the first-generation sensors

As it was seen in Section 5.2, the key components of the bimodal sensor are the mode converter, the sensing bimodal waveguide, the 1×2- and 2×3-MMIs and the grating couplers. In this case, the designs were made for a SOI platform.

Mode converter

The mode converter and demultiplexer included in the first generation of bimodal sensors takes advantage of mode evolution in a counter-tapered coupler. The design, schematized in Fig. 5.4 and whose dimensions can be found in Table 5.1, is adapted from the

Table 5.1: Geometry of the mode converter based on counter-tapered couplers employed for the first-generation sensors, implemented in SOI.

$W_{\mathrm{SM,0}}$ [µm]	$W_{\mathrm{SM,1}}$ [µm]	W_{MM} [µm]	W_{tip} [µm]	L_{taper} [µm]	W_{s} [µm]
0.51	0.42	0.73	0.2	150	0.12

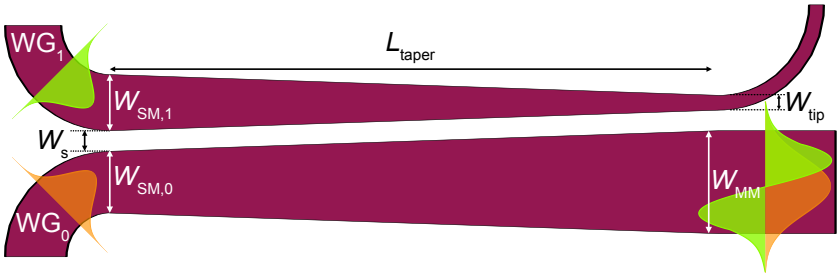

Figure 5.4: Schematic representation of the mode converter employed in first-generation sensors, implemented in SOI. The device is based on a counter-tapered coupler.

one proposed in [234]. The fundamental mode of the lower waveguide (WG_0) propagates to the device output without coupling to any of the modes of the upper waveguide (WG_1), while the fundamental mode of WG_1 is adiabatically coupled to the first high-order mode of WG_0. This behavior is achieved by properly selecting the width-change ratio of the tapers so that the phase-matching condition between the fundamental mode of WG_1 and the first high-order mode of WG_0 is fulfilled around the center of the taper, but not at its ends. The distance L_{taper} is set to guarantee an adiabatic transition. There is no phase matching between the fundamental mode of WG_0 and any of the modes of WG_1. The coupler is embedded between waveguide bends to avoid coupling between the input waveguides and reduce radiation from the tip of WG_1. Owing to the reciprocity theorem, the same architecture acts as a mode demultiplexer when it is mirrored.

Bimodal waveguides

Sensors with bimodal waveguides supporting the fundamental and first high-order TE modes were implemented in two different widths, $W_1 = 0.7\,\mu\text{m}$ and $W_2 = 0.6\,\mu\text{m}$. A short summary of their performance is given in Table 5.2, where $L_{\text{H}_2\text{O},0}$ and $L_{\text{H}_2\text{O},1}$ denote water absorption losses for the TE_{00} and the TE_{10}, respectively. Closer attention will be paid to the bimodal waveguides of the second-generation sensors, as the experimental results presented in this thesis were obtained with them.

MMIs and grating couplers

The employed MMIs were classic homogeneous SOI designs, and their geometries can be found in Table 5.3. The transition between the $W_{\text{SM}} = 0.4\,\mu\text{m}$ interconnection waveguides and the access ports of the MMIs was implemented by a $20\,\mu\text{m}$-long taper. Surface grating couplers were single-etched and silica-cladded, with the geometry indicated in Table 5.4, where a_0 and b_0 are the dimensions of the adaptation tooth (see Fig. 4.7(b) in Chapter 4). They radiated with an angle of -29° to a polished fiber (see Appendix A) and achieved a maximum coupling efficiency $\text{CE} = -4.32\,\text{dB}$.

Table 5.2: Summary of the performance, in terms of sensitivity and water absorption losses, of the bimodal SOI waveguides included in first-generation sensors.

Width [μm]	S_{d} **[RIU/RIU]**	$L_{\text{H}_2\text{O},0}$ **[dB cm^{-1}]**	$L_{\text{H}_2\text{O},1}$ **[dB cm^{-1}]**
0.7	0.085	0.33	0.86
0.6	0.17	0.39	1.53

Table 5.3: Dimensions of the MMIs of the first-generation sensor layout, implemented on a SOI platform.

Type	W_{MMI} [μm]	L_{MMI} [μm]	W_{a} [μm]	W_{s} [μm]
1×2	3.85	16.2	1.5	0.5
2×3	6.05	108	1.5	0.5

Table 5.4: Dimensions of the surface grating couplers of the first-generation sensor layout, implemented on a SOI platform.

W_{GC} [μm]	L_{GC} [μm]	a [nm]	b [nm]	a_0 [nm]	b_0 [nm]
13	51.85	206	309	265	90

5.3.2 Layout of the first-generation sensors

The mask layout of one of the implemented sensors is shown in Fig. 5.5(a), where the main components are augmented and long straight interconnecting waveguides are omitted. The spiral bimodal waveguide was around 15 mm-long, and adjacent waveguides were separated by 7 μm. Grating couplers were pitched to match the fiber array, and rotated so the microfluidics and array configuration described in Section 3.3.2 could be kept despite the negative radiation angle. SEM images of the mode converter, taken by the foundry before depositing the silica cladding, can be seen in Fig. 5.5(b). The fabricated dimensions agreed with the nominal design.

5.3.3 Optical and sensing evaluation of the first-generation sensors

Propagation losses around 5 dB cm^{-1} at $\lambda_0 = 1.31$ μm were measured in the cladded waveguides by the cut-back method. While this value was much higher than the anticipated losses of 1–2 dB cm^{-1}, it was manageable, especially considering that relatively low water absorption losses were expected. After the protective resist was removed (Section 3.5.1 of Chapter 3), sensing experiments using NaCl solutions were performed. However, as can be seen from Fig. 5.6(a), interferograms were not correctly formed in the transitions between buffer and sample solutions, and the distortion was beyond the corrective capabilities of the calibration algorithm (Section 3.4 of Chapter 3). As the 2×3-MMI design was well trusted, the principal suspects were the mode converter and the bent waveguide sections. Figure 5.6(b) shows an example of the calculated complex signal, even after undergoing careful calibration. The phase read-out was thus considered invalid. All sensors from the four chips were measured with identical outcome, suggesting that the design flaw was systematic.

More experiments were planned for a deeper investigation of this misbehavior, but, after applying the cleaning protocols (Chapter 3, Section 3.5.2), most of the sensing waveguides stopped transmitting light. After inspection under the SEM, it was found out that parts of the waveguides had broken, as shown in Fig. 5.6(c), most likely during the sonication steps. Furthermore, it was observed that a pedestal was etched around uncladded waveguides, which made them very fragile. It was then decided to use HCl as an analyte instead of NaCl, as it should leave no residues, thereby avoiding the sonication steps to clean the chips. Here it is worth considering that HCl solutions had been previously and successfully employed with SiN sensing chips by other members of the group, as well as by different groups with experience in photonic sensors [225]. Unexpectedly, after performing such experiments, none of the sensors transmitted anymore. SEM images and energy dispersive X-ray spectroscopy (EDS) analysis revealed chemical damage and depositions, seemingly caused by the interaction of HCl with silicon. Some examples can be seen in Figs. 5.6(d)–(e). It was hypothesized that opening the sensing windows during

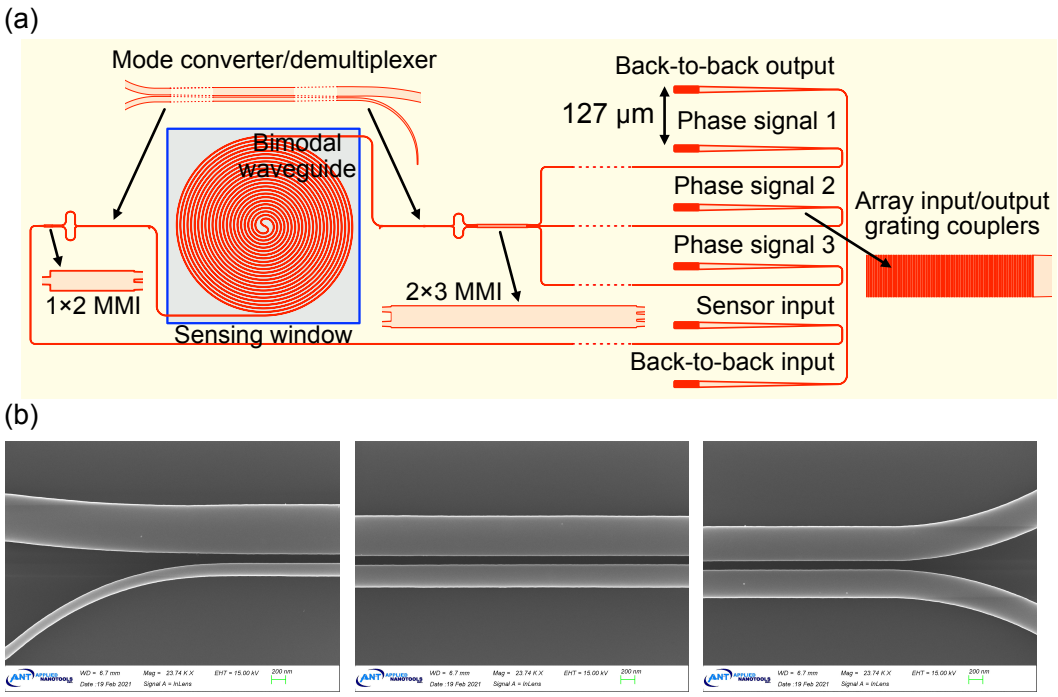

Figure 5.5: (a) Mask layout for the first-generation sensor, designed for ANT's SOI platform. (b) SEM images of the mode converter, based on a counter-tapered coupler.

the fabrication process had chemically activated the silicon waveguides, making them reactive to these kind of samples. As a result of the accumulated damage, the chips were discarded.

Conclusions after optical and sensing evaluation

Three main conclusions were extracted from the challenges brought by the first generation of bimodal sensors:

- The mode conversion scheme based on a counter-tapered coupler, besides the correct fabrication of the device, did not optimally work. It remains unclear if this was due to a design flaw regarding the coupler or due to mode cross-coupling in the curved bimodal waveguides caused by light scattering in fabrication defects. Unfortunately, it was not possible to conduct further verification measurements because the chips were damaged.
- Narrow SOI waveguides are vulnerable to the mechanical stress produced by the sonication steps needed to clean residues. This issue worsens considering that pedestal waveguides were produced by the cladding-removal process.
- Silicon surfaces can react to chemical analytes such as HCl, generating residual depositions and irreversible damage.

5.3.4 Components of the second-generation sensors

All components were designed for SiN at the operation wavelength $\lambda_0 = 1.55$ µm for the detection of analytes in water-based samples. The designs of the surface grating couplers and the MMIs used for input light splitting and coherent detection are shared with the second-generation complex refractive index sensors from Chapter 4, so the details can be found in Section 4.3.1.

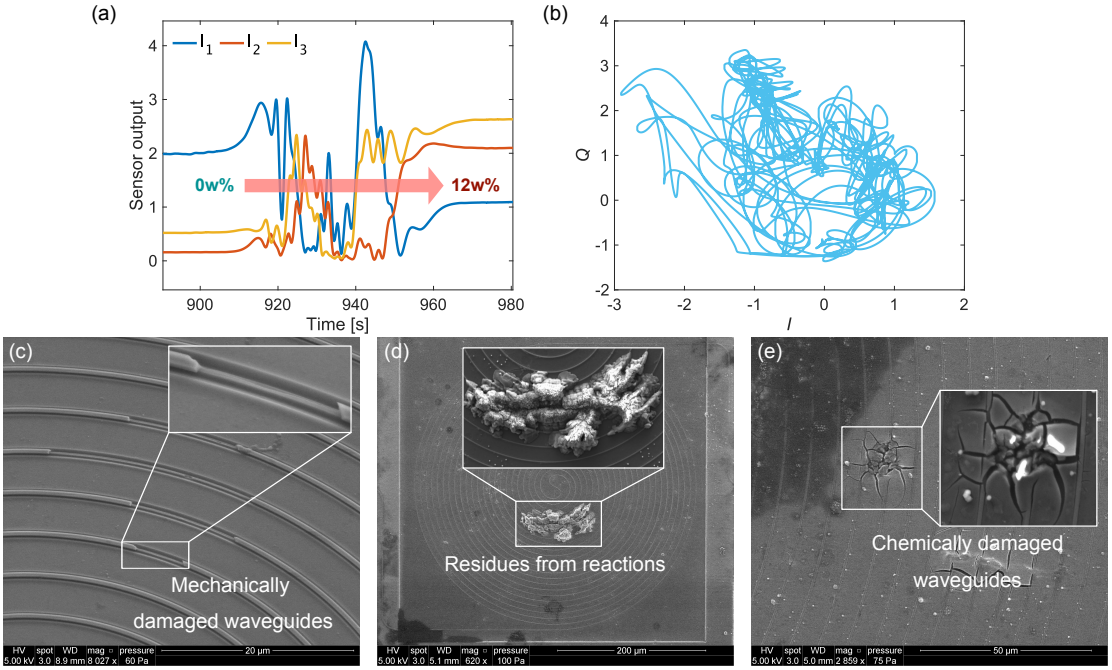

Figure 5.6: (a) First-generation sensor output in the transition from a buffer to a NaCl solution. (b) Generated IQ signal after calibration. The read-out was invalid. (c) Damaged waveguides due to mechanical stress. (d) Deposited residues after HCl sensing experiments. (e) Damaged surface and waveguides due to uncontrolled chemical reactions.

Mode converter

The mode converter implemented for the second-generation sensors is schematized in Fig. 5.7. The device, based on the design proposed in [91] and validated in [92], has three sub-components: a 2×2-MMI working as a 3 dB-90° hybrid coupler, a phase shifter (PS) and a sinusoidal-profile Y-junction. The phase shifter is composed of two parallel waveguides. While the lower arm is a straight single-mode waveguide, the upper arm comprises two trapezoidal tapers in back-to-back configuration. The purpose of such tapers is increasing the effective index, therefore generating a delay in propagation. Specifically, the length of the PS is designed so that a 90° phase shift with respect to the lower branch is achieved. The output port of the Y-junction is a multimode waveguide with a width $W_{\mathrm{MM}} = 2W_{\mathrm{SM}}$, which supports the fundamental and the first high-order TE modes. The dimensions of the different components can be found in Table 5.5. Here it is worth mentioning that, if a

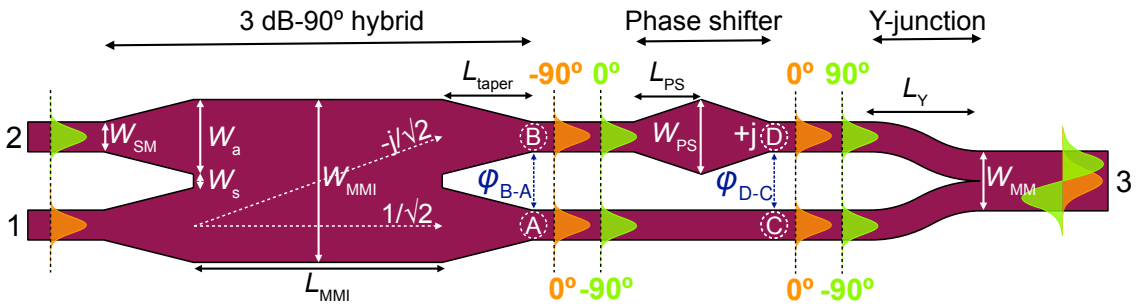

Figure 5.7: Mode converter used in the second-generation sensors, implemented in SiN. The device is composed of a 90° hybrid, a phase shifter and a Y-junction, which in combination transform the fundamental mode in Port 1 into the fundamental mode in Port 3, and the fundamental mode in Port 2 into the first high-order mode in Port 3. The most relevant dimensions are indicated.

Table 5.5: Geometry of the components of the mode converter and demultiplexer of the second-generation sensors.

Component	Parameter	Value [μm]
MMI	W_{MMI}	7.4
	L_{MMI}	167
	W_{a}	3
	W_{s}	1.5
PS	W_{PS}	1.1
	W_{PS}	13.25
Y-junction	L_{Y}	30

different combination of widths of the interconnecting and sensing waveguides is desired, tapers can be included adjacently to the device input and output ports.

The mode converter operates as follows. The fundamental TE mode injected through Port 1 is split by the MMI into its upper (B) and lower (A) arms, with a phase difference $\Delta\phi_{\text{B-A}} = \phi_{\text{B}} - \phi_{\text{A}} = -90^\circ$ between them. The PS adds on a 90° phase difference between the upper (D) and lower (C) branches, so that, at the input of the Y-junction, $\Delta\phi_{\text{D-C}} = \phi_{\text{D}} - \phi_{\text{C}} = 0^\circ$. The two in-phase TE modes are adiabatically combined by the Y-junction into the fundamental mode (TE_{00}) of the bimodal waveguide. On the other hand, the fundamental TE mode in Port 2 is equally split by the MMI, but now the defined phase difference between the upper and lower branches is $\Delta\phi_{\text{B-A}} = \phi_{\text{B}} - \phi_{\text{A}} = 90^\circ$. At the end of the PS this difference has evolved into $\Delta\phi_{\text{D-C}} = \phi_{\text{D}} - \phi_{\text{C}} = 180^\circ$. The combination of the two out-of-phase modes in the Y-junction generates the first high-order mode (TE_{10}) supported by the bimodal waveguide. When the device works as a demultiplexer, the TE_{00} mode of the bimodal waveguide is split by the Y-junction into two in-phase fundamental modes, which, after going through the PS section, are coupled into the fundamental mode of Port 1. In contrast, the TE_{10} mode is split into two out-of-phase fundamental modes, and coupled to the fundamental mode of Port 2 after undergoing the 90° phase shifting. Thanks to the explained behavior, the two modes of the sensing waveguide are excited, and, once they have gone through the sensing pathlength, they are demultiplexed into two fundamental modes whose relative phase shift can be coherently detected.

The 3D-FDTD simulated field propagation (RSoft FullWAVE™) in the mode converter is shown in Fig. 5.8(a), when light is launched through Port 1 and the fundamental mode of the bimodal waveguide is excited, and in Fig. 5.8(b), when the launch is through Port 2 and thus the first high-order mode is excited. The different sections of the device are indicated. The most important figures of merit are insertion loss (IL) and cross-talk (XT). Insertion loss

$$\text{IL}_k = -10\log_{10}\left(\frac{P_k}{P_{\text{in}}}\right), \quad k = \{0, 1\}, \tag{5.11}$$

where $k = 0$ refers to the TE_{00} mode and $k = 1$ to the TE_{10}, is defined as the ratio between the power transferred to the desired excited mode in Port 3 (P_0 and P_1) and the input power (P_{in}) of the mode launched through either Port 1, to excite TE_{00}, or Port 2, to excite TE_{10}. Cross-talk

$$\text{XT}_k = 10\log_{10}\left(\frac{P_k}{P_l}\right), \quad k, l = \{0, 1\},\ k \neq l \tag{5.12}$$

measures the power ratio between the desired and the undesired mode. The evolution of these parameters around the operation wavelength can be observed in Figs. 5.8(c)–(d), whereas the performance at $\lambda_0 = 1.55$ μm can be found in Table 5.6. The low insertion loss and cross-talk of the structure allow for a virtually lossless and efficient mode conversion and separation. The same device was also simulated with a width fabrication bias

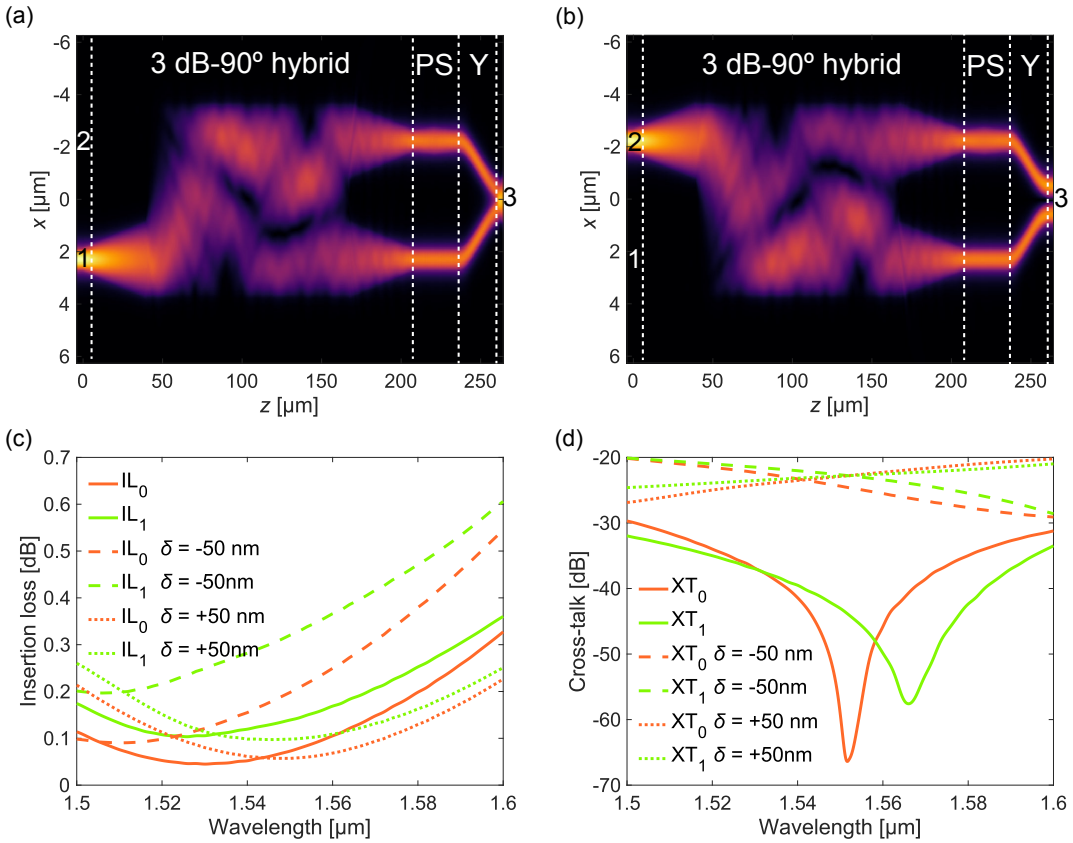

Figure 5.8: Field propagation in the mode converter when light is launched through (a) Port 1, exciting the fundamental mode, and (b) Port 2, exciting the first high-order mode. Device sections are indicated. Simulated (c) insertion loss and (d) cross-talk for the nominal dimensions and a ± 50 nm fabrication bias. The values remain low at λ_0 even when fabrication tolerances are considered.

Table 5.6: Performance of the second-generation mode converter and demultiplexer at $\lambda_0 = 1.55$ μm.

$\mathbf{IL_0}$ [dB]	$\mathbf{IL_1}$ [dB]	$\mathbf{XT_0}$ [dB]	$\mathbf{XT_1}$ [dB]
0.07	0.14	-59.42	-43.05

$\delta = \pm 50$ nm, yielding the results shown in Figs. 5.8(c)–(d) in dashed and dotted lines. Insertion loss and cross-talk remain below 0.5 dB and -20 dB, respectively, around λ_0, thus anticipating robustness against typical fabrication errors. Finally, as the sensing region is embedded between two mirrored mode converters (see Fig. 5.2), back-reflections were calculated by measuring the power reflected back to the input port in order to determine whether a FP cavity could be created. The predicted value of BR < -30 dB for both modes, even when fabrication tolerances are considered, makes any expected FP ripple related to this device negligible.

Bimodal waveguides

A cross section of the bimodal sensing waveguide, with dimensions $H = 0.3$ μm and $W_{\mathrm{MM}} = 1.8$ μm, is shown in Fig. 5.9(a), where pure water is selected as the cladding material. The complex refractive indices of the materials are those given in Table 4.1 of Chapter 4. At the operation wavelength $\lambda_0 = 1.55$ μm, the waveguide supports the fundamental and the first high-order TE modes, whose field distribution and complex effective

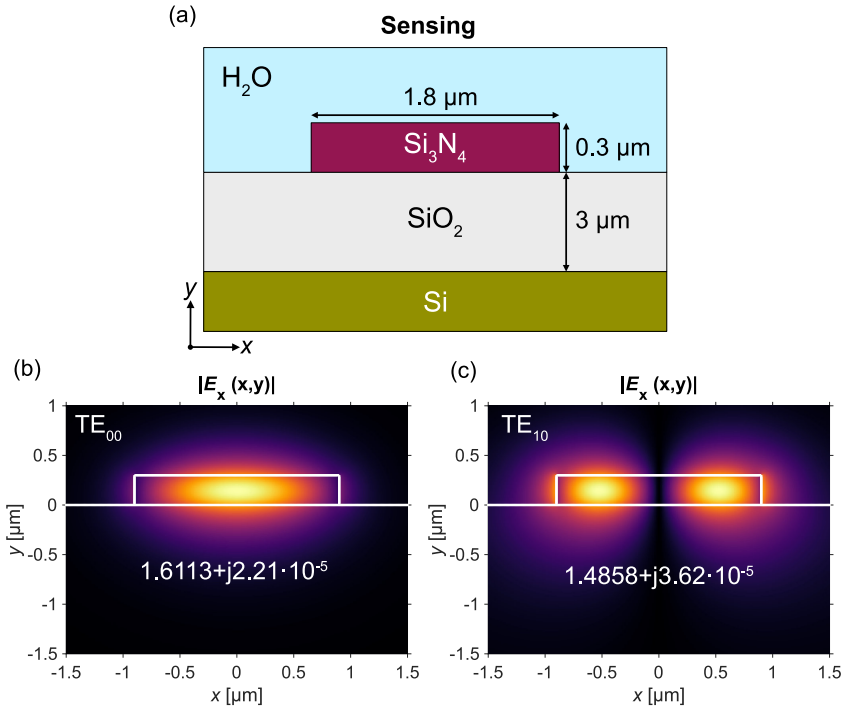

Figure 5.9: (a) Cross section of the bimodal sensing waveguide. Thickness is not to scale. Profile of the (b) fundamental and (c) first high-order TE modes of the waveguide.

Table 5.7: Differential sensitivities to bulk refractive index changes (S_{d}), the thickness of an adsorbed protein layer ($S_{\mathrm{d,surf}}$) and temperature fluctuations ($S_{\mathrm{d,temp}}$).

S_{d} [RIU/RIU]	$S_{\mathrm{d,surf}}$ [RIU/nm]	$S_{\mathrm{d,temp}}$ [RIU/°C]
0.094	$3.67 \cdot 10^{-5}$	$-1.14 \cdot 10^{-5}$

indices can be seen in Figs. 5.9(b)–(c). Here it is worth mentioning that, with these dimensions, if an air cladding is considered, the TE_{10} mode would not be supported, making this design suitable only to measure aqueous solutions. Due to its higher confinement to the waveguide core, the fundamental mode experiences less water absorption losses, and thus its imaginary effective index is smaller. The characteristics of the waveguide are calculated as described in Section 3.1 of Chapter 3.

The confinement factors of each mode, $\Gamma_0 = 0.15$ and $\Gamma_1 = 0.24$ for the fundamental and first high-order modes, respectively, were calculated from the curves in Fig. 5.10(a), resulting in a differential modal sensitivity $S_{\mathrm{d}} = 0.094\,\mathrm{RIU/RIU}$ (Eq. (5.7)). A differential surface sensitivity of $S_{\mathrm{d,surf}} = 3.67{\cdot}10^{-5}\,\mathrm{RIU/nm}$ was obtained from the lineal segments of the curves shown in Fig. 5.10(b). As both modes travel through the same waveguide, they are subject to the same thermal fluctuations, but, due to their different field distributions (Figs. 5.9(b)–(c)), the thermal sensitivities of each mode differ. Specifically, the value of the thermal sensitivity of the fundamental mode is $S_{\mathrm{m0,temp}} = \partial n_{\mathrm{eff,0}}/\partial T = 2.01 \cdot 10^{-5}\,\mathrm{RIU/°C}$, whereas the one of the first high-order is $S_{\mathrm{m1,temp}} = \partial n_{\mathrm{eff,1}}/\partial T = 8.68 \cdot 10^{-6}\,\mathrm{RIU/°C}$, yielding a differential thermal sensitivity $S_{\mathrm{d,temp}} = \partial(n_{\mathrm{eff,1}} - n_{\mathrm{eff,0}})/\partial T = -1.14{\cdot}10^{-5}\,\mathrm{RIU/°C}$, which is two times lower than that obtained for the MZI-based sensor of Chapter 4 (Section 4.3.1). All the calculated differential sensitivities are compiled in Table 5.7.

Being the most weakly guided of the two modes, the TE_{10} is the critical one with regards to losses. Water absorption causes losses $L_{\mathrm{H_2O,0}} = 7.79\,\mathrm{dB\,cm^{-1}}$ and $L_{\mathrm{H_2O,1}} = 12.74\,\mathrm{dB\,cm^{-1}}$, calculated from $k_{\mathrm{eff,0}}$ and $k_{\mathrm{eff,1}}$, respectively. As seen in Fig. 5.10(c), leak-

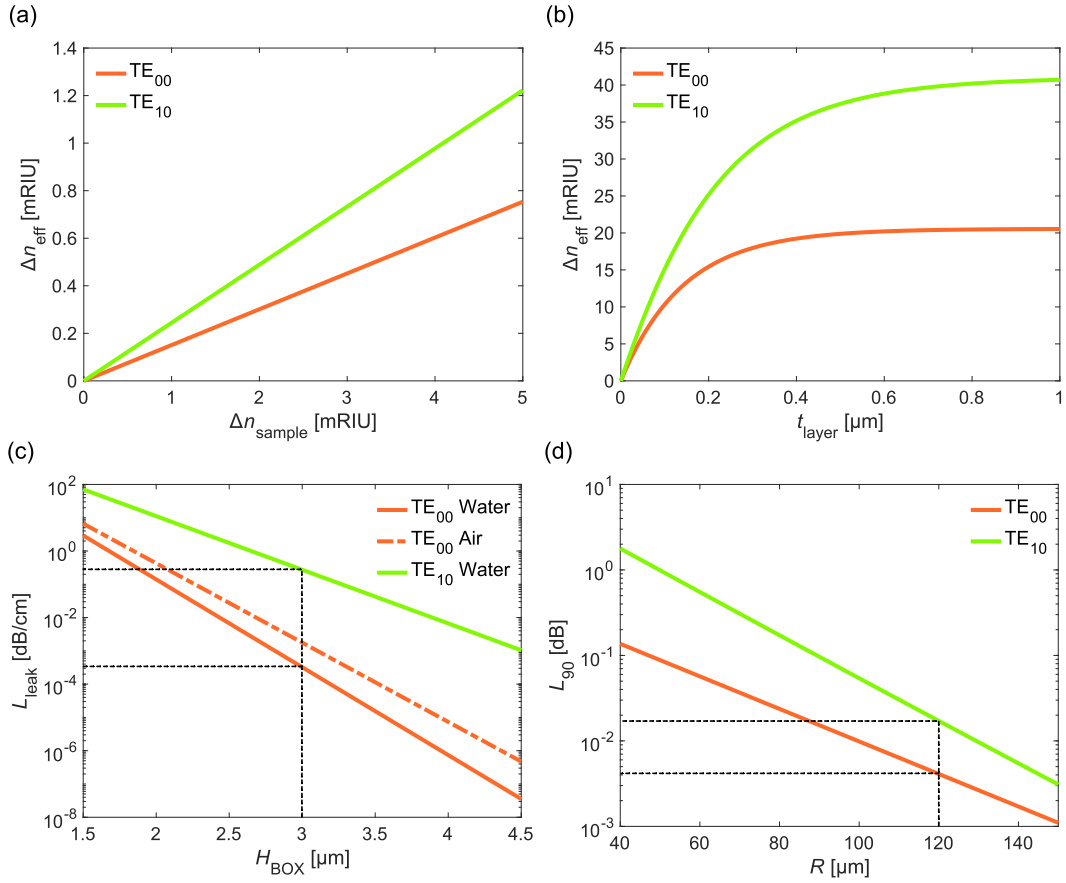

Figure 5.10: Simulation results for the bimodal sensing waveguide. (a) Differential bulk sensitivity. (b) Differential surface sensitivity. (c) Leakage loss. The value obtained for the fundamental mode when waveguides are exposed to air is shown for comparison. The first high-order mode would not be guided in this latter case. (d) Loss per 90-degree bend.

Table 5.8: Propagation losses of two TE modes due to water absorption (L_{H_2O}), leakage (L_{leak}) and curves (L_{90}).

Mode	L_{H_2O} [dB cm^{-1}]	L_{leak} [dB cm^{-1}]	L_{90} [dB]
TE_{00}	7.79	$6.54 \cdot 10^{-4}$	0.0041
TE_{10}	12.74	0.27	0.017

age losses for the TE_{00} mode are negligible, while a reasonable $L_{leak,1} = 0.27\,\text{dB cm}^{-1}$ is obtained for the TE_{10}. Sharp bends in multimode waveguides can be problematic, not only due to radiation and mode mismatch losses, but also due to inter-modal cross-talk. A high bending radius of 120 μm was chosen, for which no cross-talk between the modes occurs. Losses per 90-degree bend as a function of the radius are shown in Fig. 5.10(d). For the chosen radius, they amount to $L_{90,0} = 0.0041$ dB, dominated by transitions losses, and $L_{90,1} = 0.017$ dB, where the contributions of mode mismatch and radiation are comparable. Even though these values are manageable, only two 90-degree curves were implemented in the layout, as it will be seen in Section 5.3.5. Here it is worth reminding that most routing is done using single-mode interconnection waveguides. Table 5.8 includes all calculated loss coefficients.

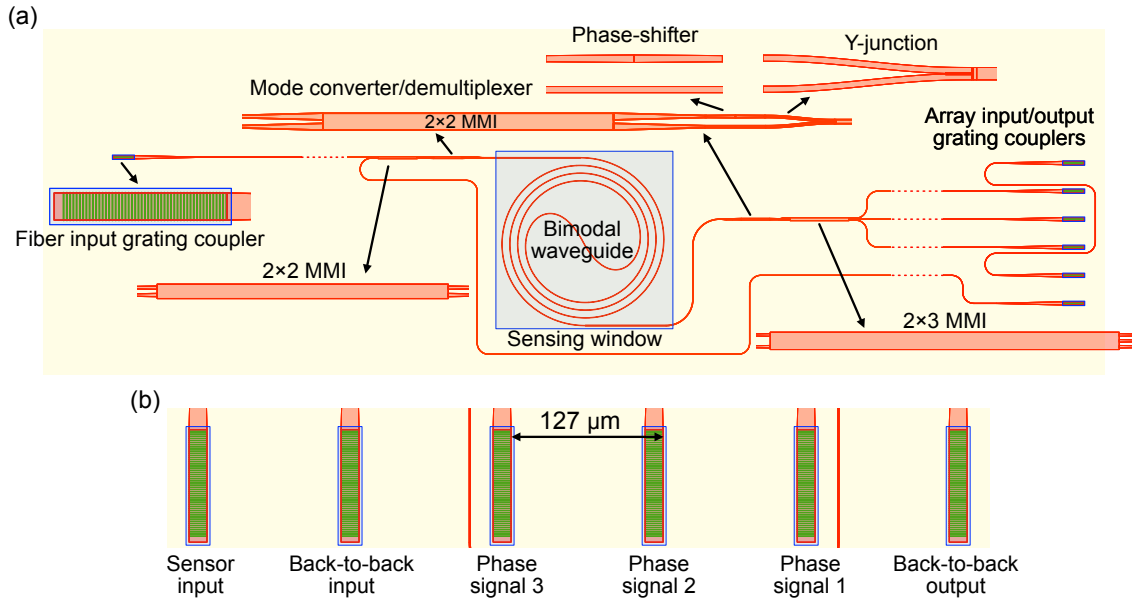

Figure 5.11: (a) Second-generation sensor layout. The most relevant building blocks are zoomed. Long straight sections of interconnecting waveguides have been omitted. (b) Array input/output grating couplers. Interleaving back-to-back gratings minimizes the risk of cross-coupling from the sensor input to their outputs.

5.3.5 Layout of the second-generation sensors

The mask layout of the second-generation sensor is shown in Fig. 5.11(a). When compared to the first implementation (Section 5.3.2), even though the size of the subcomponents is larger due to the lower index-contrast of the SiNOI platform, sensor footprint is roughly the same, as it is conditioned by the separation between grating couplers. As in the complex refractive index sensors (Section 4.3.4, Chapter 4), a 2×2-MMI allows for in-coupling light with a separate optical fiber and out-coupling using the array. The grating coupler of the back-to-back alignment waveguide separates the input from the closest output, which is the phase signal I_3, as can be seen in Fig. 5.11(b).

The designed spiral had a length $L = 7.81\,\text{mm}$, and adjacent waveguides were separated by $35\,\mu\text{m}$, thus avoiding coupling between neighboring modes. With these considerations, the occupied area is only $0.72\,\text{mm}^2$ and the device achieves a sensitivity $S_\text{n} =$

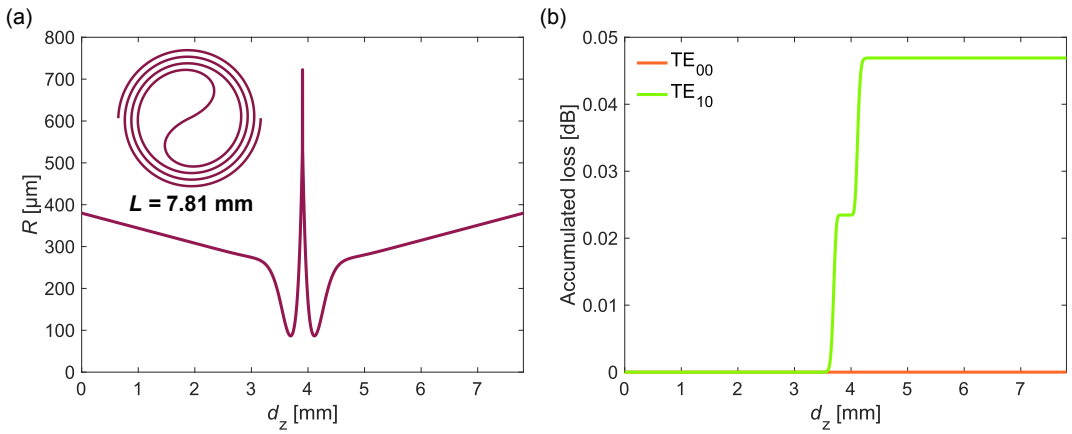

Figure 5.12: Evolution of (a) the bending radius and (b) accumulated radiation loss with propagation distance in the spiral. The fundamental mode exhibits negligible radiation losses.

Table 5.9: Characteristics of the spiral sensing waveguide. The fundamental mode experiences negligible radiation losses.

L [mm]	Area [mm^2]	S_n [rad/RIU]	$L^{tot}_{rad,1}$ [dB]	$L^{tot}_{H_2O,0}$ [dB]	$L^{tot}_{H_2O,1}$ [dB]
7.81	0.72	$2.85 \cdot 10^3$	0.05	6.02	9.95

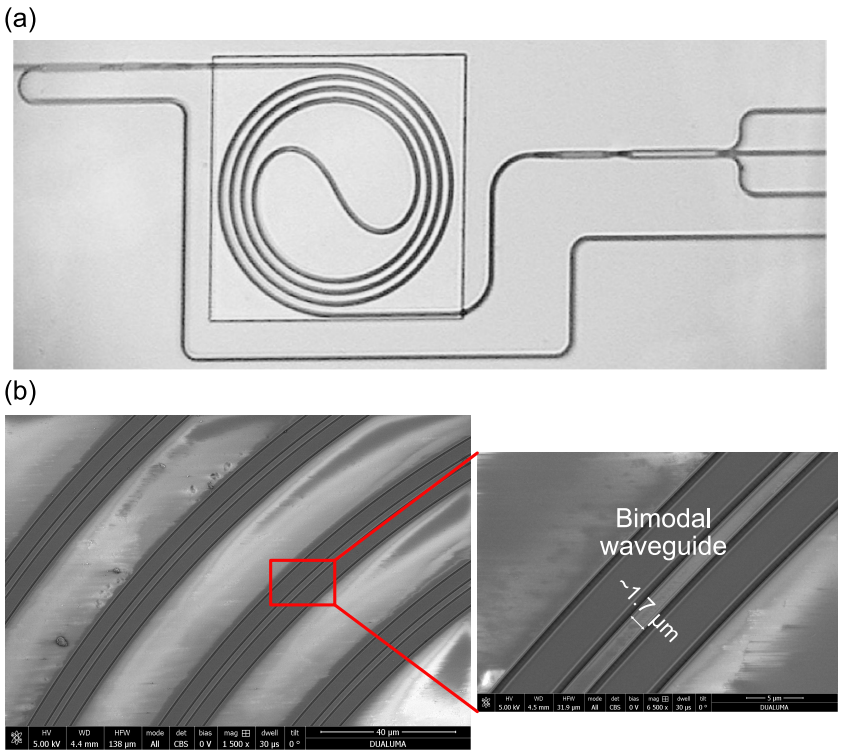

Figure 5.13: (a) Optical microscope picture of the bimodal sensor. (b) SEM images of the bimodal sensing waveguides. A waveguide width around 1.7 µm was measured.

$2.85 \cdot 10^5$ rad/RIU, as indicated in Table 5.9. The variation of the bending radius along the spiral path (d_z) can be observed in Fig. 5.12(a). For the majority of the propagation distance, the radius is kept high, taking values above 240 µm, while a minimum of 86.6 µm, which still guarantees low losses and negligible cross-talk, is reached at the vicinity of the center. The radiation losses accumulated along the spiral path (see Eq. (4.18) of Chapter 4) are shown in Fig. 5.12(b), where it is clear that the fundamental mode suffers virtually no attenuation. The total loss accumulated by the TE_{10} mode ammounts to only $L^{tot}_{rad,1} = 0.05$ dB. Total water-induced absorption, whose value can be found in Table 5.9, is significant for both modes. In this sensor configuration, the optimum interaction length depends on the loss difference, i.e., $L_{opt} \approx [(\Gamma_1 - \Gamma_0)\alpha_{H_2O}]^{-1} \approx 9$ mm. The implemented pathlength was shorter, adopting a more conservative approach to prevent an excessive degradation in performance due to unexpected additional losses. Finally, the thermal sensitivity of the device was calculated as $S_{n,temp} = \partial\Delta\varphi/\partial T = -0.36$ rad/°C.

5.3.6 Optical evaluation of the second-generation sensors

After applying the resist removal protocol (Chapter 3, Section 3.5), chips were imaged both under an optical microscope and a SEM to verify their correct fabrication. An optical image of the sensor body and SEM images of the spiral bimodal waveguides can be seen in Figs. 5.13(a)–(b), respectively. The only deviations observed were a $\sim$ 100 nm overetching of the sensing waveguides, whose width was measured around $W_{MM} = 1.7$ µm,

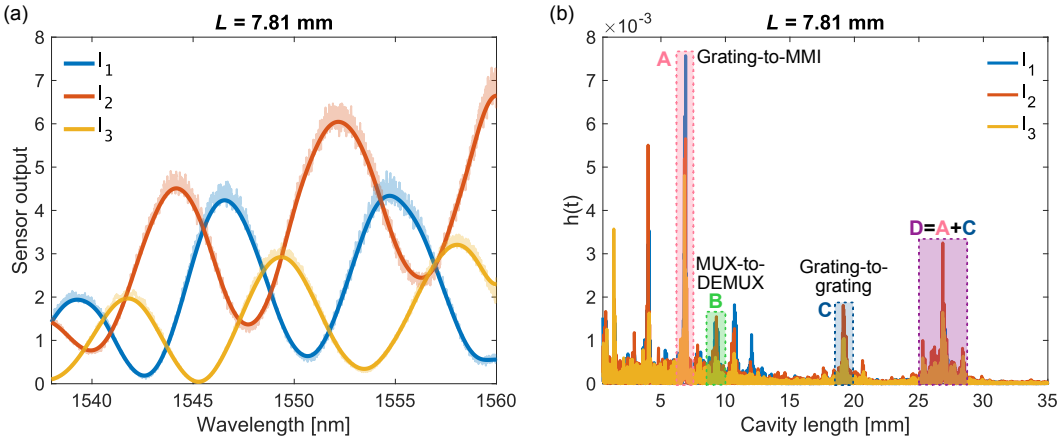

Figure 5.14: (a) Sensor output during a wavelength scan. The oscillations caused by spurious cavities were mitigated by the minimum phase filter. (b) Reflectograms of the three interferometric signals. The origin of some of the most important echoes is indicated.

and the fact that the SWG adaptation teeth of the grating couplers were not etched, as was indicated in Chapter 4 (Section 4.3.5). Back-reflections from the grating couplers were thus expected. The propagation losses of interconnection single-mode waveguides were assumed similar to those included in Table 4.6 (Chapter 4, Section 4.3.3).

To assess the correct operation of the sensor before performing sensing experiments, the wavelength of the source was scanned around λ_0 and the interferometric outputs were recorded. This was done while the sensors were exposed to pure DI water, flowing through the microfluidics channel, to make sure that the TE_{10} mode was guided. The results from one of the measured sensors are shown in Fig. 5.14(a) in soft lines, where the effect of spurious on-chip cavities can be appreciated. To investigate the origin of such cavities, the reflectogram of each signal, shown in Fig. 5.14(b), was generated. The observed echo pattern was equivalent for the three outputs and consistent among sensors from different chips. The origin of some relevant cavities, marked as A, B, C, and D, could be determined. Cavity A is the one created between the output grating coupler and the 2×3-MMI. Cavity B is formed between the two mode converters which embed the sensing waveguide. The fact that this echo is one of the weakest is consistent with the theoretically low reflections obtained by simulations (see Section 5.3.4). The input and output grating couplers originate cavity C. Finally, cavity D likely corresponds to the combination of cavities A and C. Here it is worth noting that no cavity is created between the start and the end of the sensing window. Output signals were filtered by the minimum phase algorithm to remove fringes, as can be appreciated in Fig. 5.14(a) (bright lines). Studying the origin of reflections provides information for further design improvements, but, in practice, reflections are not expected to be problematic for this sensor, as it is meant to be measured always at a fixed wavelength.

The results obtained from this preliminary evaluation, including the high contrast of the interferogram, encouraged performing bulk sensing experiments with these sensors.

5.4 Bulk sensing experiments

Bulk sensing experiments with the laser source operating at a fixed wavelength $\lambda_0 = 1.55\,\mu m$ were performed in the optics and microfluidics setup (Chapter 3, Section 3.3). As in Chapter 4 for the complex refractive index sensors, the low calculated thermal sensitivity did not motivate implementing a thermal control loop at this stage. With the aim of evaluating the sensor in terms of sensitivity, linearity and LOD, sensing experiments

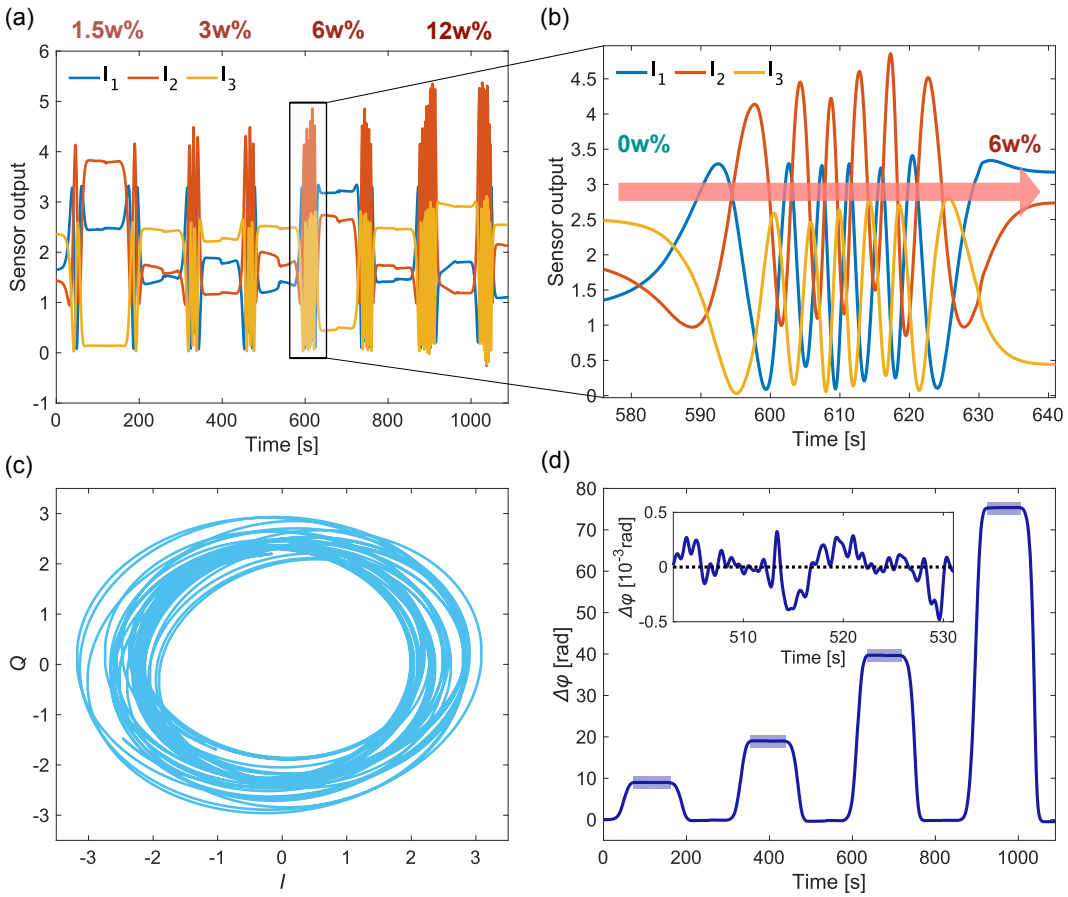

Figure 5.15: (a) Sensor output during a bulk sensing experiment with different NaCl solutions. (b) Close-up of the interferometric signals during the transition from the buffer to a 6w% NaCl sample. (c) Generated complex signal, from which (d) the phase shift is extracted. The areas employed in the calculation of saturation values are highlighted. A representative noise fragment is shown in the inset.

alternating NaCl solutions with a DI water buffer were performed. The pumping speed was kept at a constant rate of 30 µL/min. The refractive index of each prepared sample, with concentrations of 1.5w%, 3w%, 6w% and 12w%, was given in Chapter 4 (Table 4.9, Section 4.4). For the present architecture, only the real part of the index is relevant.

5.4.1 Sensor output

The three outputs of the sensor were recorded during experiments, and low-pass filtered with a bandwidth of 1 Hz to reduce the noise level. Figure 5.15(a) shows the complete record of an experiment, while a fragment corresponding to the transition between the buffer solution and a 6w% sample can be observed in Fig. 5.15(b). The pronounced contrast of the interferograms indicates a correct modal excitation, resulting in highly readable signals. An averaged differential loss around $11.4\,\mathrm{dB\,cm^{-1}}$ between the modes was calculated, a value which is much higher than the $4.9\,\mathrm{dB\,cm^{-1}}$ expected from the simulated difference in water absorption (see Table 5.8). This may indicate that the high-order mode suffers from unconsidered additional attenuation, possibly due to a greater effect of sidewall roughness. It is also possible that the differential confinement factor is higher than designed, as will be further discussed in Section 5.4.2.

The blind calibration algorithm (Chapter 3, Section 3.4) was applied to correct amplitude imbalances and phase deviations, resulting in IQ signals as the exemplary one

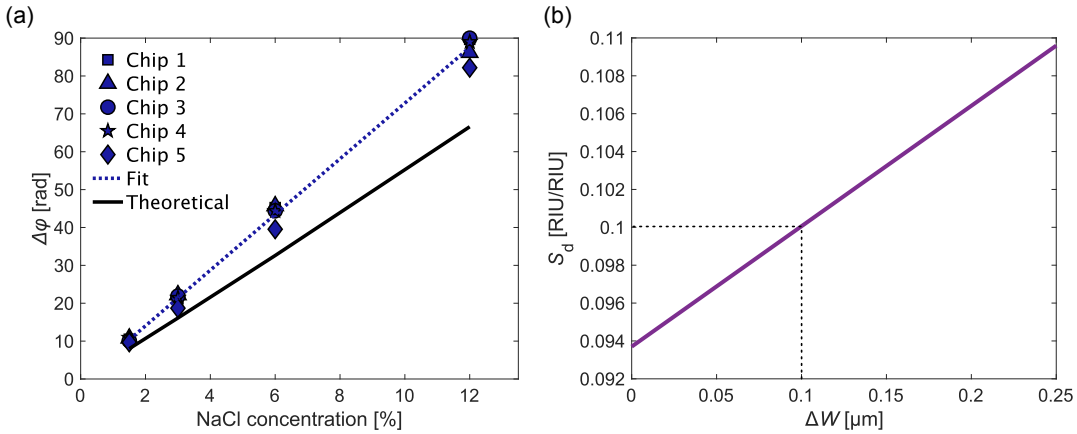

Figure 5.16: (a) Saturation phase shift as a function of NaCl concentration achieved in bulk sensing experiments with sensors from 5 different chips. The theoretically expected response is represented for reference. (b) Simulated evolution of the modal differential sensitivity with an increase in over-etching.

Table 5.10: Sensitivity and limit of detection results of the fixed-wavelength bulk sensing experiments. Abbreviations: standard deviation (Std.), theoretical (Theo.).

Chip	S_n **[rad/w%]**	S_n **[rad/RIU]**	$\sigma_{\Delta\varphi}$ **[rad]**	**LOD [RIU]**
1	7.57	$4.43 \cdot 10^3$	0.0019	$1.29 \cdot 10^{-6}$
2	7.17	$4.19 \cdot 10^3$	0.0002	$1.59 \cdot 10^{-7}$
3	7.59	$4.44 \cdot 10^3$	0.0016	$1.07 \cdot 10^{-6}$
4	7.46	$4.37 \cdot 10^3$	0.0004	$3.01 \cdot 10^{-7}$
5	6.95	$4.07 \cdot 10^3$	0.0032	$2.36 \cdot 10^{-6}$
Mean	**7.35**	$\mathbf{4.30 \cdot 10^3}$	**0.0015**	$\mathbf{1.03 \cdot 10^{-6}}$
Std.	0.28	162.87	0.0012	$8.85 \cdot 10^{-7}$
Theo.	4.87	$3.13 \cdot 10^3$	–	–

shown in Fig. 5.15(c), whose changes in the amplitude are ignored in the read-out. Finally, a phase-shift signal, which linearly follows analyte concentration changes, is unambiguously extracted. As can be observed in Fig. 5.15(d), no baseline-drift correction is required. An additional low-pass filtering step with a bandwidth of 0.2 Hz was applied to $\Delta\varphi$ to further reduce read-out noise.

5.4.2 Results and discussion

Bulk sensitivity

Bulk sensing experiments were performed in sensors from 5 different chips. The saturation values of the retrieved phase shift, calculated as the mean of the fragments highlighted in Fig. 5.15(d), are shown in Fig. 5.16(a) as a function of analyte concentration. All sensors show high linearity, with $R^2 > 0.9986$, and inter-chip variations are small, thus showing that the sensor delivers a consistent measurement. Bulk device sensitivities were calculated with regards to NaCl concentration and refractive index changes, and are presented in Table 5.10. A mean sensitivity $S_n = 4.30 \cdot 10^3$ rad/RIU was obtained, a higher value than the expected $S_{n,theo} = 3.13 \cdot 10^3$ rad/RIU for the designed waveguide. Note that the 770 μm of straight waveguides exposed to the sample (see input and output of the spiral in Fig. 5.11(a)) have been taken into account in the calculation of the total interaction length. This discrepancy can be appreciated in Fig. 5.16(a), where the expected sensor response for each concentration is represented in a black solid line. The experi-

mental results suggest a differential modal sensitivity $S_{\mathrm{d,exp}} = 0.12\,\mathrm{RIU/RIU}$, which is about 31.5% higher than the predicted $S_{\mathrm{d}} = 0.094\,\mathrm{RIU/RIU}$ (Table 5.7). To investigate the origin of such deviation, simulations considering typical fabrication errors were performed. Close attention was paid to the effect of over-etched sensing waveguides, as this is a common consequence of removing the cladding over the sensing areas which was already observed in the SEM evaluation. The evolution of S_{d} with a width difference ΔW, so that $W = 1.8 - \Delta W$ µm, is shown in Fig. 5.16(b). Over-etching beyond 250 nm is not considered because it is not consistent with the observed quality of the fabrication run and, most importantly, the TE_{10} mode would not be guided in such scenario. A value $\Delta W = 100\,\mathrm{nm}$ is consistent with what was appreciated in SEM images (Section 5.3.6), but that alone does not justify the observed increase in sensitivity. Studying additional variations from the nominal design, such as the indices of the waveguide materials, could help further explain the experimental behavior.

Limit of detection

The noise-floor for the determination of the LOD was evaluated over 30-second long fragments of the near-zero sensor response to the water buffer solution. A representative noise fragment, which, just as it happened in Chapter 4 (Section 4.4.3), can be approximated as AWGN, is shown in the inset of Fig. 5.15(d). The calculated standard deviations and the resulting LOD of each measured sensor, expressed in RIU for analyte independence, can be found in Table 5.10. Even though the sensitivity remains similar among different chips, different noise levels determine limits of the detection both in the 10^{-7} and 10^{-6} orders of magnitude, arriving to a mean value $\mathrm{LOD} = 1.03 \cdot 10^{-6}\,\mathrm{RIU}$. This result is competitive with the current state of the art of bimodal integrated sensors. Moreover, contemplating the best results, corresponding to the measurements of Chip 2, yielding a $\mathrm{LOD} = 1.59 \cdot 10^{-7}\,\mathrm{RIU}$, the presented architecture is, to the best of the author's knowledge, the best one reported in the NIR regime, as evidenced in the comparative included in Table 5.11. As can be seen in the table, this remarkably high performance is accompanied by the additional advantages of fixed-wavelength operation, controlled modal excitation and demultiplexing and an inherently linear read-out.

5.5 Conclusions

In this chapter, a refractive index sensor based on a spiral bimodal waveguide, combining a controlled modal excitation and demultiplexing with a coherent phase retrieval was presented. A first generation was implemented in SOI, but was not suitable for sensing due to practical complications derived from the platform and the sensor design. As a consequence, second-generation sensors were fabricated on a SiNOI platform, and the original mode converter and demultiplexer was switched for a robust and well-trusted architecture. The designed spiraled waveguide provided almost lossless propagation and negligible mode crosstalk, achieving a $\sim$8 mm interaction length, limited only by water absorption, while still occupying a small area of $0.7\,\mathrm{mm}^2$. Bulk sensing experiments revealed a high-performance device, reaching top-of-state-of-the-art LODs in the order of 10^{-7} RIU for the best devices. To the best of the author's understanding, this is the best value reported up to date for bimodal interferometers working at NIR wavelengths. These remarkable results are reinforced by the advantages of a fully controlled modal excitation and demultiplexing and a linear and unambiguous read-out, two traits that are often lacking in existent bimodal sensors. This new architecture leverages bimodal sensors to MZI-based solutions, while reducing sensor footprint by half. The implemented sensors are readily applicable to biosensing purposes, and suitable for dense integration in multi-analyte detection platforms.

Table 5.11: Limits of detection of state-of-the-art integrated BI sensors operating in the VIS and NIR regimes. Results from this work are written in bold letters. Abbreviations: height (h.), width (w.), tapered (tap.), mode-engineered (ME), trigonometric (trig.), not determined (n.d.).

Ref.	Regime	Platform	Type	Modal excitation	Read-out	S_n [10^3rad/RIU]	LOD [10^{-7}RIU]
[226]	VIS	SiNOI	Straight	H. discontinuity	Conventional	13	0.5
[231]		SiNOI	Straight	H. discontinuity	Trig. algorithm	17	0.32
[233]	NIR	SOI	Spiral	W. discontinuity	Conventional	1.45	220
[228]		SOI	SWG	W. discontinuity	Spectral	2.27*	200
[229]		SOI	PC	W. discontinuity	Spectral	0.95	66
[232]		SOI	Straight	Tap. w. discontinuity	Coherent	8†	n.d.
[161]		SOI	ME straight	W. discontinuity	Conventional	0.73	244
This work		**SiNOI**	**Spiral**	**Mode converter**	**Coherent**	**4.19**	**1.59**

* Units of 10^3nm/RIU

† Estimated from wavelength scans.

Chapter 6

Mid-infrared thin-film waveguides for absorption spectroscopy

In this chapter, a theoretical study of thin-film waveguides for absorption spectroscopy in the mid-infrared is presented, with the aim of establishing a rigorous design pathway and comparing four representative waveguide platforms under fair conditions. After a brief introduction and review of the state of the art (Section 6.1), a system-level model of a waveguide-based absorption sensor is developed (Section 6.2) and a parametric expression for the limit of detection is derived. Afterwards, sensing waveguides are designed in four widely used platforms for liquid-phase spectroscopy (gallium arsenide, chalcogenide glass, germanium and diamond) and their performance is compared (Section 6.3). The followed design criteria are then summarized as a set of general guidelines (Section 6.4). The chapter ends by emphasizing the main conclusions drawn (Section 6.5).

Most of the work included in this chapter was done during a four-month (2nd May - 31st August 2023) research stay at the University of Ulm (Ulm, Germany) under the supervision of Prof. Boris Mizaikoff. The obtained results have been published in A. Torres-Cubillo, A. Teuber, R. Halir, and B. Mizaikoff, "Optimized waveguides for mid-infrared lab-on-chip systems: A rigorous design approach," Sensors and Actuators A: Physical **378**, 115797 (2024).

6.1 Introduction

In Chapter 2 (Section 2.4), it was explained how molecular absorption fingerprints of chemical compounds, such as gases or amino acids, provide inherent selectivity, without the need of chemically functionalizing the waveguide surface. Waveguide spectroscopic sensors taking advantage of this principle have proven to be powerful analytical tools [235]. Specifically, those working at MIR wavelengths are well suited for the detection of low concentrations of analytes, e.g., CO_2, acetone or taurine, which present unique and strong spectral features in this region [236, 237]. Even though dispersion spectroscopy is emerging as an interesting alternative [141], absorption spectroscopy is by far the dominant technique. This is mostly because, as was explained in Section 2.2.2 (Chapter 2), only a sensing waveguide, without further architectural complexity, is needed to implement an absorption sensor. The Beer-Lambert law can be applied to calculate the absorbance of a sample thank to the interaction of the latter with the evanescent field of guided light.

Among the wide variety of samples subject to be analyzed via waveguide-based spectroscopy, aqueous solutions are of particular interest both in environmental and biomedical applications, because water, besides being a common element of most ecosystems, is the main component of bodily fluids, such as blood, saliva or urine. However, working

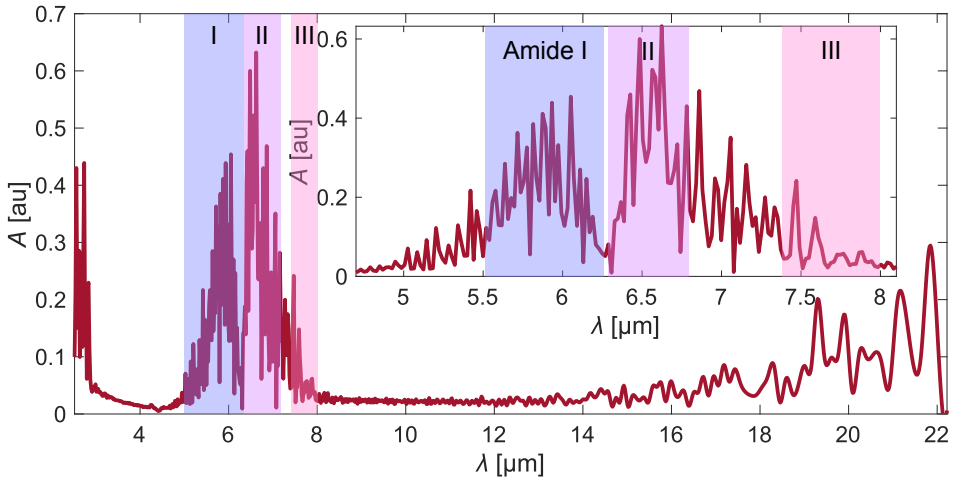

Figure 6.1: Water absorbance spectrum in the mid-infrared. The inset shows the high-absorption region between 5 and 8 μm. Data extracted from [139].

with aqueous samples is especially challenging [238]. In the first place, a certain degree of mechanical robustness is required, as water flow, or even water droplets, can damage fragile structures such as the suspended waveguides often employed in trace-gas detection (see Appendix E). Therefore, solid thin-film waveguides (TFWGs) are preferred, at the expense of a moderate confinement factor, resulting from the fact that the majority of the field travels through the waveguide core. Furthermore, water, whose absorption spectrum is shown in Fig. 6.1, is an exceptional absorbent in the MIR, inducing even higher propagation losses than in the NIR (see Chapters 4 and 5). Moreover, this molecule presents spectral overlaps with some organic components. For example, a fraction of its absorption bands coincide with the Amide I (5.55–6.25 μm), II (5.37–6.8 μm) and III (7.4–85 μm) bands [239], highlighted in Fig. 6.1 and which are essential regions for the analysis of proteins. It is therefore critically important that waveguide-based absorption sensors intended for liquid samples are carefully designed to maximize their performance.

6.1.1 State of the art

Despite the drawbacks associated with the aqueous background, very low LODs have been reported with TFWGs fabricated in different materials [94]. Gallium arsenide slab waveguides achieved a LOD of 56.9 mM for ammonium perchlorate [240]. The surface of a GaAs waveguide was enhanced with gold nanoparticles and was used for direct broadband spectroscopy, achieving a LOD of 3500 ppb of AFB1 mycotoxin [241]. Chalcogenide waveguides combined with paper microfluidics have been demonstrated for absorption spectroscopy, analyzing isopropyl alcohol in water as low as 20% [242]. Ge-Sb-Se waveguides functionalized with a hydrophobic polymer could reach an estimated LOD of 26 ppb of toluene in water [243]. The protein aggregates of a 900 μM bovine serum albumine solution could be precisely distinguished from the spectra provided by a germanium-on-silicon multimode waveguide [167]. A rib GOS waveguide was topped with a mesoporous silica cladding and achieved a LOD of 7 ppm of toluene in water [244]. A 5 μm-thick polycrystalline diamond waveguide on aluminum nitride obtained a LOD of 0.05% for acetone [172]. A diamond TFWG was employed to precisely retrieve the IR signature of caffeine around the 6-μm wavelength [245]. By enhancing the surface of that same waveguide with graphene, taurine concentrations below 0.4w% were detected [142].

Considering this plethora of implementations, designed and validated at different

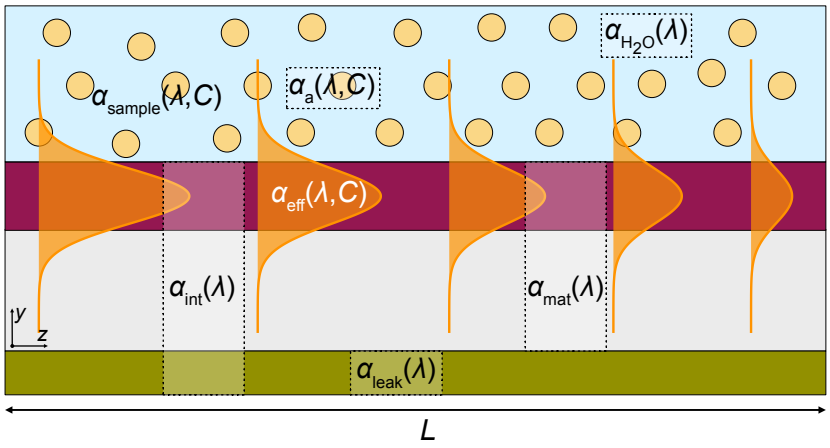

Figure 6.2: Thin-film waveguide exposed to an aqueous solution, composed by a water solvent and a dissolved analyte. Absorption spectroscopy measurements can be performed by monitoring the output intensity. The different sources of modal loss are highlighted.

central wavelengths and for the detection of different analytes, making comparisons between platforms is challenging. Indeed, such a comparative study cannot be found in the literature, even though it would be of great practical interest, as it could lead research efforts toward improved absorption spectroscopy sensors, and, further on, lab-on-chip concepts as those mentioned in Chapter 1 (Section 1.2.3). The aim of this chapter is establishing, for the first time, a fair comparison between four state-of-the-art waveguide platforms. This is performed by rigorously designing optimized waveguide-based absorption sensors in the different materials, with the goal of minimizing the achievable LOD. This seminal work encourages the development of improved MIR absorption sensors for the spectroscopic analysis of liquid samples.

6.2 System-level model

In this section, an absorption spectroscopy system based on a TFWG is analyzed from a system perspective. This brings insight into the factors influencing the limit of detection and enables defining useful metrics for waveguide evaluation.

6.2.1 Sensing waveguide

The generic thin-film waveguide represented in Fig. 6.2 is exposed to a liquid sample, composed of water, acting as a solvent, and an analyte diluted in a concentration C. For small analyte concentrations, the absorption coefficient of the sample can be expressed as

$$\alpha_{\text{sample}}(\lambda, C) = \alpha_{\text{H}_2\text{O}}(\lambda) + \alpha_{\text{a}}(\lambda, C), \tag{6.1}$$

where $\alpha_{\text{H}_2\text{O}}$ is the absorption coefficient of pure water and α_{a} is the additional absorption introduced by the analyte. The relationship between α_{a} and C can be written explicitly by introducing the molar napierian (κ) and decadic (ϵ) absorption coefficients:

$$\alpha_{\text{a}}(\lambda, C) = \kappa(\lambda)C = \frac{\epsilon(\lambda)}{\log_{10}(e)}C. \tag{6.2}$$

As already indicated in Section 2.2.2 of Chapter 2, and considering a constant confinement factor over the operation bandwidth, the loss of the mode propagating through the

waveguide can be expressed as

$$\alpha_{\text{eff}}(\lambda, C) = \alpha_{\text{int}}(\lambda) + \Gamma\alpha_{\text{sample}}(\lambda, C) \approx \underbrace{\underbrace{\alpha_{\text{mat}}(\lambda) + \alpha_{\text{leak}}(\lambda)}_{\alpha_{\text{int}}} + \Gamma\alpha_{\text{H}_2\text{O}}(\lambda)}_{\alpha_{\text{wg}}} + \Gamma\alpha_{\text{a}}(\lambda, C), \quad (6.3)$$

where α_{int} are the intrinsic losses of the waveguide, which can be interpreted as the propagation losses suffered by the mode if lossless water was assumed. In this chapter, intrinsic losses are approximated by the combination of leakage loss (α_{leak}) and absorption by all the waveguide materials (α_{mat}), with the exception of the water cladding. Water absorption losses are considered independently for illustrative purposes. In practice, it is more convenient to express Eq. (6.3) as

$$\alpha_{\text{eff}}(\lambda, C) = \alpha_{\text{wg}}(\lambda) + \Gamma\alpha_{\text{a}}(\lambda, C), \quad (6.4)$$

so that the analyte-independent contribution to modal loss, i.e., the losses of the water-cladded waveguide ($\alpha_{\text{wg}} = \alpha_{\text{int}} + \Gamma\alpha_{\text{H}_2\text{O}}$) can be distinguished from the absorption induced by the analyte itself (α_{a}). Here it is worth recalling that α_{a} is the target quantity to be measured, as it contains the qualitative and quantitative information about the analyte. The output intensity, after light has traveled through a sensing pathlength L, can be expressed as

$$I_{\text{S}}(\lambda, C) = I_{\text{S}}(\lambda, 0)e^{-\Gamma\alpha_{\text{a}}(\lambda, C)L}, \quad (6.5)$$

where the background intensity $I_{\text{S}}(\lambda, 0) \propto e^{-\alpha_{\text{wg}}L}$ corresponds to measurements with pure water. Finally, the absorbance spectrum can be calculated by taking

$$A(\lambda, C) = -\log_{10}\left(\frac{I_{\text{S}}(\lambda, C)}{I_{\text{S}}(\lambda, 0)}\right) = \log_{10}(e)\Gamma\alpha_{\text{a}}(\lambda, C)L \quad (6.6)$$

and the concentration of analyte found as

$$C = \frac{A(\lambda, C)}{\Gamma\epsilon(\lambda)L} \quad (6.7)$$

by using Eq. (2.11) from Chapter 2.

6.2.2 Noise-floor

Spectroscopic measurements, independently on whether the calculated parameter is absorbance, transmittance or any other expression of light attenuation, rely on measurements of I_{S}. In practice, the acquired signal is often a digitized voltage, proportional to the optical power incident on a photodiode, which is in turn proportional to I_{S}. Figure 6.3 shows a typical MIR spectroscopic setup, whose most important components are the laser source, the focusing lenses, the amplified detector, the data acquisition board and the signal processing (DSP) stage, often performed by a computer. The main difference with respect to the NIR setup described in Section 3.3 of Chapter 3 is that edge coupling is used instead of grating coupling. This is typically done to increase the bandwidth of the system. For simplicity, the hypothetical microfluidics system has been omitted and a deposited sample droplet is shown instead. To model the read-out noise introduced by the different components, a noise current is added to the signal photocurrent between the photodiode and the transimpedance amplifier, which are usually integrated on the same device. At that point, the signal photocurrent can be expressed as

$$i_{\text{signal}} = P_{\text{LD}}\text{CE}_{\text{i}}\text{CE}_{\text{o}}Re^{-(\alpha_{\text{wg}}+\Gamma\alpha_{\text{a}})L} = S_0e^{-(\alpha_{\text{wg}}+\Gamma\alpha_{\text{a}})L}, \quad (6.8)$$

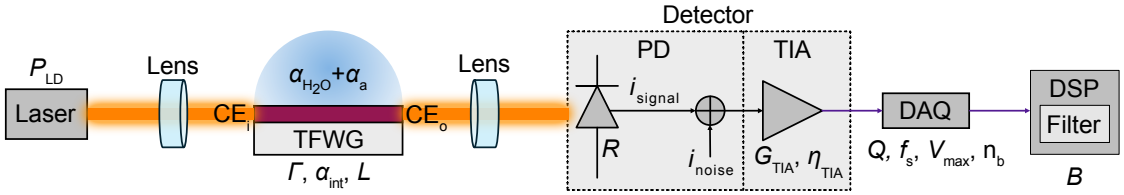

Figure 6.3: Schematic representation of a typical MIR absorption spectroscopy setup. The noise model considers that a noise current is added to the signal photocurrent at the input of the TIA.

where P_{LD} is the output power of the laser, $\mathrm{CE_i}$ and $\mathrm{CE_o}$ are the in- and out-coupling efficiencies, respectively, and R is the responsivity of the photodiode. The constant parameter $S_0 = P_{\mathrm{LD}}\mathrm{CE_i}\mathrm{CE_o}R$ is introduced to simplify notation.

Among the different sources of noise discussed in Section 3.3.1 (Chapter 3), the three considered as the most problematic for this study are shot noise from the photodiode, electrical noise from the amplifier and quantization noise from the DAQ. The expressions of their variances are included in Appendix B and reproduced here for convenience. Shot noise scales with incident power, so that

$$\sigma^2_{\mathrm{shot}} = 2qS_0e^{-(\alpha_{\mathrm{wg}}+\Gamma\alpha_{\mathrm{a}})L}B \overset{\alpha_{\mathrm{wg}} \gg \Gamma\alpha_{\mathrm{a}}}{\approx} 2qS_0e^{-\alpha_{\mathrm{wg}}L}B, \tag{6.9}$$

where $q = 1.6 \cdot 10^{-19}\,\mathrm{C}$ is the electron charge, B is the bandwidth of the filter at the DSP stage and the assumption that $\alpha_{\mathrm{wg}} \gg \Gamma\alpha_{\mathrm{a}}$ generally holds in spectroscopic sensing applications, especially when aqueous solutions are considered. The latter claim will be supported by the results presented in Section 6.3.2. The noise introduced by the TIA can be expressed in terms of its current noise power spectral density (η_{TIA}):

$$\sigma^2_{\mathrm{TIA}} = \eta^2_{\mathrm{TIA}}B. \tag{6.10}$$

Finally, the quantization noise from a DAQ with n_{b} bits, an input voltage range $\pm V_{\mathrm{max}}$ and a sampling frequency f_{s} is given by

$$\sigma^2_{\mathrm{DAQ}} = \frac{1}{G^2_{\mathrm{TIA}}}Q^2(\mathrm{LSB})^2\frac{1}{f_{\mathrm{s}}/2}B, \tag{6.11}$$

where G^2_{TIA} is the transimpedance gain, Q is the quality factor of the DAQ, which ideally takes a value of $12^{-1/2}$, $\mathrm{LSB} = 2V_{\mathrm{max}}/2^{n_{\mathrm{b}}}$ is the least significant bit, and $f_{\mathrm{s}}/2$ is the Nyquist bandwidth [246]. These three noise contributions are considered independent AWGN sources, so they can be added in power, resulting in a total white noise-floor

$$\sigma = \sqrt{\sigma^2_{\mathrm{shot}} + \sigma^2_{\mathrm{TIA}} + \sigma^2_{\mathrm{DAQ}}}. \tag{6.12}$$

6.2.3 Figures of merit

Sensor figures of merit

To define the sensor figures of merit in the described scenario, the analyte absorption and the signal photocurrent are considered as monitored physical parameter and output signal, respectively, i.e., $\xi = \alpha_{\mathrm{a}}$ and $X = i_{\mathrm{signal}}$ (see Chapter 2, Section 2.5). The modal sensitivity coincides with the confinement factor:

$$S_{\mathrm{m}} = \frac{\partial\alpha_{\mathrm{eff}}}{\partial\alpha_{\mathrm{a}}} = \Gamma. \tag{6.13}$$

The architectural sensitivity can be expressed as

$$S_{\mathrm{a}} = \frac{\partial i_{\mathrm{signal}}}{\partial \alpha_{\mathrm{eff}}} = -S_0 L e^{-(\alpha_{\mathrm{wg}}+\Gamma\alpha_{\mathrm{a}})L} \overset{\alpha_{\mathrm{wg}} \gg \Gamma\alpha_{\mathrm{a}}}{\approx} -S_0 L e^{-\alpha_{\mathrm{wg}}L}, \tag{6.14}$$

and the device's sensitivity to changes in α_{a} can be calculated by multiplying S_{m} and S_{a}:

$$S_\alpha = \frac{\partial i_{\mathrm{signal}}}{\partial \alpha_{\mathrm{a}}} = -S_0 \Gamma L e^{-\alpha_{\mathrm{wg}}L}. \tag{6.15}$$

Equation (6.15) indicates the existence of an optimum length, as the result of the trade-off between a larger interaction with the analyte (ΓL) and higher accumulated propagation losses ($e^{-\alpha_{\mathrm{wg}}L}$). The LOD can thus be expressed as

$$\mathrm{LOD} = \frac{3\sigma}{|S_\alpha|} = \frac{3\sigma}{S_0 \Gamma L e^{-\alpha_{\mathrm{wg}}L}} \tag{6.16}$$

and has the units of α_{a}, which is usually in cm^{-1}. The length that minimizes the LOD (and maximizes device sensitivity) can be calculated by optimizing Eq. (6.16), yielding

$$L_{\mathrm{opt}} = \frac{1}{\alpha_{\mathrm{wg}}} = \frac{1}{\alpha_{\mathrm{int}} + \Gamma\alpha_{\mathrm{H_2O}}}. \tag{6.17}$$

Here it is worth mentioning that a similar optimum length was described in [247] for gas sensors. In scenarios dominated by water absorption ($\Gamma\alpha_{\mathrm{H_2O}} \gg \alpha_{\mathrm{int}}$), the optimum length can be approximated to $L_{\mathrm{opt}} \approx (\Gamma\alpha_{\mathrm{H_2O}})^{-1}$, which is the approximation assumed in Chapters 4 and 5 (Eq. (4.19)) to estimate the optimum spiral length.

Waveguide figure of merit

As one of the purposes of this chapter is comparing different waveguide platforms, it is useful to define an additional waveguide figure of merit to evaluate the acknowledged trade-off between modal sensitivity and losses. The proposed figure of merit, similar to that previously derived by Kita et al. [100], is defined as

$$\mathrm{FOM} = \frac{\Gamma}{\alpha_{\mathrm{wg}}} = \frac{\Gamma}{\alpha_{\mathrm{int}} + \Gamma\alpha_{\mathrm{H_2O}}}, \tag{6.18}$$

and measures the ratio between Γ and α_{wg} rather than their absolute values. Henceforth, a high-sensitivity, high-loss waveguide and a low-sensitivity, low-loss waveguide can potentially achieve the same FOM, despite being very different. This simplifies comparisons among a variety of possible designs. When intrinsic waveguide losses can be neglected, $\mathrm{FOM} \approx \alpha_{\mathrm{H_2O}}^{-1}$, which is independent on the waveguide and can be interpreted as the distance at which the power of a plane wave propagating in pure water decays by a factor $1/e$. The smaller the FOM with respect to that limit, the more inefficient the waveguide. Furthermore, the optimum LOD can be expressed in terms of the FOM as

$$\mathrm{LOD}_{\mathrm{opt}} = \mathrm{LOD}(L_{\mathrm{opt}}) = \frac{3\sigma}{\frac{S_0}{e}\mathrm{FOM}}, \tag{6.19}$$

proving that the optimum achievable performance is determined by the FOM.

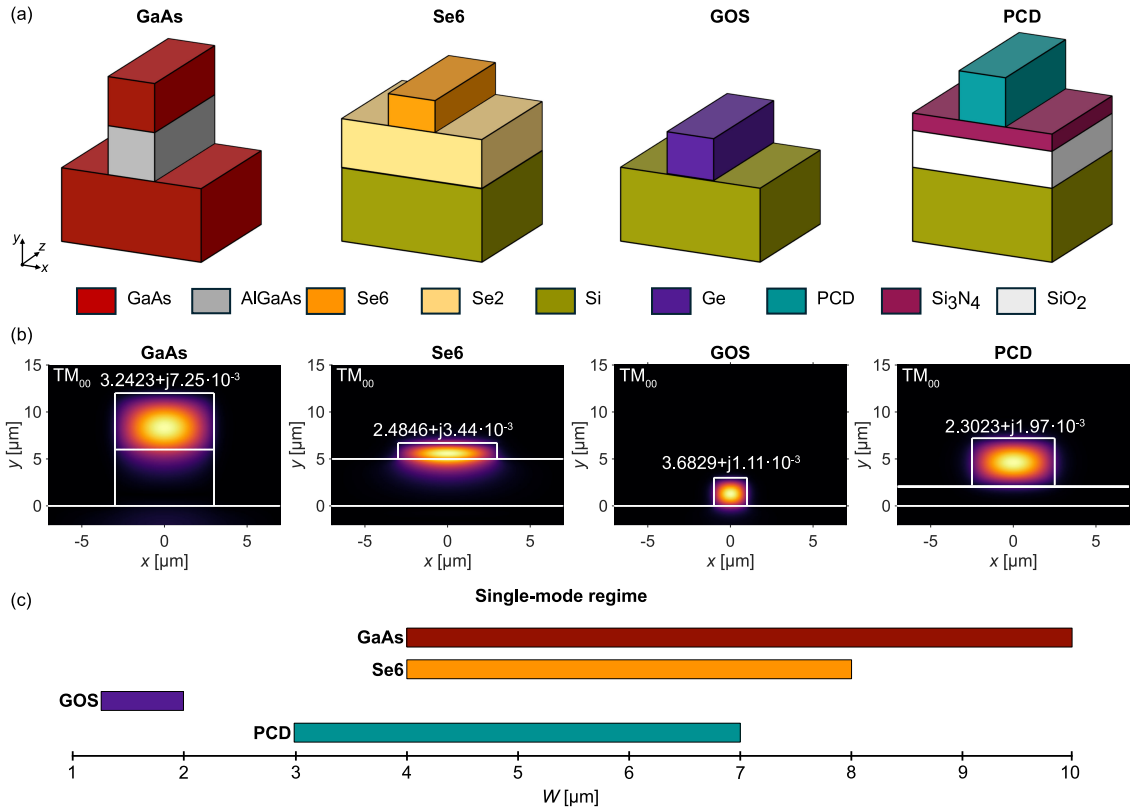

Figure 6.4: (a) Strip waveguides in the platforms under study: GaAs, Se6, GOS and PCD. Waveguide layer thicknesses are not drawn to scale and their actual values are given in Table 6.1. All waveguides incorporate a pure-water cladding which is not represented for visibility. (b) Profiles of the fundamental TM mode of the GaAs ($W = 6\,\mu$m), Se6 ($W = 6\,\mu$m), GOS ($W = 2\,\mu$m) and PCD ($W = 5\,\mu$m) waveguides. (c) Graphical representation of the single-mode width range of each waveguide.

6.3 Comparison between platforms

In this section, four waveguide platforms, which are commonly used among the spectroscopy community [94], are studied. Namely, gallium arsenide (GaAs), chalcogenide glass (specifically Se6), germanium-on-silicon (GOS) and polycrystalline diamond (PCD) are considered. By following a rigorous approach, single-mode sensing waveguides are simulated, designed and compared. The selected operation wavelength is $\lambda_0 = 6\,\mu$m ($1667\,\text{cm}^{-1}$), which has a significant analytical interest, as it falls within the amide vibrational band and is thus employed in the detection of several proteins, such as taurine or BSA. Replicating the following study in a different band would only require adapting the optical properties, i.e., refraction and absorption, of the TFWG materials. TM polarization is studied for maximum compatibility with quantum cascade laser (QCL) sources, potentially integrated with the waveguides. For simplicity and ease of fabrication, fully etched waveguides are considered. A homogeneous design criterion will be followed for all waveguides, thus facilitating the comparative analysis.

6.3.1 Platforms

An overview of the selected platforms can be found in Fig. 6.4(a), where the different strip waveguides are shown. The thickness of each layer and its complex refractive index at $\lambda_0 = 6\,\mu$m are compiled in Table 6.1. Here it is worth noting that water, which is considered as the waveguide upper cladding, and whose optical constants at $\lambda_0 = 6\,\mu$m

Table 6.1: Platform materials, thicknesses and complex refractive indices at $\lambda_0 = 6\,\mu m$. An infinite thickness is considered for the waveguide substrate.

Platform	Layer	Material	Thickness [μm]	n	k
GaAs	Core	GaAs [248, 249]	6	3.3	$4.69 \cdot 10^{-4}$
	Buffer	$Al_{0.2}Ga_{0.8}As$ [248]	6	3.2	$2.40 \cdot 10^{-3}$
	Substrate	GaAs [248, 249]	∞	3.3	$4.69 \cdot 10^{-4}$
Se6	Core	$Ge_{12.5}Sb_{25}Se_{62.5}$ [250]	1.7	2.8	0
	Buffer	$Ge_{28.1}Sb_{6.3}Se_{65.6}$ [250]	5	2.4	0
	Substrate	Si [251]	∞	3.4698	$1.70 \cdot 10^{-6}$
GOS	Core	Ge [252]	3	3.9671	0
	Substrate	Si [251]	∞	3.4698	$1.70 \cdot 10^{-6}$
PCD	Core	PCD [253]	5	2.4214	$5.53 \cdot 10^{-4}$
	Buffer	Si_3N_4 [254]	0.2	2.2236	$3.23 \cdot 10^{-2}$
	Buffer	SiO_2 [254]	2	1.2713	$1.61 \cdot 10^{-3}$
	Substrate	Si [251]	∞	3.4698	$1.70 \cdot 10^{-6}$
All	Cladding	H_2O [255]	3	1.265	0.107

are $n = 1.265, k = 0.107\,(\alpha_{H_2O} = 2241\,cm^{-1})$ [255], absorbs more light than any other of the waveguide materials. A brief description of each platform follows:

Gallium arsenide (GaAs). GaAs/AlGaAs waveguides are composed of a GaAs guiding layer and an AlGaAs buffer layer over a GaAs substrate. The proportions of aluminum and gallium in the AlGaAs alloy can be modified to obtain the desired index contrast. In the present case, $Al_{0.2}Ga_{0.8}As$ is considered [162, 240].

Chalcogenides (Se6). Among the different chalcogenide glasses, GeSbSe thin-films were studied. The waveguide core material is $Ge_{12.5}Sb_{25}Se_{62.5}$ (Se6), while the buffer layer is $Ge_{28.1}Sb_{6.3}Se_{65.6}$ (Se2) [243]. A silicon substrate is employed.

Germanium-on-silicon (GOS). GOS waveguides simply incorporate a germanium guiding layer over a silicon substrate [167]. No buffer is required, as germanium has a higher refractive index than silicon at MIR wavelengths.

Polycrystalline diamond (PCD). The selected diamond waveguide includes a PCD guiding layer, a thin Si_3N_4 additional layer and a SiO_2 buffer over a silicon substrate. The addition of Si_3N_4 between PCD and SiO_2 increments the transmission window of the waveguide [256].

Other conventional MIR platforms, such as silver halides, were discarded for this study because they were unsuitable for working with aqueous solutions due to high instability and hygroscopicity, meaning that water molecules are adsorbed by the material, or because they are difficult to grow as thin films.

6.3.2 Results and discussion

The water-cladded strip waveguides in the selected platforms were modeled and simulated as described in Section 3.1 of Chapter 3. Figure 6.4(b) shows the profile of the fundamental TM mode supported by each waveguide, along with its complex effective index, for a width inside the SM regime. The high values of k_{eff} compared to those typically obtained in NIR strip waveguides (see Chapters 4 and 5) anticipate high propagation losses. The whole single-mode width range of each waveguide is graphically represented in Fig. 6.4(c). Here it is worth noting that the SM regime of GOS waveguides for the

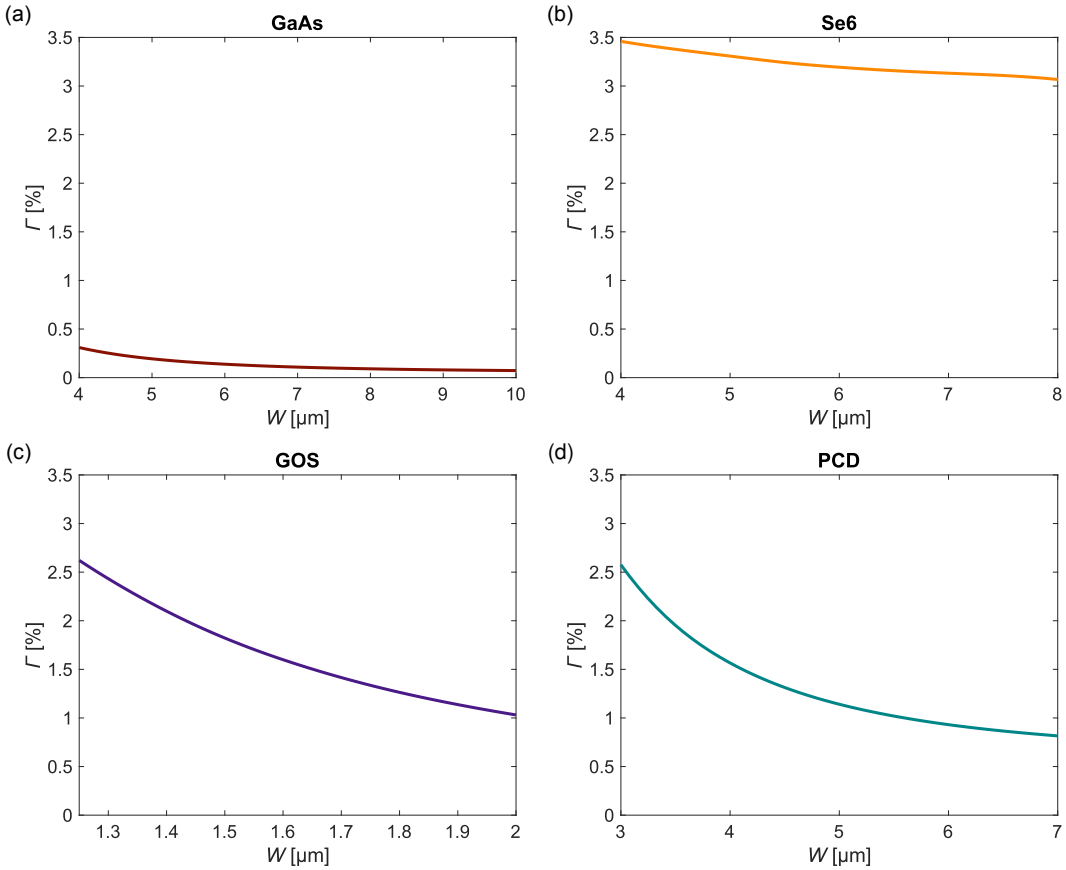

Figure 6.5: Calculated confinement factors of the (a) GaAs, (b) Se6, (c) GOS and (d) PCD waveguides, evaluated in the single-mode regime.

TM polarization is very narrow and these widths result in high aspect-ratio waveguides, considering that, as indicated in Table 6.1, the guiding layer is 3 μm-thick.

Confinement factor

The confinement factor of each waveguide was evaluated over the SM regime. As this study is focused on absorption sensors, it was calculated as $\Gamma = \partial k_{\text{eff}}/\partial k_{\text{sample}}$. The results, expressed in % for better legibility, are shown in Fig. 6.5. The fact that Γ decays with an increased width in a quasi-exponential manner is consistent with a greater mode confinement in the waveguide core. GaAs waveguides exhibit a confinement factor one order of magnitude below the remaining platforms, due to the combination of a high index contrast and a thick guiding layer. The values for the other three TFWGs are still moderate, in the range of 1–3.5%. The Se6 platform achieves a slightly higher Γ than the rest, with a small variation along the SM range, while GOS and PCD waveguides yield very similar results.

Propagation loss

As defined in Eq. (6.3), the total propagation losses of the waveguide mode is the result of adding the intrinsic loss of the waveguide (α_{int}) to water absorption ($\Gamma\alpha_{H_2O}$). The sources of intrinsic loss considered in this study are leakage to a higher-index substrate (α_{leak}) and light absorption by the platform materials (α_{mat}), so that

$$\alpha_{\text{int}} = \alpha_{\text{leak}} + \alpha_{\text{mat}}. \tag{6.20}$$

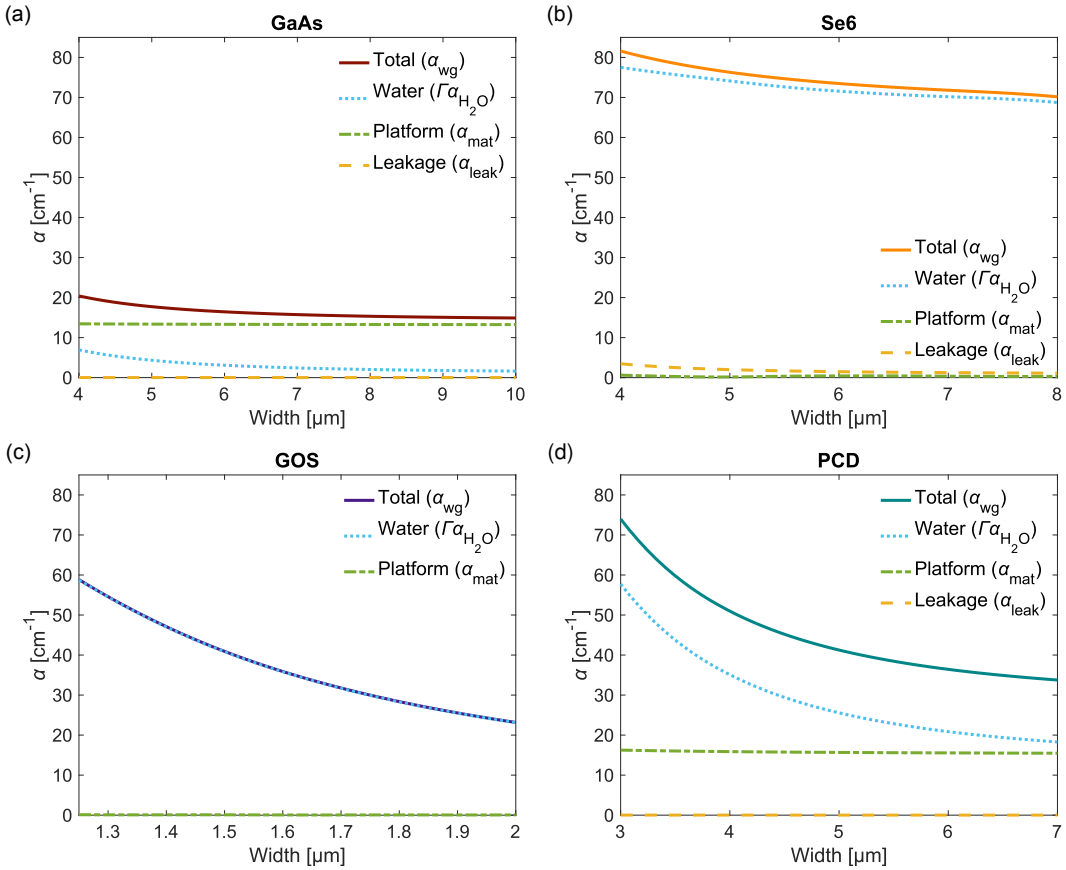

Figure 6.6: Propagation loss in the (a) GaAs, (b) Se6, (c) GOS and (d) PCD waveguides, evaluated in the single-mode regime. The contributions of the different loss sources are shown separately.

As seen in Section 2.2.1 of Chapter 2, α_{mat} can be calculated as

$$\alpha_{\text{mat}} = \sum_i \Gamma_i \alpha_i, \tag{6.21}$$

where Γ_i and α_i are the confinement factor in and the absorption coefficient of the i-th layer of the waveguide, respectively, excluding the water cladding. The contribution of scattering loss due to sidewall roughness, which is caused by defects derived from the fabrication process, is not considered here. According to the Payne-Lacey model, said coefficient is inversely proportional to the cubed wavelength [257] and can hence be disregarded in the MIR regime. In Fig. 6.6, the total waveguide loss (α_{wg}) for each TFWG platform is presented and the contributions of water absorption ($\Gamma\alpha_{\text{H}_2\text{O}}$), leakage ($\alpha_{\text{leak}}$), and material absorption (α_{mat}) are individually shown. The value and evolution of Γ (Fig. 6.5) conditions the impact of water absorption, thus affecting overall losses. For this reason, GaAs waveguides, which are the least sensitive, suffer the lowest propagation loss. Water absorption dominates in Se6, GOS and PCD waveguides. While the remaining loss contributions can be neglected in the Se6 and GOS platforms, in PCD TFWGs water and material absorption losses become comparable with an increase in width, due to a higher mode overlap with the Si_3N_4 and SiO_2 layers. In GaAs waveguides, absorption by the materials is more important than that from water, mostly because of the high losses of the thick AlGaAs buffer layer (Table 6.1), into which, as seen in Fig. 6.4(b), a significant fraction of the field extends. Leakage is not problematic, and null for the GOS platform, as there is no higher-index substrate. The variation α_{leak} with waveguide width is minimal when the TM polarization is considered.

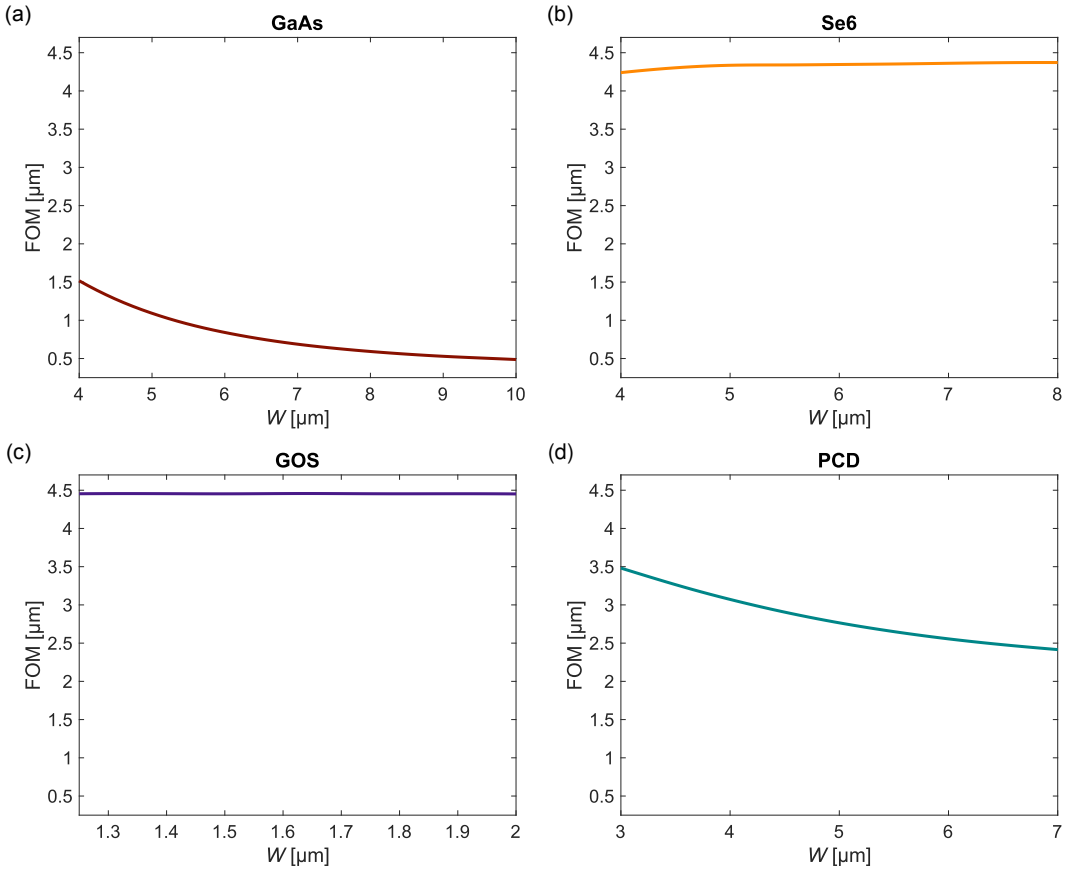

Figure 6.7: Figure of merit of the (a) GaAs, (b) Se6, (c) GOS and (d) PCD waveguides, evaluated in the single-mode regime.

Waveguide figure of merit

The FOM defined in Eq. (6.18) was evaluated for the different TFWG implementations, obtaining the results shown in Fig. 6.7. Here it is worth reminding that, as observed in Figs. 6.5 and 6.6, with an increase in width the mode is further confined to the waveguide core, and, therefore, Γ decreases, and so does the influence of water absorption. In GaAs and PCD waveguides, however, a higher mode confinement also results in significantly enlarged material absorption losses. As a consequence, their FOM quasi-exponentially decays with waveguide width. On the other side, in GOS waveguides, sensitivity and total loss are almost perfectly balanced, so the approximation FOM $\approx \alpha_{H_2O}^{-1}$ holds, and the FOM is nearly constant with a value FOM $\approx 4.46\,\mu$m. Such a value is indeed the upper limit of this metric, as indicated in Section 6.2.3. The same approximation reasonably agrees with Se6 waveguides as well, but, in this case, a slight improvement of the FOM with width is observed. This is due to lower loss induced by leakage to and absorption from the silicon substrate.

Limit of detection

As a fixed waveguide width has to be selected for the evaluation of the LOD, the center of the SM regime was chosen as a compromise solution, given the observed sensitivity-loss trade-off. This criterion was preferred over FOM optimization because following the latter would imply a width in the lower end of the SM regime for GaAs and PCD waveguides. Doing so would result in a challenging aspect ratio for the fabrication and a risk of the mode not being guided if waveguides are over-etched and the fabricated waveguide is

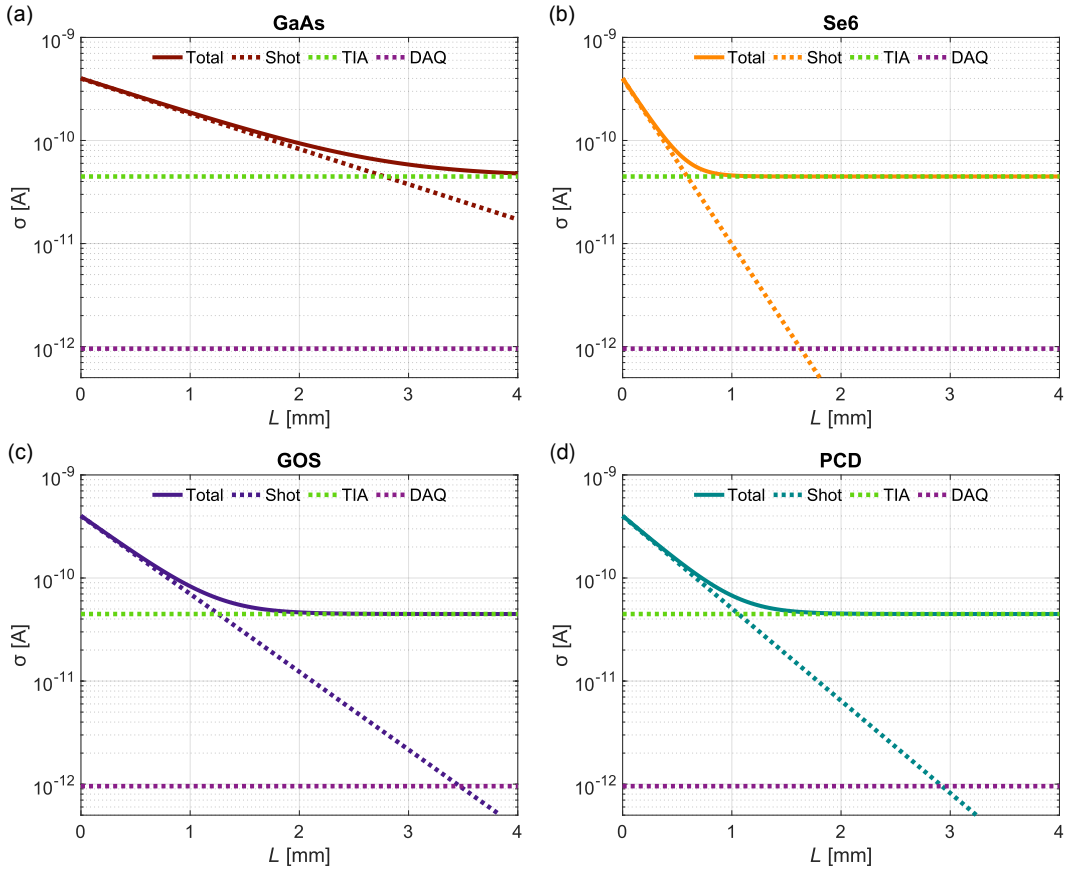

Figure 6.8: Noise-floor of the spectroscopic system incorporating a (a) GaAs, (b) Se6, (c) GOS or (d) PCD waveguide. The different contributions to the total noise level are represented in dotted lines.

finally narrower than the nominal design. The trade-off width was thus considered a safer choice, and enabled applying a homogeneous rule to all platforms, as was initially desired. Table 6.2 includes the chosen widths and their associated performance metrics.

To achieve a realistic estimation of the LOD of a spectroscopic system incorporating each TFWG, the noise-floor of the setup from Fig. 6.3 was calculated according to the parameters from Table 6.3, which are compatible with a MIRcat 2100 QCL source (DRS Daylight Solutions, USA), a PVI-4TE-10.6/MIP-10-1M-F-M4 amplified detector (Vigo System S.A., Poland) and a NI USB-6002 data acquisition board (National Instruments Corp., USA). These components are typical in MIR spectroscopic setups found in literature [258]. The values of the coupling efficiencies, CE $= -2$ dB, were set based on experience. Figure 6.8 shows the calculated noise-floor for the different TFWGs as a function of interaction length. The individual contributions of shot (σ_{shot}), TIA (σ_{TIA}) and DAQ (σ_{DAQ}) noise have also been represented. While TIA and DAQ noise remain constant, shot noise de-

Table 6.2: Selected waveguide widths for the different platforms and associated performance metrics.

Platform	W **[µm]**	Γ **[%]**	α_{wg} **[cm^{-1}]**	**FOM [µm]**
GaAs	7	0.11	15.75	0.69
Se6	5.75	3.22	74.05	4.34
GOS	1.62	1.55	34.79	4.46
PCD	5	1.14	41.26	2.77

Table 6.3: System configuration considered in the evaluation of the LOD.

Component	Parameter	Value
LD	P_{LD}	500 mW
TFWG	$\mathrm{CE_o}$	-2 dB
	$\mathrm{CE_i}$	-2 dB
PD	R	0.5 A/W
TIA	G_{TIA}	$2 \cdot 10^6$ V/A
	η_{TIA}	0.02 nA/Hz$^{1/2}$
DAQ	Q	0.7
	V_{max}	10 V
	n_{b}	16
	f_{s}	125 kHz
DSP	B	1 Hz

Table 6.4: Estimated optimum sensing pathlength and achieved LOD for the different evaluated platforms.

Platform	L_{opt} [mm]	$\mathrm{LOD_{opt}}$ [10^{-5}cm^{-1}]
GaAs	1.18	11.1
Se6	0.25	1.75
GOS	0.54	1.51
PCD	0.45	2.75

pends on each platform and decreases with L, i.e., as the output signal gets weaker. In the selected configuration, shot noise dominates for shorter pathlengths, until reaching a point where TIA noise becomes higher. Afterwards, the noise-floor is essentially flat, taking a value $\sigma_{\mathrm{tot}} \approx \sigma_{\mathrm{TIA}}$.

The LOD was evaluated (Eq. (6.16)), yielding the results shown in Fig. 6.9(a). As it was anticipated in Section 6.2.3, there is an optimum interaction length for every configuration, determined by the propagation loss of each waveguide (Eq. (6.17)). These lenghts can be found in Table 6.4 together with the optimum LOD. For Se6, GOS and PCD waveguides, L_{opt} is sub-millimetric. As $\mathrm{LOD_{opt}}$ is governed by the FOM (Eq. (6.19)), the obtained results are consistent with those from Table 6.2, this is, the higher the FOM, the lower (better) the optimum LOD. According to Fig. 6.8, at the optimum length the performance of all sensors is limited by shot noise, which is desirable. Se6 and GOS waveguides achieve virtually the same FOM, and, as a consequence, their $\mathrm{LOD_{opt}}$ is almost identical, with GOS waveguides showing a slightly better result. However, the performance of the Se6 platform quickly degrades with the increase in L, due to its high propagation losses (see Table 6.3), which are mostly induced by water. GaAs waveguides reach an optimum LOD one order of magnitude higher (worse), than their counterparts, as the consequence of exhibiting the worst FOM. Nevertheless, their comparatively low losses make this option more tolerant to the sensing pathlength. In fact, if for practical reasons the interaction length has to exceed 1.8 mm, then the GaAs platform would be the best choice. PCD waveguides stand out as an intermediate solution, with an optimum LOD in the order of magnitude of that of Se6 and GOS waveguides, albeit slightly worse, and a similar tolerance to the sensing length than GOS, as both implementations show similar total losses. Here it is worth recalling that, while the origin of such losses is mostly water absorption for GOS waveguides, in PCD ones there is a significant contribution from absorption by the platform materials (see Fig. 6.6(d)).

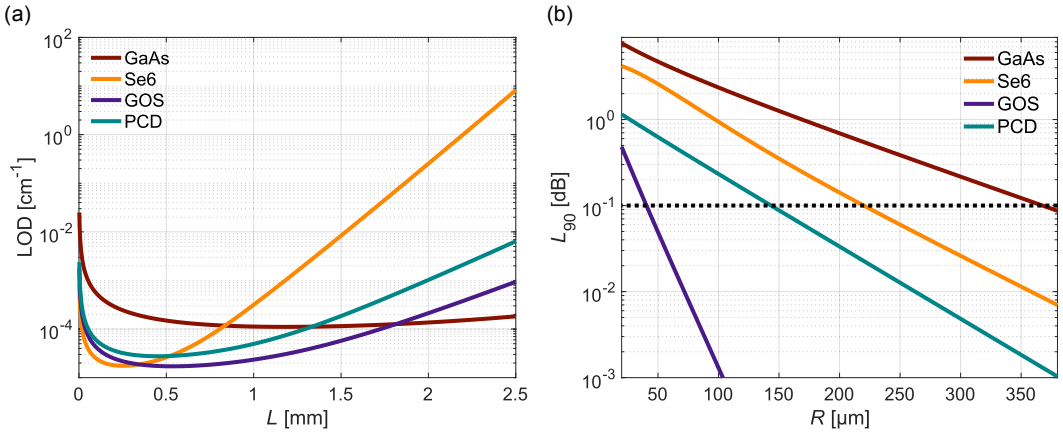

Figure 6.9: (a) LOD achieved by the evaluated platforms under the assumed experimental conditions. For each waveguide there is an optimum interaction length. (b) Losses per 90°-bend in the different waveguides as a function of the radius.

Table 6.5: Bent radii yielding 90-degree losses below 0.1 dB for the different platforms. The contributions of radiation and transition losses are specified.

Platform	R [µm]	L_{rad} [dB]	L_{trans} [dB]
GaAs	369.1	0	0.05
Se6	221.2	0.003	0.05
GOS	40.5	0.004	0.04
PCD	144.4	0	0.05

Bending loss

Even though the obtained optimum interaction pathlengths can be implemented with straight waveguides, bends may be necessary for on-chip routing and the implementation of more complex sensing architectures. Losses per 90-degree bend were evaluated (Section 3.1.4, Chapter 3) as a function of bending radius and are shown in Fig. 6.9(b). The minimum radius to guarantee $L_{90} < 0.1$ dB for each platform can be found in Table 6.5, where the different contributions of pure radiation and mode mismatch losses are specified. Transition losses are the dominant loss source in all the study cases, and must therefore be handled by carefully optimizing the bend geometry [259] or implementing Euler bends [260]. GaAs waveguides are a paramount example, as they exhibit the worst radii, even though radiation losses are null. As was to be expected due to their smaller dimensions and superior index contrast, the GOS platform achieves the most compact curves, thus making it especially attractive for densely integrated photonic circuits. While moderately small bends could be theoretically implemented with PCD waveguides, even more if mismatch losses are managed, the fabrication of bent diamond TFWGs remains challenging up to date and must be performed by costly and complicated techniques [261, 262]. The Se6 platform offers an intermediate solution between their GaAs and GOS counterparts.

6.4 General design guidelines

A systematic waveguide design approach was followed throughout this chapter, with the aim of minimizing the LOD defined in Eq. (6.16). Said approach is summarized in the following guidelines, which are general and can be applied to any specific waveguide configuration to achieve optimum performance:

1. Model the desired TFWG platform at the selected working wavelength in a suitable mode solver. Determine the width range that yields single-mode operation and evaluate the confinement factor (Eq. (3.2), Chapter 3), losses (Eq. (6.3)) and FOM (Eq. (6.18)) in said range.

2. Select a waveguide width based on a criterion such as sensitivity-loss trade-off, FOM optimization or fabrication constrains.

3. Identify the critical noise sources and estimate the noise-floor (Eq. (6.12)) of the spectroscopic system, including the modeled waveguide as a transducer element. Note that, when shot noise is significant, it must be calculated on a waveguide-specific basis, as it depends on propagation losses (α_{wg}).

4. Evaluate the LOD (Eq. (6.16)) as a function of the interaction pathlength, using the calculated confinement factor, losses and noise-floor.

5. Select the waveguide length that minimizes the LOD. If the outcome is not practically suitable, consider using a different width (step 2) or further optimization of the TFWG geometry.

6. Evaluate the impact of additional implementation aspects, such as bent sections, in the designed waveguide. Make adjustments if needed.

In these guidelines, waveguide width and length are considered the only degrees of freedom in the design, but the process can be easily extended to more complex geometries, such as rib or slot waveguides, by repeating steps 1 and 2 for each additional parameter.

6.5 Conclusions

In this chapter, a rigorous waveguide design approach oriented toward MIR absorption spectroscopic sensors operating with aqueous solutions has been developed, arising from the fundamental study of the achievable limit of detection. The existence of an optimum interaction length has been analytically shown. A waveguide figure of merit has been used to evaluate the observed trade-off between sensitivity and losses, demonstrating that this FOM, which can be shared by waveguides with very different characteristics, determines the optimum achievable LOD (see Eq. (6.19)).

The established design work-flow has been applied to compare, for the first time, four state-of-the-art TFWG platforms (GaAs, Se6, GOS and PCD) under fair conditions. The estimated LOD of each waveguide has been analyzed in terms of optimum performance and tolerance to the sensing pathlength. Specifically, GaAs waveguides were shown to exhibit the worst FOM, mostly due to a lower confinement factor. However, the smaller impact of water absorption makes this architecture the most suitable for implementing long interaction pathlenghts, which may be of practical interest. Chalcogenide waveguides achieve the highest confinement factor and, therefore, the highest water-induced losses. Their high FOM leads to a good LOD, but their performance quickly degrades for beyond-optimal interaction lengths, making these waveguides vulnerable to deviations from the design set-point. GOS provides a nearly perfect balance between sensitivity and losses, reaching the highest possible FOM ($\sim \alpha_{\mathrm{H_2O}}^{-1}$) and the best optimum LOD. However, due to the high index contrast of the platform, single-mode waveguides for the TM polarization have a high aspect ratio which can make them fragile. A good FOM can be obtained with PCD waveguides, but they are limited by absorption in the silica lower cladding. Their performance is similar to GOS in terms of LOD, but mass production of such waveguides is not yet consolidated.

This systematic study, which can be easily extended to different platforms and operation wavelengths, paves the way toward the development of next-generation MIR sensors, ready for integration into lab-on-chip sensing concepts. With the help of these devices, rapid advances in fields such as clinical diagnosis, water quality monitoring and food safety are expected.

Chapter 7

Conclusions and prospects

In this final chapter, the most important challenges and achievements of this thesis are summarized (Section 7.1) and further research activities to continue with this work are suggested (Section 7.2).

7.1 Conclusions

This thesis has contributed to the advance toward improved near-infrared interferometric-based sensing architectures (Sections 7.1.1 and 7.1.2) and optimized waveguides for mid-infrared absorption spectroscopy (Section 7.1.3).

7.1.1 Near-infrared complex refractive index sensor

In Chapter 4, the interest of complex refractive index sensors as tools for complete sample characterization, which could potentially leverage the specificity of absorption sensing with the sensitivity of refraction sensing, was evidenced. Despite this interest, very few implementations of such sensors can be found in the field of integrated photonics, where they could find applications in areas such as space exploration or VOC detection. Here, a MZI-based sensor which simultaneously provides a coherent phase read-out and absorbance measurements has been proposed to prove this sensing concept.

The first generation of such sensors was designed for NIR wavelengths and implemented in Cornerstone's SiNOI platform. After initial optical evaluations, these sensors were discarded, mostly due to excessive propagation losses in the sensing waveguides and a strong reflection pattern, with unclear origin, affecting the sensing path. These chips were also taken abroad to the UiT The Arctic University of Norway to perform gas detection experiments during a four-month research stay (see Appendix D). Even though the gas spectroscopy measurements were unsuccessful, changing the setup to one with a camera read-out deeply helped identifying problems arising from the fiber array used in Málaga. Second-generation sensors were designed, incorporating improvements such as SWG adaptation teeth in the grating couplers to minimize reflections and a modified layout to avoid input-to-output masking and the formation of Fabry-Pérot cavities. The adaptation teeth were not successfully etched in the fabrication process but, even so, on-chip reflections were better controlled than in the previous generation. Moreover, the fabricated sensing waveguides exhibited the expected propagation losses and no additional degradation was observed. However, while input-to-output masking was solved, inter-output cross-talk between one of the interferometric outputs and the sensing intensity signal precluded precise absorbance measurements by creating strong fringes. An analytical model was developed and employed to mitigate the effect of this cross-talk, thus improving the quality of the calculated absorbance.

Bulk sensing experiments using NaCl dissolved in deionized water were performed at the fixed wavelength $\lambda_0 = 1.55\,\mu$m. The limits of detection obtained, in the order of 10^{-6} RIU, are among the best of the state of the art of complex refractive index sensors. In fact, both parts of the index had never been detected simultaneously with such a low LOD ($\text{LOD}_\text{n} = 1.9 \cdot 10^{-6}$ RIU, $\text{LOD}_\text{k} = 2.1 \cdot 10^{-6}$ RIU), to the best of the author's knowledge. Exploratory spectroscopic measurements were carried out using pure IPA and water samples, as well as NaCl-water mixtures, showing promising results. Further experimental verification and structural improvements should be carried out for an accurate evaluation of the architecture as a simultaneous spectroscopic absorption and dispersion sensor. The main results associated with this contribution are published in [89].

7.1.2 Near-infrared bimodal refractive index sensor

Interferometric refractive index sensors based on bimodal waveguides were proposed in Chapter 5 to achieve results equivalent to those obtained with MZIs, but occupying roughly half the footprint by eliminating the need of a reference arm. However, conventional bimodal sensors suffer from spurious effects arising from an uncontrolled high-order mode excitation, which is typically performed by an abrupt discontinuity in either the width or the height of the waveguide, and the challenges associated with reading-out a sinusoidal interferometric output, i.e., sensitivity fading and directional ambiguity. As an answer to these problems, a NIR bimodal sensor combining a spiral bimodal waveguide with a controlled modal excitation and a coherent phase read-out has been developed.

First-generation sensors were designed at $\lambda_0 = 1.31\,\mu$m for the SOI platform provided by Applied Nanotools, incorporating a mode converter based on mode evolution in a counter-tapered coupler. Unfortunately, these chips turned out unsuitable for sensing experiments. In the first place, the designed mode-conversion scheme did not work properly, impeding a correct phase extraction. Furthermore, SOI waveguides resulted fragile and many of them collapsed due to the mechanical stress provoked by the sonication steps of the standard cleaning protocol. Last, silicon surfaces reacted to HCl when it was used as an analyte, generating residual depositions and irreversible damage to the waveguides. To overcome these limitations, the second generation of sensors was designed for Cornerstone's SiNOI platform, allowing for larger waveguide sizes and improved mechanical robustness. In addition to incorporating the preventive measurements against reflections and signal masking included in the complex refractive index sensors, the initial mode converter was changed for a well-trusted architecture based on a MMI, a phase shifter and a Y-junction. Additionally, the bimodal sensing spiral, with $L = 7.81\,$mm and supporting the first two TE modes, was carefully designed to avoid excessive losses.

After successful initial validations, bulk sensing experiments at $\lambda_0 = 1.55\,\mu$m using NaCl-water samples were conducted to evaluate the sensing performance of the architecture. The achieved LODs are comparable to those obtained with MZI configurations. Moreover, the best measured sensor, with a $\text{LOD} = 1.59 \cdot 10^{-7}$ RIU, features the highest performance reported, as far as the author can tell, for a bimodal sensor operating at NIR wavelengths. This is the first time that the combination of a bimodal waveguide, controlled modal excitation and coherent read-out was demonstrated with sensing experiments. This contribution is published in [93].

7.1.3 Mid-infrared thin-film waveguides for absorption spectroscopy

Solid thin-film waveguides operating in the MIR are presented in Chapter 6 as a simple yet effective approach to implement absorption spectroscopy sensors designed for aqueous solutions, such as most biological samples. Using water as a solvent poses specific difficulties, like a strong background absorption and spectral overlaps with clinically relevant

wavelength regions, e.g., the amide bands. Even though a myriad of implementations using several distinct materials have been proposed, the different options have been validated using a variety of wavelengths and analytes, thus complicating an inter-platform comparison to help selecting the best choice for a given application. In this work, a theoretical study of popular TFWG platforms has been undertaken, with the aim of establishing a rigorous analysis of the different implementations, guided by rational design criteria.

Four representative platforms were selected and modeled at $\lambda_0 = 6\,\mu\text{m}$: gallium arsenide (GaAs), chalcogenide glass (Se6), germanium-on-silicon (GOS) and polycrystalline diamond (PCD). Starting from a general system-level perspective, a expression for the limit of detection was derived, proving the existence of an optimum interaction length, $L_{\text{opt}} = \alpha_{\text{wg}}^{-1}$, which is the inverse of total propagation loss. A waveguide figure of merit (FOM) was used to evaluate the trade-off between confinement factor and losses, finding that it determined the optimum achievable LOD. For each alternative, the confinement factor, the propagation loss and the FOM were evaluated over the single-mode regime via FEM simulations. A design width was selected, and the LOD was evaluated as a function of the interaction length under standard conditions. The estimated optimum pathlengths were sub-millimetric for Se6, GOS and PCD waveguides, and below 2 mm for GaAs. Even though the optimum LODs of the three former platforms were comparable, GOS being the best overall with a LOD $= 1.51 \cdot 10^{-5}\,\text{cm}^{-1} \approx 7.2 \cdot 10^{-10}\,\text{RIU}$, the performance of Se6 waveguides suffered from a strong degradation for beyond-optimal pathlengths due to its higher losses. GOS and PCD exhibited a similar tolerance to the length set-point. GaAs waveguides, while showing the worst optimum performance, can be useful candidates if longer waveguides are required in practice. The followed design approach was summarized and generalized, so it can be used as a reference guide to optimize any waveguide geometry with independence of the chosen wavelength or materials.

This is the first fair comparison between state-of-the-art TFWG alternatives, derived from a rigorous and uniform design approach, which can be easily generalized. The findings of this seminal study are expected to favor the development of optimized MIR lab-on-chip devices. The core of this work was performed during a research stay at the University of Ulm. The main results can be found in [95].

7.2 Prospects

The work summarized in the previous section has set the basis for promising new research lines, including systemic improvements to the NIR sensors (Section 7.2.1), an experimental validation of the theoretical work on MIR waveguides (Section 7.2.2) and the development of novel sensing architectures to further advance the field (Section 7.2.3).

7.2.1 System-level improvements to the near-infrared sensors

The results obtained from the experimental validation of the near-infrared complex and bimodal refractive index sensors presented in Chapters 4 and 5, respectively, could potentially be extended and improved by making systemic changes to the measurement setup, without the need of fabricating another generation of chips. In the first place, thermal control could be implemented. Although the spurious impact of thermal fluctuations was theoretically estimated as small compared to the phase shifts induced by the measured samples, this may not be the case when operating with concentrations close to the LOD. Introducing a feedback loop incorporating a thermo-electric controller (TEC) would suppress thermal drifts, therefore decreasing the measurement uncertainty and minimizing the need of software baseline correction at the post-processing stage. Furthermore, the fiber-array coupling scheme, associated to reflection and cross-talk issues, especially relevant in absorbance measurements, could be replaced by a more convenient approach. For

example, by using the single-fiber input included on the layout and reading-out the outputs with a CMOS camera or charge coupled device (CCD) line photodetectors, placed above the output gratings. From the experience at the University of Tromsø (see Appendix D), it is known that the 127-μm inter-grating separation is enough to define appropriate regions of interest. An additional benefit from this approach would be a substantial reduction of mechanical noise (see Appendix B).

Moreover, the sensors could be used in the analysis of different samples. Bulk sensing experiments both at a fixed and a scanned wavelength with the complex refractive index sensors could be performed with isopropanol-water mixtures to avoid uncertainties in the imaginary index of the sample, as isopropanol absorption coefficients in the NIR are well recorded [263, 197]. In fact, by using isopropanol as a solvent and water as an analyte, propagation losses could be reduced down to $\sim$4.5 dB cm^{-1}, yielding an optimum pathlength of roughly 1 cm. The bimodal sensor could be demonstrated in biosensing experiments, e.g., using relevant nucleic-acid sequences, such as microRNAs, as analytes. Early detection of these biomarkers is key to address complex illnesses such as cancer and dementia. To achieve specificity, a biofunctionalization (see Section 2.4.2 in Chapter 2) is required. Specifically, for RNA analysis, a DNA probe complementary to the target sequence should be used as a recognition element [264].

7.2.2 Experimental comparison between mid-infrared waveguides

An experimental validation of the theoretical study of TFWG platforms presented in Chapter 6 could be of great practical interest, as further technical challenges may arise from the fabrication and measurement processes, adding additional design and selection criteria to those already indicated.

For that matter, waveguides should be fabricated in the investigated platforms with different width variations, corresponding to strategic points in the single-mode regime. For each width, several interaction lengths, with and without bends, should be implemented. Afterwards, propagation losses and confinement factors should be measured, the former by the cut-back method and the latter by comparing measured absorption to that expected from free-space interaction. The FOM could then be calculated from these quantities. With these experimental data, a set of discrete points of the curves in Figs. 6.5, 6.6 and 6.7 could be reproduced, and the deviation from simulations assessed. Afterwards, the noise-floor of the available MIR setup, ideally the one considered in Section 6.2.2, and the LOD achieved by each alternative should both be measured and compared with theoretical predictions. Another interesting activity would be selecting the waveguides with an optimum geometry and compare their measured LOD to the state of the art of that given platform, in order to find out whether a substantial improvement was accomplished. In this case, the experiments should be performed at the same wavelength and with the same analyte as the work selected as a reference to ensure maximal comparability.

7.2.3 Development of advanced mid-infrared spectroscopic sensors

The niche of simultaneous absorption and dispersion spectroscopy is rapidly growing, with an emphasis on free-space systems [87, 265]. The preliminary spectroscopic measurements carried out with the first and second complex refractive index sensors of Chapter 4, at the universities of Tromsø and Málaga, respectively, were tentative approaches toward achieving comparable results to free-space on a chip. However, the implemented sensors were designed for fixed-wavelength operation, so their components did not exhibit remarkably broad bandwidths nor flat spectral responses. These attributes would be extremely interesting for the analysis of complex molecules such as amino acids or VOCs,

where broader fractions of the spectra are required. Furthermore, shifting from NIR to MIR wavelengths would be advantageous, as it would enable operation in the molecular fingerprint region, thus achieving inherent selectivity without any chemical surface modification or intricate multivariate data analysis. As a consequence, the development of interferometric architectures specifically designed for absorption and dispersion spectroscopy in the mid-infrared could be an appealing prospect, especially considering that, to the best of the author's knowledge, such devices cannot still be found in the literature.

The most critical sensor components in terms of bandwidth, an important feature of any spectroscopic device, are the MMIs, especially the 2×3 ones, and the grating couplers. An increase in the bandwidth of the former can be achieved by using SWG metamaterials, a subject which has been vastly exploited by the Photonics and RF Research Lab in Málaga [266, 267]. Even though plenty of broadband grating couplers have been proposed [268, 269] and similar designs could be adapted, changing the scheme to edge coupling would facilitate experimental measurements and layout design, while improving the bandwidth response [270]. The main advantage of this approach in the context of integrated photonic sensors is that it increases freedom in the placement of liquid or gas cells (see Section 3.1.5 of Chapter 3) and even enables putting the chip into a miniaturized gas chamber with transparent sidewalls (see Appendix D), therefore avoiding the need of designing and fabricating custom flow-cells (see Appendix C).

Low-loss MIR waveguides have been demonstrated on a SiNOI platform with a 4-μm core thickness up to $\lambda_0 = 3.7\,\mu\text{m}$ [271, 272], but the absorption induced by the silica lower cladding precludes operation at longer wavelengths [273]. As a consequence, changing the platform would be beneficial for high-performance sensors working on the MIR regime. Potential CMOS-compatible candidates that enable operation over nearly the entire MIR range are germanium-core platforms [273]. Suspended platforms are different alternatives, particularly well suited for trace-gas detection. Several membrane and SWG-cladding suspended platforms have been proposed and demonstrated with outstanding results [115, 274] and could be explored for sensor implementation. In fact, Appendix E includes information about suspended silicon waveguides for methane detection, which were already designed and fabricated during this thesis.

Finally, it is worth mentioning that the operation of absorption spectroscopic sensors relying on the Beer-Lambert's law is limited to low analyte concentration ranges and the study of compounds with a linear behavior. Therefore, this approach is invalid for highly concentrated samples or molecules with strong oscillations. Dispersion spectroscopic techniques can overcome such drawbacks by providing a linear output which is highly robust against spurious intensity fluctuations, while extending the dynamic measurement range [141]. In this context, high-performance dispersion spectrometers operating in the MIR could be promising. For instance, the bimodal refractive index sensor developed in this thesis could be analogously adapted in terms of broadband operation and platform choice, with an emphasis on guaranteeing an effective mode conversion. Furthermore, the differential sensitivity could be enhanced by exciting second or third high-order modes or implementing regional mode engineering techniques [161].

Appendix A

Radiation angle of a grating coupler

This appendix explains the relationship between the radiation angle of a grating coupler to an upper medium and to a polished optical fiber.

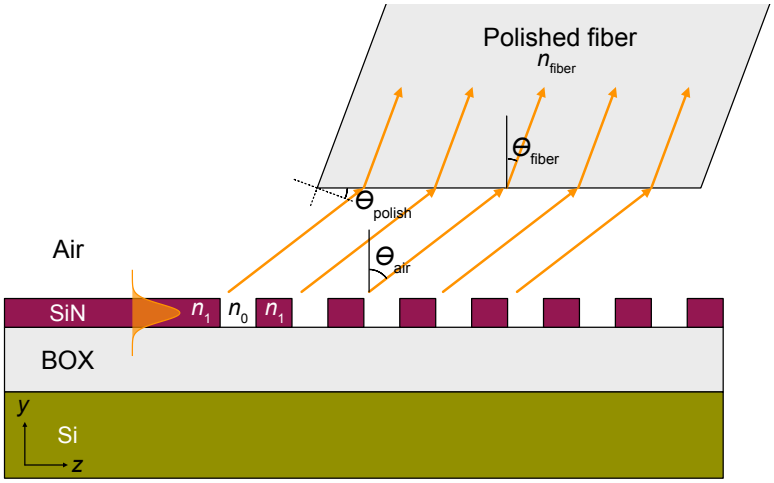

Figure A.1: Side view of a silicon nitride grating coupler radiating to air and coupled to an angled-polished fiber.

In the side view depicted in Fig. A.1, a silicon nitride grating coupler is radiating to air with an angle Θ_{air}. The radiated wavefront impinges into a polished fiber array, with a refractive index n_{fiber}. The radiation angle to said fiber can be calculated by Snell's law:

$$\sin(\Theta_{\text{air}}) = n_{\text{fiber}} \sin(\Theta_{\text{fiber}}), \tag{A.1}$$

yielding

$$\Theta_{\text{fiber}} = \arcsin\left(\frac{\sin(\Theta_{\text{air}})}{n_{\text{fiber}}}\right). \tag{A.2}$$

For example, considering the standard silica SMF-28 operating at $\lambda_0 = 1.55\,\mu\text{m}$ ($n_{\text{fiber}} \approx 1.444$ [211]), a grating coupler with a radiation angle $\Theta_{\text{air}} = 39°$ radiates with $\Theta_{\text{fiber}} = 25.8°$ to the fiber. This is the polishing angle (Θ_{polish}) that needs to be specified when an angled-polished fiber array as those employed in this thesis is acquired.

Appendix B

Noise-floor of a sensing setup

In this appendix the signal and noise models employed to estimate the noise-floor of a sensing setup are explained (Section B.1) and some good practices for noise reduction are suggested (Section B.2). A more comprehensive analysis can be found in [191].

B.1 Signal and noise models

The measurement setup described in Section 3.3 of Chapter 3 is considered for the evaluation of the system noise-floor. Figure B.1 reproduces the schematized setup, where the microfluidic components and the polarization controller have been removed for simplicity, as they do not contribute to the noise level. Lossless propagation is assumed in the interconnecting fibers and wires. Light is emitted from the laser with a power P_{LD}, amplified with a gain G_{EDFA} by the EDFA and in-coupled to the chip with a coupling efficiency $\mathrm{CE_i}$. After propagation through the sensor, with a complex transfer function H_{s}, which is different for each possible light path, light is out-coupled to the output fiber with an efficiency $\mathrm{CE_o}$ and directed toward the detector. The photodiode, with a responsivity R, produces a photocurrent, which is proportional to the incident power. In the TIA, this current is transformed into a voltage with a transimpedance gain G_{TIA}. Finally, this voltage is sampled with a frequency f_{s} by the DAQ, and the digital signal is low-pass filtered with a bandwidth B at the signal-processing stage.

B.1.1 Signal-level

Regardless of the type of sensor being measured, each acquired signal is a digitized voltage produced as described above, which is then processed to calculate the required output parameter. In the sensors presented in this thesis, this parameter would be either phase shift, for which three output voltages, carrying the interferometric signals, are needed, or absorbance. In a noiseless scenario, the average value of the digital signal can be expressed as

$$v_{\mathrm{signal}} = G_{\mathrm{EDFA}} G_{\mathrm{TIA}} \mathrm{CE_i CE_o} R P_{\mathrm{LD}} |H_{\mathrm{s}}|^2. \tag{B.1}$$

As represented in Fig. B.1, it is common practice to express the incorporation of additive noise at the input of the TIA. In this case, it is more convenient to consider the signal photocurrent

$$i_{\mathrm{signal}} = \frac{v_{\mathrm{signal}}}{G_{\mathrm{TIA}}} = G_{\mathrm{EDFA}} \mathrm{CE_i CE_o} R P_{\mathrm{LD}} |H_{\mathrm{s}}|^2. \tag{B.2}$$

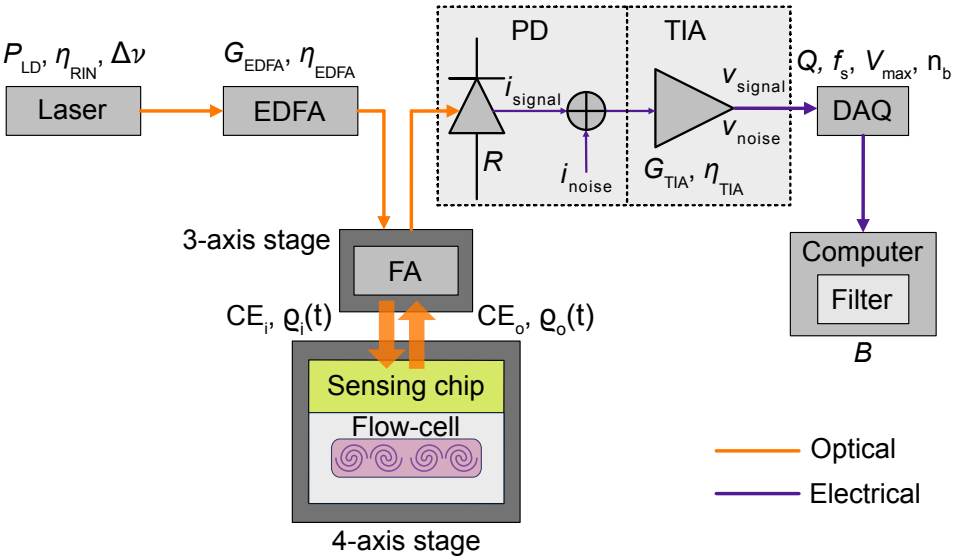

Figure B.1: Schematic representation of a measurement setup for the determination of the noise-floor. Microfluidics components are omitted for simplicity. Abbreviations: erbium-doped fiber amplifier (EDFA), fiber array (FA), photodetector (PD), transimpedance amplifier (TIA), data acquisition (DAQ).

B.1.2 Noise-level

The amount of noise coming from a certain source that is present in the output signal is determined by the noise power spectral density (PSD, η) and the measurement bandwidth, which for the described setup is the bandwidth of the low-pass filter at the DSP stage (B), so that

$$\sigma^2 = \int_B \eta^2(f)df, \tag{B.3}$$

where f is the independent variable in the frequency domain. In the case of additive white gaussian noise (AWGN), η is constant and Eq. (B.3) yields $\sigma^2 = \eta^2 B$. To calculate the impact of several independent noise sources, their power spectral densities are added:

$$\sigma^2_{\text{tot}} = \int_B \sum_k \eta^2_k(f)df. \tag{B.4}$$

When all considered sources are uncorrelated AWGN, then $\sigma^2_{\text{tot}} = \sum_k \sigma^2_k$.

The digitization process in the DAQ can increase the noise-floor if the sampling frequency is not adequately chosen. According to the Nyquist-Shannon sampling theorem [275, 276], noise digitization will be accurate if the noise bandwidth (B_{n}) is such that $B_{\text{n}} < f_{\text{s}}/2$. In this case, there is no noise amplification, as shown in Fig. B.2(a). On the contrary, when $B_{\text{n}} > f_{\text{s}}/2$, spectral aliasing occurs, and the noise power spectral density is increased by a factor which can be approximated as

$$F_{\text{us}} = \frac{B_{\text{n}}}{f_{\text{s}}/2}. \tag{B.5}$$

This case is illustrated in Fig. B.2(b). Here it is worth reminding that, even when only AWGN sources are considered, the different components of the setup, e.g., the TIA, impose their own bandwidth. This means that, in practice, infinite PSDs are filtered with a finite bandwidth. By using a high-end DAQ incorporating anti-aliasing filters, $F_{\text{us}} \approx 1$, so this factor will not be considered for the remainder of this appendix.

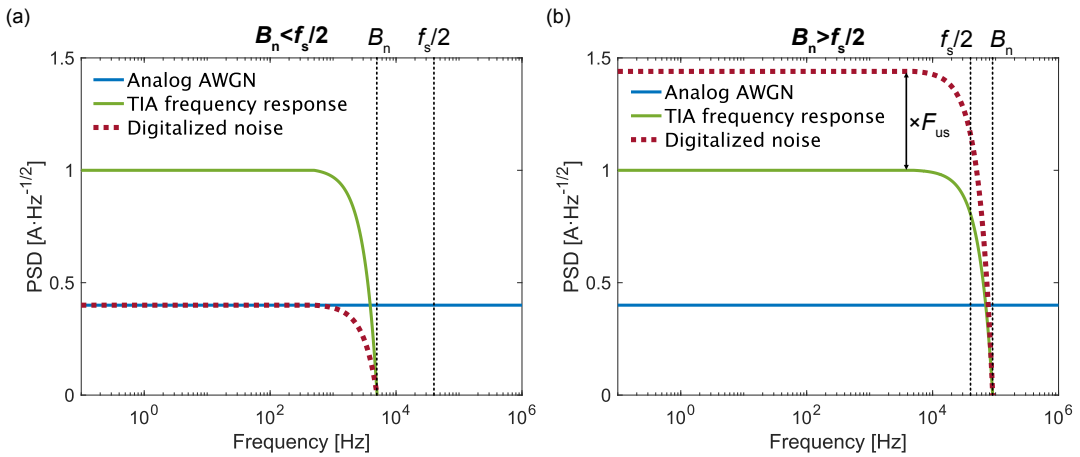

Figure B.2: Results of sampling a noise signal, whose bandwidth is limited by the TIA. (a) When the Nyquist condition is satisfied, noise is correctly sampled. (b) If the noise bandwidth is greater than the half of the sampling frequency, the noise PSD is amplified as a consequence of spectral aliasing.

B.1.3 Noise sources

The most important noise sources are described here, and parametric expressions for their contributions are given whenever possible.

Light source

The laser source introduces phase and relative intensity (RIN) noises. Following [277], a phase noise with a Lorentzian shape with full width at half maximum (FWHM) $\Delta\nu$ is considered. If i_{signal} is an interferometric signal, it is affected by phase noise, whose variance can be approximated as

$$\sigma^2_{\text{PN}} = (2\Delta\tau)^2 \pi \Delta\nu B, \tag{B.6}$$

where $\Delta\tau$ is the group-delay difference between the sensing and the reference branches [189]. RIN noise, with a spectral density η_{RIN}, can be approximated as white, so that

$$\sigma^2_{\text{RIN}} = \eta^2_{\text{RIN}} B. \tag{B.7}$$

This contribution affects intensity measurements, but it has been shown that the phase read-out in coherently detected sensors is immune to RIN noise [189]. This is due to the orthogonality of RIN noise to the evolution of the complex signal.

Optical amplifier

The EDFA degrades the signal-to-noise ratio by a factor determined by its noise figure (NF), which is typically specified by the manufacturer. The introduced excess noise can be written as

$$\sigma^2_{\text{EDFA}} = \eta^2_{\text{EDFA}} B, \tag{B.8}$$

where the spectral density η_{EDFA} incorporates all the contributions to excess noise, such as beat and pump noises [278].

Photodiode

The photocurrent includes shot noise, which scales with incident optical power, so that

$$\sigma^2_{\text{shot}} = 2q i_{\text{signal}} B, \tag{B.9}$$

where $q = 1.6 \cdot 10^{-19}$ C is the electron charge.

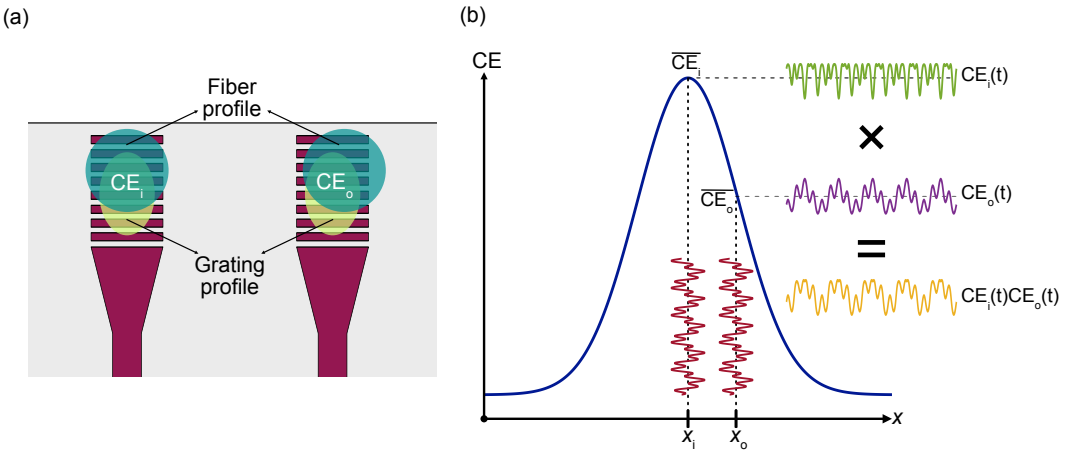

Figure B.3: (a) Top view of two grating couplers. Fabrication deviations in the fiber array induce different coupling efficiencies for each grating. (b) Schematic representation of the stochastic modulation of the coupling efficiency induced by mechanical vibrations.

Transimpedance amplifier

The noise introduced by the TIA can be expressed in terms of its current noise power spectral density (η_{TIA}):

$$\sigma^2_{\mathrm{TIA}} = \eta^2_{\mathrm{TIA}} B. \tag{B.10}$$

The value of η_{TIA} can be calculated from the noise equivalent power (NEP), a gain-dependent parameter which is often provided by the manufacturer, as

$$\eta_{\mathrm{TIA}} = G_{\mathrm{TIA}} R\mathrm{NEP}(G_{\mathrm{TIA}}). \tag{B.11}$$

Data acquisition

The digitization process occurred in a DAQ with n_{b} bits and an input voltage range $\pm V_{\mathrm{max}}$ can be modeled as a quantization noise with a variance

$$\sigma^2_{\mathrm{DAQ}} = \frac{1}{G^2_{\mathrm{TIA}}} Q^2 (\mathrm{LSB})^2 \frac{1}{f_{\mathrm{s}}/2} B, \tag{B.12}$$

where Q is the quality factor of the DAQ, which ideally takes a value of $12^{-1/2}$, $\mathrm{LSB} = 2V_{\mathrm{max}}/2^{n_{\mathrm{b}}}$ is the least significant bit and the factor $f_{\mathrm{s}}/2$ stretches the noise over the Nyquist bandwidth.

Mechanical vibrations

Fabrication tolerances in the fiber array result in different relative positions of the fibers with respect to their associated grating, as schematized in Fig. B.3(a), thus inducing a different coupling efficiency for each fiber-grating pair. On top of this, ambient mechanical vibrations can slightly move the fiber array, provoking a spurious modulation of the coupling efficiency of each grating coupler. For the k-th grating coupler, this can be expressed as

$$\mathrm{CE}_k(t) = \overline{\mathrm{CE}_k} \varrho_k(t), \tag{B.13}$$

where $\overline{\mathrm{CE}_k}$ is the average coupling efficiency and $\varrho_k(t)$ is an unknown stochastic process, governed by the mechanical properties of the setup and centered at unity. An intuitive graphical explanation of this phenomenon can be observed in Fig. B.3(b), where the same mechanical vibrations have been assumed for the input and output fibers. This is a multiplicative noise source (see Eq. (B.2)) and cannot be completely filtered out. In practice,

$\varrho_k(t)$ needs to be minimized by dampening vibrations as will be suggested in Section B.2. The mechanical noise level can be calculated by applying Eq. (B.3) to the PSD of $\varrho_k(t)$.

B.2 Noise-floor optimization strategy

Apart from opting for high-performance, low-noise components whenever it is possible, the following noise-floor optimization guidelines can be derived from the analysis of Section B.1:

- Implement the narrowest possible filter at the signal processing stage, considering the bandwidth of the acquired signal (Eq. (B.3)).
- Avoid noise amplification (Eq. (B.5)) by choosing a DAQ with a high sampling frequency and anti-aliasing filters. If this is not possible, include electrical low-pass filters in the setup to decrease the noise bandwidth.
- If the sensor is detecting phase shift with an interferometric configuration, balance the sensing and reference paths in the design process to mitigate laser phase noise (Eq. (B.6)).
- Study the relative impact of the different noise sources. If the system is dominated by shot noise (Eq. (B.9)), maximize detected signal power, without saturating the detector. If not, select the optimum configuration in terms of SNR (see the two following points).
- Choose the TIA gain with the least associated noise (Eq. (B.11)) that provides an acceptable signal level.
- Select the highest possible sampling frequency and number of bits for the DAQ in order to reduce the impact of quantization noise (Eq. (B.12)). If possible, adjust the input voltage range to the signal level or vice versa.
- Damp mechanical vibrations by pressing the fiber array to the chip surface in the aligning process and use a floating table if it is available. Avoid touching the setup during experiments.

Appendix C

Fabrication of PDMS flow-cells

This appendix explains the procedure followed to fabricate the microfluidics flow-cells used for the sensing experiments performed in this thesis. The chemicals employed were the PDMS and the curing agent included in the Dow SYLGARD™ 182 Silicone Elastomer Clear 0.5 kg Kit provided by Ellsworth Adhesives. A mold with capacity to accommodate 6 cells was designed, fabricated in transparent PMMA, polished and cleaned. Once the mold was ready, the following steps were taken:

1. Prepare a 5:1 PDMS-curing agent mixture in a Falcon container. Stir with a pipette until achieving a homogeneous fluid.
2. Degasify the mixture in a vacuum dryer for 40 minutes.
3. Pour the mixture over the mold and degasify for 5 minutes.
4. Cure the mixture in the mold for 3 hours in a pre-heated heating plate at $50°$C.
5. Turn the heating plate off and leave the mold overnight.

Afterwards, the fabricated PDMS can be separated from the mold and individual channels can be cut out using a 3D-printed pattern, perforated and cleaned for their use in sensing experiments. The mold is reusable for multiple PDMS batches.

Appendix D

Gas sensing experiments at the University of Tromsø

A four-month research stay at UiT The Arctic University of Norway (Tromsø, Norway) was carried out from 16th May to 12th September 2022 under the supervision of Prof. Jana Jágerská. The purpose of the visit was performing gas sensing measurements with the first-generation NIR complex refractive index sensors ($\lambda_0 = 1.65\,\mu m$) introduced in Section 4.3 of Chapter 4, taking advantage of the experience of the hosting group in on-chip trace-gas detection. This appendix includes brief information about the measurement setup and the obtained results.

D.1 Measurement setup

D.1.1 Setup components

A schematic representation of the employed measurement setup is shown in Fig. D.1(a). Light from a Exfo T100S-HP tunable laser source was coupled into the sensor, which was placed into a hermetic gas cell. Both the focusing lens and the gas cell were placed on top of nanopositioning stages (Thorlabs MAX302) to facilitate alignment. To enable edge coupling, the chips were cleaved with a LatticeAx 225 cleaver at the input of the 1×2-MMI, just before light is separated into the sensing and reference arms (see Fig. 4.8 of Chapter 4), as can be seen in Fig. D.1(b). The gas cell, of which a close-up picture can be observed in Fig. D.1(c), had transparent side and upper walls to let the light go in and out. Output grating couplers were read by a Raptor Photonics Ninox 640 InGaAs camera, controlled by the EPIX XCAP image processing software. Either pure N_2 or 4% CH_4 were alternatively brought to the gas cell by Bronkhorst EL-FLOW mass-flow controllers (MFCs), configured by a custom LabVIEW program. Additional measurements with 10% acetylene (C_2H_2, $\lambda_0 = 1.52\,\mu m$) instead of methane were also performed. The gas outlet was directed to a flow-meter to verify the flow rate and detect possible gas leaks.

D.1.2 Read-out algorithm

For spectroscopic measurements, the wavelength was scanned in step-mode around the desired absorption line. The infrared camera was configured to acquire an image sequence, at the same rate as the laser switched wavelength. Both the wavelength scan and the image acquisition were simultaneously started. At the signal processing stage, the time axis of the images was mapped into the wavelength axis. Ideally, the laser and the camera should have been automatically synchronized by implementing a controlling routine based on LabVIEW or Matlab, but it could not be accomplished due to time con-

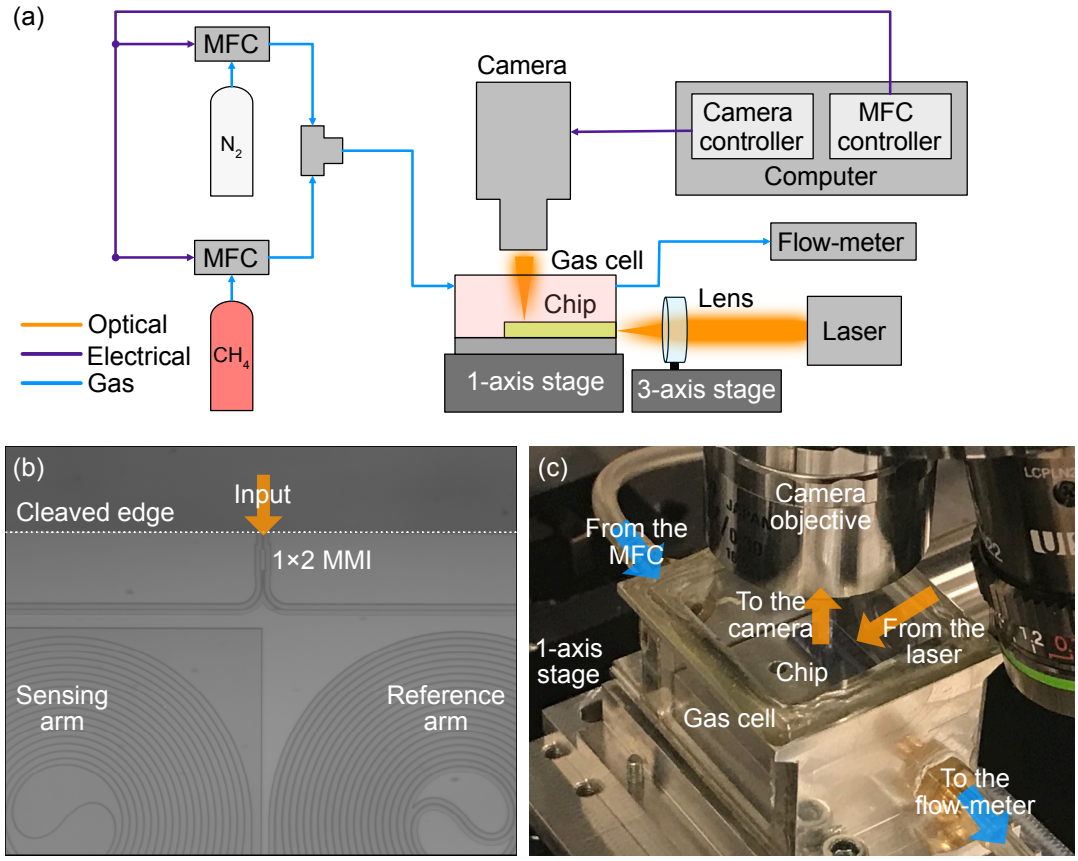

Figure D.1: (a) Schematic representation of the measurement setup for gas sensing. Abbreviations: mass-flow controller (MFC). (b) Cleaved chip to enable edge coupling. The sensor was cleaved at the input of the 1×2-MMI. (c) Close-up of the gas cell. Light can be coupled in and read-out thank to transparent side and upper walls.

strains. A custom Matlab script was developed to transform the images of the grating couplers, of which an example can be observed in Fig. D.2(a), into numerical intensity vectors. The algorithm steps are the following:

1. Define the regions of interest (ROI) containing each grating coupler.
2. Apply a binary mask to each ROI.
3. Sum the values of the pixels of each masked ROI. This value is proportional to the output intensity.

A background cancellation algorithm, consisting of calculating the light background by applying the described method to a dark region, and then subtracting it to the obtained signals, was developed to improve read-out quality.

D.2 Results and discussion

Intensity vectors were low-pass filtered and background-corrected using the results from the nitrogen flow. Afterwards, the absorbance and dispersion spectra were calculated. Figures D.2(b)–(c) show such spectra for a representative C_2H_2 spectroscopy measurement. The observed oscillations are explained by residual fringes caused by reflections in the setup. In Fig. D.2(b), it can be seen that the obtained absorbance peak corresponds to the free-space propagation of the output beam in a 14-mm pathlength, which agrees with the distance from the chip to the upper wall of the gas cell (see Fig. D.1(a)). This

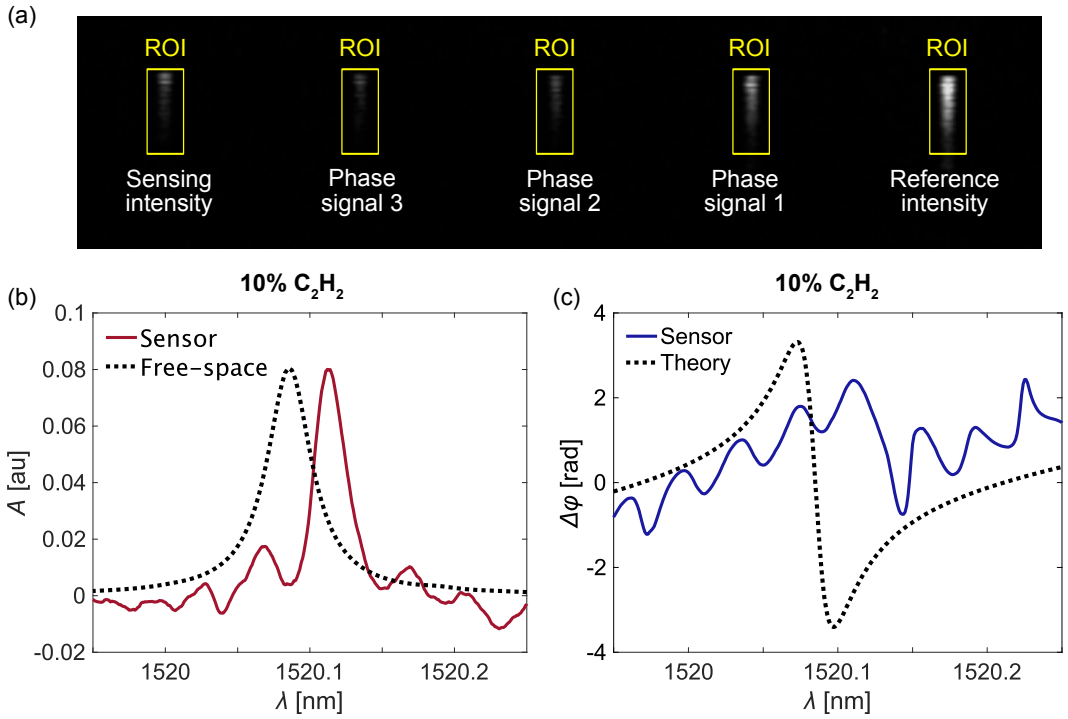

Figure D.2: (a) Image of the grating couplers during a gas sensing experiment. (b) Absorbance spectrum of C_2H_2. The observed response corresponds to the free-space propagation [46] of the output beam in the cell. (c) Dispersion spectrum of C_2H_2. The scaled shape of the theoretically expected response [50] is represented in dotted lines.

means that there is no added contribution from the waveguide, and therefore the sensor is not suitable to perform gas absorption spectroscopy. The reason for the displacement of the peak would require deeper investigation. The phase response represented in Fig. D.2(c), shows a certain degree of similarity to the theoretically expected curve, but the poor quality of the signal prevents making further claims.

Although the measured devices were not reliable complex refractive index sensors for the detection of gases, their evaluation in the described setup was fundamental for troubleshooting. When the fiber array was substituted by edge input-coupling and the camera read-out, the spurious artifacts previously observed in the sensing intensity signals, described in Section 4.3.3 of Chapter 4, ceased. This confirmed the suspicions about the influence of the fiber array in the problems encountered while evaluating the chips in Málaga.

Appendix E

Mid-infrared suspended silicon waveguides

Suspended waveguides for methane detection in the mid-infrared were designed for Cornerstone's suspended silicon platform and fabricated on the commercial Suspended Si MPW#1. Unfortunately, these waveguides could not be experimentally characterized during this thesis due to lack of equipment. This appendix summarizes the main aspects regarding the design (Section E.1) and visual inspection under the SEM (Section E.2) of the implemented devices. Finally, brief conclusions about the expected performance are drawn (Section E.3).

E.1 Sensor design

E.1.1 Sensor components

Cornerstone's platform offers a 0.5-µm silicon guiding layer an a 3-µm BOX buffer layer, which is removed from the areas underneath the waveguides, as shown in Fig. E.1, by HF etching. According to the information provided by the foundry, the etching process reduces the final thickness of the guiding layer to ∼0.45 µm, so $H = 0.45$ µm is the considered nominal waveguide height in the designs. The operation wavelength corresponds to the methane absorption line at $\lambda_0 = 3.27$ µm and the polarization is TE. The main characteristics of the waveguides, i.e., confinement factor and leakage, both vertical and lateral, were calculated as described in Section 3.1 of Chapter 3, using rigorous Bloch–Floquet simulations.

Sensing waveguides

Two different waveguide designs (A and B), based on those previously described in [279, 280], and whose nominal dimensions can be found in Table E.1, were studied. The combination of the core (W) and lateral-cladding (W_{clad}) widths guaranteed a lateral leakage ($L_{\text{leak,lat}}$) below 0.1 dB cm^{-1}. The periodic lateral cladding, operating in the SWG regime, provided mechanical support and refractive-index contrast, in addition to allowing the HF to flow for BOX removal. Figure E.2 shows the transversal field distribution of the fundamental TE mode of each waveguide, for a z-position corresponding to a lateral

Table E.1: Nominal dimensions of the designed suspended silicon waveguides for $\lambda_0 = 3.27$ µm, $H = 0.45$ µm and $H_{\text{BOX}} = 3$ µm.

Design	W [µm]	W_{clad} [µm]	L_{strip}[µm]	L_{hole}[µm]
A	1.2	4	0.23	0.32
B	0.95	5.5	0.23	0.32

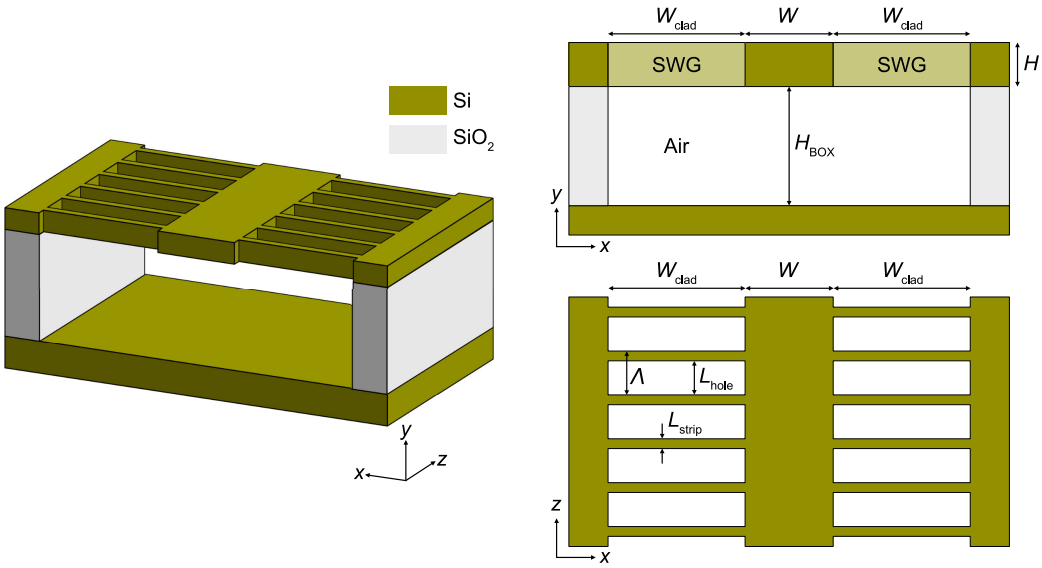

Figure E.1: Schematic representation of a suspended silicon waveguide for operation in the mid-infrared.

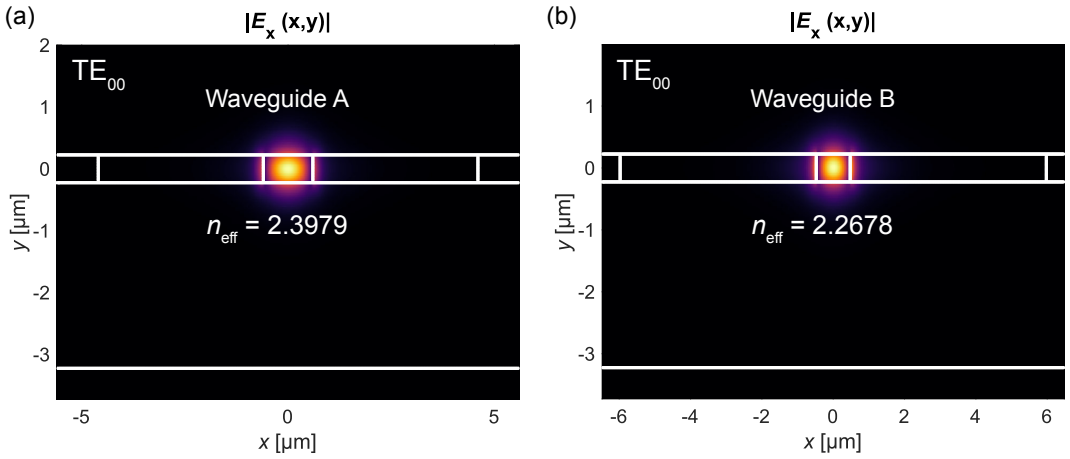

Figure E.2: Field profile of the fundamental TE mode of the (a) A and (b) B waveguide designs, for a z-cut corresponding to an air hole. Only the real part of the effective index is given.

hole. Confinement factors of $\Gamma_{\mathrm{A}} = 0.19$ and $\Gamma_{\mathrm{B}} = 0.27$ were obtained for waveguides A and B, respectively, while vertical leakage was negligible ($L_{\mathrm{leak,ver}} < 10^{-4}\,\mathrm{dB\,cm^{-1}}$) in both designs. Here it is worth acknowledging that, despite suspending the waveguides, the obtained sensitivities are comparable to those of the NIR strip waveguides used in the sensors from Chapter 4. This is the result of prioritizing low-loss propagation in the design. In fact, beyond-free-space interaction ($\Gamma > 1$) could be achieved with both A and B waveguide geometries by exciting the fundamental TM mode instead of the TE. However, while a vertical leakage loss around $6\,\mathrm{dB\,cm^{-1}}$ for the A waveguide could be managed, values above $100\,\mathrm{dB\,cm^{-1}}$ would impede practical operation of the B waveguide.

Grating couplers

Suspended surface grating couplers, as the one shown in Fig. E.3, featuring the dimensions included in Table E.2, were designed to enable coupling to and from the chip [274], incorporating a SWG adaptation tooth to minimize back-reflections. To connect the gratings with the waveguides, an adiabatic taper with length $L_{\mathrm{taper}} = 500.5\,\mu\mathrm{m}$ was imple-

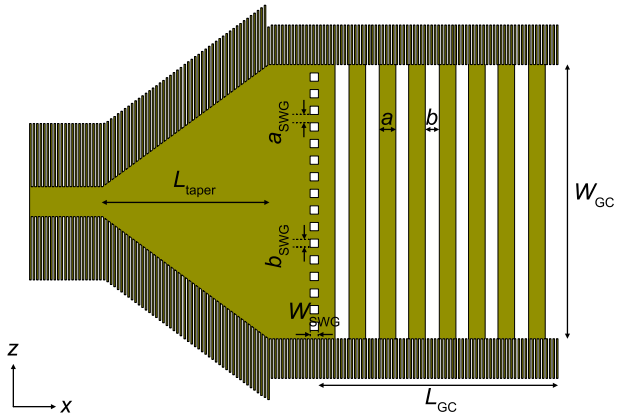

Figure E.3: Schematic top view of a suspended surface grating coupler.

Table E.2: Nominal dimensions of the designed suspended grating couplers for $\lambda_0 = 3.27\,\mu m$, $H = 0.45\,\mu m$ and $H_{BOX} = 3\,\mu m$.

W_{GC} [µm]	L_{GC} [µm]	a [µm]	b [µm]	W_{SWG} [µm]	a_{SWG} [µm]	b_{SWG} [µm]
16	94.55	1.24	0.31	0.45	0.52	0.27

mented. The grating radiated with an angle of 12° to the air and achieved a maximum coupling efficiency CE $= -5.5$ dB. The calculated back-reflections amounted to BR $= -34$ dB.

E.1.2 Chip layout

Waveguides with designs A and B and different lengths ranging from roughly 4 to 40 mm were integrated on the chip. Figure E.4 shows the layout of one of such waveguides, where long straight fragments have been omitted for compactness. To achieve the desired sensing pathlengths within a chip area of $5.5 \times 4.9\,mm^2$, 180°-bends with a radius of 45 µm were added. In addition to the grating-coupled waveguides, four A waveguides with edge couplers, implemented with 500.5 µm-long tapers, were included. This was done to facilitate future gas sensing measurements, placing the chip inside a gas chamber in a similar setup as the one described in Appendix D.

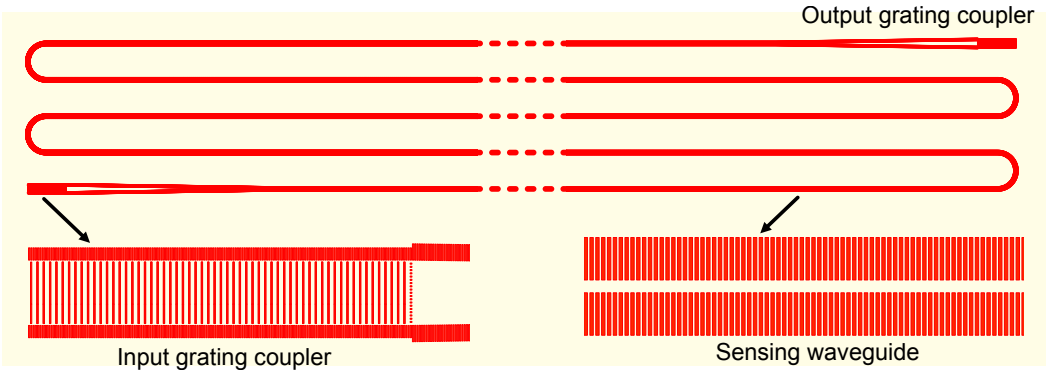

Figure E.4: Mask layout of a suspended silicon waveguide accessed via grating couplers.

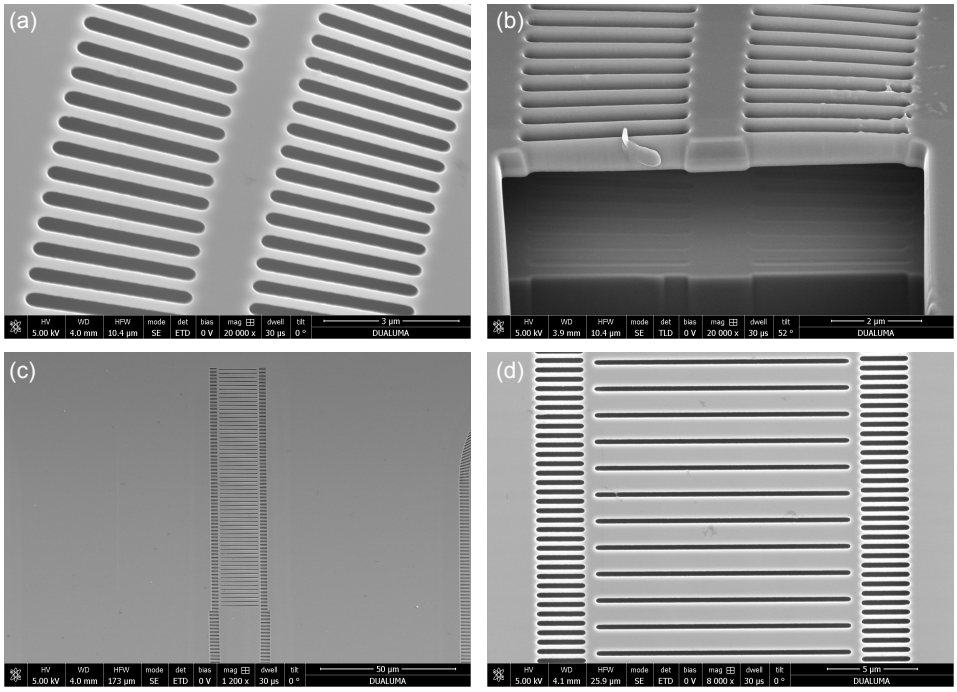

Figure E.5: (a) Top view and (b) cross section of a bent suspended waveguide with design A. (c) Full view and (d) close-up of a suspended grating coupler.

E.2 SEM images of the fabricated sensors

The fabricated chips were inspected under the SEM to verify their correct processing by the foundry. Images of the waveguides, as those shown in Figs. E.5(a)–(b) for the top view and a cross section of a bent waveguide, confirmed the complete suspension of all the structures, both with A and B designs. No significant deviations from the nominal dimensions were observed. The measured thickness of the silicon guiding layer was around 0.46 µm, so slightly lower confinement factors than those obtained in simulations should be expected. Regarding the grating couplers, of which full and close views can be observed in Figs. E.5(c)–(d), respectively, the designed SWG adaptation tooth, despite adjusting to the design rules of the foundry, was not etched. This same issue was previously experienced with the SiNOI platform (SiN MPW#3) used to fabricate the sensors from Chapters 4 and 5, and is expected to increase back-reflections. Overall, the fabricated waveguides were considered suitable for experimental demonstration.

E.3 Conclusions

Suspended silicon waveguides for methane detection at $\lambda_0 = 3.27\,\mu\text{m}$ were designed and successfully fabricated in Cornerstone's Suspended Si MPW#1. Even acknowledging the moderate confinement factors ($\Gamma \sim 0.2$) of the waveguides, low concentrations of methane could potentially be detected with an optimized read-out system. Owing to the low simulated lateral and vertical leakage, scattering loss due to surface roughness is expected to dominate. Considering practical propagation losses around $3.5\,\text{dB}\,\text{cm}^{-1}$, similar to those reported in [281] at $\lambda_0 = 3.8\,\mu\text{m}$, the optimum sensing length (see Eq. (6.17) of Chapter 6) amounts to $L_{\text{opt}} \approx 12.41\,\text{mm}$. The closest implemented pathlength is $L = 13.46\,\text{mm}$, so those should be the best-performing sensors in the chip. Assuming an absorbance noise $\sigma_{\text{A}} \sim 2 \cdot 10^{-5}$ au [116], and following the 1-σ criterion, typical in gas sensing, 13.46 mm-long waveguides A and B could reach $\text{LOD}_{\text{A}} = 4.1\,\text{ppm}$ and

$LOD_B = 2.8$ ppm of CH_4, respectively. Optical characterization and sensing experiments are needed to verify these estimations.

Appendix F

Curriculum vitae

F.1 International journal papers

1. **A. Torres-Cubillo**, A. Teuber, R. Halir, and B. Mizaikoff, "Optimized waveguides for mid-infrared lab-on-chip systems: A rigorous design approach," Sensors and Actuators A: Physical 378, 115797 (2024).

2. **A. Torres-Cubillo**, A. Sánchez-Postigo, J. Jágerská, J. G. Wangüemert-Pérez, and R. Halir, "Simultaneous measurement of refraction and absorption with an integrated near-infrared Mach–Zehnder interferometer," Optics & Laser Technology 177, 111154 (2024).

3. **A. Torres-Cubillo**, J. M. Luque-González, A. Sánchez-Postigo, A. Fernández-Gavela, J. G. Wangüemert-Pérez, I. Molina-Fernández, and R. Halir, "High-performance bimodal evanescent-field sensor with coherent phase readout," Journal of Lightwave Technology 42(8), 3010–3015 (2024).

F.2 Conference proceedings

1. **A. Torres-Cubillo**, A. Teuber, R. Halir, and B. Mizaikoff, "Optimized thin-film waveguide sensors for liquid-phase mid-infrared spectroscopy," FLAIR (2024).

2. **A. Torres-Cubillo**, A. Sánchez-Postigo, J. G. Wangüemert-Pérez, I. Molina-Fernández, and R. Halir, "Towards simultaneous absorption and refractive index sensing using integrated photonics," Optica Sensing Congress (2023).

3. **A. Torres-Cubillo**, J. M. Luque-González, A. Sánchez-Postigo, J. G. Wangüemert-Pérez, I. Molina-Fernández, and R. Halir, "Towards bimodal photonic sensing with coherent readout in silicon nitride", ECIO (2023).

4. **A. Torres-Cubillo**, J. G. Wangüemert-Pérez, A. Sánchez-Postigo, I. Molina-Fernández, and R. Halir, "Mitigating reflections in integrated gas sensors", NEO (2022).

5. **A. Torres-Cubillo**, C. Pérez-Armenta, A. Sánchez-Ramírez, J. Leuermann, A. Fernández-Gavela, A. Ortega-Moñux. J. G. Wangüemert-Pérez, I. Molina-Fernández, and R. Halir, "Towards a silicon-on-insulator bimodal refractive index sensor with a coherent readout," OPTOEL (2021).

F.3 Research stays at foreign centers

1. **May–September 2023:** 4-month research stay at the Institute of Analytical and Bionanalytical Chemistry (IABC) of the University of Ulm (Ulm, Germany) to develop optimized mid-infrared waveguide-based spectroscopic sensors under the supervision of Prof. Boris Mizaikoff.

2. **May–September 2022:** 4-month research stay at the Department of Physics and Technology of the Arctic University of Norway (UiT, Tromsø, Norway) to perform methane detection experiments with interferometric integrated sensors under the supervision of Prof. Jana Jágerská.

F.4 Courses

1. **October 2022:** 12th Advanced Study Course on Optical Chemical Sensors (ASCOS 2022), at the Alpine Research Centre of the University of Innsbruck (Obergurgl, Austria).

F.5 Teaching

1. **Señales y sistemas (Signals and systems):** 36 lecture hours.

2. **Redes y servicios de telecomunicación (Telecommunication networks and services):** 72 lecture hours.

Appendix G

Resumen en español

Esta tesis está dedicada la investigación y el desarrollo de diferentes arquitecturas de sensado fotónico integrado, aportando novedades y mejoras respecto al estado de la cuestión. El presente apéndice contiene un resumen español del trabajo realizado. En primer lugar, se introducirá la el campo del sensado fotónico y se indicarán las principales aportaciones de esta tesis (Sección G.1). A continuación, se repasarán los fundamentos de los sensores fotónicos integrados (Sección G.2) y se describirá la metodología de trabajo empleada (Sección G.3). Después, se presentarán las tres contribuciones principales: un sensor de índice de refracción complejo (Sección G.4), un sensor bimodal de índice de refracción (Sección G.5) y un estudio riguroso sobre el diseño de guías para espectroscopía de absorción (Sección G.6). El apéndice concluirá recogiendo las conclusiones mas importantes (Sección G.7).

G.1 Introducción

G.1.1 Afrontando los desafíos del S. XXI mediante sensores fotónicos

En su informe sobre tendencias globales de cara a 2040 [1], publicado en abril de 2024, el Sistema Europeo de Análisis de Estrategias y Políticas definió la época venidera como una de múltiples crisis. Entre los distintos desafíos identificados, las emergencias climáticas y la salud global tienen un papel sobresaliente. El cambio climático, agravado por la ingente emisón de gases de efecto invernadero originada por la actividad humana, es probablemente la amenaza medioambiental más visible. Reducir el nivel de emisiones hasta los niveles recomendados por la comunidad científica [5] es imposible con las medidas de control vigentes, por lo que es previsible un recrudecimiento de las mismas. A los riesgos para la salud humana causados por la degradación medioambiental, se añaden otros como la proliferación de enfermedades infecciosas o la mayor prevalencia de enfermades ligadas al envejecimiento de la población, como el cáncer, la diabetes o el Alzheimer. Una población envecejida demandará mayores servicios médicos y, para que los sitemas sanitarios puedan gestionar esa carga, será necesario acelerar los procesos de diagnóstico y monitorización de tratamientos en curso, así como solventar los problemas causados por la falta de personal cualificado [10].

Un paso clave para enfrentarse a los problemas mencionados es detectar y monitorizar las sustancias que los originan, como gases contaminantes o patógenos. En este punto, los sensores juegan un papel decisivo. Habitualmente, un sensor, como el mostrado en el esquema genérico de la Fig. G.1(a), se compone de una fuente de señal, un elemento de transducción, en contacto con la muestra a analizar, un detector de señal y una etapa de procesado que produce la señal de salida. De entre las diversas categorías de sensores existentes [15], los sensores fotónicos basados en guías de onda, que son un subconjunto

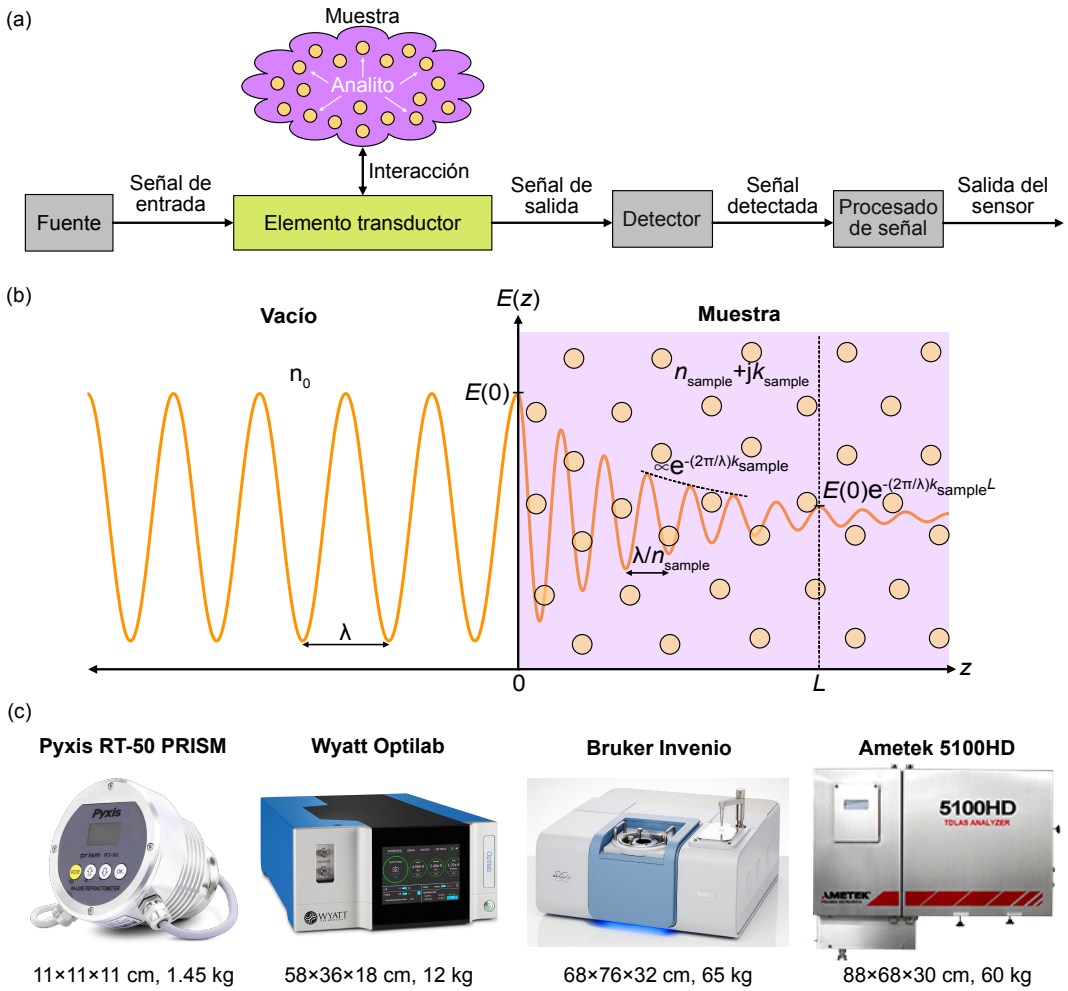

Figura G.1: (a) Componentes de un sensor genérico. (b) Propagación de una onda plana en un medio homogéneo, constituido por la muestra a analizar. (c) Modelos de sensores ópticos comerciales.

de los sensores ópticos, centran el interés de esta tesis y por ello se introducen expresamente en la Sección G.1.2. Las características deseables en un sensor son comunes a las distintas implementaciones. En primer lugar, el límite de deteccion (LOD, por sus siglas en inglés) debe ser lo menor posible, esto es, deben poderse detectar cantidades muy pequeñas de analito. Un LOD bajo se beneficia de una sensibilidad alta, definida como la relación entre la señal de salida y la cantidad de analito, y de una baja incertidumbre en la lectura. Además, muchas aplicaciones requieren especificidad para garantizar que el sensor sólo reacciona ante el analito de interés. Otras propiedades interesantes son un tamaño compacto, precios competitivos, velocidad de operación y facilidad de uso.

G.1.2 Sensores ópticos

En un sensor óptico, cambios en las propiedades de la luz, producidos como resultado de la interacción entre ésta y la muestra, se transforman en una señal medible mediante fotodetectores. Concretamente, en esta tesis se tratan los sensores que detectan cambios en el índice de refracción o en la absorción de la luz, y que operan tanto en el infrarrojo medio (MIR, por sus siglas en inglés) como en el cercano (NIR, por sus siglas en inglés). Para comprender el funcionamiento de dichos sensores, resulta de ayuda contemplar la propagación de una onda plana en un medio homogéneo, caracterizado por su índice de

refracción complejo $(n + \mathrm{j}k)$, representada en la Fig. G.1(b). La longitud de onda en el medio es inversamente proporcional a la parte real del índice de refracción (n) y, por lo tanto, el desfase que acumula la onda puede escribirse como

$$\varphi = \varphi_{\text{in}} + \frac{2\pi}{\lambda} nL, \tag{G.1}$$

donde φ_{in} es el desfase inicial y L es la longitud de interacción. Asimismo, la absorción de la luz está regida por la parte imaginaria del índice (k), y sigue una evolución exponencial descrita por la ley de Beer-Lambert [44]:

$$I = I_{\text{in}} e^{(-\alpha L)}, \tag{G.2}$$

donde I es la intensidad transmitida, I_{in} es la intensidad previa a la interacción con el medio y $\alpha = (4\pi/\lambda)k$ es el coeficiente de absorción de potencia (en m^{-1}). Los cambios tanto en la parte real como en la imaginaria del índice se pueden relacionar unívocamente con la presencia y concentración del analito y, por tanto, la detección de los primeros implica la detección cuantitativa del último.

La detección de analitos mediante su índice de refracción, especialmente en muestras líquidas, puede ejecutarse mediante refractómetros basados en prismas [55] o en interferómetros [56]. Por su parte, las técnicas más extendidas para sensado de absorción, ya sea en fase líquida, sólida o gaseosa, emplean espectrómetros FTIR [57] y TDLAS [59], por sus siglas en inglés, que analizan el espectro de absorción de la luz tras atravesar una celda donde se encuentra la muestra. Pese las altas prestaciones de modelos comerciales como los ejemplos recogidos en la Fig. G.1(c), estos aparatos son voluminosos, caros y frágiles, por lo que no son aptos para operarse fuera del laboratorio o para desplegar de redes de sensores inteligentes. En este contexto, la fotónica integrada aparece como una potente herramienta de miniaturización.

Sensores fotónicos integrados

La fotónica integrada se ha convertido en una tecnología de referencia en telecomunicaciones y centros de datos a lo largo de las últimas décadas [60], y está expandiendo su campo de aplicación a áreas como la automoción [63] y el sensado [65]. Las plataformas basadas en materiales del Grupo IV, como el germanio o el silicio, son especialmente interesantes, ya que permiten utilizar las avanzadas tecnologías de fabricación de la industria microelectrónica. Confinando y guiando la luz en guías de ondas en lugar de depender de la propagación en el espacio libre, los sensores fotónicos integrados ofrecen soluciones submilimétricas, que pueden operar con tan sólo microlitros de muestra y que son aptos para integrarse en plataformas de detección múltiple [69, 70]. Estos dispositivos exhiben unas prestaciones excelentes, entregando resultados cuantitativos en tiempo real y sin necesidad de un tratamiento previo de la muestra o de operarios altamente cualificados. Además, pueden producirse en masa en fábricas de microconductores, abarantando así los costes y promoviendo dispositivos total o parcialmente desechables. Además, son piezas claves de los laboratorios-en-chip (LOC, por sus siglas en inglés) [72, 73], un concepto que puede revolucionar el campo del sensado químico. Por ejemplo, LOCs para diagnóstico clínico podrían llevarse a regiones con acceso limitado a instalaciones sanitarias, o dispositivos para monitorización medioambiental podrían colocarse en ubicaciones remotas para la creación mapas de contaminación actualizados en tiempo real. Por su interés y versatilidad, este trabajo se centra en el desarrollo de sensores fotónicos integrados basados en guías de onda dieléctricas.

Sección 4 | Sensor de índice de refracción complejo en el infrarrojo cercano

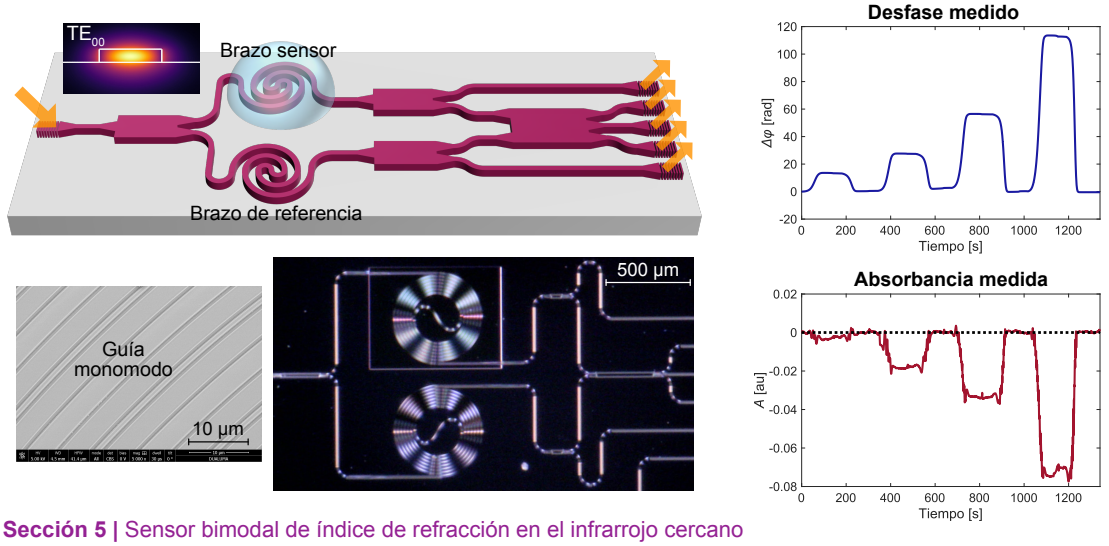

Sección 5 | Sensor bimodal de índice de refracción en el infrarrojo cercano

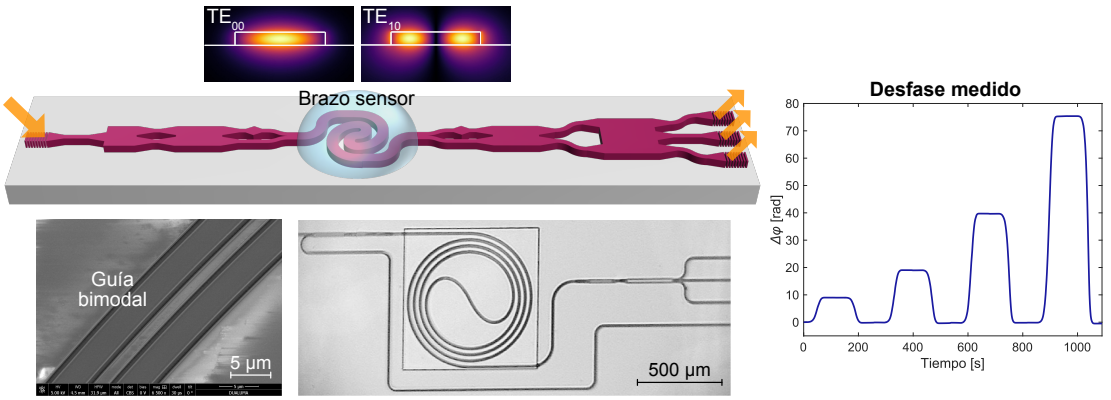

Sección 6 | Guías para espectroscopía de absorción en el infrarrojo medio

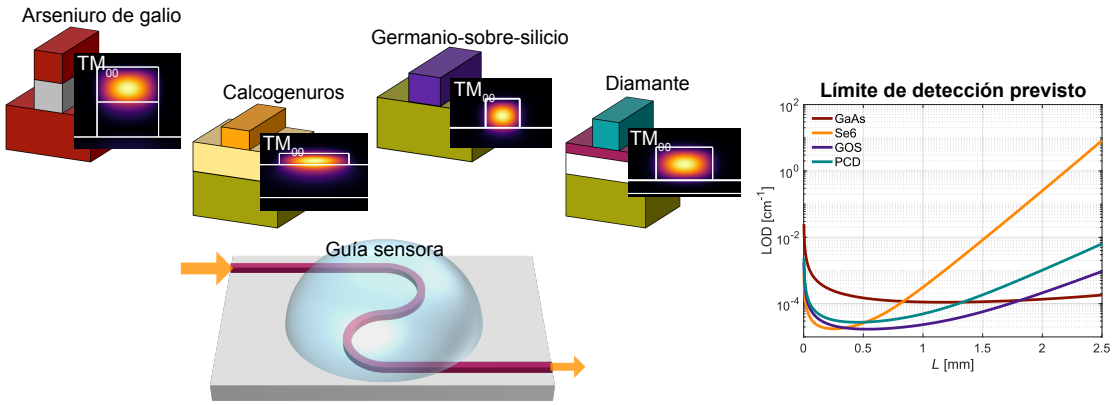

Figura G.2: Resumen de las contribuciones principales de esta tesis, incluyendo ilustraciones 3D (no a escla), perfiles de campo simulados, imágenes de microscopio óptico y SEM y resultados.

G.1.3 Contribuciones de esta tesis

Tres contribuciones principales avalan el trabajo de la presente tesis: dos sensores operando en el infrarrojo cercano, que utilizan la técnica de detección coherente anteriormente propuesta por el grupo de Fotónica y RF de la Universidad de Málaga [218] y un estudio teórico acerca de la optimización de guías para espectroscopía de absorción en el infrarrojo medio. A continuación se incluye una breve descripción de cada contribución, las cuales se resumen gráficamente en la Fig. G.2.

Sensor de índice de refracción complejo

Los sensores fotónicos integrados que detectan cambios simultáneos en la absorción y la refracción de una muestra tienen un gran potencial, pues pueden combinar la gran sensibilidad del sensado índice de refracción con la especificidad del de absorción. Sin embargo, se encuentran pocos ejemplos en la literatura, especialmente en implementaciones en chip. Un sensor de este tipo, basado en un interferómetro de Mach-Zehnder modificado, se ha implementado en una plataforma de nitruro de silicio para operar en longitudes de onda del infrarrojo cercano. Estos sensores se han validado experimentalmente, obteniendo un LOD del orden de 10^{-6} RIU tanto para la parte real como la imaginaria del índice. Hasta donde alcanza el conocimiento de la autora, estas cantidades nunca se habían detectado simultáneamente con un LOD tan bajo. Los principales resultados se encuentran publicados en [89].

Sensor bimodal de índice de refracción

Los sensores basados en guías bimodales están apareciendo con el objetivo de reducir el área ocupada por las arquitecturas interferométricas convencionales, ya que no requieren de un camino de referencia físico. Sin embargo, sufren desventajas asociadas con una incorrecta excitación de modos superiores y de la lectura de su salida sinusoidal. Una novedosa arquitectura de sensado que combina una guía bimodal con una excitación modal controlada y detección coherente de fase se ha propuesto y validado como sensor de índice de refracción. Los chips se fabricaron en una plataforma de nitruro de silicio y se midieron a la longitud de onda 1.55 μm con excelentes resultados, alcanzando límites de detección en torno a 10^{-7} RIU. Esta cifra es la mejor que se ha reportado, hasta donde llegan los conocimientos de la autora, en un sensor bimodal operando en el del infrarrojo cercano. Esta contribución está publicada en [93].

Guías de onda para espectroscopía de absorción

Pese a que existe una amplia variedad de guías de onda orientadas a la espectroscopía de absorción en el infrarrojo medio, comparar entre sí las distintas alternativas es complicado, pues habitualmente han sido diseñadas siguiendo distintos criterios y para distintas aplicaciones. Para abordar este problema, con foco en el análisis de muestras líquidas, aquí se ha desarrollado una expresión analítica para el LOD, que anticipa la exitencia de una longitud óptima de interacción. Guías en cuatro plataformas convencionales han sido diseñadas con el objetivo de optimizar su LOD, y sus características (sensibilidad, pérdidas, límite de detección) han sido estudiadas mediante simulaciones electromagnéticas. Este enfoque no sólo ha permitido proponer un paradigma general para el diseño de guías de sensado de absorción con óptimas prestaciones, sino también establecer, por vez primera, una comparación justa entre plataformas. Este estudio y sus resultados se hallan publicados en [95].

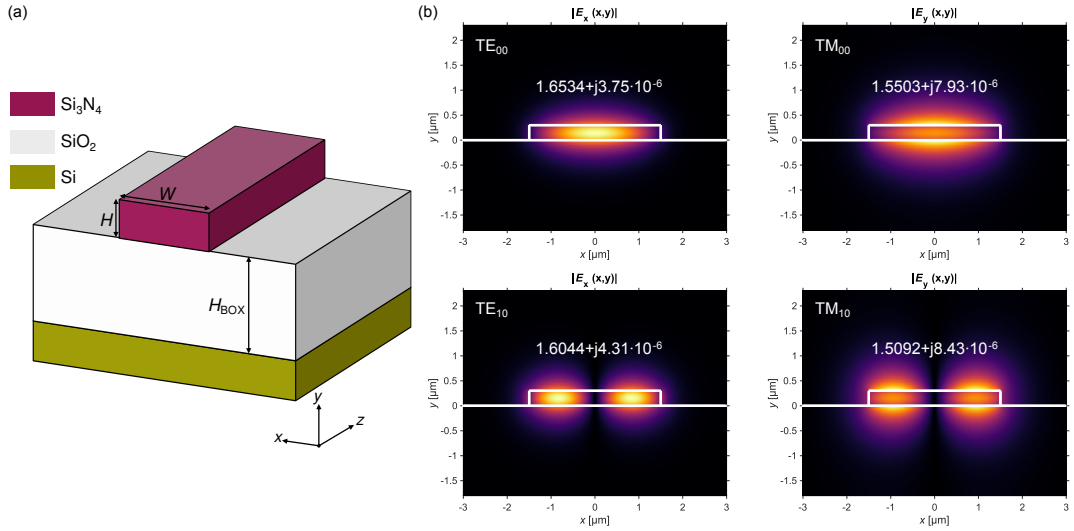

Figura G.3: (a) Guía *strip* en una plataforma de nitruro de silicio, donde la cubierta de dióxido de silicio no se muestra por visibilidad (b) Perfil de campo de los modos soportados por una guía de nitruro de silicio de dimensiones $H = 0.3$ µm, $H_{\text{BOX}} = 3$ µm y $W = 3$ µm.

G.2 Sensores fotónicos integrados basados en guías de onda

Los principios fundamentales de los sensores basados en guías de onda, que son la base del trabajo de esta tesis, se recogen en esta sección.

G.2.1 Guías sensoras

Una guía dieléctrica, como la *strip* de nitruro de silicio representada en la Fig. G.3(a), es una estructura formada por capas de materiales dieléctricos, en la que la luz se confina en una capa de guiado, que tiene un índice de refracción mayor que en el de las cubiertas inferior y superior. La descripción electromagnética de las guías se obtiene mediante la resolución de las ecuaciones de Maxwell [97]. En la Fig. G.3(b), pueden verse los perfiles de campo soportados por una guía de Si_3N_4 con cubierta de SiO_2 y dimensiones $H = 0.3$ µm y $W = 3$ µm. Aunque la mayor parte del campo se concentra en el núcleo de la guía, una fracción se extiende por la cubierta como una onda evanescente. Cada modo tiene un índice efectivo complejo $(n_{\text{eff}} + \text{j}k_{\text{eff}})$, que determina sus características de propagación. Un modo está guiado cuando su n_{eff} es superior al mayor de los índices de las cubiertas y exhibe unas pérdidas de propagación regidas por k_{eff}, como se explica a continuación.

Interacción luz-muestra

En un sensor fotónico integrado, al menos una guía actúa como elemento transductor. Para ello, tal y como se muestra en la Fig. G.4(a), el núcleo de la gúia se expone a la muestra, que se considera la cubierta superior de la guía. La muestra, que puede entenderse como un analito disuelto en una concentración C en un solvente como agua o aire, tiene un índice de refracción complejo $n_{\text{sample}} + \text{j}k_{\text{sample}}$, que depende tanto de la longitud de onda (λ) como de la concentración de analito (C). El modo fundamental que se propaga por la guía, esquematizado en la Fig. G.4(b), tiene un índice effectivo complejo, influenciado por el índice de la muestra. El factor de confinamiento (Γ) da una medida de dicha interacción [114], de modo que

$$\frac{\partial n_{\text{eff}}}{\partial n_{\text{sample}}} = \frac{\partial k_{\text{eff}}}{\partial k_{\text{sample}}} = \Gamma. \tag{G.3}$$

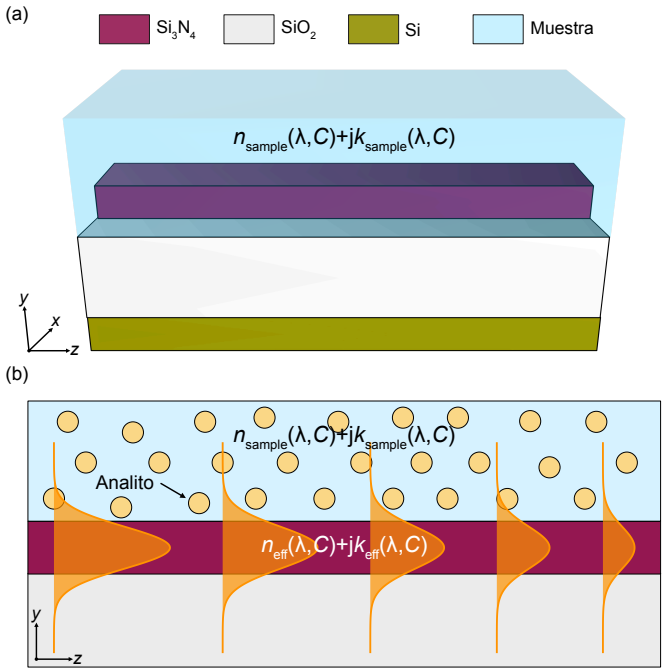

Figura G.4: (a) Guía sensora, en la que el núcleo está expuesto a la muestra. (b) Interacción luz-muestra mediante campo evanescente.

Tras propagarse durante una distancia de interacción L, la amplitud del campo eléctrico puede expresarse como

$$E(L) = E(0)e^{\mathrm{j}\frac{2\pi}{\lambda}(n_{\text{eff}}+\mathrm{j}k_{\text{eff}})L}. \tag{G.4}$$

De aquí, puede definirse una constante de fase

$$\beta_{\text{eff}} = \frac{2\pi}{\lambda}n_{\text{eff}}, \tag{G.5}$$

proporcional a n_{eff}. El desfase acumulado por el modo es por tanto

$$\varphi(L) - \varphi(0) = \beta_{\text{eff}}L = \frac{2\pi}{\lambda}n_{\text{eff}}L, \tag{G.6}$$

donde $\varphi(0)$ es el valor inicial del desfase. Detectar φ conduce a una medida de n_{eff}, que puede relacionarse con n_{sample} mediante Γ. Finalmente, conocer n_{sample} equivale a determinar la cantidad de analito. De manera análoga a β_{eff}, se puede definir un coeficiente de absorción modal, expresado en términos de potencia ($I \propto |E|^2$),

$$\alpha_{\text{eff}} = \frac{4\pi}{\lambda}k_{\text{eff}}, \tag{G.7}$$

directamente proporcional a k_{eff}. La absorción de la muestra contribuye a la modal, de modo que

$$\alpha_{\text{eff}} = \alpha_{\text{int}} + \Gamma\alpha_{\text{sample}}, \tag{G.8}$$

donde α_{int} son las pérdidas intrínsecas de la guía, y $\alpha_{\text{sample}} = (4\pi/\lambda)k_{\text{sample}}$ incluye las pérdidas del solvente (α_{solvent}) y las del analito (α_{a}). Al fotodetectar la señal óptica se obtiene una medida de la intensidad de campo, que puede expresarse como

$$I(L) = I(0)e^{-\alpha_{\text{eff}}L}. \tag{G.9}$$

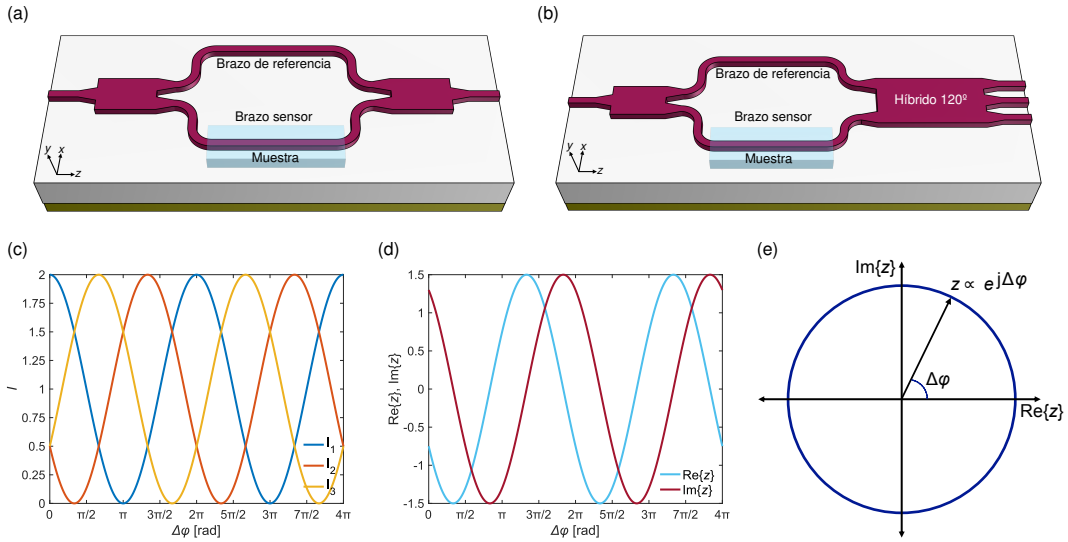

Figura G.5: (a) Sensor MZI convencional. (b) Sensor MZI con lectura coherente de fase. (c) Señales de salida del MZI coherente. (d) Señales en-fase y cuadratura de la señal compleja. (e) Representación en el plano IQ de la señal compleja generada.

De aquí, puede calcularse la absorbancia del analito:

$$A = -\log_{10}\left(\frac{I(L)}{I_0(L)}\right) = \Gamma\epsilon CL, \tag{G.10}$$

donde $I_0 = I(0)e^{-(\alpha_{\text{int}}+\Gamma\alpha_{\text{solvent}})L}$ es la intensidad de base y $\epsilon = \log_{10}(e)\alpha_{\text{a}}/C$ es el coeficiente de absorción molar. Por lo tanto, un analito con ϵ conocido puede detectarse cuantitativamente monitorizando cambios en la absorción de la luz. Sin embargo, con esta técnica, la información de fase se ha perdido en el proceso de detección, por lo que harán falta enfoques más sofisticados para recuperarla.

G.2.2 Arquitecturas para sensado de índice de refracción

El objetivo de las arquitecturas de sensado de índice de refracción es transformar cambios en n_{eff} en magnitudes calculables mediantes señales de intensidad, que pueden extraerse con fotodetectores. Por simplicidad, en esta sección se omitirá la parte imaginaria del índice. Aunque los cambios en n_{eff} pueden medirse mediante resonadores [117], las arquitecturas de interés para esta tesis son las interferométricas. Los interferómetros generan interferencias constructivas o destructivas entre señales de luz con distintos caminos ópticos. Estas configuraciones muestran una gran sensibilidad, por lo que a menudo se usan en aplicaciones de alta exigencia [123, 124].

En un interferómetro de Mach-Zehnder (MZI, por sus siglas en inglés) convencional como el esquematizado en la Fig. G.5(a), el modo que se propaga por el brazo de referencia tiene un índice efectivo $n_{\text{eff}}^{\text{R}}$, diferente al del modo de la rama sensora, $n_{\text{eff}}^{\text{S}}$. A consecuencia, tras viajar por las ramas del sensor, que en este ejemplo se consideran de igual longitud, los modos han acumulado un desfase relativo

$$\Delta\varphi(\Delta n_{\text{eff}}) = \frac{2\pi}{\lambda}\Delta n_{\text{eff}}L, \tag{G.11}$$

donde $\Delta n_{\text{eff}} = n_{\text{eff}}^{\text{S}} - n_{\text{eff}}^{\text{R}}$. Una ventaja de esta arquitectura es que puede trabajar a longitud de onda fija, cuando los cambios en la concentración de analito suceden de manera

dinámica. En los MZI convencionales, los brazos sensor y de referencia se combinan directamente, resultando en una intensidad de salida

$$I(\Delta\varphi) = I_{\mathrm{R}} + I_{\mathrm{S}} + 2\sqrt{I_{\mathrm{R}} I_{\mathrm{S}}}\cos(\Delta\varphi), \tag{G.12}$$

donde I_{R} y I_{S} son las intensidades de los brazos de referencia y de sensado respectivamente. La naturaleza sinusoidal de esta salida genera dificultades analíticas tales como disminución de sensibilidad en los máximos y mínimos y ambigüedad en la dirección del cambio. Una posible solución a estas limitaciones surge de la adaptación de las técnicas de recepción coherente usadas en telecomunicaciones al ámbito del sensado [111, 84].

Detección coherente de fase

Por su importancia en las arquitecturas de sensado NIR de esta tesis, se explica la detección coherente de fase, particularizada a un MZI como el representado en la Fig. G.5(b). El combinador 2×1 de un MZI convencional se sustituye por un MMI 2×3, que actúa como híbrido 120°. Así, cada salida del sensor,

$$I_m(\Delta\varphi) = \frac{1}{3}\left[I_{\mathrm{R}} + I_{\mathrm{S}} + 2\sqrt{I_{\mathrm{R}} I_{\mathrm{S}}}\cos\left(\Delta\varphi + \frac{2\pi}{3}(m-2)\right)\right] \quad m = \{1,2,3\} \tag{G.13}$$

constituye una señal interferométrica equivalente a las obtenidas de manera convencional (Eq. (G.12)), pero desfasadas 120° entre sí, como puede verse en la Fig. G.5(c). Una vez digitalizadas, las salidas se combinan mediante una matriz de lectura, con coeficientes

$$\mathbf{C} = \begin{bmatrix} \frac{-1}{2} + \mathrm{j}\frac{\sqrt{3}}{2} \\ 1 \\ \frac{-1}{2} - \mathrm{j}\frac{\sqrt{3}}{2} \end{bmatrix}, \tag{G.14}$$

para generar una señal compleja en el plano en-fase y quadratura (IQ, por sus siglas en inglés),

$$z = \mathbf{C}^{\mathrm{T}} \cdot \mathbf{I}, \tag{G.15}$$

donde $\mathbf{I} = [I_1\, I_2\, I_3]^{\mathrm{T}}$. Expresando z por sus partes real e imaginaria, representadas en la Fig. G.5(d), se obtiene

$$z = \sqrt{I_{\mathrm{R}} I_{\mathrm{S}}}\,(\cos(\Delta\varphi) + \mathrm{j}\sin(\Delta\varphi)) = \sqrt{I_{\mathrm{R}} I_{\mathrm{S}}}e^{\mathrm{j}\Delta\varphi}, \tag{G.16}$$

que, con cambios continuos de $\Delta\varphi$, proyecta un círculo en el plano IQ, como se muestra en la Fig. G.5(e). Ahora, el desfase buscado puede obtenerse directamente como $\Delta\varphi = \arg(z)$, obteniendo una medida unívoca con sensibilidad constante.

G.2.3 Mecanismos de especificidad

Además de traducir cambios en la parte real o imaginaria del índice efectivo en señales de intensidad medibles, es necesario garantizar la especificidad del sensor, esto es, asegurar que sólo reacciona ante la presencia del analito deseado. Los dos enfoques más comunes para conseguir especificidad son las huellas dactilares espectrales y la funcionalización de superficies, que pueden combinarse para obtener mejores resultados [137, 138]. En espectroscopía de gases, es habitual guiarse por las huellas espectrales de cada molécula, que están consitutuidas por líneas de absorción características como las mostradas en la Fig. G.6(a), y que están relacionadas con movimientos vibraciones y rotacionales a nivel atómico. Estos espectros sirven para identificar y cuantificar los distintos compuestos. Aquí es necesario destacar que la región del MIR es donde estas líneas aparecen con más fuerza. En biosensado, la estrategia dominante es la modificación química de la superficie, añadiendo una capa de biorreconocimiento como la representada en la Fig. G.6(b). Dicha capa hace que únicamente el analito objetivo se adhiera al elemento biorreceptor, garantizando que sólo éste interactúe con la luz guiada [145].

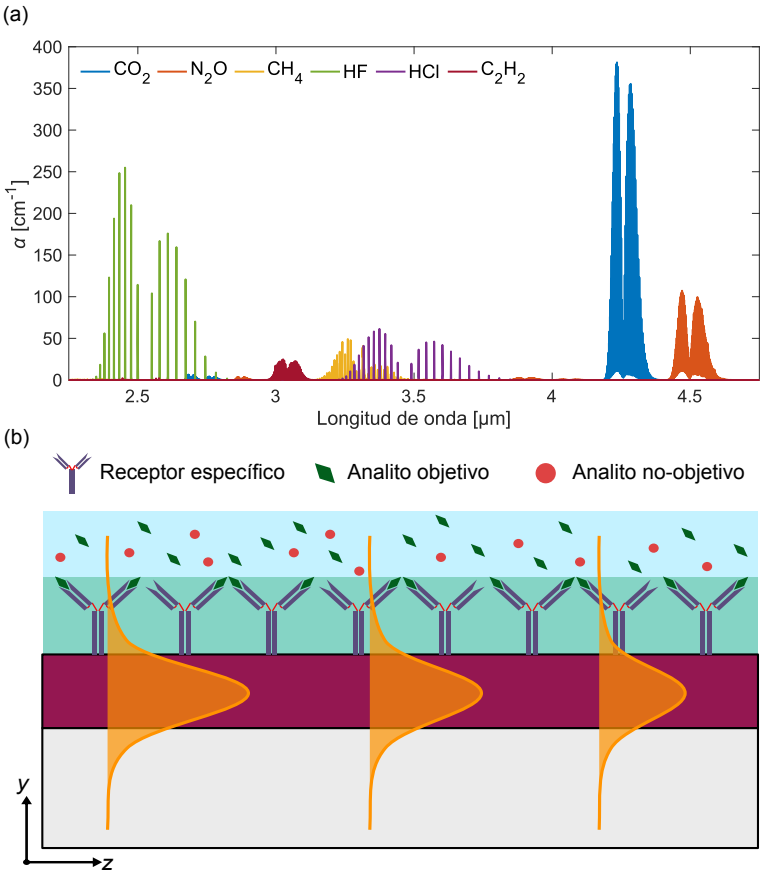

Figura G.6: (a) Espectro característico de absorción de diferentes moléculas en estado gaseoso. Datos extraídos de [46]. (b) Guía funcionalizada para biosensado específico.

G.3 Metodología

En esta sección se resume la metodología de trabajo empleada en el desarrollo de esta tesis, con especial énfasis en el diseño de las guías sensoras, las plataformas de fabricación empleadas, el sistema de caracterización experimental y la técnica de calibración de señales de fase.

G.3.1 Diseño fotónico

La mayor parte del diseño fotónico de esta tesis ha estado centrado en las características de las guías de onda, ya que son el elemento crucial de las arquitecturas de sensado desarrolladas. El análisis de las guías se ha llevado a cabo mediante FemSIM, de Synopsys, un resolutor modal basado en el método de diferencias finitas (FEM, por sus siglas en inglés) [177]. Una vez modelada la guía, especificando su geometría y las características de sus materiales, y calculado el perfil de un modo soportado por la misma, las pérdidas de propagación de dicho modo pueden obtenerse mediante k_{eff}. Para diseñadores fotónicos, es útil expresar estas pérdidas en $\text{dB}\,\text{cm}^{-1}$,

$$L_{\text{prop}} = 10\log_{10}(e)\frac{4\pi}{\lambda_0}k_{\text{eff}}10^{-2}. \tag{G.17}$$

La sensibilidad *bulk* de la guía, que coincide con su factor de confinamiento, puede calcularse simulando variaciones en el índice real o imaginario de la cubierta, y viendo cómo

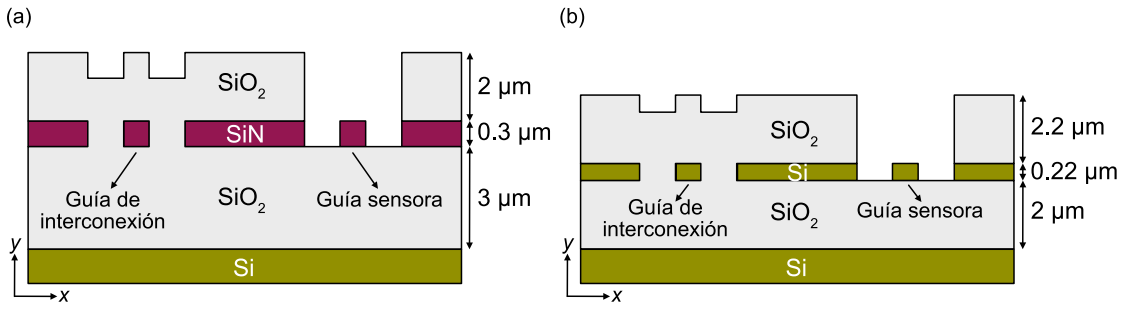

Figura G.7: Plataformas de (a) SiNOI y (b) SOI ofrecidas por Cornerstone y ANT respectivamente. Ambos fabricantes permiten la apertura de ventanas de sensado.

cambia la parte correspondiente del índice efectivo del modo.

$$\Gamma \approx \frac{\Delta n_{\text{eff}}}{\Delta n_{\text{sample}}} \approx \frac{\Delta k_{\text{eff}}}{\Delta k_{\text{sample}}} \tag{G.18}$$

Para calcular pérdidas por fugas de potencia al substrato de silicio, es necesario omitir las pérdidas de los materiales, incluir un fragmento del substrato en la ventana de simulación e introducir capas absorbentes perfectamente adaptadas (PML, por sus siglas en inglés) como condiciones de contorno verticales. En este caso, el valor de L_{prop} calculado corresponderá por completo a este fenómeno. FemSIM soporta el cálculo de modos de guías curvas, por lo que es posible calcular las pérdidas por radiación pura (L_{rad}) de manera análoga a las fugas al substrato, pero introduciendo PML horizontales. Las pérdidas de transición entre guías rectas y curvas (L_{trans}) se calculan mediante el cálculo de la integral de solape [181] entre los modos de ambas guías.

G.3.2 Fabricación de chips

La fabricación de las diferentes generaciones de chips desarrolladas en esta tesis se ha llevado a cabo en empresas que comercializan obleas multiproyecto (MPW, por sus siglas en inglés). Concretamente, se han fabricado chips tanto en Cornerstone [185] como en Applied Nanotools (ANT) [186]. La plataforma de nitruro de silicio sobre aislante (SiNOI, por sus siglas en inglés) ofrecida por Cornerstone, esquematizada en la Fig. G.7(a), se compone de un substrato de silicio cristalino, una capa inferior de SiO_2 de 3 µm y una capa de guiado de 0.3 µm de Si_3N_4. Las guías de interconexión se protegen mediante una cubierta de 2 µm de SiO_2, que puede eliminarse para fabricar guías sensoras. Por su parte, la plataforma de silicio sobre aislante (SOI, por sus siglas en inglés) de ANT, descrita en la Fig. G.7(b) contiene un susbtrato de silicio, 2 µm de SiO_2 inferior y una capa de guiado de silicio de 0.22 nm. De igual manera al caso anterior, las guías de interconexión se protegen con una cubierta de 2.2 µm de SiO_2, estableciendo ventanas sobre las áreas sensoras. Para poder fabricar los sensores diseñados, es necesario enviar a la fábrica una máscara del chip. En esta tesis, las máscaras se han preparado utilizando las herramientas de software libre conocidas como Nazca Design Tools [187], basadas en Phython-3.

G.3.3 Sistema de medidas

El sistema de medidas con el que se han caracterizado los sensores que se presentarán en las Secciones G.4 y G.5 se muestra esquemáticamente en la Fig. G.8. Pueden distinguirse distintos componentes: optoelectrónica, microfluídica e interfaz software. El comportamiento del sistema es el siguiente. Una fuente láser emite luz NIR, que se amplifica en un amplificador de fibra dopada con erbio (EDFA, por sus siglas en inglés). La polarización

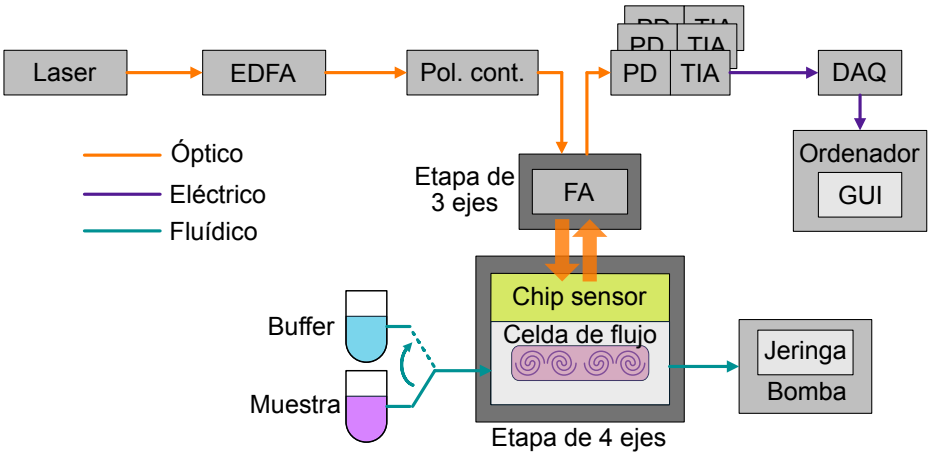

Figura G.8: Esquemático del sistema de medidas, que incorpora elementos ópticos, electrónicos y fluídicos.

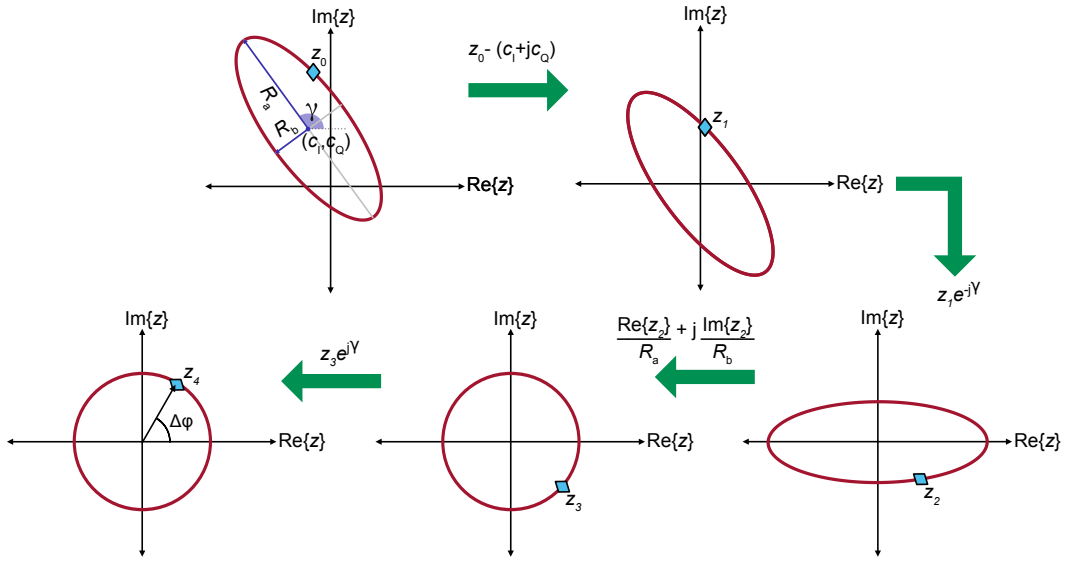

Figura G.9: Ilustración del funcionamiento del algoritmo de calibración utilizado para recuperar la señal de fase, basado en ajustar los puntos medidos a una elipse y transformarla en un círculo.

de entrada al chip se controla manualmente mediante un controlador de polarización. Un array de fibras (FA, por sus siglas en inglés) angularmente pulido, montado sobre una plataforma de tres ejes, se utiliza para acoplar la luz al chip, que a su vez se halla montado sobre una plataforma de cuatro ejes para facilitar el alineamiento. La muestra a analizar circula sobre el área de sensado en un canal de microfluídica, en alternancia con una sustancia *buffer*. Las señales de salida del sensor se acoplan de nuevo al FA y se dirigen a fotodetectores (PD, por sus siglas en inglés) amplificados por transimpedancia (TIA, por sus siglas en inglés). Los voltajes resultantes se digitalizan mediante una tarjeta de adquisición de datos (DAQ, por sus siglas en inglés) y se graban con una interfaz de usuario gráfica (GUI, por sus siglas en inglés) controlada por Matlab.

G.3.4 Calibración de la señal de fase

Los coeficientes de la matriz de calibración de la Eq. (G.14) (Sección G.2.2) son válidos bajo la asunción de componentes ideales. Sin embargo, en sistemas prácticos, las tolerancias

de fabrición y la diferencias en la eficiencia de acoplamiento de las distintas salidas del sensor provocan distorsiones en la señal. A consecuencia, la señal compleja generada se asemeja a una elipse en el plano IQ en lugar de a un círculo. Esto a su vez provoca errores en la lectura de fase. Para corregir dichos errores, se emplea una téncica de calibración ciega basada en ajustar los puntos medidos a una elipse, que posteriormente se transforma en un círculo mediante operaciones lineales [84]. Los pasos del algoritmo, gráficamente descrito en la Fig. G.9, se resumen a continuación.

1. Aplicar la matriz de calibración ideal a las señales de salida para obtener la señal inicial z_0.

2. Seleccionar un fragmento de la señal z_0 y ajustar los puntos a los coeficientes de una elipse siguiendo el método de Taubin [192].

3. Convertir los coeficientes algebraicos obtenidos en el radio del eje mayor (R_a) y el del eje menor (R_b), el ángulo del eje mayor con el eje real (γ) y el punto central de la elipse $(c_\mathrm{I} + \mathrm{j}c_\mathrm{Q})$.

4. Centrar en el origen: $z_1 = z_0 - (c_\mathrm{I} + \mathrm{j}c_\mathrm{Q})$.

5. Rotar para alinear el eje mayor con el real: $z_2 = z_1 e^{-\mathrm{j}\gamma}$.

6. Escalar a un círculo: $z_3 = \frac{\mathrm{Re}\{z_2\}}{R_\mathrm{a}} + \mathrm{j}\frac{\mathrm{Im}\{z_2\}}{R_\mathrm{b}}$.

7. Restaurar el ángulo original: $z_4 = z_3 e^{\mathrm{j}\gamma}$.

G.4 Sensor de índice de refracción complejo en el infrarrojo cercano

La mayoría de los sensores fotónicos detectan analitos basándose únicamente en medidas bien de la parte real, bien de la parte imaginaria, del índice de refracción. No obstante, resultaría interesante disponer de ambas magnitudes simultáneamente para caracterizar completamente una muestra, además de combinar la extrema sensibilidad del sensado de índice de refracción con la especificidad inherente de la espectroscopía de absorción. Estos dispositivos encontrarían aplicaciones en áreas como la ciencia de materiales [86, 198] y la detección de compuestos orgánicos volátiles (VOC, por sus siglas en inglés) [201]. En esta sección se presenta un sensor de índice de refracción complejo basado en un MZI integrado en una plataforma de nitruro de silicio, que opera en el infrarrojo cercano. Esta es una de las contribuciones centrales de esta tesis y los principales resultados se encuentran publicados en A. Torres-Cubillo, A. Sánchez-Postigo, J. Jágerská, J. G. Wangüemert-Pérez, and R. Halir, "Simultaneous measurement of refraction and absorption with an integrated near-infrared Mach–Zehnder interferometer," Optics & Laser Technology **177**, 111154 (2024).

G.4.1 Arquitectura del sensor

La Fig. G.10 muestra un diagrama del sensor propuesto, que se diferencia del MZI coherente de la Fig. G.5(b) en la incoroporación de MMIs 1×2 para entregar lecturas directas de las intensidades de las ramas de sensado y referencia.

La luz acoplada al chip se divide entre los brazos sensor y de referencia, de longitud L. En el brazo de referencia, el modo se propaga sin perturbaciones, con un índice efectivo $n_\mathrm{eff}^\mathrm{R}(\lambda) + \mathrm{j}k_\mathrm{eff}^\mathrm{R}(\lambda)$. Por su parte, el brazo sensor está expuesto a la muestra, compuesta por un disolvente y un analito disuelto en una concentración C. El modo sensor posee un

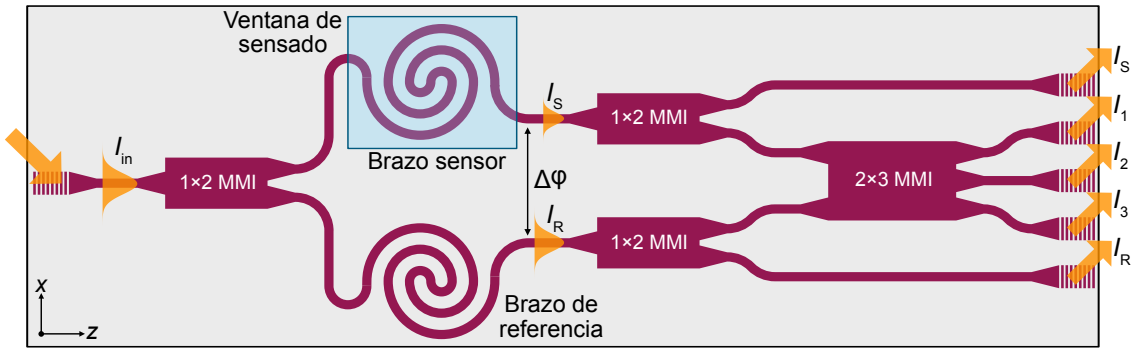

Figura G.10: Diagrama esquemático del sensor de índice de refracción complejo, basado en un MZI con detección coherente modificado.

factor de confinamiento Γ e interactúa con la muestra a través de su campo evanescente. Un cambio en C modifica el índice de refracción de la muestra, esto es,

$$\begin{aligned} n_{\text{sample}}(\lambda, C) &= n_{\text{sample}}(\lambda, 0) + \Delta n_{\text{sample}}(\lambda, C) \\ k_{\text{sample}}(\lambda, C) &= k_{\text{sample}}(\lambda, 0) + \Delta k_{\text{sample}}(\lambda, C), \end{aligned} \tag{G.19}$$

donde $n_{\text{sample}}(\lambda, 0) + \text{j}k_{\text{sample}}(\lambda, 0)$ es el índice de refracción complejo del solvente puro. Debido a la interacción entre la luz y la muestra, el índice efectivo complejo del modo también depende de la concentración de analito, y puede expresarse como

$$\begin{aligned} n_{\text{eff}}^{\text{S}}(\lambda, C) &= n_{\text{eff}}^{\text{S}}(\lambda, 0) + \Gamma(\lambda)\Delta n_{\text{sample}}(\lambda, C) \\ k_{\text{eff}}^{\text{S}}(\lambda, C) &= k_{\text{eff}}^{\text{S}}(\lambda, 0) + \Gamma(\lambda)\Delta k_{\text{sample}}(\lambda, C), \end{aligned} \tag{G.20}$$

donde $n_{\text{eff}}^{\text{S}}(\lambda, 0)+\text{j}k_{\text{eff}}^{\text{S}}(\lambda, 0)$ es el valor del índice efectivo cuando la cubierta está compuesta por el solvente puro. Al final de los brazos del interferómetro, cada modo ha acumulado un desfase

$$\begin{aligned} \varphi_{\text{R}}(\lambda) &= \frac{2\pi}{\lambda} n_{\text{eff}}^{\text{R}}(\lambda) L \\ \varphi_{\text{S}}(\lambda, C) &= \frac{2\pi}{\lambda} n_{\text{eff}}^{\text{S}}(\lambda, C) L \end{aligned} \tag{G.21}$$

con respecto al inicio de la guía, y viaja con una intensidad

$$\begin{aligned} I_{\text{R}}(\lambda) &= \frac{I_{\text{in}}}{2} e^{-\frac{4\pi}{\lambda} k_{\text{eff}}^{\text{R}}(\lambda) L} \\ I_{\text{S}}(\lambda, C) &= \frac{I_{\text{in}}}{2} e^{-\frac{4\pi}{\lambda} k_{\text{eff}}^{\text{S}}(\lambda, C) L}, \end{aligned} \tag{G.22}$$

donde I_{in} es la intensidad acoplada al chip.

El desfase relativo entre los modos sensor y de referencia puede escribirse como

$$\Delta\varphi(\lambda, C) = \varphi_{\text{S}}(\lambda, C) - \varphi_{\text{R}}(\lambda) = \frac{2\pi}{\lambda} \Delta n_{\text{eff}}(\lambda, C) L, \tag{G.23}$$

donde $\Delta n_{\text{eff}}(\lambda, C) = n_{\text{eff}}^{\text{S}}(\lambda, C) - n_{\text{eff}}^{\text{R}}(\lambda)$. La diferencia entre el desfase relativo con y sin analito da una medida proporcional a Δn_{sample}, a partir del que puede calcularse la concentración.

$$\Delta\varphi(\lambda, C) - \Delta\varphi(\lambda, 0) = \frac{2\pi}{\lambda} \Gamma(\lambda) \Delta n_{\text{sample}}(\lambda, C) L \tag{G.24}$$

Tabla G.1: Expresiones de las métricas del sensor de índice de refracción complejo propuesto.

Métrica	**Expresión**	
	Índice real	Índice imaginario
Sensibilidad modal (S_{m})	$\frac{\partial n_{\mathrm{eff}}}{\partial n_{\mathrm{sample}}} = \Gamma$	$\frac{\partial k_{\mathrm{eff}}}{\partial k_{\mathrm{sample}}} = \Gamma$
Sensibilidad arquitectónica (S_{a})	$\frac{\partial \Delta\varphi}{\partial n_{\mathrm{eff}}} = \frac{2\pi}{\lambda} L$	$\frac{\partial A}{\partial k_{\mathrm{eff}}} = \frac{4\pi}{\lambda} \log_{10}(e) L$
Sensibilidad del dispositivo ($S_{\mathrm{n,k}}$)	$\frac{\partial \Delta\varphi}{\partial n_{\mathrm{sample}}} = \frac{2\pi}{\lambda} \Gamma L$	$\frac{\partial A}{\partial k_{\mathrm{sample}}} = \frac{4\pi}{\lambda} \log_{10}(e) \Gamma L$
Límite de detección (LOD)	$\mathrm{LOD_n} = \frac{3\sigma_{\Delta\varphi}}{S_{\mathrm{n}}}$	$\mathrm{LOD_k} = \frac{3\sigma_A}{S_{\mathrm{k}}}$

Tabla G.2: Factor de confinamiento y pérdidas de propagación de las guías sensoras de los sensores de índice de refracción complejo.

$\boldsymbol{\Gamma}$	$\boldsymbol{L_{\mathrm{H2O}}}$ **[dB cm^{-1}]**	$\boldsymbol{L_{\mathrm{leak}}}$ **[dB cm^{-1}]**	$\boldsymbol{L_{90}}$ **[dB]**
0.22	11.38	0.018	0.011

Para detectar el desfase con la técnica de detección coherente explicada en la Sección G.2.2, las señales sensora y de referencia se llevan hasta un híbrido 120°, implementado mediante un MMI 2×3. La señal compleja

$$z(\lambda, C) = \frac{1}{2}\sqrt{I_{\mathrm{R}}(\lambda) I_{\mathrm{S}}(\lambda, C)} e^{\mathrm{j}\Delta\varphi(\lambda, C)}, \tag{G.25}$$

se genera al combinar las salidas de dicho MMI.

Introduciendo un MMI 1×2 al final de cada espiral, se pueden detectar directamente señales de intensidad proporcionales a I_{R} e I_{S}. Así, la absorbancia del analito se puede calcular como

$$A(\lambda, C) = -\log_{10}\left(\frac{I_{\mathrm{S}}(\lambda, C)}{I_{\mathrm{S}}(\lambda, 0)}\right) = \log_{10}(e)\frac{4\pi}{\lambda}\Gamma(\lambda)\Delta k_{\mathrm{sample}}(\lambda, C) L, \tag{G.26}$$

donde $I_{\mathrm{S}}(\lambda, 0)$ es la intensidad detectada con el solvente puro. La absorbancia es directamente proporcional a $\Delta k_{\mathrm{sample}}$ y, además, la relación entre $\Delta k_{\mathrm{sample}}$ y C se puede explicitar haciendo uso del coeficiente de absorción molar introducido en la Sección G.2.1.

$$\Delta k_{\mathrm{sample}}(\lambda, C) = \frac{\epsilon(\lambda)}{\log_{10}(e)\frac{4\pi}{\lambda}} C \tag{G.27}$$

Las expresiones de las métricas para evaluar el sensor propuesto en términos de sensibilidad (modal, de la arquitectura y del dispositivo) y límite de detección, determinado por el suelo de ruido de la señal de salida (σ), se recogen en la Tabla G.1.

G.4.2 Diseño del sensor

La primera generación de sensores se diseñó para la plataforma de SiNOI de Cornerstone, descrita en la Sección G.3.2, en el marco de una colaboración con la Universidad de Southampton. Desaforturnadamente, tras una serie de evaluaciones previas, estos sensores se descartaron, mayoritariamente debido a su altas pérdidas de propagación. Para corregir los problemas diagnosticados, se diseñó y fabricó una segunda generación de chips, que se fabricaron en misma plataforma, en la tirada comercial SiN MPW#3. Estos sensores resultaron exitosos y con ellos se han realizado los experimentos presentados en esta tesis. Las principales características sobre sus componentes y disposición en la máscara del sensor se resumen en esta sección.

La sección transversal de las guías de referencia y sensado diseñadas para $\lambda_0 = 1.55$ µm se muestran en la Fig. G.11(a), así como los modos TE fundamentales soportados por dichas guías. La guía sensora es el elemento crítico de la arquitectura, por lo que centró el

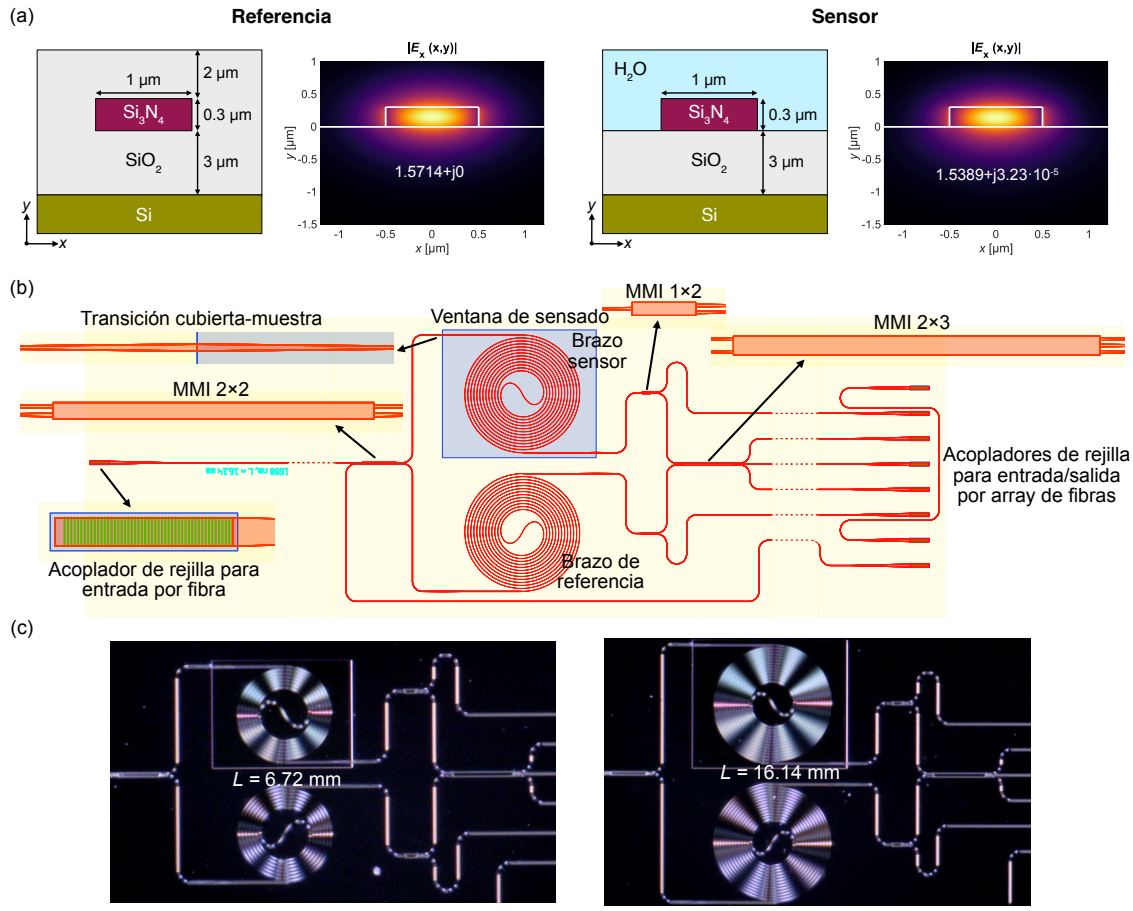

Figura G.11: (a) Sección transversal y perfil de campo del modo TE fundamental de las guías de referencia y sensora. (b) Disposición de los elementos del sensor de segunda generación en la máscara preparada para su fabricación. (c) Fotografías al microscopio óptico de dos de los sensores desarrollados.

Tabla G.3: Características de las guías en espiral de los sensores complejos implementados.

L [mm]	Área [mm^2]	S_n [rad/RIU]	S_k [au/RIU]	L_{rad}^{tot} [dB]	L_{H2O}^{tot} [dB]
6.72	0.39	$5.97 \cdot 10^3$	$5.14 \cdot 10^3$	$3.57 \cdot 10^{-3}$	7.65
16.14	0.57	$14.35 \cdot 10^3$	$12.34 \cdot 10^3$	$3.58 \cdot 10^{-3}$	18.37

análisis electromagnético. La Tabla G.2 muestra los valores calculados de factor de confinamiento (Γ), pérdidas de propagación por absorción del agua (L_{H2O}), pérdidas por fugas al substrato (L_{leak}) y por cada curva de 90° (L_{90}). Aquí se evidencia que las pérdidas del agua son dominantes frente al resto. Los MMI y los acopladores de rejilla son diseños homogéneos convencionales para esta plataforma. La disposición de los componentes diseñados en la máscara del sensor puede observarse en la Fig. G.11(b). La distribución de los acopladores responde al objetivo de evitar que la señal de entrada enmascare a las señales de salida, más débiles. Para incrementar la longitud de interacción sin comprometer el espacio ocupado, se integraron guías en espiral con distintas longitudes. En la Tabla G.3 se recogen las caraceterísticas de dichas espirales en términos de sensibilidad, pérdidas de radiación y pérdidas por absorción esperadas. Por último, la Fig. G.11(c) muestra fotografías al microscopio óptico de dos de los sensores, una vez fabricados. La evaluación óptica de estos sensores resultó satisfactoria debido a las bajas pérdidas de propagación y reflexiones en-chip medidas.

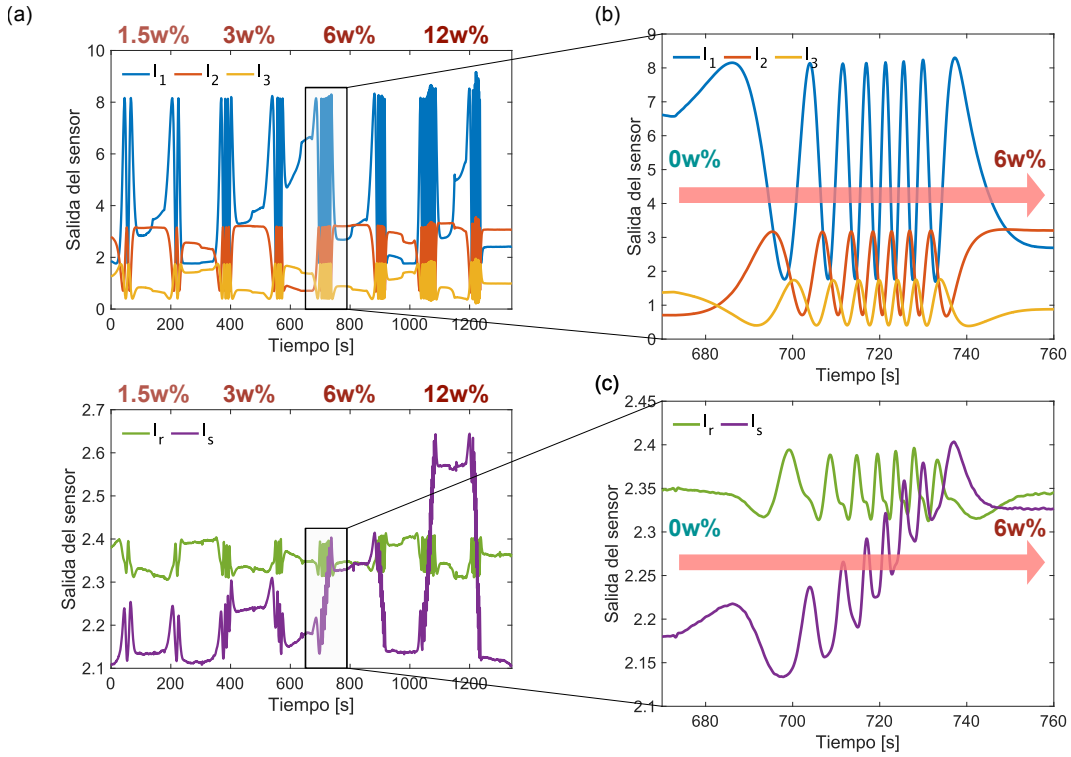

Figura G.12: (a) Salida del sensor L_1 durante un experimento de sensado homogéneo. Fragmento de las señales (b) interferométricas y (c) de intensidad.

G.4.3 Experimentos de sensado homogéneo

Los sensores $L_1 = 6.72\,\text{mm}$ y $L_2 = 16.14\,\text{mm}$ se evaluaron en términos de linealidad, sensibilidad y LOD mediante experimentos de sensado homogéneo utilizando disoluciones salinas (NaCl) en agua deionizada con concentraciones $C = \{1.5, 3, 6, 12\}\,\text{w}\,\%$. La parte real del índice de refracción de las muestras se calculó a partir del modelo desarrollado en [221]. Desafortunadamente, en el caso de la parte imaginaria del índice, no fue posible encontrar la información necesaria en la literatura de manera precisa, ya que la absorción del NaCl es muy pequeña en relación a la del agua. Por lo tanto, los valores asumidos se estimaron a partir de los datos de [222]. Cabe destacar aquí que el cambio esperado en la absorbancia con la adición de sal es negativo, pues una mayor concentración de sal supone una leve disminución de la cantidad de agua y, por tanto, de las pérdidas asociadas a su absorción. Las muestras se hicieron fluir por el canal de microfluidica a una velocidad de $30\,\mu\text{L/min}$ en alternancia con el agua pura.

La Fig. G.12 muestra las señales de salida de uno de los sensores (L_1) medidos durante un experimento de sensado homogéneo a longitud de onda fija $\lambda_0 = 1.55\,\mu\text{m}$. En la Fig. G.12(b), pueden apreciarse las señales interferométricas, desfasadas 120°, como cabía esperar. Sin embargo, atendiendo a las señales de intensidad, tal y como se muestra en la Fig. G.12(c), se observan unas fuertes oscilaciones espurias en los periodos de transición entre el agua pura y las muestras. Dichas oscilaciones se trasladan al cálculo de la absorbancia, degradando la medida. Tras comparar las oscilaciones de las señales de intensidad con las de las señales de fase adyacentes, se llegó a la conclusión de que existía interferencia provocada por las señales interferométricas. Para mejorar la calidad de la lectura de la absorbancia, se desarrolló un modelo analítico de dicha interferencia, dando como resultado la siguiente ecuación:

$$I_S^{\text{PD}} \approx (1 + 2\gamma)|s|^2 + 2\gamma \cos(\Delta\varphi - \Theta_1)|s|. \tag{G.28}$$

Tabla G.4: Límites de detección de sensores integrados de índice de refracción complejo operando en distintos regímenes espectrales. Los resultados de este trabajo se muestran en negritas.

Ref.	**Régimen**	**Arquitectura**	$\mathbf{LOD_n}[\mathbf{10^{-6}RIU}]$	$\mathbf{LOD_k}[\mathbf{10^{-6}RIU}]$
[202]	VIS	YI	15	1.6
[203]		Microdisco de PC	30	200
[204]	NIR	RR SWG	55	1.7
Este trabajo		**MZI coherente**	**1.9**	**2.1**
[208]	MIR	RR suspendido	8	13
[154]		RR en cascada	9900	210

Aquí, I_S^{PD} es la intensidad detectada por el fotodetector designado a la lectura de la intesidad del brazo sensor, $\Delta\varphi$ es el desfase medido mediante las señales interferométricas y γ y Θ_1 son parámetros ajustables que definen la interferencia. La Ec. (G.28) se utilizó para corregir las lecturas de intensidad, obteniendo reducciones significativas en la amplitud de las oscilaciones y corrigiendo así las señales de absorbancia calculadas.

Dos ejemplos de lecturas finales de desfase y absorbancia se enseñan en las Figs. G.13(a)-(b) para los sensores L_1 y L_2 respectivamente, donde los intervalos considerados en el cálculo de los valores de saturación se hallan señalados. Dichos valores se muestran en en las Figs. G.13(c)-(d) para tres chips diferentes. Todos los sensores muestran una buena linealidad, con $R^2 > 0.9861$ para el desfase y $R^2 > 0.9631$ para la absorbancia. La absorbancia del sensor L_1 exhibe una mayor variabilidad entre chips, lo que se puede atribuir a un mayor impacto de las interferencias o de otros factores externos cuando los valores de absorbancia objetivo son pequeños. Las sensibilidades medias del dispositivo frente a cambios en el índice de refracción complejo se calcularon como $S_n = 5.07 \cdot 10^3$ rad/RIU, $S_k = 2.23 \cdot 10^3$ au/RIU y $S_n = 10.69 \cdot 10^3$ rad/RIU, $S_k = 3.55 \cdot 10^3$ au/RIU para los sensores L_1 y L_2 respectivamente. Para determinar el LOD, se evaluó el ruido de fragmentos de 30 s de ruido de las señales de desfase y absorbancia correspondientes a la circulación de agua pura, en las que la salida era estable y cercana a cero. Los LOD medios calculados son $\text{LOD}_n = 1.93 \cdot 10^{-6}$ RIU, $\text{LOD}_k = 2.09 \cdot 10^{-6}$ RIU y $\text{LOD}_n = 2.48 \cdot 10^{-6}$ RIU, $\text{LOD}_k = 2.77 \cdot 10^{-6}$ RIU para los sensores L_1 y L_2 respectivamente. Las mejores prestaciones se obtuvieron para el sensor más corto, debido a la menor influencia de las pérdidas del agua. Considerando este resultado, este trabajo se encuentra entre los mejores del estado de la cuestión de los sensores integrados de índice de refracción complejo, como puede verse en la Tabla G.4. Es más, la arquitectura propuesta es la única con idénticas capacidades para detectar tanto n como k, lo que es especialmente desafiante mientras se opera en el NIR.

Para complementar los resultados a longitud de onda fija, se llevaron a cabo una serie de medidas espectroscópicas, utilizando tanto las disoluciones salinas descritas anteriormente como muestras de isopropanol y agua puros. Los resultados obtenidos fueron prometedores, mostrando un buen ajuste con las predicciones teóricas, pero para una evaluación precisa del sensor como dispositivo para espectroscopía de dispersión (refracción) y absorción simultáneas aún es necesario emprender mejoras en el diseño y el sistema de medida. No obstante, la arquitectura demostrada resulta prometedora para su extensión al MIR, donde podría operar en las regiones de huella dactilar de numerosos compuestos químicos, obteniendo valiosos resultados.

G.5 Sensor bimodal de índice de refracción en el infrarrojo cercano

Los sensores basados en guías bimodales han aparecido con la intención de reducir el área ocupada por las arquitecturas interferométricas convencionales, que requieren tanto un

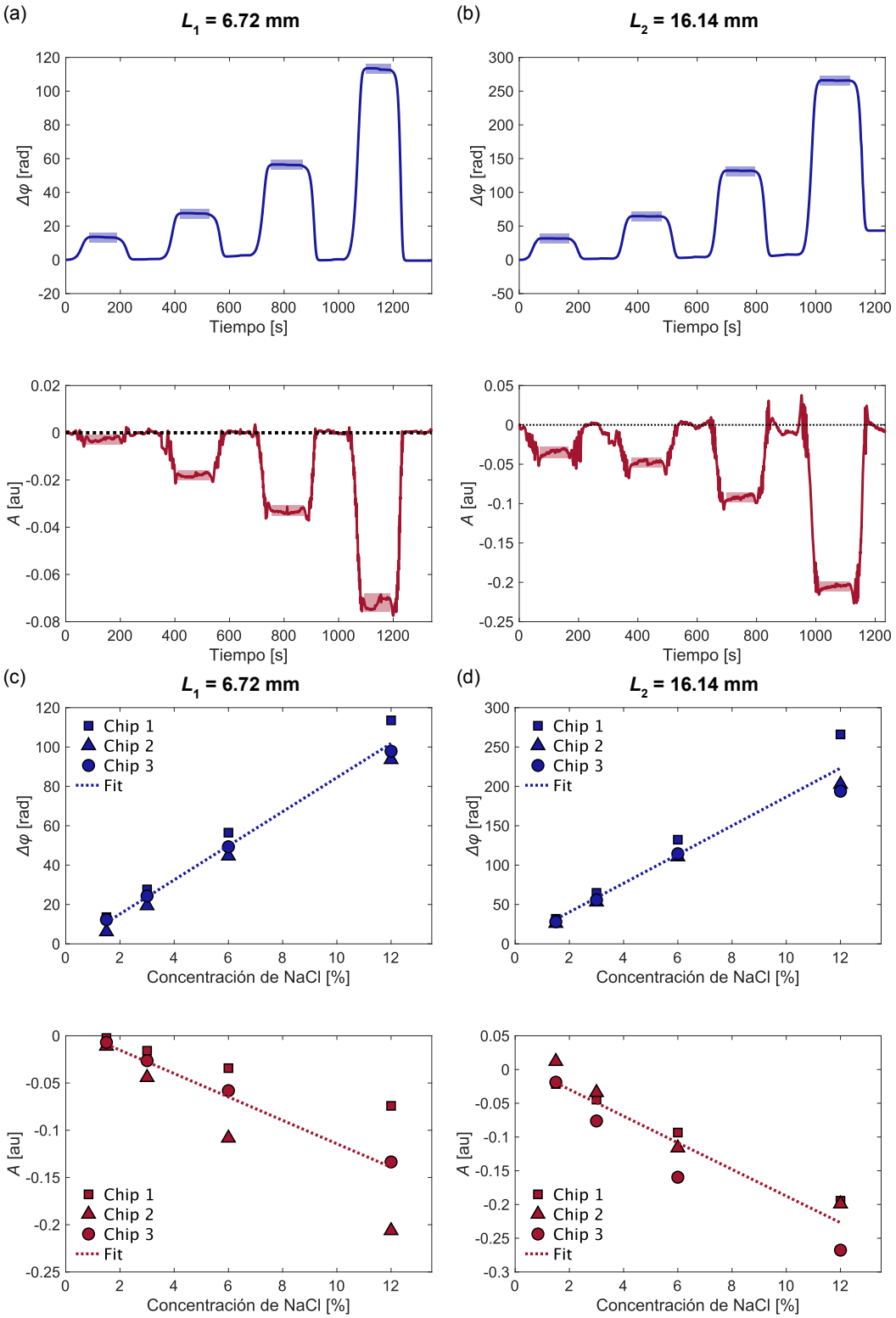

Figura G.13: Señales de desfase y absorbancia calculadas a partir de dos medidas de los sensores (a) L_1 y (b) L_2. Valores de saturación de desfase y absorbancia para los sensores (c) L_1 y (d) L_2 en tres chips diferentes.

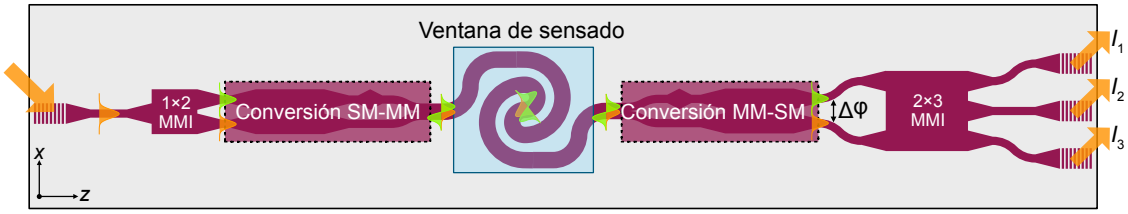

Figura G.14: Diagrama esquemático del sensor bimodal de índice de refracción con excitación controlada de modos y detección coherente.

brazo sensor como uno de referencia [90]. Para conseguir el mismo resultado con un único brazo, se excitan dos modos ortogonales soportados por una guía multimodo (MM). Sin embargo, estos sensores sufren las desventajas de una excitación modal incontrolada, que puede provocar fuertes reflexiones, y de las limitaciones de la lectura de señales sinusoidales, destacadas en la Sección G.2.2. En esta sección se presenta un novedoso sensor de índice de refracción, que combina una guía sensora bimodal con una excitación y separación de modos controlada y una lectura coherente de fase. Este sensor constituye una de las contribuciones principales de este trabajo y los principales resultados están publicados en A. Torres-Cubillo, J. M. Luque-González, A. Sánchez-Postigo, A. Fernández-Gavela, J. G. Wangüemert-Pérez, Í. Molina-Fernández, and R. Halir, "High-performance bimodal evanescent-field sensor with coherent phase readout," Journal of Lightwave Technology **42(8)**, 3010-3015 (2024).

G.5.1 Arquitectura del sensor

La Fig. G.14 muestra un diagrama esquemático del sensor propuesto, que está basado en una guía bimodal, que soporta dos modos TE. Un convertidor de modos produce una excitación modal controlada a la entrada de la guía sensora. La misma arquitectura, dispuesta de manera simétrica, separa entre sí los modos para que constituyan las entradas de la etapa de detección coherente.

El funcionamiento es el siguiente. La luz acoplada al chip se divide para alimentar el conversor de modos, mediante el cual se excitan los dos primeros modos TE de la guía sensora bimodal. En dicha guía, el modo fundamental (TE_{00}) se propaga con un índice efectivo $n_{\text{eff},0}$ y tiene un factor de confinamiento Γ_0, mientras que el primer modo superior (TE_{10}) hace lo propio con $n_{\text{eff},1}$ y Γ_1. El solapamiento entre el primer modo superior y la muestra es mayor al que experimenta el fundamental, que está más confinado en el núcleo ($\Gamma_1 > \Gamma_0$). Como el sensor opera a longitud de onda constante, se puede considerar que los índices efectivos de los modos dependen únicamente del analito,

$$\begin{aligned} n_{\text{eff},0}(C) &= n_{\text{eff},0}(0) + \Gamma_0 \Delta n_{\text{sample}}(C) \\ n_{\text{eff},1}(C) &= n_{\text{eff},1}(0) + \Gamma_1 \Delta n_{\text{sample}}(C), \end{aligned} \tag{G.29}$$

donde $n_{\text{eff},0}(0)$ y $n_{\text{eff},1}(0)$ son los valores tomados en presencia del solvente puro. Tras propagarse por la guía, cada modo ha acumulado un desfase

$$\begin{aligned} \varphi_0(C) &= \frac{2\pi}{\lambda_0} n_{\text{eff},0}(C) L \\ \varphi_1(C) &= \frac{2\pi}{\lambda_0} n_{\text{eff},1}(C) L. \end{aligned} \tag{G.30}$$

La diferencia en el desfase de los modos puede definirse de manera análoga a un MZI (ver Sección G.2.2).

$$\Delta\varphi(C) = \varphi_1(C) - \varphi_0(C) = \frac{2\pi}{\lambda_0} \Delta n_{\text{eff}}(C) L, \tag{G.31}$$

Tabla G.5: Expresiones de las métricas del sensor bimodal de índice de refracción propuesto.

Métrica	**Expresión**
Sensibilidad modal diferencial (S_d)	$\frac{\partial n_{\mathrm{eff},1}}{\partial n_\mathrm{sample}} - \frac{\partial n_{\mathrm{eff},0}}{\partial n_\mathrm{sample}} = \Gamma_1 - \Gamma_0$
Sensibilidad arquitectónica (S_a)	$\frac{\partial \Delta\varphi}{\partial n_\mathrm{eff}} = \frac{2\pi}{\lambda} L$
Sensibilidad del dispositivo ($S_\mathrm{n,k}$)	$\frac{\partial \Delta\varphi}{\partial n_\mathrm{sample}} = \frac{2\pi}{\lambda}(\Gamma_1 - \Gamma_0)L$
Límite de detección (LOD)	$\mathrm{LOD_n} = \frac{3\sigma_{\Delta\varphi}}{S_\mathrm{n}}$

donde $\Delta n_\mathrm{eff}(C) = n_{\mathrm{eff},1}(C) - n_{\mathrm{eff},0}(C)$. Normalizando este desfase relativo, de manera que

$$\Delta\varphi(C) - \Delta\varphi(0) = \frac{2\pi}{\lambda_0}(\Gamma_1 - \Gamma_0)\Delta n_\mathrm{sample}(C)L, \tag{G.32}$$

se obtiene una medida proporcional a Δn_sample. Los modos de la guía bimodal se dividen en dos modos fundamentales de guías monomodo (SM, por sus siglas en inglés) por la operación inversa del conversor modal. Estos dos modos conservan $\Delta\varphi$, y son las entradas del MMI 2×3. Así se permite ejecutar la detección coherente, generando la señal compleja

$$z(C) = \sqrt{I_0 I_1} e^{\mathrm{j}\Delta\varphi(C)}, \tag{G.33}$$

donde I_0 and I_1 son las intensidades de los modos TE_{00} y TE_{10} respectivamente y $\Delta\varphi = \arg(z)$.

Las expresiones de las métricas para evaluar el sensor propuesto en términos de sensibilidad (diferencial, de la arquitectura y del dispositivo) y límite de detección, determinado por el suelo de ruido de la señal de salida ($\sigma_{\Delta\varphi}$), se recogen en la Tabla G.5.

G.5.2 Diseño del sensor

Se diseñó una primera generación de chips para la plataforma de SOI ofrecida por ANT e introducida en la Sección G.3.2 para la longitud de onda de trabajo $\lambda_0 = 1.31$ µm. Desafortunadamente, debido a problemas asociados tanto a la plataforma como al diseño de los sensores, no fue posible obtener resultados de sensado válidos. Sin embargo, gracias a la experiencia adquirida se desarrolló una segunda generación de sensores con altas prestaciones, cuyas caracteristicas se abordan en esta sección. Estos sensores se fabricaron para $\lambda_0 = 1.55$ µm en los mismos chips que los sensores de índice de refracción complejo presentados en la Sección G.4 (MPW#3 de Cornerstone).

El conversor modal implementado para la segunda generación de sensores se muestra esquemáticamente en la Fig. G.15(a). Este dispositivo está basado en el diseño propuesto y validado en [91, 92] y tiene tres subcomponentes: un MMI 2×2 operando como acoplador híbrido a 3 dB-90°, un desfasador (PS, por sus siglas en inglés) y una unión en Y de perfil sinusoidal. El desfasador se compone de dos guías paralelas. Mientras el brazo inferior es una guía monomodo recta, el brazo superior incluye dos transiciones adiabáticas contrapuestas, que tienen el objetivo de incrementar el índice efectivo del modo, introduciendo así un retardo en la propagación, que se corresponde con un desfase de 90° respecto al modo del brazo inferior. Estos modos desfasados se transforman mediante la unión en Y en el modo fundamental y el primer modo superior de la guía bimodal. La sección transversal de dicha guía, así como los perfiles de los modos TE_{00} y TE_{10} excitados, se muestran en la Fig. G.15(b). Tal y como se aprecia en los mapas de campo, el primer modo superior está menos confinado en el núcleo, por lo que, además de ser más sensible, se espera que experimente más perdidas por absorción del agua, fugas al substrato y curvaturas. Los valores calculados de estos parámetros se encuentran recogidos en la Tabla G.6. Con estos valores de factor de confinamiento, la sensibilidad modal diferencial

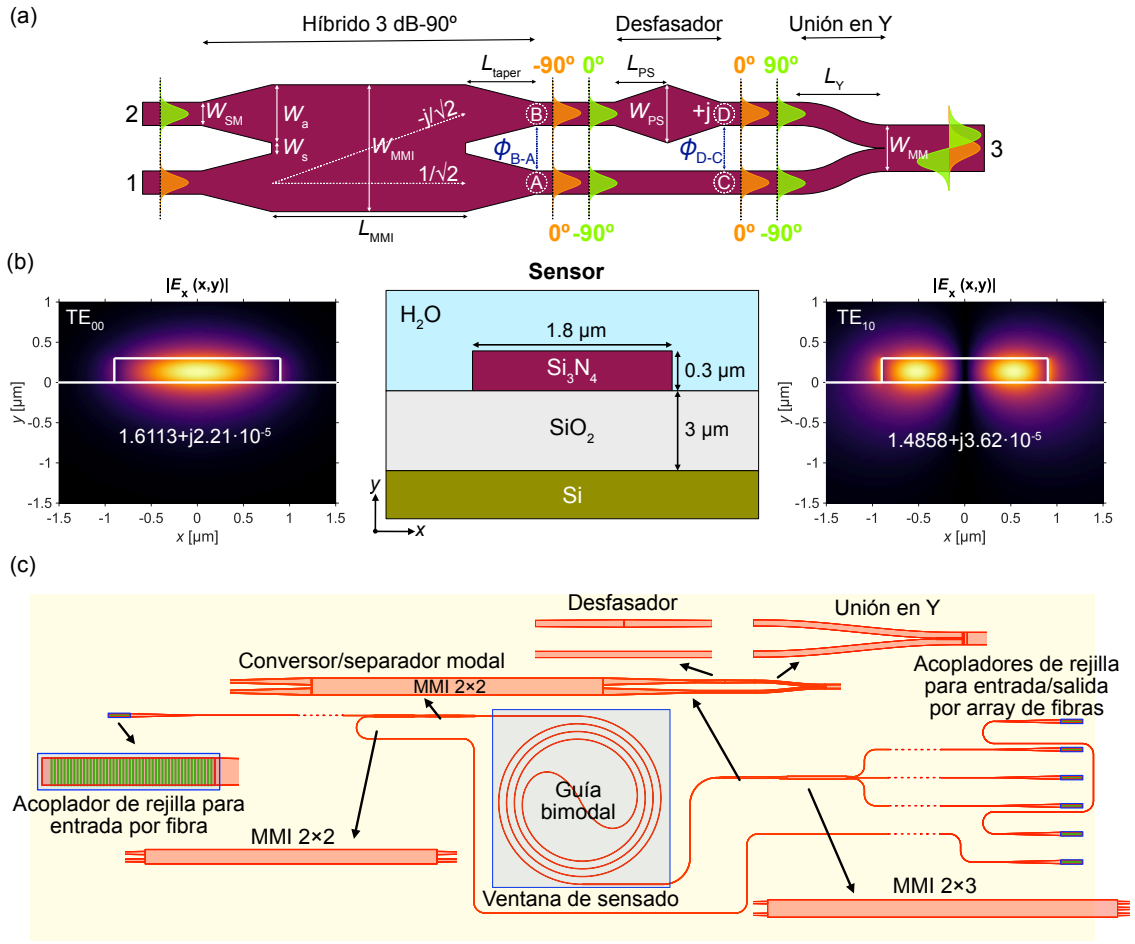

Figura G.15: (a) Conversor de modos empleado en los sensores de segunda generación, basado en un MMI, un desfasador y una unión en Y. (b) Sección transversal de la gúia bimodal y perfil de campo de los modos TE soportados. (c) Disposición de los elementos del sensor de segunda generación en la máscara preparada para su fabricación.

es $S_\mathrm{d} = \Gamma_1 - \Gamma_0 = 0.094\,\mathrm{RIU/RIU}$. La Fig. G.15(c) muestra la disposición de los elementos del sensor en la máscara para su fabricación. La espiral bimodal diseñada tiene una longitud $L = 7.81\,\mathrm{mm}$ y el resto de sus características se recogen en la Tabla G.7. Estos sensores se evaluaron ópticamente en términos de pérdidas de propagación y reflexiones, y los favorables resultados obtenidos promovieron la realización de experimentos de sensado con los mismos.

G.5.3 Experimentos de sensado homogéneo

La validación de los sensores mediante experimentos de sensado homogéneo a longitud de onda fija $\lambda_0 = 1.55\,\mu\mathrm{m}$ se hizo de forma análoga a lo especificado en la Sección G.4.3 para los sensores de índice de refracción complejo, utilizando las mismas disoluciones de

Tabla G.6: Factor de confinamiento (Γ) y pérdidas de propagación de ambos modos por absorción del agua (L_H2O), fugas al substrato (L_leak) y curvas (L_{90}).

Modo	Γ	L_H2O [dB cm^{-1}]	L_leak [dB cm^{-1}]	L_{90} [dB]
TE_{00}	0.15	7.79	$6.54 \cdot 10^{-4}$	0.0041
TE_{10}	0.24	12.74	0.27	0.017

Tabla G.7: Características de la guía sensora en espiral. El modo fundamental no experimenta pérdidas por radiación en las curvas.

L [mm]	Área [mm^2]	S_n [$\frac{rad}{RIU}$]	$L^{tot}_{rad,1}$ [dB]	$L^{tot}_{H2O,0}$ [dB]	$L^{tot}_{H2O,1}$ [dB]
7.81	0.72	$2.85 \cdot 10^3$	0.05	6.02	9.95

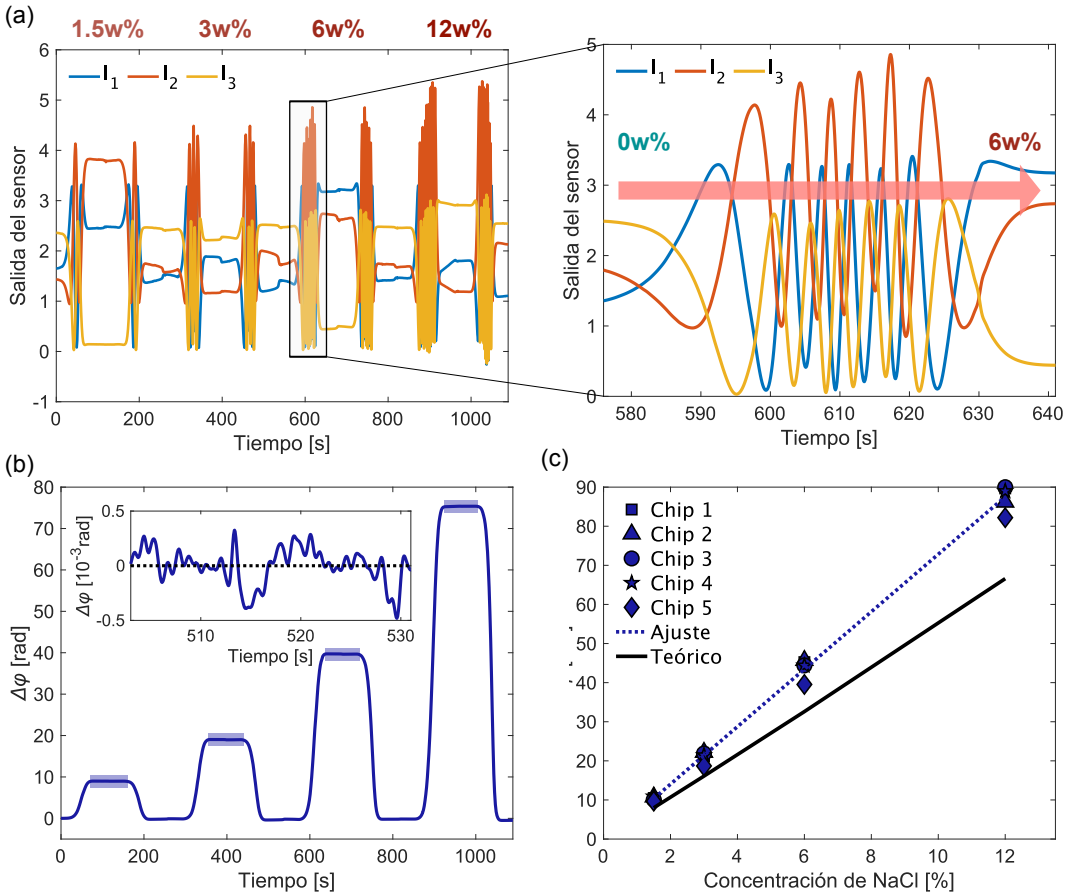

Figura G.16: (a) Salida del sensor durante un experimento de sensado homogéneo con disoluciones salinas. (b) Desfase calculado a partir de la señal compleja. Las áreas utilizadas para calcular los valores de saturación se han destacado. (c) Desfases obtenidos en función de la concentración de NaCl en experimentos de sensado homogéneo con 5 chips diferentes.

NaCl en agua deionizada. La señal de salida del sensor durante uno de estos experimentos puede verse en la Fig. G.16, así como el detalle de las oscilaciones de las señales interferométricas, que se comportan de la manera esperada. A partir de estas señales, es posible calcular una señal compleja, la evolución de cuya fase puede observarse en la Fig. G.16(b), donde los fragmentos utilizados en el cálculo de los valores de saturación se han resaltado. Dichos valores se representan en la Fig. G.16(c) en función de la concentración de NaCl. Todos los sensores muestran una gran linealidad ($R^2 > 0.9986$) y las variaciones entre chips son pequeñas. La sensibilidad media obtenida, $S_n = 4.30 \cdot 10^3$ rad/RIU, es ligeramente superior a la teórica, lo que puede deberse a la combinación de un sobregrabado de la guía con otras no-idealidades no consideradas. Para calcular el LOD se evaluó el suelo de ruido durante fragmentos de 30 segundos de las medidas, como el ejemplo representativo insertado en la Fig. G.16(b). El valor medio obtenido es LOD $= 1.03 \cdot 10^{-6}$ RIU, que es competitivo con el estado actual de la cuestión en sensores bimodales. Además, considerando el mejor resultado, correspondiente al Chip 2, con LOD $= 1.59 \cdot 10^{-7}$ RIU, la arquitectura aquí presentada es, hasta donde llega el conocimiento de la autora, la mejor

Tabla G.8: Límites de detección de sensores integrados bimodales operando en distintos regímenes de longitud de onda. Los resultados de este trabajo se muestran en negrita. Abreviaturass: altura (h.), anchura (w.), algoritmo (alg.), no determinado (n.d.).

Ref.	Régimen	Excitación modal	Lectura	LOD $[10^{-7}$RIU$]$
[226]	VIS	Discontinuidad h.	Convencional	0.5
[231]		Discontinuidad h.	Alg. trigonométrico	0.32
[233]	NIR	Discontinuidad w.	Convencional	220
[228]		Discontinuidad w.	Espectral	200
[229]		Discontinuidad w.	Espectral	66
[232]		Discontinuidad w.	Coherente	n.d.
[161]		Discontinuidad w.	Convencional	244
Este trabajo		**Conversor modal**	**Coherente**	**1.59**

reportada en el NIR, como se evidencia en la Tabla G.8. Estas elevadas prestaciones se ven reforzadas por una excitación modal controlada y una lectura lineal de fase.

G.6 Guías para espectroscopía de absorción en el infrarrojo medio

La espectroscopía de absorción en el infrarrojo medio es una potente herramienta para la detección cuantitativa de analitos. Para detectar muestras acuosas, algo especialmente interesante en aplicaciones medioambientales y biomédicas, es preferible usar guías de onda basadas en láminas finas (TFWGs, por sus siglas en inglés), por su mayor robustez mecánica. Se han propuesto una gran variedad de plataformas materiales para implementar dichas guías en el MIR [94], pero la falta de un criterio homogéneo en el diseño y posterior caracterización dificulta establecer una comparación entre alternativas que permita seleccionar la opción más oportuna. En esta sección se realiza un estudio teórico de cuatro plataformas de TFWGs, proponiendo un criterio de diseño para óptimas prestaciones y estableciendo una comparación justa entre implementaciones. La mayor parte del trabajo aquí presentado se realizó durante una estancia en la Universidad de Ulm y los principales resultados pueden leerse en A. Torres-Cubillo, A. Teuber, R. Halir, and B. Mizaikoff, "Optimized waveguides for mid-infrared lab-on-chip systems: A rigorous design approach," Sensors and Actuators A: Physical **378**, 115797 (2024).

G.6.1 Modelo sistémico

Guía sensora

La guía genérica representada en la Fig. G.17(a) está expuesta a una muestra líquida, compuesta por agua (el solvente) y un analito en concentración C. Cuando la concentración de analito es pequeña, el coeficiente de absorción de la muestra puede expresarse como

$$\alpha_{\text{sample}}(\lambda, C) = \alpha_{\text{H}_2\text{O}}(\lambda) + \alpha_{\text{a}}(\lambda, C), \tag{G.34}$$

donde $\alpha_{\text{H}_2\text{O}}$ es el coeficiente de absorción del agua pura y α_{a} es la absorción adicional que introduce el analito, tal que

$$\alpha_{\text{a}}(\lambda, C) = \frac{\epsilon(\lambda)}{\log_{10}(e)} C. \tag{G.35}$$

Las pérdidas sufridas por el modo guiado pueden expresarse como

$$\alpha_{\text{eff}}(\lambda, C) = \alpha_{\text{int}}(\lambda) + \Gamma\alpha_{\text{sample}}(\lambda, C) \approx \underbrace{\underbrace{\alpha_{\text{mat}}(\lambda) + \alpha_{\text{leak}}(\lambda)}_{\alpha_{\text{int}}} + \Gamma\alpha_{\text{H}_2\text{O}}(\lambda)}_{\alpha_{\text{wg}}} + \Gamma\alpha_{\text{a}}(\lambda, C), \tag{G.36}$$

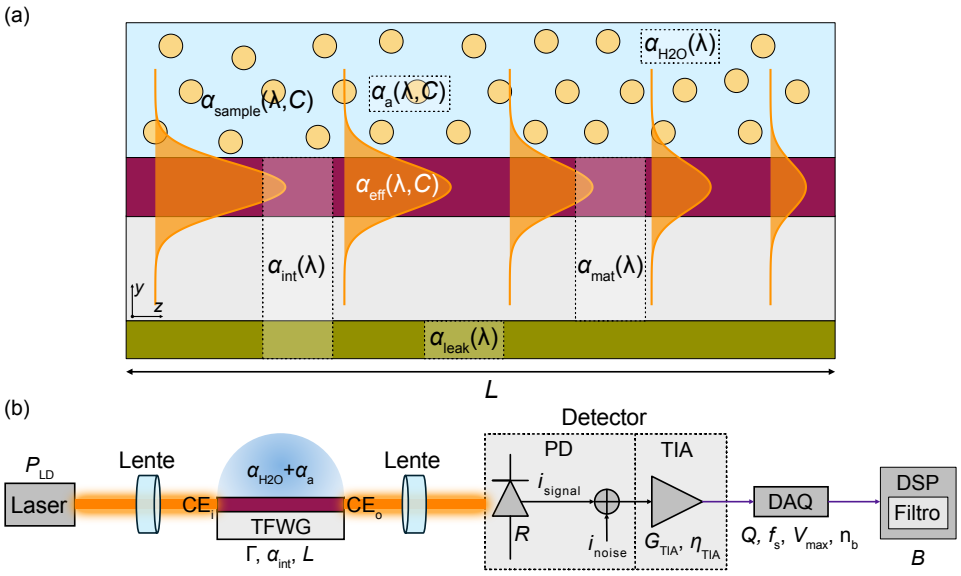

Figura G.17: (a) Guía para espectroscopía de absorción expuesta a una muestra acuosa. Las fuentes de pérdidas del modo se hallan señaladas. (b) Esquemático del sistema de medidas típico considerado en el análisis de ruido.

donde α_{int} son las pérdidas intrínsecas de la guía, que pueden aproximarse como una combinación de las pérdidas por fugas al substrato (α_{leak}) y la absorción por todos los materiales de la guía (α_{mat}), exceptuando la cubierta de agua. En la práctica conviene expresar la Ec. (G.36) como

$$\alpha_{\text{eff}}(\lambda, C) = \alpha_{\text{wg}}(\lambda) + \Gamma\alpha_{\text{a}}(\lambda, C), \tag{G.37}$$

con $\alpha_{\text{wg}} = \alpha_{\text{int}} + \Gamma\alpha_{\text{H}_2\text{O}}$, para separar las pérdidas que dependen del analito de las que no lo hacen. La intensidad a la salida de la guía es

$$I_{\text{S}}(\lambda, C) = I_{\text{S}}(\lambda, 0)e^{-\Gamma\alpha_{\text{a}}(\lambda,C)L}, \tag{G.38}$$

donde la intensidad de fondo $I_{\text{S}}(\lambda, 0) \propto e^{-\alpha_{\text{wg}}L}$ corresponde al agua pura. Finalmente, se puede calcular la absorbancia tomando

$$A(\lambda, C) = -\log_{10}\left(\frac{I_{\text{S}}(\lambda, C)}{I_{\text{S}}(\lambda, 0)}\right) = \log_{10}(e)\Gamma\alpha_{\text{a}}(\lambda, C)L, \tag{G.39}$$

de donde se puede obtener C.

Relación señal a ruido

Considerando el sistema de medida típico representado en la Fig. G.17(b), la fotocorriente de señal entregada por el fotodetector, que es proporcional a I_{S}, puede expresarse como

$$i_{\text{signal}} = P_{\text{LD}}\text{CE}_{\text{i}}\text{CE}_{\text{o}}Re^{-(\alpha_{\text{wg}}+\Gamma\alpha_{\text{a}})L} = S_0e^{-(\alpha_{\text{wg}}+\Gamma\alpha_{\text{a}})L}, \tag{G.40}$$

donde P_{LD} es la potencia de salida del laser, CE_{i} y CE_{o} son las eficiencias de acoplamiento de entrada y salida respectivamente y R es la responsividad del fotodiodo. Para simplificar la notación se introduce el parámetro constante $S_0 = P_{\text{LD}}\text{CE}_{\text{i}}\text{CE}_{\text{o}}R$.

Las fuentes de ruido consideradas en este estudio son el ruido de disparo (*shot*) del fotodiodo, el ruido eléctrico del TIA y el ruido de cuantificación introducido por el DAQ.

Tabla G.9: Expresiones de las métricas de la guía para espectroscopía de absorción y del sistema sensor que la incorpora.

Nivel	Métrica	Expresión
Guía	Figura de mérito (FOM)	$\frac{\Gamma}{\alpha_{\mathrm{wg}}} = \frac{\Gamma}{\alpha_{\mathrm{int}}+\Gamma\alpha_{\mathrm{H_2O}}}$
Sensor	Sensibilidad del dispositivo (S_α)	$\frac{\partial i_{\mathrm{signal}}}{\partial \alpha_a} = -S_0\Gamma L e^{-\alpha_{\mathrm{wg}}L}$
	Límite de detección (LOD)	$\frac{3\sigma}{\lvert S_\alpha\rvert} = \frac{3\sigma}{S_0\Gamma L e^{-\alpha_{\mathrm{wg}}L}}$
	Longitud óptima (L_{opt})	$\frac{1}{\alpha_{\mathrm{wg}}} = \frac{1}{\alpha_{\mathrm{int}}+\Gamma\alpha_{\mathrm{H_2O}}}$

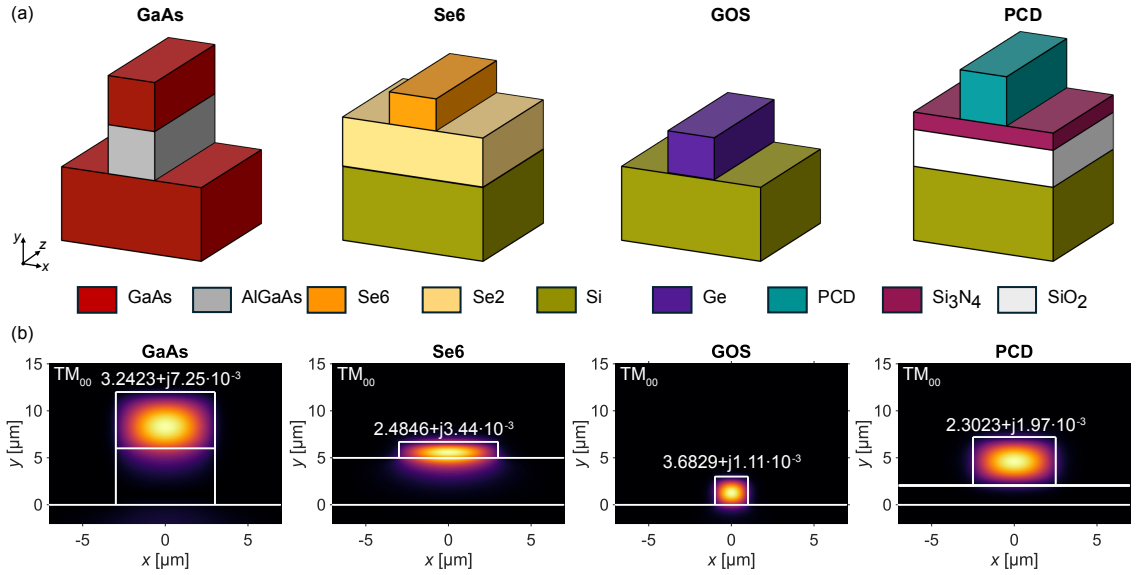

Figura G.18: (a) Guías en las plataformas estudiadas: GaAs, Se6, GOS and PCD. La cubierta de agua no se ha representado por visibilidad. (b) Perfiles de los modos TM fundamentales de las distintas guías.

De éstas, sólo el ruido de fotodiodo depende de la señal recibida. Considerando que las fuentes son independientes, el suelo total de ruido es:

$$\sigma = \sqrt{\sigma^2_{\mathrm{shot}} + \sigma^2_{\mathrm{TIA}} + \sigma^2_{\mathrm{DAQ}}}. \tag{G.41}$$

Las expresiones de las métricas para evaluar el sistema de espectroscopía de absorción basado en una guía fotónica pueden encontrarse en la Tabla G.9.

G.6.2 Comparación entre plataformas

Se han estudiado cuatro plataformas habitualmente empleadas para espectroscopía de muestras líquidas en el MIR: arseniuro de galio (GaAs), calcogenuro (Se6), germanio sobre silicio (GOS, por sus siglas en inglés) y diamante policristalino (PCD, por sus siglas en inglés). La longitud de onda central es $\lambda_0 = 6\,\mu$m, que tiene gran interés analítico al encontrarse en la banda vibracional de las amidas, esencial para detectar proteínas. La polarización estudiada es TM. Siguiendo un criterio de diseño sistemático, se han modelado guías en dichas plataformas, cuyas secciones transversales y perfiles de sus modos fundamentales se muestran en la Fig. G.18(a)-(b). Los parámetros Γ y α_{wg} se han obtenido mediante simulaciones electromagnéticas (ver Sección G.3.1), y la FOM de cada guía, representada en las Fig. G.19(a)-(d), se ha calculado a partir de ellos. Puede observarse cómo en las guías de GaAs y PCD, la FOM decae exponencialmente con el ancho de la guía. Esto es debido a la acción combinada de un menor Γ y unas mayores pérdidas in-

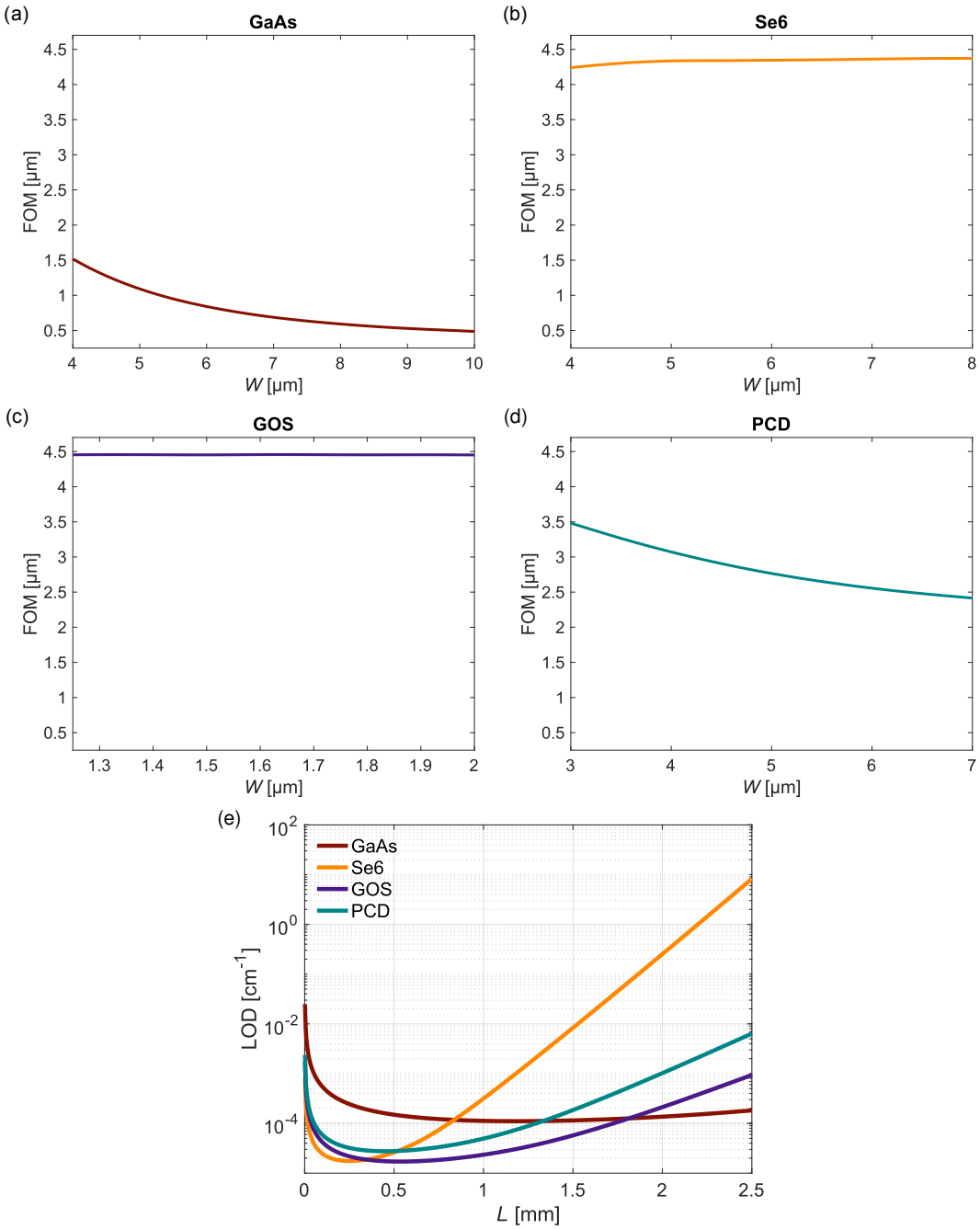

Figura G.19: Figura de mérito de las guías de (a) GaAs, (b) Se6, (c) GOS y (d) PCD waveguides, evaluada en el régimen monomodo. (e) Estimación del límite de detección de cada plataforma.

Tabla G.10: Geometría y características de las guías diseñadas en las distintas plataformas.

Plat.	W **[µm]**	Γ **[%]**	α_{wg} **[cm^{-1}]**	**FOM [µm]**	L_{opt} **[mm]**	**LOD [cm^{-1}]**
GaAs	7	0.11	15.75	0.69	1.8	$11.1{\cdot}10^{-5}$
Se6	5.75	3.22	74.05	4.34	0.25	$1.75{\cdot}10^{-5}$
GOS	1.62	1.55	34.79	4.46	0.54	$1.51{\cdot}10^{-5}$
PCD	5	1.14	41.26	2.77	0.45	$2.75{\cdot}10^{-5}$

trínsecas (α_{int}). En el caso del GOS, α_{int} es prácticamente nulo, así que el deterioro de la sensibilidad y la reducción en las pérdidas del agua están equilibrados y FOM $\approx 1/\alpha_{H_2O}$ es constante. Algo parecido ocurre en el caso del Se6, con la salvedad de que el FOM mejora con una mayor anchura, pues en el límite inferior del régimen monomodo las pérdidas inducidas por el agua son muy elevadas.

Para calcular el LOD, se seleccionó una anchura en el centro del régimen monomodo, que pueede consultarse en la Tabla G.10, así como los parámetros asociados a este ancho. Para evaluar el suelo de ruido, se asumieron unas condiciones de medida compatibles con un sistema típico de espectroscopía MIR. Los resultados obtenidos tras evaluar el LOD en función de la longitud de interacción se muestran en la Fig. G.19(e). Para cada opción existe una L_{opt}, cuyo valor y el LOD correspondiente se encuentran en la Tabla G.10. Aquí es necesario observar que, mientras que el valor óptimo del LOD está determinado por el inverso del FOM (ver Tabla G.9), cuanto mayores son las pérdidas de la guía, menor es su tolerancia a incrementos en la longitud de interacción. Con esto, puede concluirse que un diseño adecuado puede conducir a prestaciones análogas en las guías de Se6, GOS y PCD, pero que, si no se puede garantizar el punto de trabajo, es preferible optar por las de GOS o PCD, de menores pérdidas. Las guías de GaAs, pese a su menor sensibilidad, son una opción interesante si por limitaciones prácticas es necesario implementar una longitud de interacción superior a 1.8 mm. Con el presente estudio, generalizable a otros materiales y longitudes de onda, se pretende impulsar el desarrollo de nuevos sensores de espectroscopía de absorción optimizados.

G.7 Conclusiones

A continuación se resumen las principales conclusiones derivadas del trabajo realizado en esta tesis:

1. Se ha desarrollado una arquitectura de sensado de índice de refracción complejo basada en un MZI modificado, que otorga medidas directas de intesidad y lectura coherente de fase, operando en el infrarrojo cercano. El sensor se ha fabricado en una plataforma de SiNOI y se ha evaluado mediante experimentos de sensado homogéneo. Los límites de detección obtenidos, $\text{LOD}_{\text{n}} = 1.9 \cdot 10^{-6}$ RIU, $\text{LOD}_{\text{k}} = 2.1 \cdot 10^{-6}$ RIU, son los mejores reportados, hasta donde llegan los conocimientos de la autora, en la detección simulatánea de ambas partes del índice de refracción utilizando una arquitectura integrada. Los resultados principales están publicados en [89].

2. Se ha propuesto un sensor de índice de refracción en el infrarrojo cercano que combina una guía bimodal con una excitación y separación de modos controladas y una lectura coherente de fase. El sensor se ha fabricado en SiNOI, y se ha validado mediante experimentos de sensado homogéneo, mostrando una elevada sensibilidad y buen LOD. El mejor resultado obtenido, $\text{LOD} = 1.59 \cdot 10^{-7}$ RIU, es el mejor para un sensor bimodal operando en el NIR, hasta donde la autora alcanza a conocer. Los resultados principales están publicados en [93].

3. Se ha llevado a cabo un estudio teórico, basado en un modelo analítico y en simulaciones electromagnéticas, de cuatro plataformas distintas (GaAs, Se6, GOS, PCD) para implementar guías de espectroscopía de absorción en el infrarrojo medio, orientadas al análisis de muestras acuosas. Con esto se ha conseguido, por primera vez, establecer una comparación objetiva entre plataformas, así como establecer un criterio de diseño riguroso para óptimas prestaciones. Los resultados principales están publicados en [95].

Bibliography

[1] European Parliament, *Global trends to 2040 – Choosing Europe's future* (Publications Office of the European Union, 2024).

[2] J. Rockström, W. Steffen, K. Noone, Å. Persson, F. S. Chapin, E. F. Lambin, T. M. Lenton, M. Scheffer, C. Folke, H. J. Schellnhuber, *et al.*, "A safe operating space for humanity," Nature **461**(7263), 472–475 (2009).

[3] J. Rockström, W. Steffen, K. Noone, Å. Persson, F. S. Chapin III, E. Lambin, T. M. Lenton, M. Scheffer, C. Folke, H. J. Schellnhuber, *et al.*, "Planetary boundaries: exploring the safe operating space for humanity," Ecology and society **14**(2) (2009).

[4] Eropean Environmental Agency, *European Risk Assessment* (Publications Office of the European Union, 2024).

[5] H. Lee, K. Calvin, D. Dasgupta, G. Krinner, A. Mukherji, P. Thorne, C. Trisos, J. Romero, P. Aldunce, and A. C. Ruane, "Climate Change 2023 synthesis report summary for policymakers," Climate Change 2023 Synthesis Report: Summary for Policymakers (2024).

[6] K. R. van Daalen, C. Tonne, J. C. Semenza, J. Rocklöv, A. Markandya, N. Dasandi, S. Jankin, H. Achebak, J. Ballester, H. Bechara, *et al.*, "The 2024 Europe report of the Lancet Countdown on health and climate change: unprecedented warming demands unprecedented action," The Lancet Public Health (2024).

[7] K. R. Miner, J. D'Andrilli, R. Mackelprang, A. Edwards, M. J. Malaska, M. P. Waldrop, and C. E. Miller, "Emergent biogeochemical risks from Arctic permafrost degradation," Nature Climate Change **11**(10), 809–819 (2021).

[8] M. Fekete, D. Major, A. Feher, V. Fazekas-Pongor, and A. Lehoczki, "Geroscience and pathology: a new frontier in understanding age-related diseases," Pathology and Oncology Research **30** (2024).

[9] OECD/European Union, "Health at a glance: Europe 2020," State of Health in the EU Cycle (2020).

[10] M. Dritsaki and C. Dritsaki, "The relationship between health expenditure, CO2 emissions, and economic growth in G7: Evidence from heterogeneous panel data," Journal of the Knowledge Economy **15**(1), 4886–4911 (2024).

[11] J. D. Sachs, S. S. A. Karim, L. Aknin, J. Allen, K. Brosbøl, F. Colombo, G. C. Barron, M. F. Espinosa, V. Gaspar, A. Gaviria, *et al.*, "The Lancet Commission on lessons for the future from the COVID-19 pandemic," The Lancet **400**(10359), 1224–1280 (2022).

[12] L. Bruhwiler, S. Basu, J. H. Butler, A. Chatterjee, E. Dlugokencky, M. A. Kenney, A. McComiskey, S. A. Montzka, and D. Stanitski, "Observations of greenhouse gases as climate indicators," Climatic Change **165**(1), 12 (2021).

[13] R. Liu, X. Ye, and T. Cui, "Recent progress of biomarker detection sensors," Research (2020).

[14] "Sensor | Oxford English Dictionary," `https://www.oed.com/search/dictionary/?scope=Entries&q=sensor`.

[15] A. Hulanicki, S. Glab, and F. Ingman, "Chemical sensors: definitions and classification," Pure and applied chemistry **63**(9), 1247–1250 (1991).

[16] S. Rasheed, T. Kanwal, N. Ahmad, B. Fatima, M. Najam-ul Haq, and D. Hussain, "Advances and challenges in portable optical biosensors for onsite detection and point-of-care diagnostics," TrAC Trends in Analytical Chemistry p. 117640 (2024).

[17] Z. Peng, J. Chen, Y. Liu, D. Li, Y. Li, Q. Zhang, C. Chen, Y. Zhang, J. Yao, S. Wang, *et al.*, "Optical biosensor based on weak measurement for ultra-sensitive detection of calreticulin in human serum," Biomedical Optics Express **15**(2), 715–724 (2024).

[18] J. Baranwal, B. Barse, G. Gatto, G. Broncova, and A. Kumar, "Electrochemical sensors and their applications: A review," Chemosensors **10**(9), 363 (2022).

[19] Q. Chen, Y. Liu, K. Gu, J. Yao, Z. Shao, and X. Chen, "Silk-based electrochemical sensor for the detection of glucose in sweat," Biomacromolecules **23**(9), 3928–3935 (2022).

[20] M. Javaid, A. Haleem, S. Rab, R. P. Singh, and R. Suman, "Sensors for daily life: A review," Sensors International **2**, 100,121 (2021).

[21] P. F. Pereira, P. H. de Sousa Picciani, V. Calado, and R. V. Tonon, "Electrical gas sensors for meat freshness assessment and quality monitoring: A review," Trends in Food Science & Technology **118**, 36–44 (2021).

[22] A. Oprea and U. Weimar, "Gas sensors based on mass-sensitive transducers part 1: transducers and receptors—basic understanding," Analytical and bioanalytical chemistry **411**, 1761–1787 (2019).

[23] P. Joshi, S. Kumar, V. Jain, J. Akhtar, and J. Singh, "Distributed MEMS mass-sensor based on piezoelectric resonant micro-cantilevers," Journal of Microelectromechanical Systems **28**(3), 382–389 (2019).

[24] A. Hojjati-Najafabadi, M. Mansoorianfar, T. Liang, K. Shahin, and H. Karimi-Maleh, "A review on magnetic sensors for monitoring of hazardous pollutants in water resources," Science of The Total Environment **824**, 153,844 (2022).

[25] S. Zuo, H. Heidari, D. Farina, and K. Nazarpour, "Miniaturized magnetic sensors for implantable magnetomyography," Advanced Materials Technologies **5**(6), 2000,185 (2020).

[26] M. N. Popescu and S. Gáspár, "Analyte sensing with catalytic micromotors," Biosensors **13**(1), 45 (2022).

[27] H. Zhao, C. Zheng, M. Pi, L. Liang, F. Song, Y. Zhang, Y. Wang, and F. K. Tittel, "On-chip mid-infrared silicon-on-insulator waveguide methane sensor using two measurement schemes at 3.291μm," Frontiers in Chemistry **10** (2022).

[28] M. F. Ferreira, E. Castro-Camus, D. J. Ottaway, J. M. López-Higuera, X. Feng, W. Jin, Y. Jeong, N. Picqué, L. Tong, B. M. Reinhard, *et al.*, "Roadmap on optical sensors," Journal of Optics **19**(8), 083,001 (2017).

[29] Y. Chen, J. Liu, Z. Yang, J. S. Wilkinson, and X. Zhou, "Optical biosensors based on refractometric sensing schemes: A review," Biosensors and Bioelectronics **144**, 111,693 (2019).

[30] G. K. Yadav, S. K. Metya, R. Zafar, and A. K. Garg, "High sensitivity plasmonic refractive index sensor for early anaemia detection," Photonics and Nanostructures-Fundamentals and Applications **58**, 101,235 (2024).

[31] J. Li, Z. Yu, Z. Du, Y. Ji, and C. Liu, "Standoff chemical detection using laser absorption spectroscopy: a review," Remote Sensing **12**(17), 2771 (2020).

[32] J. Meng, S. Balendhran, Y. Sabri, S. K. Bhargava, and K. B. Crozier, "Smart mid-infrared metasurface microspectrometer gas sensing system," Microsystems & Nanoengineering **10**(1), 74 (2024).

[33] A. Kior, V. Sukhov, and E. Sukhova, "Application of reflectance indices for remote sensing of plants and revealing actions of stressors," Photonics **8**(12), 582 (2021).

[34] Z. Wang, P. Gao, S. Liu, and X. Chen, "A reflective methane concentration sensor based on biconvex cone photonic crystal fiber," Optik **241**, 166,983 (2021).

[35] G.-L. Yang, X.-L. Jiang, H. Xu, and B. Zhao, "Applications of MOFs as luminescent sensors for environmental pollutants," Small **17**(22), 2005,327 (2021).

[36] D. Tian, J. Wang, Q. Zhuang, S. Wu, Y. Yu, and K. Ding, "An electrochemiluminescence biosensor based on Graphitic carbon nitride luminescence quenching for detection of AFB1," Food Chemistry **404**, 134,183 (2023).

[37] H. He, D.-W. Sun, Z. Wu, H. Pu, and Q. Wei, "On-off-on fluorescent nanosensing: Materials, detection strategies and recent food applications," Trends in Food Science & Technology **119**, 243–256 (2022).

[38] Z. Wu, D.-W. Sun, H. Pu, and Q. Wei, "A novel fluorescence biosensor based on CRISPR/Cas12a integrated MXenes for detecting Aflatoxin B1," Talanta **252**, 123,773 (2023).

[39] S. Caron, M. Farchado, G. San Vicente, A. Morales, J. Ballestrín, M. J. Carvalho, S. Pascoa, E. Le Baron, A. Disdier, E. Guillot, *et al.*, "Intercomparison of opto-thermal spectral measurements for concentrating solar thermal receiver materials from room temperature up to 800° C," Solar Energy Materials and Solar Cells **266**, 112,677 (2024).

[40] X. Zhang, C. Bontozoglou, and P. Xiao, "In vivo skin characterizations by using opto-thermal depth-resolved detection spectra," Cosmetics **6**(3), 54 (2019).

[41] Y. Hang, J. Boryczka, and N. Wu, "Visible-light and near-infrared fluorescence and surface-enhanced Raman scattering point-of-care sensing and bio-imaging: A review," Chemical Society Reviews **51**(1), 329–375 (2022).

[42] W. Du, S. Wei, N. Li, Z. Hao, Y. Li, and M. Wang, "Highly sensitive fiber optic enhanced Raman scattering sensor," Optics & Laser Technology **168**, 109,879 (2024).

[43] B. E. A. Saleh and M. C. Teich, *Ray optics* (John Wiley & sons, 2007).

[44] D. F. Swinehart, "The beer-lambert law," Journal of chemical education **39**(7), 333 (1962).

[45] P. R. Griffiths, *Handbook of vibrational spectroscopy* (Wiley Hoboken, NJ, USA, 2006).

[46] I. Gordon, L. Rothman, R. Hargreaves, *et al.*, "The HITRAN2020 molecular spectroscopic database," Journal of Quantitative Spectroscopy and Radiative Transfer **277**, 107,949 (2022).

[47] R. P. Feynman, *Feynman Lectures on Physics: Electrical and Magnetic Behavior. Volume 4* (Perseus Books, 1999).

[48] C. N. Banwell and E. M. McCash, *Fundamentals of molecular spectroscopy* (Indian Edition, 2017).

[49] B. E. A. Saleh and M. C. Teich, *Light and matter* (John Wiley & sons, 2007).

[50] B. E. A. Saleh and M. C. Teich, *Electromagnetic optics* (john Wiley & sons, 2007).

[51] "RT-50 PRISM Inline Refractive Index & BRIX Sensor for Cutting Fluid," `https://www.pyxis-lab.com/product/rt-50-prism-inline-refractometer/`.

[52] "RT-50 PRISM Inline Refractive Index & BRIX Sensor for Cutting Fluid," `https://www.wyatt.com/products/instruments/optilab-refractive-index-detector.html#optilab-1`.

[53] "INVENIO FT-IR Spectrometer | Bruker," `https://www.bruker.com/es/products-and-solutions/infrared-and-raman/ft-ir-research-spectrometers/invenio-ft-ir-spectrometer.html`.

[54] "Laser - 5100HD | Ametek Process Instruments," `https://www.ametekpi.com/products/brands/process-instruments/laser-5100-hd`.

[55] G. Meeten and A. North, "Refractive index measurement of absorbing and turbid fluids by reflection near the critical angle," Measurement Science and Technology **6**(2), 214 (1995).

[56] P. Hariharan, *Basics of interferometry* (Elsevier, 2010).

[57] B. C. Smith, *Fundamentals of Fourier transform infrared spectroscopy* (CRC press, 2011).

[58] J. Faist, F. Capasso, D. L. Sivco, C. Sirtori, A. L. Hutchinson, and A. Y. Cho, "Quantum cascade laser," Science **264**(5158), 553–556 (1994).

[59] J. Sun, J. Chang, C. Wang, and J. Shao, "Tunable diode laser absorption spectroscopy for detection of multi-component gas: a review," Applied Spectroscopy Reviews pp. 1–22 (2024).

[60] S. Shekhar, W. Bogaerts, L. Chrostowski, J. E. Bowers, M. Hochberg, R. Soref, and B. J. Shastri, "Roadmapping the next generation of silicon photonics," Nature Communications **15**(1), 751 (2024).

[61] S. Bernabe, Q. Wilmart, K. Hasharoni, K. Hassan, Y. Thonnart, P. Tissier, Y. Desieres, S. Olivier, T. Tekin, and B. Szelag, "Silicon photonics for terabit/s communication in data centers and exascale computers," Solid-State Electronics **179**, 107,928 (2021).

[62] B. J. Shastri, A. N. Tait, T. Ferreira de Lima, W. H. Pernice, H. Bhaskaran, C. D. Wright, and P. R. Prucnal, "Photonics for artificial intelligence and neuromorphic computing," Nature Photonics **15**(2), 102–114 (2021).

[63] W. Xu, Y. Guo, X. Li, C. Liu, L. Lu, J. Chen, and L. Zhou, "Fully integrated solid-state LiDAR transmitter on a multi-layer silicon-nitride-on-silicon photonic platform," Journal of Lightwave Technology **41**(3), 832–840 (2022).

[64] N. Jovanovic, P. Gatkine, N. Anugu, R. Amezcua-Correa, R. B. Thakur, C. Beichman, C. F. Bender, J.-P. Berger, A. Bigioli, J. Bland-Hawthorn, *et al.*, "2023 astrophotonics roadmap: pathways to realizing multi-functional integrated astrophotonic instruments," Journal of Physics: Photonics **5**(4), 042,501 (2023).

[65] M. A. Butt, X. Mateos, and R. Piramidowicz, "Photonics Sensors: A perspective on current advancements, emerging challenges, and potential solutions," Physics Letters A p. 129633 (2024).

[66] S. Y. Siew, B. Li, F. Gao, H. Y. Zheng, W. Zhang, P. Guo, S. W. Xie, A. Song, B. Dong, L. W. Luo, *et al.*, "Review of silicon photonics technology and platform development," Journal of Lightwave Technology **39**(13), 4374–4389 (2021).

[67] C. J. Mitchell, T. Hu, S. Sun, C. J. Stirling, M. Nedeljkovic, A. C. Peacock, G. T. Reed, G. Z. Mashanovich, and D. J. Rowe, "Mid-infrared silicon photonics: From benchtop to real-world applications," APL Photonics **9**(8), 080,901 (2024).

[68] G. F. Rangel, L. D. de León Martínez, L. S. Walter, and B. Mizaikoff, "Recent Advances and Trends in Mid-Infrared Chem/Bio Sensors," TrAC Trends in Analytical Chemistry p. 117916 (2024).

[69] M. Soler, O. Calvo-Lozano, M. C. Estévez, and L. M. Lechuga, "Nanophotonic biosensors: driving personalized medicine," Optics & Photonics News (2020).

[70] C. Dhote, A. Singh, and S. Kumar, "Silicon Photonics Sensors for Biophotonic Applications—A Review," IEEE Sensors Journal **22**(19), 18,228–18,239 (2022).

[71] A. Hänsel and M. J. Heck, "Opportunities for photonic integrated circuits in optical gas sensors," Journal of Physics: Photonics **2**(1), 012,002 (2020).

[72] B. Hinkov, F. Pilat, L. Lux, P. L. Souza, M. David, A. Schwaighofer, D. Ristanić, B. Schwarz, H. Detz, A. M. Andrews, *et al.*, "A mid-infrared lab-on-a-chip for dynamic reaction monitoring," Nature communications **13**(1), 4753 (2022).

[73] J. Zhou, X. Liu, H. Zhou, S. Xu, J. Xie, C. Xu, W. Liu, Z. Zhang, and C. Lee, "Artificial-Intelligence-Enhanced Mid-infrared Lab-on-a-Chip for Mixture Spectroscopy Analysis," Laser & Photonics Reviews p. 2400754 (2024).

[74] M. A. Butt, N. L. Kazanskiy, S. N. Khonina, G. S. Voronkov, E. P. Grakhova, and R. V. Kutluyarov, "A Review on Photonic Sensing Technologies: Status and Outlook," Biosensors **13**(5) (2023).

[75] Y. Huang, R. Singh, L. Xie, and Y. Ying, "Attenuated total reflection for terahertz modulation, sensing, spectroscopy and imaging applications: A review," Applied Sciences **10**(14), 4688 (2020).

[76] C. Pendão and I. Silva, "Optical fiber sensors and sensing networks: overview of the main principles and applications," Sensors **22**(19), 7554 (2022).

[77] Y. Zhao, Y. Liu, B. Han, M. Wang, Q. Wang, and Y.-n. Zhang, "Fiber optic volatile organic compound gas sensors: A review," Coordination Chemistry Reviews **493**, 215,297 (2023).

[78] A. Teuber and B. Mizaikoff, "Robust Attenuated Total Reflection Infrared Spectroscopic Sensors Based on Quantum Cascade Lasers for Harsh Environments," IEEE Sensors Journal (2023).

[79] P. Fomina, A. Femenias, M. Hlavatsch, J. Scheuermann, N. Schäfer, S. Freitag, N. Patel, A. Kohler, R. Krska, J. Koeth, *et al.*, "A portable infrared attenuated total reflection spectrometer for food analysis," Applied Spectroscopy **77**(9), 1073–1086 (2023).

[80] T. Li, G. Liu, H. Kong, G. Yang, G. Wei, and X. Zhou, "Recent advances in photonic crystal-based sensors," Coordination Chemistry Reviews **475**, 214,909 (2023).

[81] M. H. Jokar, A. Naraghi, M. Seifouri, and S. Olyaee, "Photonic crystal bio-sensor for highly sensitive label-free detection of cancer cells," Optical and Quantum Electronics **55**(7), 660 (2023).

[82] D. Capelli, V. Scognamiglio, and R. Montanari, "Surface plasmon resonance technology: Recent advances, applications and experimental cases," TrAC Trends in Analytical Chemistry **163**, 117,079 (2023).

[83] M. Danaie, L. Hajshahvaladi, and E. Ghaderpanah, "A single-mode tunable plasmonic sensor based on an 8-shaped resonator for cancer cell detection," Scientific Reports **13**(1), 13,976 (2023).

[84] R. Halir, L. Vivien, X. Le Roux, D.-X. Xu, and P. Cheben, "Direct and sensitive phase readout for integrated waveguide sensors," IEEE Photonics Journal **5**(4), 6800,906–6800,906 (2013).

[85] J. Leuermann, V. Stamenkovic, P. Ramirez-Priego, A. Sánchez-Postigo, A. Fernández-Gavela, C. A. Chapman, R. C. Bailey, L. M. Lechuga, E. Perez-Inestrosa, D. Collado, R. Halir, and I. nigo Molina-Fernández, "Coherent silicon photonic interferometric biosensor with an inexpensive laser source for sensitive label-free immunoassays," Optics Letters **45**(24), 6595–6598 (2020).

[86] G. A. Ermolaev, Y. V. Stebunov, A. A. Vyshnevyy, D. E. Tatarkin, D. I. Yakubovsky, S. M. Novikov, D. G. Baranov, T. Shegai, A. Y. Nikitin, A. V. Arsenin, *et al.*, "Broadband optical properties of monolayer and bulk MoS2," npj 2D Materials and Applications **4**(1), 21 (2020).

[87] D. Lisak, D. Charczun, A. Nishiyama, T. Voumard, T. Wildi, G. Kowzan, V. Brasch, T. Herr, A. J. Fleisher, J. T. Hodges, *et al.*, "Dual-comb cavity ring-down spectroscopy," Scientific reports **12**(1), 2377 (2022).

[88] A. Cygan, A. J. Fleisher, R. Ciuryło, K. A. Gillis, J. T. Hodges, and D. Lisak, "Cavity buildup dispersion spectroscopy," Communications Physics **4**(1), 14 (2021).

[89] A. Torres-Cubillo, A. Sánchez-Postigo, J. Jágerská, J. G. Wangüemert-Pérez, and R. Halir, "Simultaneous measurement of refraction and absorption with an integrated near-infrared Mach–Zehnder interferometer," Optics & Laser Technology **177**, 111,154 (2024).

[90] L. Torrijos-Morán, B. D. Lisboa, M. Soler, L. M. Lechuga, and J. García-Rupérez, "Integrated optical bimodal waveguide biosensors: Principles and applications," Results in Optics **9**, 100,285 (2022).

[91] D. González-Andrade, J. G. Wangüemert-Pérez, A. V. Velasco, A. Ortega-Moñux, A. Herrero-Bermello, I. Molina-Fernández, R. Halir, and P. Cheben, "Ultra-broadband mode converter and multiplexer based on sub-wavelength structures," IEEE Photonics Journal **10**(2), 1–10 (2018).

[92] D. González-Andrade, A. Dias, J. G. Wangüemert-Pérez, A. Ortega-Moñux, Í. Molina-Fernández, R. Halir, P. Cheben, and A. V. Velasco, "Experimental demonstration of a broadband mode converter and multiplexer based on subwavelength grating waveguides," Optics & Laser Technology **129**, 106,297 (2020).

[93] A. Torres-Cubillo, J. M. Luque-González, A. Sánchez-Postigo, A. Fernández-Gavela, J. G. Wangüemert-Pérez, I. Molina-Fernández, and R. Halir, "High-Performance Bimodal Evanescent-Field Sensor With Coherent Phase Readout," Journal of Lightwave Technology **42**(8), 3010–3015 (2024).

[94] V. Mittal, G. Z. Mashanovich, and J. S. Wilkinson, "Perspective on thin film waveguides for on-chip mid-infrared spectroscopy of liquid biochemical analytes," Analytical Chemistry **92**(16), 10,891–10,901 (2020).

[95] A. Torres-Cubillo, A. Teuber, R. Halir, and B. Mizaikoff, "Optimized waveguides for mid-infrared lab-on-chip systems: A rigorous design approach," Sensors and Actuators A: Physical **378**, 115,797 (2024).

[96] T. Sharma, J. Wang, B. K. Kaushik, Z. Cheng, R. Kumar, Z. Wei, and X. Li, "Review of recent progress on silicon nitride-based photonic integrated circuits," IEEE Access **8**, 195,436–195,446 (2020).

[97] K. Kawano and T. Kitoh, *Introduction to Optical Waveguide Analysis: Solving Maxwell's Equation and the Schrödinger Equation* (John wiley & sons, 2001).

[98] D. Melati, A. Melloni, and F. Morichetti, "Real photonic waveguides: guiding light through imperfections," Advances in Optics and Photonics **6**(2), 156–224 (2014).

[99] F. P. Payne and J. P. Lacey, "A theoretical analysis of scattering loss from planar optical waveguides," Optical and Quantum Electronics **26**, 977–986 (1994).

[100] D. M. Kita, J. Michon, S. G. Johnson, and J. Hu, "Are slot and sub-wavelength grating waveguides better than strip waveguides for sensing?" Optica **5**(9), 1046–1054 (2018).

[101] P.-J. Chiang and T.-T. Shih, "Analysis of leakage loss in silicon photonics with finite gain compensation," IEEE Photonics Journal **9**(5), 1–10 (2017).

[102] D. Marcuse, "Bending losses of the asymmetric slab waveguide," Bell System Technical Journal **50**(8), 2551–2563 (1971).

[103] R. G. Hunsperger, *Losses in Optical Waveguides*, pp. 107–128 (Springer New York, 2009).

[104] P. Sethi, R. Kallega, A. Haldar, and S. K. Selvaraja, "Compact broadband low-loss taper for coupling to a silicon nitride photonic wire," Optics Letters **43**(14), 3433–3436 (2018).

[105] L. Stefan, M. Bernard, R. Guider, G. Pucker, L. Pavesi, and M. Ghulinyan, "Ultra-high-Q thin-silicon nitride strip-loaded ring resonators," Optics Letter **40**(14), 3316–3319 (2015).

[106] N. C. Harris, Y. Ma, J. Mower, T. Baehr-Jones, D. Englund, M. Hochberg, and C. Galland, "Efficient, compact and low loss thermo-optic phase shifter in silicon," Optics Express **22**(9), 10,487–10,493 (2014).

[107] W. D. Sacher, Y. Huang, L. Ding, T. Barwicz, J. C. Mikkelsen, B. J. F. Taylor, G.-Q. Lo, and J. K. S. Poon, "Polarization rotator-splitters and controllers in a Si3N4-on-SOI integrated photonics platform," Optics Express **22**(9), 11,167–11,174 (2014).

[108] D. Pereira-Martín, J. M. Luque-González, J. G. Wangüemert-Pérez, A. Hadij-ElHouati, I. Molina-Fernández, P. Cheben, J. H. Schmid, S. Wang, W. N. Ye, J. Čtyroký, and A. Ortega-Moñux, "Complex spectral filters in silicon waveguides based on cladding-modulated Bragg gratings," Optics Express **29**(11), 15,867–15,881 (2021).

[109] M. Bachmann, P. A. Besse, and H. Melchior, "General self-imaging properties in N × N multimode interference couplers including phase relations," Applied Optics **33**(18), 3905–3911 (1994).

[110] L. Soldano and E. Pennings, "Optical multi-mode interference devices based on self-imaging: principles and applications," Journal of Lightwave Technology **13**(4), 615–627 (1995).

[111] P. J. Reyes-Iglesias, I. Molina-Fernández, A. Moscoso-Mártir, and A. O.-M. nux, "High-performance monolithically integrated 120° downconverter with relaxed hardware constraints," Optics Express **20**(5), 5725–5741 (2012).

[112] T. Tamir and S. T. Peng, "Analysis and design of grating couplers," Applied Physics **14**(3), 235–254 (1977).

[113] T. Visser, H. Blok, B. Demeulenaere, and D. Lenstra, "Confinement factors and gain in optical amplifiers," IEEE Journal of Quantum Electronics **33**(10), 1763–1766 (1997).

[114] J. T. Robinson, K. Preston, O. Painter, and M. Lipson, "First-principle derivation of gain in high-index-contrast waveguides," Optics Express **16**(21), 16,659–16,669 (2008).

[115] J. Salaj, M. Vlk, R. Zakoldaev, R. Seton, J. Čtyroký, S. Alberti, A. Aksnes, and J. Jágerská, "Suspended nanophotonic waveguide for isotope-specific CO2 detection," Optica **11**(12), 1654–1662 (2024).

[116] M. Vlk, A. Datta, S. Alberti, H. D. Yallew, V. Mittal, G. S. Murugan, and J. Jágerská, "Extraordinary evanescent field confinement waveguide sensor for mid-infrared trace gas spectroscopy," Light: Science & Applications **10**(1), 26 (2021).

[117] P. Steglich, D. G. Rabus, C. Sada, M. Paul, M. G. Weller, C. Mai, and A. Mai, "Silicon photonic micro-ring resonators for chemical and biological sensing: A tutorial," IEEE Sensors Journal **22**(11), 10,089–10,105 (2022).

[118] J. Flueckiger, S. Schmidt, V. Donzella, A. Sherwali, D. M. Ratner, L. Chrostowski, and K. C. Cheung, "Sub-wavelength grating for enhanced ring resonator biosensor," Optics Express **24**(14), 15,672–15,686 (2016).

[119] L. Huang, H. Yan, L. Xiang, N. Zhou, D. He, and X. Mi, "Subwavelength racetrack resonators with enhanced critically coupled tolerance for on-chip sensing," IEEE Access **9**, 23,424–23,431 (2021).

[120] S. M. Grist, S. A. Schmidt, J. Flueckiger, V. Donzella, W. Shi, S. T. Fard, J. T. Kirk, D. M. Ratner, K. C. Cheung, and L. Chrostowski, "Silicon photonic micro-disk resonators for label-free biosensing," Optics Express **21**(7), 7994–8006 (2013).

[121] X. Wu, T. Fan, A. A. Eftekhar, A. H. Hosseinnia, and A. Adibi, "High-Q spiral-based coupled-resonator device on a Si3N4 platform for ultrasensitive sensing applications," OSA Continuum **3**(12), 3390–3398 (2020).

[122] I. J. M. Aslam, V. Muniswamy, L. Singh, M. Sathish, and R. V. Honnungar, "Design and modeling of ultra-compact and highly-sensitive silicon Bragg grating sensor for biochemical sensing applications," Silicon **14**(16), 10,909–10,917 (2022).

[123] M. A. Fedderke, P. W. Graham, B. Macintosh, and S. Rajendran, "Astrometric gravitational-wave detection via stellar interferometry," Physical Review D **106**, 023,002 (2022).

[124] J. Crawford, D. Dolzhenko, M. Keach, A. Mueninghoff, R. A. Abrahao, J. Martinez-Rincon, P. Stankus, S. Vintskevich, and A. Nomerotski, "Towards quantum telescopes: demonstration of a two-photon interferometer for precision astrometry," Optics Express **31**(26), 44,246–44,258 (2023).

[125] L. Ahmadi, M. Hiltunen, P. Stenberg, J. Hiltunen, S. Aikio, M. Roussey, J. Saarinen, and S. Honkanen, "Hybrid layered polymer slot waveguide Young interferometer," Optics Express **24**(10), 10,275–10,285 (2016).

[126] B. Schneider, E. Dickinson, M. Vach, J. Hoijer, and L. Howard, "Optical chip immunoassay for hCG in human whole blood," Biosensors and Bioelectronics **15**(11-12), 597–604 (2000).

[127] A. Nabok, A. M. Al-Jawdah, B. Gémes, E. Takács, and A. Székács, "An optical planar waveguide-based immunosensor for determination of fusarium mycotoxin Zearalenone," Toxins **13**(2) (2021).

[128] F. Vogelbacher, T. Kothe, P. Muellner, E. Melnik, M. Sagmeister, J. Kraft, and R. Hainberger, "Waveguide Mach-Zehnder biosensor with laser diode pumped integrated single-mode silicon nitride organic hybrid solid-state laser," Biosensors and Bioelectronics **197**, 113,816 (2022).

[129] J. Maldonado, M.-C. Estévez, A. Fernández-Gavela, J. J. González-López, A. B. González-Guerrero, and L. M. Lechuga, "Label-free detection of nosocomial bacteria using a nanophotonic interferometric biosensor," Analyst **145**(2), 497–506 (2020).

[130] A. B. González-Guerrero, J. Maldonado, S. Herranz, and L. M. Lechuga, "Trends in photonic lab-on-chip interferometric biosensors for point-of-care diagnostics," Analytical Methods **8**, 8380–8394 (2016).

[131] M. Angelopoulou, P. Petrou, and S. Kakabakos, "Advances in interferometric sensors for the detection of food contaminants," Trends in Analytical Chemistry **175**, 117,714 (2024).

[132] J. Shen, A. Perera, A. Rai, M. Kango-Singh, and S. Chakravarty, "Experimental Comparison of Slow Light and Subwavelength Waveguide Interferometer Sensors," IEEE Sensors Journal (2024).

[133] U. Minoni, E. Sardini, E. Gelmini, F. Docchio, and D. Marioli, "A high-frequency sinusoidal phase-modulation interferometer using an electro-optic modulator: Development and evaluation," Review of Scientific Instruments **62**(11), 2579–2583 (1991).

[134] V. M. N. Passaro, F. Magno, and A. V. Tsarev, "Investigation of thermo-optic effect and multireflector tunable filter/multiplexer in SOI waveguides," Optics Express **13**(9), 3429–3437 (2005).

[135] P. Kozma, A. Hamori, K. Cottier, S. Kurunczi, and R. Horvath, "Grating coupled interferometry for optical sensing," Applied Physics B **97** (2009).

[136] M. Kitsara, K. Misiakos, I. Raptis, and E. Makarona, "Integrated optical frequency-resolved Mach-Zehnder interferometers for label-free affinity sensing," Optics Express **18**(8), 8193–8206 (2010).

[137] G. Antonacci, J. Goyvaerts, H. Zhao, B. Baumgartner, B. Lendl, and R. Baets, "Ultra-sensitive refractive index gas sensor with functionalized silicon nitride photonic circuits," APL Photonics **5**(8), 081,301 (2020).

[138] M. Baillieul, E. Rinnert, J. Lemaitre, K. Michel, F. Colas, L. Bodiou, G. Demésy, S. Kakuta, A. Rumyantseva, G. Lerondel, *et al.*, "Surface functionalization with polymer membrane or SEIRA interface to improve the sensitivity of chalcogenide-based infrared sensors dedicated to the detection of organic molecules," ACS omega **7**(51), 47,840–47,850 (2022).

[139] N. I. of Standards and Technology, *NIST Chemistry WebBook*, NIST Standard Reference Database Number 69 (2023).

[140] N. T. Anderson and K. B. Walsh, "Review: The evolution of chemometrics coupled with near infrared spectroscopy for fruit quality evaluation," Journal Near Infrared Spectroscopy **30**(1), 3–17 (2022).

[141] A. Dabrowska, S. Lindner, A. Schwaighofer, and B. Lendl, "Mid-IR dispersion spectroscopy – A new avenue for liquid phase analysis," Spectrochimica Acta Part A: Molecular and Biomolecular Spectroscopy **286**, 122,014 (2023).

[142] A. Teuber, G. Caniglia, C. Kranz, and B. Mizaikoff, "Graphene-enhanced quantum cascade laser infrared spectroscopy using diamond thin-film waveguides," Analyst **148**(20), 5144–5151 (2023).

[143] S. Alberti and J. Jágerská, "Sol-gel thin film processing for integrated waveguide sensors," Frontiers in Materials **8**, 629,822 (2021).

[144] J. F. Olorunyomi, S. T. Geh, R. A. Caruso, and C. M. Doherty, "Metal–organic frameworks for chemical sensing devices," Materials Horizons **8**(9), 2387–2419 (2021).

[145] P. Estrela, P. Damborský, J. Švitel, and J. Katrlík, "Optical biosensors," Essays in Biochemistry **60**(1), 91–100 (2016).

[146] M. Soler and L. M. Lechuga, "Biochemistry strategies for label-free optical sensor biofunctionalization: Advances towards real applicability," Analytical and bioanalytical chemistry **414**(18), 5071–5085 (2022).

[147] J. G. Wangüemert-Pérez, A. Hadij-ElHouati, A. Sánchez-Postigo, J. Leuermann, D.-X. Xu, P. Cheben, A. Ortega-Moñux, R. Halir, and Íñigo Molina-Fernández, "Subwavelength structures for silicon photonics biosensing," Optics & Laser Technology **109**, 437–448 (2019).

[148] H.-P. Loock and P. D. Wentzell, "Detection limits of chemical sensors: Applications and misapplications," Sensors and Actuators B: Chemical **173**, 157–163 (2012).

[149] M. R. Bryan, J. N. Butt, J. Bucukovski, and B. L. Miller, "Biosensing with silicon nitride microring resonators integrated with an on-chip filter bank spectrometer," ACS Sensors **8**(2), 739–747 (2023).

[150] L. Liu, Z. Hu, M. Ye, Z. Yu, C. Ma, and J. Li, "On-Chip refractive index sensor with ultra-high sensitivity based on sub-wavelength grating racetrack microring resonators and Vernier effect," IEEE Photonics Journal **14**(5), 1–7 (2022).

[151] M. Yadav and A. Aksnes, "Multiplexed Mach-Zehnder interferometer assisted ring resonator sensor," Optics Express **30**(2), 1388–1396 (2022).

[152] S. Hassan, C. C. Schreib, X. Zhao, G. Duret, D. S. Roman, V. Nair, T. Cohen-Karni, O. Veiseh, and J. T. Robinson, "Real-time in vivo sensing of nitric oxide using photonic microring resonators," ACS Sensors **7**(8), 2253–2261 (2022).

[153] H.-T. Kim, B. Ramdam, and M. Yu, "Silicon ring resonator with ZIF-8/PDMS cladding for sensing dissolved CO2 gas in perfluorocarbon solutions," Sensors and Actuators B: Chemical **404**, 135,305 (2024).

[154] Y. Chang, B. Dong, Y. Ma, J. Wei, Z. Ren, and C. Lee, "Vernier effect-based tunable mid-infrared sensor using silicon-on-insulator cascaded rings," Optics Express **28**(5), 6251–6260 (2020).

[155] R. Guo, Q. He, Z. Zhang, Y. Xu, S. Zhang, Q. Lang, S. Xiao, P. Han, J. Wang, T. Ding, T. Liu, H. K. Tsang, K. Goda, and Z. Cheng, "High-Q silicon microring resonator with ultra-thin sub-wavelength thicknesses for sensitive gas sensing," Applied Physics Reviews **11**(2), 021,417 (2024).

[156] G. Antonacci, J. Goyvaerts, H. Zhao, B. Baumgartner, B. Lendl, and R. Baets, "Ultra-sensitive refractive index gas sensor with functionalized silicon nitride photonic circuits," APL Photonics **5**(8), 081,301 (2020).

[157] S. Gali, A. Keloth, and S. K. Selvaraja, "On-chip chemical sensing using double-slot silicon waveguide," IEEE Sensors Journal **23**(8), 8360–8365 (2023).

[158] Y. Luo, R. Yin, L. Lu, Q. Huang, S. Jiang, F. Liu, Q. Liu, and Q. Li, "Asymmetric Mach–Zehnder interferometer-based optical sensor with characteristics of both wavelength and temperature independence," Journal of Optics **52**(3), 1008–1021 (2023).

[159] A. M. Taha, S. Yousuf, M. S. Dahlem, and J. Viegas, "Highly-sensitive unbalanced MZI gas sensor assisted with a temperature-reference ring resonator," IEEE Photonics Journal **14**(6), 1–9 (2022).

[160] F. Piretta, F. Samà, F. Bontempi, J. Elaskar, D. Angeloni, and C. J. Oton, "Interferometer-based chemical sensor on chip with enhanced responsivity and low-cost interrogation," Biomedical Optics Express **15**(5), 2767–2779 (2024).

[161] R. Li, L. Yu, J. Li, W. Li, Y. Feng, J. Wang, and X. Xu, "Sensitivity enhancement of bimodal waveguide interferometric sensor based on regional mode engineering," Optics Express **32**(6), 10,274–10,283 (2024).

[162] M. Sieger, F. Balluff, X. Wang, S.-S. Kim, L. Leidner, G. Gauglitz, and B. Mizaikoff, "On-chip integrated mid-infrared GaAs/AlGaAs Mach–Zehnder interferometer," Analytical chemistry **85**(6), 3050–3052 (2013).

[163] I. Doughan, K. Oyemakinwa, O. Ovaskainen, and M. Roussey, "Strip-loaded Mach–Zehnder interferometer for absolute refractive index sensing," Scientific Reports **14**(1), 3064 (2024).

[164] L. Tombez, E. J. Zhang, J. S. Orcutt, S. Kamlapurkar, and W. M. J. Green, "Methane absorption spectroscopy on a silicon photonic chip," Optica **4**(11), 1322–1325 (2017).

[165] N. Barua, W. T. Winter, S. McAuley, J. Prestage, A. R. Salmon, P. T. Clarkson, H.-J. Lee, T.-A. Lee, Y. Wang, and T. Hutter, "Spectral comparison of nanoporous silica-adsorbed organic molecules with gaseous and liquid states using a new waveguide technology," Vibrational Spectroscopy **125**, 103,496 (2023).

[166] M. Pi, J. Ji, C. Zheng, X. Li, H. Zhao, Z. Peng, J. Lang, Y. Zhang, Y. Wang, and F. K. Tittel, "On-chip near-infrared absorption enhancement of liquid water using chalcogenide waveguide with silver island film," Microwave and Optical Technology Letters **65**(5), 1060–1064 (2023).

[167] V. Mittal, G. Devitt, M. Nedeljkovic, L. G. Carpenter, H. M. H. Chong, J. S. Wilkinson, S. Mahajan, and G. Z. Mashanovich, "Ge on Si waveguide mid-infrared absorption spectroscopy of proteins and their aggregates," Biomedical Optics Express **11**(8), 4714–4722 (2020).

[168] R. Zegadi, N. Lorrain, L. Bodiou, M. Guendouz, L. Ziet, and J. Charrier, "Enhanced mid-infrared gas absorption spectroscopic detection using chalcogenide or porous germanium waveguides," Journal of Optics **23**(3), 035,102 (2021).

[169] M. Pi, Y. Huang, H. Zhao, Z. Peng, J. Lang, J. Ji, L. Teng, F. Song, L. Liang, Y. Zhang, C. Zheng, Y. Wang, and F. K. Tittel, "Theoretical and experimental investigation of on-chip mid-infrared chalcogenide waveguide CH4 sensor based on wavelength modulation spectroscopy," Sensors and Actuators B: Chemical **362**, 131,782 (2022).

[170] J. Zhou, D. Al Husseini, J. Li, Z. Lin, S. Sukhishvili, G. L. Coté, R. Gutierrez-Osuna, and P. T. Lin, "Detection of volatile organic compounds using mid-infrared silicon nitride waveguide sensors," Scientific Reports **12**(1), 5572 (2022).

[171] J. Zhou, Z. Zhang, B. Dong, Z. Ren, W. Liu, and C. Lee, "Midinfrared spectroscopic analysis of aqueous mixtures using artificial-intelligence-enhanced metamaterial waveguide sensing platform," ACS Nano **17**(1), 711–724 (2023).

[172] P. Forsberg, P. Hollman, and M. Karlsson, "High sensitivity infrared spectroscopy with a diamond waveguide on aluminium nitride," Analyst **146**(22), 6981–6989 (2021).

[173] H. D. Yallew, M. Vlk, A. Datta, S. Alberti, R. A. Zakoldaev, J. Høvik, A. Aksnes, and J. Jágerská, "Sub-ppm methane detection with mid-infrared slot waveguides," ACS photonics **10**(12), 4282–4289 (2023).

[174] M. Grayson, G. Krueper, B. Xu, M. Zohrabi, D. Hjelme, J. T. Gopinath, and W. Park, "On-chip mid-infrared optical sensing with GeSbSe waveguides and resonators," Optics Express **31**(2), 877– 889 (2023).

[175] R. Halir, "Photonic Reflectometer on Silicon-on-Insulator," Ph.D. thesis, Universidad de Málaga (2010).

[176] C. A. Aloson-Ramos, "Photonic chip interconnects and integrated polarization management for coherent communication," Ph.D. thesis, Universidad de Málaga (2014).

[177] "FEM Generalized Mode Solver - FemSIM | RSoft Photonic Device Tools," `https://www.synopsys.com/photonic-solutions/rsoft-photonic-device-tools/passive-device-femsim.html`.

[178] J. Vörös, "The density and refractive index of adsorbing protein layers," Biophysical journal **87**(1), 553–561 (2004).

[179] R. Baets and P. E. Lagasse, "Loss calculation and design of arbitrarily curved integrated-optic waveguides," Journal of the Optical Society of America **73**(2), 177–182 (1983).

[180] W. W. Lui, C.-L. Xu, and W.-P. Huang, "Full-vectorial wave propagation in semiconductor optical bending waveguides and equivalent straight waveguide approximations," Journal of Lightwave Technoly **16**(5), 910 (1998).

[181] V. Subramaniam, G. De Brabander, D. Naghski, and J. Boyd, "Measurement of mode field profiles and bending and transition losses in curved optical channel waveguides," Journal of Lightwave Technology **15**(6), 990–997 (1997).

[182] R. Alferness, W. Burns, J. Donelly, I. Kaminow, H. Kogelnik, F. Leonberger, A. Milton, T. Tamir, and R. Tucker, *Guided-wave optoelectronics*, vol. 26 (Springer Science & Business Media, 2013).

[183] "FDTD Simulation Software - FullWAVE | RSoft Photonic Device Tools," `https://www.synopsys.com/photonic-solutions/rsoft-photonic-device-tools/passive-device-fullwave.html`.

[184] "Beam Propagation Method Software - BeamPROP | RSoft Photonic Device Tools," https://www.synopsys.com/photonic-solutions/rsoft-photonic-device-tools/passive-device-beamprop.html.

[185] "Cornerstone Project," https://www.cornerstone.sotonfab.co.uk.

[186] "Applied Nanotools Inc." https://www.appliednt.com.

[187] "Nazca Design - Photonic IC design framework," https://nazca-design.org.

[188] "Nazca reference modules," https://nazca-design.org/manual/nazca.html.

[189] Í. Molina-Fernández, J. Leuermann, A. Ortega-Moñux, J. G. Wangüemert-Pérez, and R. Halir, "Fundamental limit of detection of photonic biosensors with coherent phase readout," Optics Express **27**(9), 12,616–12,629 (2019).

[190] J. Leuermann, A. Fernández-Gavela, A. Torres-Cubillo, S. Postigo, A. Sánchez-Postigo, L. M. Lechuga, R. Halir, and Í. Molina-Fernández, "Optimizing the limit of detection of waveguide-based interferometric biosensor devices," Sensors **19**(17), 3671 (2019).

[191] J. Leuermann, "Silicon Photonics Mach-Zehnder Biosensor with Coherent Detection for Point-of-Care Devices," Ph.D. thesis, Universidad de Málaga (2021).

[192] G. Taubin, "Estimation of planar curves, surfaces, and nonplanar space curves defined by implicit equations with applications to edge and range image segmentation," IEEE Transactions on Pattern Analysis & Machine Intelligence **13**(11), 1115–1138 (1991).

[193] H. Kramers, "Some remarks on the theory of absorption and refraction of X-rays," Nature **117**(2952), 774–775 (1926).

[194] R. d. L. Kronig, "On the theory of dispersion of x-rays," Journal of the Optical Society of America **12**(6), 547–557 (1926).

[195] K.-E. Peiponen, V. Lucarini, E. Vartiainen, and J. Saarinen, "Kramers-Kronig relations and sum rules of negative refractive index media," The European Physical Journal B-Condensed Matter and Complex Systems **41**, 61–65 (2004).

[196] P. Bruzzoni, R. Carranza, J. Collet Lacoste, and E. Crespo, "Kramers–Kronig transforms calculation with a fast convolution algorithm," Electrochimica Acta **48**(4), 341–347 (2002).

[197] C. C. Wang, J. Y. Tan, C. Y. Jing, and L. H. Liu, "Temperature-dependent optical constants of liquid isopropanol, n-butanol, and n-decane," Applied Optics **57**(12), 3003–3011 (2018).

[198] X. Zhang, J. Qiu, X. Li, J. Zhao, and L. Liu, "Complex refractive indices measurements of polymers in visible and near-infrared bands," Applied Optics **59**(8), 2337–2344 (2020).

[199] S. A. Rinehart, D. J. Benford, G. Cataldo, E. Dwek, R. Henry, J. Raymond E. Kinzer, J. Nuth, R. Silverberg, C. Wheeler, and E. Wollack, "Measuring the optical properties of astrophysical dust analogues: instrumentation and methods," Applied Optics **50**(21), 4115–4123 (2011).

[200] W. Rocha, S. Pilling, A. Domaracka, H. Rothard, and P. Boduch, "Infrared complex refractive index of N-containing astrophysical ices free of water processed by cosmic-ray simulated in laboratory," Spectrochimica Acta Part A: Molecular and Biomolecular Spectroscopy **228**, 117,826 (2020).

[201] X. Li, C. Wang, L. Ma, and L. Liu, "Ellipsometry-transmission measurement of the complex refractive indices for a series of organic solvents in the 200–1700 nm spectral range," Infrared Physics & Technology **125**, 104,313 (2022).

[202] C. Zhou, M. K. Hedayati, and A. Kristensen, "Multifunctional waveguide interferometer sensor: simultaneous detection of refraction and absorption with size-exclusion function," Optics Express **26**(19), 24,372–24,383 (2018).

[203] J. Bläsi and M. Gerken, "Multiplex microdisk biosensor based on simultaneous intensity and phase detection," Optics Express **31**(3), 4319–4333 (2023).

[204] Z. Tu, D. Gao, M. Zhang, and D. Zhang, "High-sensitivity complex refractive index sensing based on Fano resonance in the subwavelength grating waveguide micro-ring resonator," Optics Express **25**(17), 20,911–20,922 (2017).

[205] L. Xiang and L. Huang, "High-sensitivity complex refractive index sensor by designing a slot-waveguide side-coupled Fano resonant cavity," Optics Communications **475**, 126,298 (2020).

[206] R. S. El Shamy, M. A. Swillam, and X. Li, "On-chip complex refractive index detection at multiple wavelengths for selective sensing," Scientific Reports **12**(1), 9343 (2022).

[207] Y. Hu, Q. Ma, B. Y. Zhang, G. Ren, R. Ou, K. Xu, A. Salek, Y. Yang, X. Wen, Q. Li, N. Ha, V. Trinh, and J. Z. Ou, "Complex refractive index extraction for ultrathin molybdenum oxides using micro-photonic integrated circuit chips," Advanced Optical Materials **11**(17), 2300,340 (2023).

[208] F. Briano-Ottonello, C. Errando-Herranz, and K. B. Gylfason, "On-chip dispersion spectroscopy of CO2 using a mid-infrared microring resonator," in *CLEO: Science and Innovations*, pp. STh1N–3 (Optica Publishing Group, 2020).

[209] A. Torres-Cubillo, J. Leuermann, P. Reyes-Iglesias, A. Ortega-Moñux, J. G. Wangüemert-Pérez, I. Molina-Fernández, and R. Halir, "Towards complex refractive index sensing with a photonic integrated circuit," in *XXXV Simposium Nacional de la Unión Científica Internacional de Radio* (2020).

[210] K. Luke, Y. Okawachi, M. R. E. Lamont, A. L. Gaeta, and M. Lipson, "Broadband mid-infrared frequency comb generation in a Si3N4 microresonator," Optics Letters **40**(21), 4823–4826 (2015).

[211] Y. Arosa and R. de la Fuente, "Refractive index spectroscopy and material dispersion in fused silica glass," Optics Letters **45**(15), 4268–4271 (2020).

[212] S. Kedenburg, M. Vieweg, T. Gissibl, and H. Giessen, "Linear refractive index and absorption measurements of nonlinear optical liquids in the visible and near-infrared spectral region," Optical Materials Express **2**(11), 1588–1611 (2012).

[213] S. Novais, M. S. Ferreira, and J. L. Pinto, "Determination of thermo-optic coefficient of ethanol-water mixtures with optical fiber tip sensor," Optical Fiber Technology **45**, 276–279 (2018).

[214] D. Pérez, J. Fernández, R. Baños, J. D. Doménech, A. M. Sánchez, J. M. Cirera, R. Mas, J. Sánchez, S. Durán, E. Pardo, *et al.*, "Thermal tuners on a Silicon Nitride platform," arXiv preprint arXiv:1604.02958 (2016).

[215] "Fused Silica Glass (SiO2)," `https://www.crystran.co.uk/optical-materials/fused-silica-sio2`.

[216] R. Goldstein and S. Penner, "The near-infrared absorption of liquid water at temperatures between 27 and 209 C," Journal of Quantitative Spectroscopy and Radiative Transfer **4**(3), 441–451 (1964).

[217] J. D. Sarmiento-Merenguel, A. Ortega-Moñux, J.-M. Fédéli, J. G. Wangüemert-Pérez, C. Alonso-Ramos, E. Durán-Valdeiglesias, P. Cheben, Í. Molina-Fernández, and R. Halir, "Controlling leakage losses in subwavelength grating silicon metamaterial waveguides," Optics letters **41**(15), 3443–3446 (2016).

[218] R. Halir, I. Molina-Fernández, J. Wangüemert-Pérez, A. O.-M. nux, J. de Oliva-Rubio, and P. Cheben, "Characterization of integrated photonic devices with minimum phase technique," Optics Express **17**(10), 8349–8361 (2009).

[219] A. Torres-Cubillo, J. G. Wanguemert-Pérez, A. Sánchez-Postigo, Í. Molina-Fernández, and R. Halir, "Mitigating reflections in integrated gas sensors," in *Norwegian Electro-Optics Meeting* (2022).

[220] A. D. Simard, Y. Painchaud, and S. LaRochelle, "Integrated Bragg gratings in spiral waveguides," Optics Express **21**(7), 8953–8963 (2013).

[221] J. E. Saunders, C. Sanders, H. Chen, and H.-P. Loock, "Refractive indices of common solvents and solutions at 1550 nm," Applied Optics **55**(4), 947–953 (2016).

[222] X. Li, L. Liu, J. Zhao, and J. Tan, "Optical Properties of Sodium Chloride Solution within the Spectral Range from 300 to 2500 nm at Room Temperature," Applied Spectroscopy **69**(5), 635–640 (2015).

[223] E. Sani and A. Dell'Oro, "Spectral optical constants of ethanol and isopropanol from ultraviolet to far infrared," Optical Materials **60**, 137–141 (2016).

[224] R. Levy and S. Ruschin, "Design of a Single-Channel Modal Interferometer Waveguide Sensor," IEEE Sensors Journal **9**(2), 146–1 (2009).

[225] K. E. Zinoviev, A. B. Gonzalez-Guerrero, C. Dominguez, and L. M. Lechuga, "Integrated Bimodal Waveguide Interferometric Biosensor for Label-Free Analysis," Journal of Lightwave Technology **29**(13), 1926–1930 (2011).

[226] A. B. González-Guerrero, J. Maldonado, S. Dante, D. Grajales, and L. M. Lechuga, "Direct and label-free detection of the human growth hormone in urine by an ultrasensitive bimodal waveguide biosensor," Journal of Biophotonics **10**(1), 61–67 (2017).

[227] P. Ramirez-Priego, M.-C. Estévez, H. J. Díaz-Luisravelo, J. J. Manclús, Ángel Montoya, and L. M. Lechuga, "Real-time monitoring of fenitrothion in water samples using a silicon nanophotonic biosensor," Analytica Chimica Acta **1152**, 338,276 (2021).

[228] L. Torrijos-Morán, A. Griol, and J. García-Rupérez, "Experimental study of subwavelength grating bimodal waveguides as ultrasensitive interferometric sensors," Optics Letters **44**(19), 4702–4705 (2019).

[229] L. Torrijos-Morán, A. Griol, and J. García-Rupérez, "Slow light bimodal interferometry in one-dimensional photonic crystal waveguides," Light: Science & Applications **10**(1), 16 (2021).

[230] R. Bruck and R. Hainberger, "Sensitivity and design of grating-assisted bimodal interferometers for integrated optical biosensing," Optics Express **22**(26), 32,344–32,352 (2014).

[231] B. Bassols-Cornudella, P. Ramirez-Priego, M. Soler, M.-C. Estévez, H. J. D. Luis-Ravelo, M. Cardenosa-Rubio, and L. M. Lechuga, "Novel Sensing Algorithm for Linear Read-Out of Bimodal Waveguide Interferometric Biosensors," Journal of Lightwave Technoly **40**(1), 237–244 (2022).

[232] C. Schweikert, A. Tsianaka, N. Hoppe, R. H. Klenk, R. Elster, M. Greul, M. Kaschel, A. Southan, W. Vogel, and M. Berroth, "Integrated polarization mode interferometer in 220-nm silicon-on-insulator technology," Optics Letters **47**(17), 4536–4539 (2022).

[233] Q. Liu, K. W. Kim, Z. Gu, J. S. Kee, and M. K. Park, "Single-channel Mach-Zehnder interferometric biochemical sensor based on two-lateral-mode spiral waveguide," Optics Express **22**(23), 27,910–27,920 (2014).

[234] J. Wang, Y. Xuan, M. Qi, H. Huang, Y. Li, M. Li, X. Chen, Z. Sheng, A. Wu, W. Li, *et al.*, "Broadband and fabrication-tolerant on-chip scalable mode-division multiplexing based on mode-evolution counter-tapered couplers," Optics letters **40**(9), 1956–1959 (2015).

[235] K. B. Beć, J. Grabska, and C. W. Huck, "Biomolecular and bioanalytical applications of infrared spectroscopy–A review," Analytica Chimica Acta **1133**, 150–177 (2020).

[236] D. An, F. Sun, Y. Bian, J. Ni, Q. J. Wang, and X. Yu, "Mid-infrared absorption spectroscopy with enhanced detection performance for biomedical applications," Applied Spectroscopy Reviews **58**(10), 834–868 (2023).

[237] C. Zheng, M. Pi, F. Song, Y. Li, Z. Peng, G. Guan, L. Zhang, Y. Ma, Y. Min, W. Ye, and Y. Wang, "Recent Progress in Infrared Absorption Spectroscopy for Gas Sensing With Discrete Optics, Hollow-Core Fibers and On-Chip Waveguides," Journal of Lightwave Technology **41**(13), 4079–4096 (2023).

[238] P. S. Fomina, M. A. Proskurnin, B. Mizaikoff, and D. S. Volkov, "Infrared spectroscopy in aqueous solutions: Capabilities and challenges," Critical Reviews in Analytical Chemistry **53**(8), 1748–1765 (2023).

[239] Y. Ji, X. Yang, Z. Ji, L. Zhu, N. Ma, D. Chen, X. Jia, J. Tang, and Y. Cao, "DFT-calculated IR spectrum amide I, II, and III band contributions of N-methylacetamide fine components," ACS omega **5**(15), 8572–8578 (2020).

[240] M. Sieger, J. Haas, M. Jetter, P. Michler, M. Godejohann, and B. Mizaikoff, "Mid-infrared spectroscopy platform based on GaAs/AlGaAs thin-film waveguides and quantum cascade lasers," Analytical Chemistry **88**(5), 2558–2562 (2016).

[241] J. Haas, R. Stach, C. Kolm, R. Krska, and B. Mizaikoff, "Gallium arsenide waveguides as a platform for direct mid-infrared vibrational spectroscopy," Analytical and Bioanalytical Chemistry **412**, 3447–3456 (2020).

[242] V. Mittal, M. Nedeljkovic, D. J. Rowe, G. S. Murugan, and J. S. Wilkinson, "Chalcogenide glass waveguides with paper-based fluidics for mid-infrared absorption spectroscopy," Optics Letters **43**(12), 2913–2916 (2018).

[243] E. Baudet, A. Gutierrez-Arroyo, M. Baillieul, J. Charrier, P. Němec, L. Bodiou, J. Lemaitre, E. Rinnert, K. Michel, B. Bureau, *et al.*, "Development of an evanescent optical integrated sensor in the mid-infrared for detection of pollution in groundwater or seawater," Advanced Device Materials **3**(2), 23–29 (2017).

[244] N. T. Benéitez, B. Baumgartner, J. Missinne, S. Radosavljevic, D. Wacht, S. Hugger, P. Leszcz, B. Lendl, and G. Roelkens, "Mid-IR sensing platform for trace analysis in aqueous solutions based on a germanium-on-silicon waveguide chip with a mesoporous silica coating for analyte enrichment," Optics Express **28**(18), 27,013–27,027 (2020).

[245] A. Teuber, G. Caniglia, M. Wild, M. Godejohann, C. Kranz, and B. Mizaikoff, "Espresso science: Laser-based diamond thin-film waveguide sensors for the quantification of caffeine," ACS sensors **8**(5), 1871–1881 (2023).

[246] A. V. Oppenheim, A. S. Willsky, and S. H. Nawab, *Signals & systems*, chap. Sampling (Pearson Education, 1997).

[247] J. Shim, J. Lim, D.-M. Geum, B. H. Kim, S.-Y. Ahn, and S. Kim, "Tailoring bolometric properties of a TiO x/Ti/TiO x tri-layer film for integrated optical gas sensors," Optics Express **29**(12), 18,037–18,058 (2021).

[248] A. D. Rakić and M. L. Majewski, "Modeling the optical dielectric function of GaAs and AlAs: Extension of Adachi's model," Journal of Applied Physics **80**(10), 5909–5914 (1996).

[249] T. Skauli, P. Kuo, K. Vodopyanov, T. Pinguet, O. Levi, L. Eyres, J. Harris, M. Fejer, B. Gerard, L. Becouarn, *et al.*, "Improved dispersion relations for GaAs and applications to nonlinear optics," Journal of Applied Physics **94**(10), 6447–6455 (2003).

[250] P. Němec, M. Olivier, E. Baudet, A. Kalendova, P. Benda, and V. Nazabal, "Optical properties of $GeSe2_{100-x}Sb2Se3_x$ glasses in near-and middle-infrared spectral regions," Materials Research Bulletin **51**, 176–179 (2014).

[251] E. Shkondin, O. Takayama, M. A. Panah, P. Liu, P. V. Larsen, M. D. Mar, F. Jensen, and A. Lavrinenko, "Large-scale high aspect ratio Al-doped ZnO nanopillars arrays as anisotropic metamaterials," Optical Materials Express **7**(5), 1606–1627 (2017).

[252] T. Amotchkina, M. Trubetskov, D. Hahner, and V. Pervak, "Characterization of e-beam evaporated Ge, YbF3, ZnS, and LaF3 thin films for laser-oriented coatings," Applied Optics **59**(5), A40–A47 (2020).

[253] P. Dore, A. Nucara, D. Cannavò, G. D. Marzi, P. Calvani, A. Marcelli, R. S. Sussmann, A. J. Whitehead, C. N. Dodge, A. J. Krehan, and H. J. Peters, "Infrared properties of chemical-vapor deposition polycrystalline diamond windows," Applied Optics **37**(24), 5731–5736 (1998).

[254] J. Kischkat, S. Peters, B. Gruska, M. Semtsiv, M. Chashnikova, M. Klinkmüller, O. Fedosenko, S. Machulik, A. Aleksandrova, G. Monastyrskyi, Y. Flores, and W. T. Masselink, "Mid-infrared optical properties of thin films of aluminum oxide, titanium dioxide, silicon dioxide, aluminum nitride, and silicon nitride," Applied Optics **51**(28), 6789–6798 (2012).

[255] G. M. Hale and M. R. Querry, "Optical Constants of Water in the 200-nm to 200-μm Wavelength Region," Applied Optics **12**(3), 555–563 (1973).

[256] J. Haas, E. V. Catalán, P. Piron, F. Nikolajeff, L. Österlund, M. Karlsson, and B. Mizaikoff, "Polycrystalline diamond thin-film waveguides for mid-infrared evanescent field sensors," ACS Omega **3**(6), 6190–6198 (2018).

[257] J. Lacey and F. Payne, "Radiation loss from planar waveguides with random wall imperfections," IEE Proceedings J. (Optoelectronics) **137**(4), 282–289 (1990).

[258] A. Teuber, G. Caniglia, H. Barth, C. Kranz, and B. Mizaikoff, "Thin-Film Waveguide Laser Spectroscopy: A Novel Platform for Bacterial Analysis," Analytical Chemistry **95**(45), 16,600–16,608 (2023).

[259] S. Sharma and S. Roy, "Optimizing bend loss in optical waveguide channel routing on photonic integrated circuits," Journal of Computational Electronics **22**(1), 350–363 (2023).

[260] S. Hong, L. Zhang, Y. Wang, M. Zhang, Y. Xie, and D. Dai, "Ultralow-loss compact silicon photonic waveguide spirals and delay lines," Photonics Research **10**(1), 1–7 (2022).

[261] S. Mi, M. Kiss, T. Graziosi, and N. Quack, "Integrated photonic devices in single crystal diamond," Journal of Physics: Photonics **2**(4), 042,001 (2020).

[262] Q. Yang, C. Giese, and S. Hugger, "Calculation of coupling coefficients for diamond microring resonators," Journal of Applied Physics **135**(7) (2024).

[263] T. L. Myers, R. G. Tonkyn, T. O. Danby, M. S. Taubman, B. E. Bernacki, J. C. Birnbaum, S. W. Sharpe, and T. J. Johnson, "Accurate Measurement of the Optical Constants n and k for a Series of 57 Inorganic and Organic Liquids for Optical Modeling and Detection," Applied Spectroscopy **72**(4), 535–550 (2018).

[264] C. S. Huertas and L. M. Lechuga, "Ultrasensitive label-free nucleic-acid biosensors based on bimodal waveguide interferometers," Biomedical Engineering Technologies: Volume 1 pp. 89–125 (2022).

[265] A. Cygan, S. Wójtewicz, H. Jóźwiak, G. Kowzan, N. Stolarczyk, K. Bielska, P. Wcisło, R. Ciuryło, and D. Lisak, "Heterodyne dispersive cavity ring-down spectroscopy exploiting eigenmode frequencies for high-fidelity measurements," arXiv preprint arXiv:2403.01961 (2024).

[266] D. González-Andrade, R. F. de Cabo, J. Vilas, I. Olivares, A. Dias, J. M. Luque-González, J. G. Wangüemert-Pérez, A. Ortega-Moñux, Í. Molina-Fernández, R. Halir, *et al.*, "Mode converter and multiplexer with a subwavelength phase shifter for extended broadband operation," IEEE Photonics Technology Letters **33**(22), 1262–1265 (2021).

[267] C. J. Stirling, R. Halir, A. Sánchez-Postigo, Z. Qu, J. D. Reynolds, J. S. Penadés, G. Senthil Murugan, A. Ortega-Moñux, J. G. Wangüemert-Pérez, Í. Molina-Fernández, *et al.*, "Broadband 2×2 multimode interference coupler for mid-infrared wavelengths," Optics Letters **46**(21), 5300–5303 (2021).

[268] A. Sánchez-Postigo, R. Halir, J. G. Wangüemert-Pérez, A. Ortega-Moñux, S. Wang, M. Vachon, J. H. Schmid, D.-X. Xu, P. Cheben, and Í. Molina-Fernández, "Breaking the coupling efficiency–bandwidth trade-off in surface grating couplers using zero-order radiation," Laser & Photonics Reviews **15**(6), 2000,542 (2021).

[269] D. S. Zemtsov, D. M. Zhigunov, S. S. Kosolobov, A. K. Zemtsova, M. Puplauskis, I. A. Pshenichnyuk, and V. P. Drachev, "Broadband silicon grating couplers with high efficiency and a robust design," Optics Letters **47**(13), 3339–3342 (2022).

[270] B. Bhandari, C.-S. Im, K.-P. Lee, S.-M. Kim, M.-C. Oh, and S.-S. Lee, "Compact and broadband edge coupler based on multi-stage silicon nitride tapers," IEEE Photonics Journal **12**(6), 1–11 (2020).

[271] P. T. Lin, V. Singh, H.-Y. G. Lin, T. Tiwald, L. C. Kimerling, and A. M. Agarwal, "Low-Stress Silicon Nitride Platform for Mid-Infrared Broadband and Monolithically Integrated Microphotonics," Advanced Optical Materials **1**(10), 732–739 (2013).

[272] P. T. Lin, V. Singh, L. Kimerling, and A. Murthy Agarwal, "Planar silicon nitride mid-infrared devices," Applied physics letters **102**(25) (2013).

[273] R. Soref, "Mid-infrared photonics in silicon and germanium," Nature photonics **4**(8), 495–497 (2010).

[274] A. Sánchez-Postigo, J. G. Wangüemert-Pérez, J. Soler Penadés, A. Ortega-Moñux, M. Nedeljkovic, R. Halir, F. El Mokhtari Mimun, Y. Xu Cheng, Z. Qu, A. Z. Khokhar, *et al.*, "Mid-infrared suspended waveguide platform and building blocks," IET Optoelectronics **13**(2), 55–61 (2019).

[275] H. Nyquist, "Certain Topics in Telegraph Transmission Theory," Transactions of the American Institute of Electrical Engineers **47**(2), 617–644 (1928).

[276] C. Shannon, "Communication in the Presence of Noise," Proceedings of the IRE **37**(1), 10–21 (1949).

[277] K. Kikuchi, "Characterization of semiconductor-laser phase noise and estimation of bit-error rate performance with low-speed offline digital coherent receivers," Optics Express **20**(5), 5291–5302 (2012).

[278] D. M. Baney, P. Gallion, and R. S. Tucker, "Theory and measurement techniques for the noise figure of optical amplifiers," Optical fiber technology **6**(2), 122–154 (2000).

[279] A. Sánchez-Postigo, A. Ortega-Moñux, J. Soler Penades, A. Osman, M. Nedeljkovic, Z. Qu, Y. Wu, Í. Molina-Fernández, P. Cheben, G. Z. Mashanovich, *et al.*, "Suspended germanium waveguides with subwavelength-grating metamaterial cladding for the mid-infrared band," Optics Express **29**(11), 16,867–16,878 (2021).

[280] A. Sánchez-Postigo, "Suspended Waveguide Platforms for Mid-Infrared Group IV Photonics," Ph.D. thesis, Universidad de Málaga (2019).

[281] J. S. Penadés, C. Alonso-Ramos, A. Khokhar, M. Nedeljkovic, L. Boodhoo, A. Ortega-Moñux, I. Molina-Fernández, P. Cheben, and G. Mashanovich, "Suspended SOI waveguide with sub-wavelength grating cladding for mid-infrared," Optics letters **39**(19), 5661–5664 (2014).